

# EXOSAT AND GINGA OBSERVATIONS OF INTERACTING BINARY STARS

Mark Henry Jones

## Abstract

X-ray observations of three classes of interacting binary are presented. The systems studied are believed to be undergoing mass transfer by Roche lobe overflow onto a compact object. The observations were made between 1983 and 1989 with the EXOSAT and *Ginga* satellite observatories.

The dwarf nova SS Cygni was subject to extensive monitoring using EXOSAT. In quiescence, the source has a hard spectrum which shows thermal iron  $K\alpha$  and possibly  $K\beta$  emission. In outburst, emission is dominated by a soft component which emits at energies below  $\sim 1$  keV. This soft emission shows large amplitude, quasi-coherent sinusoidal modulation at periods in the range 7.4 to 10.8 sec. The evolution of the properties of this oscillation through outburst are studied in detail.

A two day *Ginga* observation of the x-ray pulsar 1E 2259+586 is described. The pulse arrival times were searched for orbital modulation, and an upper limit ( $3\sigma$ ) to the projected semi-major axis was found to be  $a_r \sin i < 140$  lt-msec for periods from 1000 to 5000 sec. The source spectrum shows a broad line feature at  $\sim 7$  keV. It is suggested that this may arise from cyclotron processes.

Details are given of the *Ginga* observations of low mass x-ray binary systems which show 'dip' variability, the sources being XB 1916-053, XBT 0748-676, and X 1624-490. A re-analysis of the EXOSAT observations of X 1624-490 is also presented. Modulation in dippers arises from occultation of the compact x-ray emitting regions by structure in the accretion disc. Timing measurements constrain on the size of the emitting region and the distribution of the obscuring material. Spectral changes in dip events require a two-component model of absorption. By simulation, it is shown that this behaviour may arise from single component absorption if the column density changes rapidly. Revised estimates for the metal abundances of the three sources are given.



EXOSAT AND GINGA  
OBSERVATIONS OF  
INTERACTING  
BINARY STARS

Mark Henry Jones

Thesis submitted to the University of Leicester  
for the degree of Doctor of Philosophy

May 1990

X-ray Astronomy Group  
Department of Physics and Astronomy  
University of Leicester

UMI Number: U038648

All rights reserved

INFORMATION TO ALL USERS

The quality of this reproduction is dependent upon the quality of the copy submitted.

In the unlikely event that the author did not send a complete manuscript and there are missing pages, these will be noted. Also, if material had to be removed, a note will indicate the deletion.



UMI U038648

Published by ProQuest LLC 2015. Copyright in the Dissertation held by the Author.  
Microform Edition © ProQuest LLC.

All rights reserved. This work is protected against  
unauthorized copying under Title 17, United States Code.



ProQuest LLC  
789 East Eisenhower Parkway  
P.O. Box 1346  
Ann Arbor, MI 48106-1346



0618790057

X7517 3044X

## Declaration

I hereby declare that no part of this thesis has been previously submitted to this or any other University as part of the requirement for a higher degree. The work described herein was conducted by the undersigned except for the contributions from colleagues and other workers which are acknowledged in the text, and in the following note on publications.

A handwritten signature in black ink, appearing to read "M.H. Jones" followed by a flourish and a period.

Mark Henry Jones

May 1990

## Publications

Some of the work reported here has been published elsewhere as follows:

Koyama K., Nagase F., Ogawara Y., Shinoda K., Kawai N., Jones M.H., Williams O.R., Watson M.G., Makishima K., and Ohashi T., 1989 Publ. astr. Soc. Japan, 41,461. "Ginga Observation of the X-ray Pulsar 1E 2259+586 in the Supernova Remnant G109.1-1.0".

Jones M.H., and Watson, M.G., 1989, Proc. of the 23rd ESLAB Symposium. "The X-ray dip source 4U 1624-49".

Smale A.P., Mukai K., Williams O.R., Jones M.H., Parmar A.N., and Corbett R.H.D., 1989, Proc. of the 23rd ESLAB Symposium. "Ginga Observations of dipping Low Mass X-ray Binaries"

This thesis is dedicated to

Mum and Dad

# Contents

<b>1</b>	<b>Introduction</b>	<b>1</b>
1.1	INTERACTING BINARY STARS . . . . .	1
1.2	THEORETICAL CONCEPTS . . . . .	2
1.2.1	Mass-loss Mechanisms . . . . .	2
1.2.2	Compact Objects . . . . .	4
1.2.3	Luminosities and Temperatures . . . . .	6
1.2.4	Accretion Discs . . . . .	8
1.2.5	Components of a Physical Model . . . . .	11
1.2.6	Magnetically Controlled Accretion . . . . .	13
1.2.7	Wind Accretion . . . . .	13
<b>2</b>	<b>Instrumentation and Data Reduction</b>	<b>15</b>
2.1	INTRODUCTION . . . . .	15
2.2	THE EXOSAT OBSERVATORY . . . . .	16
2.2.1	The Low Energy Telescope . . . . .	17

2.2.2	The Medium Energy Detector Array . . . . .	20
2.3	THE GINGA OBSERVATORY . . . . .	21
2.3.1	The Large Area Counter . . . . .	23
2.4	DATA REDUCTION . . . . .	24
2.4.1	X-ray Background Subtraction . . . . .	25
2.5	SPECTRAL ANALYSIS . . . . .	31
2.6	TIME SERIES ANALYSIS . . . . .	33
2.6.1	Auto and Cross Correlation . . . . .	34
2.6.2	Power Spectrum . . . . .	37
2.6.3	Periodogram Techniques . . . . .	41
2.6.4	Fractal Analysis . . . . .	41
<b>3</b>	<b>Dwarf Nova Variables</b>	<b>46</b>
3.1	INTRODUCTION . . . . .	46
3.2	CLASSIFICATION OF DWARF NOVAE . . . . .	46
3.3	THEORIES OF OUTBURST . . . . .	52
3.4	X-RAY PROPERTIES . . . . .	56
3.5	SHORT PERIOD OSCILLATIONS . . . . .	59
3.6	SUMMARY . . . . .	64
<b>4</b>	<b>The EXOSAT observations of SS Cygni</b>	<b>66</b>
4.1	INTRODUCTION . . . . .	66

4.1.1	SS Cygni . . . . .	66
4.2	OBSERVATIONS . . . . .	67
4.3	GENERAL X-RAY BEHAVIOUR . . . . .	68
4.3.1	The Soft X-ray Component . . . . .	76
4.3.2	The Hard X-ray Component . . . . .	78
4.4	SOFT X-RAY PULSATIONS . . . . .	85
4.4.1	The Search for Oscillations . . . . .	87
4.4.2	Detailed Analysis of the Pulsations . . . . .	91
4.4.3	Summary of Pulsation Properties . . . . .	109
4.5	DISCUSSION AND SUMMARY . . . . .	112
4.5.1	General X-ray Behaviour . . . . .	112
4.5.2	Hard X-ray Spectrum . . . . .	115
4.5.3	Physical Models for Soft X-ray Pulsations . . . . .	117
4.6	SUMMARY AND FUTURE PROSPECTS . . . . .	123
<b>5</b>	<b>The X-ray Pulsar 1E 2259+586</b>	<b>126</b>
5.1	INTRODUCTION . . . . .	126
5.2	OBSERVATION . . . . .	129
5.3	THE PULSE PROFILE . . . . .	129
5.4	THE ENERGY SPECTRUM . . . . .	131
5.5	PULSE TIMING MEASUREMENT . . . . .	135
5.5.1	Period Determination . . . . .	138

5.5.2	The Search for Orbital Modulation . . . . .	141
5.6	DISCUSSION . . . . .	143
5.7	SUMMARY . . . . .	153
<b>6</b>	<b>Vertical Structure in Accretion Discs</b>	<b>154</b>
6.1	INTRODUCTION . . . . .	154
6.2	ORBITAL MODULATION IN LMXB SYSTEMS . . . . .	154
6.3	DIP SOURCES . . . . .	158
6.4	ADC SOURCES . . . . .	166
6.5	THEORIES OF THICKENED DISCS . . . . .	169
6.6	SUMMARY . . . . .	171
<b>7</b>	<b>Observations of Dip Sources</b>	<b>172</b>
7.1	INTRODUCTION . . . . .	172
7.1.1	System Parameters . . . . .	173
7.2	OBSERVATIONS . . . . .	176
7.2.1	XB 1916-053 . . . . .	176
7.2.2	XBT 0748-676 . . . . .	177
7.2.3	X 1624-490 . . . . .	180
7.3	GENERAL X-RAY PROPERTIES . . . . .	181
7.3.1	XB 1916-053 . . . . .	181
7.3.2	XBT 0748-676 . . . . .	183

7.3.3	X 1624-490 . . . . .	183
7.4	MINIMUM TIMESCALES . . . . .	184
7.5	CHARACTERISTIC TIMESCALES . . . . .	187
7.5.1	Gaussian models . . . . .	193
7.5.2	Power Law models . . . . .	195
7.6	THE NON-DIP SPECTRAL BEHAVIOUR . . . . .	200
7.6.1	XB 1916-053 . . . . .	200
7.6.2	XBT 0748-676 . . . . .	202
7.6.3	X 1624-490 . . . . .	202
7.7	SPECTRAL ANALYSIS OF THE DIPS . . . . .	205
7.7.1	Simulation of the mixing effect . . . . .	217
7.7.2	Metal Abundances . . . . .	223
7.8	DISCUSSION . . . . .	224
7.9	SUMMARY . . . . .	230
<b>8</b>	<b>Conclusion</b>	<b>232</b>
8.1	SS CYGNI . . . . .	232
8.2	1E 2259+586 . . . . .	233
8.3	DIP SOURCES . . . . .	233
8.4	FUTURE PROSPECTS . . . . .	233
	<b>References</b>	<b>235</b>



An early observational result in accretion processes – the first detection of a dwarf nova outburst, seen in the cataclysmic variable U Geminorum:

---

*On a new Variable Star.* By J. R. Hind, Esq.

“On the evening of December 15th, 1855, I remarked in R.A. (1856)  $7^{\text{h}} 46^{\text{m}} 33^{\text{s}}.65$ , N.P.D.  $67^{\circ} 37' 17''.1$ , an object shining as a star of the ninth magnitude, with a very blue planetary light, which I have never seen before during the five years that my attention has been directed to this quarter of the heavens. On the next fine night, Dec. 18, it was certainly fainter than on the 15th by half a magnitude or more. Since that date I have not had an opportunity of examining it till last evening, January 10th, when its brightness was not greater than that of stars of the twelfth magnitude. It is evidently a variable star of a very interesting description, inasmuch as the minimum brightness appears to extend over a great part of the whole period, contrary to what happens with *Algol* and *S Cancri*.

“The position given above was deduced by micrometrical comparisons with the principal component of the double star  $\Sigma 1158$ . The *variable* precedes  $1^{\text{m}} 26^{\text{s}}.53$ , and is N.  $7' 30''.8$ .

“*Mr. Bishop's Observatory, 1856, January 11.*”

---

Mon. Not. R. astr. Soc., 16, 56. (1856).

# Chapter 1

## Introduction

### 1.1 INTERACTING BINARY STARS

By definition all binary stars interact, but the term is generally used to describe systems which have physical properties which differ from those of the two components considered in isolation. The objects which are studied in this thesis are systems in which this interaction occurs by transfer of material from one star onto a degenerate companion. This process allows the infalling gas to be heated, such that much of the accretion luminosity is radiated at x-ray wavelengths. Systems in which the accreting body is a white dwarf are termed cataclysmic variables (CV), and those which contain neutron stars come under the general heading of x-ray binaries. Other types of object such as contact binaries, Algols and even some chemically peculiar giants such as the Ba stars also come under the general class of 'interacting binary', (see Eggleton, 1985, for a review). Such systems are of great astrophysical interest, but shall not be considered here.

This thesis presents x-ray observations of CV and x-ray binary systems made with the EXOSAT and *Ginga* satellite observatories. Before describing these observations and their implications for the classes of source studied, it is useful to outline some of the processes which are important in the consideration of mass transfer, and to illustrate the typical magnitudes of relevant physical parameters. Much of the following section on the basic physics of accretion onto compact objects is drawn from reviews by Frank, King and Raine (1985), Pringle (1985), Bath and Pringle (1985) and King (1989).

## 1.2 THEORETICAL CONCEPTS

### 1.2.1 Mass-loss Mechanisms

Two stars with masses  $M_1$  and  $M_2$  (expressed in solar masses,  $M_\odot \approx 2.0 \times 10^{33}$  g) with a binary separation  $a$  will have an orbital period given by Kepler's law;

$$P = 2\pi \left( \frac{a^3}{G(M_1 + M_2)M_\odot} \right)^{1/2} \quad (1.1)$$

Defining the mass ratio  $q = M_2/M_1$ , it is convenient to express the binary separation as;

$$a = 3.5 \times 10^{10} M_1^{1/3} (1 + q)^{1/3} P_{hr}^{2/3} \text{ cm} \quad (1.2)$$

Where  $P_{hr}$  is the period in hours. Thus for two solar type stars, an orbital period of 5.6 hrs would imply a system in which the components are in contact.

Mass transfer in a binary system may occur in two ways:

1. The non-compact star may have a substantial stellar wind.
2. The stars may be in such a close orbit that matter on the surface of one star is drawn off by the gravitational field of its companion.

The systems in which wind-driven mass transfer causes significant effects contain early-type mass stars. Typical mass loss rates for O type stars may be as high as  $\sim 10^{-5} M_\odot \text{ yr}^{-1}$ . The wind-driven systems are termed the high mass x-ray binaries (HMXB). In comparison, the mass loss rate for late type main-sequence stars is  $\sim 10^{-14} M_\odot \text{ yr}^{-1}$  and wind-driven accretion is negligible effect in these systems. Wind accretion and HMXB will be mentioned briefly in section 1.2.7.

The second case, that of the components being close enough for matter to be drawn off one star, is the only efficient mechanism of mass transfer available to late type stars ( $M \lesssim 1M_\odot$ ). These systems are termed low mass x-ray binaries (LMXB). A brief overview of this type of mass transfer process is given below.

The equation of motion of a fluid with velocity  $\mathbf{v}$ , density  $\rho$ , and pressure  $P$  in a frame of reference which is rotating with an angular velocity  $\omega$  is given by the Euler equation,

$$\frac{\partial \mathbf{v}}{\partial t} + (\mathbf{v} \cdot \nabla) \mathbf{v} = -\nabla \Phi - 2\omega \wedge \mathbf{v} - \frac{1}{\rho} \nabla P \quad (1.3)$$

For a Keplerian orbit,  $\omega$  is given by;

$$\omega = \left( \frac{(M_1 + M_2)M_\odot}{q^3} \right) \hat{\mathbf{u}} \quad (1.4)$$

where  $\hat{\mathbf{u}}$  is the unit vector normal to the orbital plane. The term in  $\omega \wedge \mathbf{v}$  in equation 1.3 represents the Coriolis force, and  $\Phi = \Phi(\mathbf{r})$  is the potential at position vector  $\mathbf{r}$  in the rotating frame of reference. In general,  $\Phi$  is difficult to calculate exactly because the density profiles for each star must be known. An approximation made by Roche was to consider the stars as point masses, which, given the central condensation in real stellar structures, is usually accurate to within a few percent. This gives the Roche potential,  $\Phi = \Phi_R$ , which for stars with position vectors  $\mathbf{r}_1$  and  $\mathbf{r}_2$ , is

$$\Phi_R = -\frac{GM_1M_\odot}{|\mathbf{r} - \mathbf{r}_1|} - \frac{GM_2M_\odot}{|\mathbf{r} - \mathbf{r}_2|} - \frac{1}{2}(\omega \wedge \mathbf{r})^2 \quad (1.5)$$

Figure 1.1 shows equipotential surfaces of  $\Phi_R$  in the orbital plane of the binary. Considering the star at  $O$  it can be seen that at small radii (from  $O$ ), the potential is similar to that which would be obtained for an isolated star (inner circle). As the radius increases, the potential becomes distorted, eventually forming an hour-glass shape which envelopes both stars. At the minimum radius which satisfies this condition, the surface consists of two so-called Roche lobes, which are in contact at one point. This is termed the inner Lagrangian (or L1) point. If a star fills its Roche lobe the material at the L1 point is unstable to small displacement towards the other star and will overflow into the other lobe. Thus a mechanism for mass transfer has been established.

The nomenclature used by authors to describe the mass donating star and the accreting body varies. Throughout this work the convention shall be adopted that star which is losing mass will be termed the secondary, the accreting object will always be referred to as the primary.

Two useful approximations for distances relevant to Roche lobes are, the Roche lobe ‘radius’ and the distance from the stellar centers to the L1 point. An expression given by Eggleton (1983) for the lobe radius is,

$$R_2 = \frac{0.49q^{2/3}}{0.6q^{2/3} + \ln(1 + q^{1/3})} \quad (1.6)$$

Which is accurate to  $\sim 1\%$  and is valid for all  $q$ . This formulation has the advantage over other approximations for  $R_L$  (such as given by Paczyński, 1971) that its derivative is continuous.

Plavec and Kratochvil (1964) give the distance of the L1 point from the centre of the primary as,

$$b_1 = a(0.500 - 0.227) \log q \quad (1.7)$$

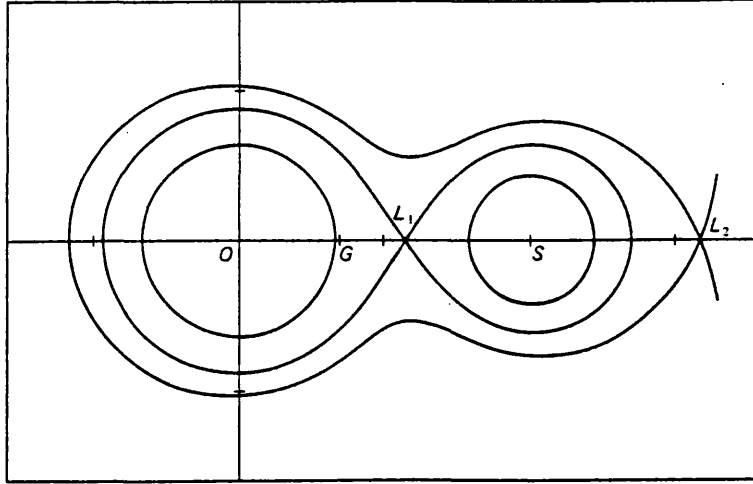


Figure 1.1: Roche equipotentials in the orbital plane of the binary. The centres of stars 1 and 2 are at  $O$  and  $S$  respectively. The centre of mass is at  $G$ . The mass ratio is  $M_1/M_2=2$ . The surface passing through the inner Lagrangian point ( $L_1$ ) defines the Roche lobes for this system.

### 1.2.2 Compact Objects

Once inside the other lobe, the potential seen by the infalling matter is similar to that around an isolated star. The two types of compact object that of interest here are white dwarfs and neutron stars. Both are supported not by thermal pressure as is the case in main-sequence and giant stars, but by the degeneracy pressure of particles obeying Fermi-Dirac statistics. In white dwarfs it is the electrons in the gas which provide this support. Above a certain mass however it becomes energetically favourable for electrons and protons to undergo inverse  $\beta$  decay, and a star consisting predominantly of neutrons is formed. Detailed discussion of the structure of degenerate stars is given by Shapiro and Teukolsky (1983). The properties that are important in the context of accretion processes are the possible masses of these stars and the mass-radius relationships.

#### White Dwarfs

The upper limit for the mass of a white dwarf is  $\approx 1.4M_{\odot}$  and is named after its discoverer, Chandrasekhar (1931). The mass radius relationship ( $M(R)$ ) is fairly well determined, it is also a function of chemical composition. White dwarfs form after nuclear burning has been exhausted and different initial masses will yield a range of final compositions. Figure 1.2 shows a set of

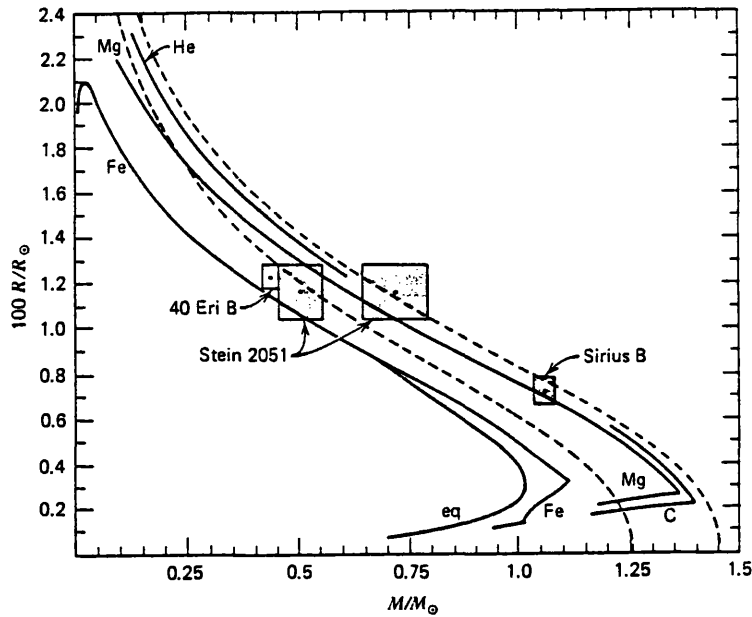


Figure 1.2: The mass–radius relation for zero temperature stars composed of  ${}^4\text{He}$ ,  ${}^{12}\text{C}$ ,  ${}^{24}\text{Mg}$ , and  ${}^{56}\text{Fe}$ . The curve marked *eq* denotes the equilibrium composition at each density, the dashed curves represent the models of Chandrasekhar. The points inside the grey  $1\sigma$  error boxes show the best estimates for masses and radii for three white dwarfs (note that there are two solutions for Stein 2051). From Hamada & Salpeter (1961).

predicted curves for  $M(R)$ , for He, C, Mg and Fe as main constituents, with the error boxes for three white dwarfs whose masses and radii have been determined. Agreement between models and data is good, and the differences between models are not substantial. For the purposes required here, it is sufficient to use the approximate analytic solution given by Nauenberg (1972),

$$R(M) = 0.78 \left( \left( \frac{1.44}{M_1} \right)^{2/3} - \left( \frac{M_1}{1.44} \right)^{2/3} \right)^{1/2} \times 10^9 \text{cm} \quad (1.8)$$

Thus a  $1M_\odot$  white dwarf will have a radius of  $\sim 5 \times 10^8$  cm. Figure 1.2 and equation 1.8 illustrate an important property of white dwarfs, that the radius decreases for an increase in mass.

## Neutron Stars

The theoretical understanding of the structure of neutron stars is rather poor. Although detailed models have been developed (e.g. Panharipande, Pines and Smith, 1976) it is not clear if they are

based on the correct physical principles, due to the uncertainty about the behaviour of the strong nuclear force. A limit analogous to the Chandrasekhar mass is believed to apply to neutron stars. If exceeded, the star collapses to a singularity and a black hole is formed. Estimates for this mass vary from about 1.5 to  $\sim 3M_{\odot}$ . The form as  $M(R)$  is also unclear, however it will suffice here to assume that for a neutron star with mass of order  $1M_{\odot}$  radius is  $\sim 10$  km.

### 1.2.3 Luminosities and Temperatures

The potential well offered by compact objects may yield a significant fraction ( $\eta$ ) of the rest mass energy. A test particle of mass  $m$ , which falls from infinity and is brought to rest at the surface of a body of radius  $R_1$  will liberate an energy  $\Delta E$  such that,

$$\eta = \frac{\Delta E}{mc^2} = \frac{GM_1M_{\odot}}{R_1c^2} \quad (1.9)$$

For a  $1M_{\odot}$  neutron star and white dwarf this fraction is  $\sim 15\%$  and  $\sim 0.025\%$  respectively. For neutron stars then, accretion processes may be more efficient than thermonuclear burning ( $\eta \sim 0.7\%$ ), but will be a factor of  $\sim 30$  lower for white dwarfs.

Nevertheless, both sources of energy have important observational consequences for both types of object. This is due to the different timescales on which these processes release the available energy. The gravitational potential is liberated as the material falls to the surface of the object. However, the energy from nuclear burning may be released episodically, following a build-up of hydrogen rich fuel on the surface of the compact object. For neutron stars, this process is observed as outbursts in which the source luminosity rises dramatically in a few seconds, and thereafter decays exponentially on timescales of 10–100 sec. These outbursts, which are termed ‘type I bursts’, may recur on timescales as short as a few hours. In contrast, the episodic burning of accreted material in CVs results in a longer duration outburst, termed a ‘nova’ outburst, which has a duration of months to years, and recurs (if at all) on timescales greater than tens of years. Between outbursts then, it is the accretion luminosity which dominates the source emission, even though for CVs it is a less efficient process than nuclear burning.

If the material escaping through the L1 point were to fall directly to the surface of the compact object and release all its kinetic energy as radiation, then for an accretion rate  $\dot{M}$ , the luminosity would be

$$L_{acc} = \frac{G\dot{M}M_1M_{\odot}}{R_1} \quad (1.10)$$

An estimate may then be made for the magnitude of  $\dot{M}$  for these systems. Given that typical

observed luminosities of CVs and LMXBs are  $\sim 10^{33}$  and  $\sim 10^{36}$  ergs sec $^{-1}$  respectively, then assuming accretion onto  $1M_{\odot}$  objects, it is found that  $\dot{M} \sim 10^{16}$  g sec $^{-1}$  for both types of system. The similarity is perhaps not surprising since it may be expected that mass transfer rates would depend on the process which sustains the secondary in its Roche lobe filling state, rather than on the nature of the compact object.

A limit to the luminosity occurs when the radiation pressure becomes sufficient to stop the infalling matter. A crude estimate of the magnitude of this limit can be made assuming radial accretion, and is termed the Eddington luminosity,

$$L_{edd} = 4\pi GM_1 M_{\odot} m_p c / \sigma_T \quad (1.11)$$

$$\approx 1.3 \times 10^{38} M_1 \text{ erg sec}^{-1} \quad (1.12)$$

where  $m_p$ , and  $\sigma_T$  are the proton mass and Thomson cross-section respectively. It appears that type I bursts in LMXB sources typically reach the Eddington luminosity. By assuming a reasonable value for  $M_1$  (usually  $1.4M_{\odot}$ ),  $L_{edd}$  may be calculated, and thus the measured flux may be used to derive the distance to the source.

The lowest temperature at which a body of radius  $R_1$  can radiate at a luminosity  $L_{acc}$  is the black body temperature,

$$T_{bb} = \left( \frac{L_{acc}}{4\pi R_1^2 \sigma} \right)^{1/4} \quad (1.13)$$

where  $\sigma$  is the Stefan-Boltzmann constant. The maximum temperature that may be attained by the accreting gas is that reached when its gravitational potential energy is converted entirely into thermal energy,

$$T_{th} = \frac{GM_1 M_{\odot} m_p}{3kR_1} \quad (1.14)$$

The temperature at which the accretion luminosity is radiated ( $T_{rad}$ ) would be expected to lie between these two limits,

$$T_{bb} \lesssim T_{rad} \lesssim T_{th}$$

For  $1M_{\odot}$  neutron stars and white dwarfs, using typical luminosities of  $\sim 10^{36}$  and  $\sim 10^{33}$  ergs sec $^{-1}$  mentioned above, the respective ranges of expected temperatures are,

$$1 \text{ keV} \lesssim kT \lesssim 50 \text{ MeV}$$

$$6 \text{ eV} \lesssim kT \lesssim 100 \text{ keV}$$

These limits illustrate that accreting compact objects may emit at x-ray wavelengths. They do not however, constrain the expected temperatures very well and a more detailed consideration of

the accretion and emission processes is required to obtain limits similar to those observed. In particular, LMXB systems have a much smaller measured range of temperatures than that implied above, being  $kT \sim 2$  to 20 keV. Some types of CV system however, do show a wide range of observed temperature, with  $10 \text{ eV} \lesssim kT \lesssim 20 \text{ keV}$ .

#### 1.2.4 Accretion Discs

The angular momentum of the material injected through the L1 point will prevent it from falling directly onto the compact star. Figure 1.3 shows a numerical simulation (from Flannery, 1975) in which test particles with three different initial velocities are allowed to fall from the L1 point. The trajectories pass close to the compact object and then out again almost to the edge of the Roche lobe, before returning to intersect their path at some intermediate radius. A stream of gas would be expected to collide with itself and dissipate energy, eventually forming a circular orbit appropriate to the initial angular momentum of the gas.

Using Kepler's law and equation 1.7 it may be shown that this circularisation radius is,

$$R_{circ} = a(1 + q)(0.500 - 0.227 \log q)^4 \quad (1.15)$$

For values of  $q$  of interest it is found that  $R_{circ}$  is a factor of  $\sim 3$  smaller than the lobe radius, but is larger than the maximum radius of any compact object ( $\sim 10^9$  cm for a low mass white dwarf). Thus the stream will form a ring in Keplerian orbit around the degenerate star.

This ring however, is unlikely to be stable. Turbulent motion and viscosity in the gas are likely to convert kinetic energy into thermal energy which will then be radiated away. With the loss of kinetic energy the gas must fall deeper into the potential well, but to remove angular momentum, some material must move to larger radii. The overall effect is a smearing out of the ring to form an accretion disc.

It is not appropriate here to enter into a full discussion of the theoretical modelling of accretion discs, but it is useful to indicate to what level the behaviour of such systems is understood. The standard theory (e.g. Pringle 1981) assumes that the disc is thin, i.e. the scale height ( $H$ ) is much less than radius ( $R$ ). The model describes the behaviour of the surface density of the disc  $\Sigma$  as a function of radius and time ( $t$ ). From the conservation of mass and angular momentum, it may be shown that for a Keplerian disc,

$$\frac{\partial \Sigma}{\partial t} = \frac{3}{R} \frac{\partial}{\partial R} \left( R^{1/2} \frac{\partial}{\partial R} (\nu \Sigma R^{1/2}) \right) \quad (1.16)$$

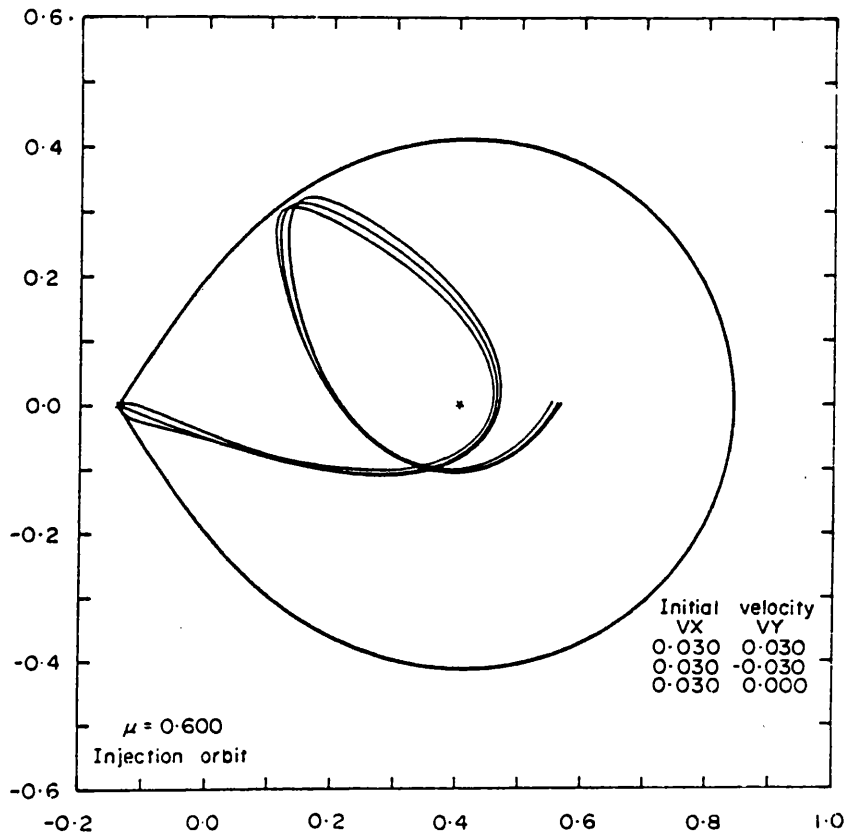


Figure 1.3: The trajectories in the orbital plane of a Roche lobe of three test particles with different initial velocities at the L1 point. The mass ratio of the binary is  $q = M_2/M_1 = 2/3$ . All particles have an initial velocity of  $0.03(G(M_1 + M_2)/a)^{1/2}$  in the  $x$  direction, but have velocities of  $+0.03$ ,  $0.00$ , and  $-0.03$  in the same units in the  $y$  direction. For small initial velocities, the trajectories are similar. From Flannery (1975).

Where  $\nu$  is the viscosity of the disc. The important feature of equation 1.16 is that it is a diffusion equation which implies that the surface density of the disc can only change at each radius on the viscous timescale,

$$t_\nu(R) \sim R^2/\nu \quad (1.17)$$

The problem facing the application of this theory is that the form of the viscosity is unknown, although it is expected to be a function of  $R$ ,  $\Sigma$  and  $t$ . Thus equation 1.16 is in general a non-linear equation and will not have an analytic solution. Numerical simulation using simple forms of viscosity (e.g.  $\nu = \text{constant}$ ), show that the time evolution of a ring will smear out in the way described above. The steady state solution of equation 1.16 has received much attention. One of the most important results is that the dissipation of energy  $D(R)$  per unit area of the disc is independent of the form of  $\nu$ .

$$D(R) = \frac{3GM_1M_\odot}{8\pi R^3} \left( 1 - \left( \frac{R_1}{R} \right)^{1/2} \right) \quad (1.18)$$

And the total disc luminosity can be found by integration from the inner radius (assumed to be at  $R_1$ ) to  $\infty$ ,

$$L_{disc} = \frac{GM_1M_\odot\dot{M}}{2R_1} = \frac{1}{2}L_{acc} \quad (1.19)$$

So half the available accretion luminosity is radiated in the disc. Assuming the disc is optically thick and locally radiates as a blackbody, the spectrum of the disc can be determined and may be shown to be of the form,

$$F_\nu \propto \int_{R_{inner}}^{R_{outer}} \frac{R dR}{e^{h\nu/kT}-1} \quad (1.20)$$

Where  $R_{inner}$  and  $R_{outer}$  are the inner and outer radii of the disc, note also that  $T$  is a function of  $R$ . This is essentially a modified blackbody spectrum. At low energies it has the Rayleigh-Jeans form,  $F_\nu \propto \nu^2$ , and at high energies follows the Wien distribution  $F_\nu \propto \nu^3 e^{-h\nu/kT}$ . For intermediate energies, when  $h\nu/k$  is lies in the range of disc temperatures,  $F_\nu \propto \nu^{1/3}$ .

The rate at which energy must be dissipated by gas at the innermost Keplerian orbit to come rest on a compact object which has an angular velocity  $\omega_{spin}$  is

$$\begin{aligned} L_{bl} &= \frac{1}{2}\dot{M} \left( \frac{GM_1M_\odot}{R_1} - (R_1\omega_{spin})^2 \right) \\ &= L_{disc} \left( 1 - \left( \frac{\omega_{spin}}{\omega(R_1)} \right) \right) \end{aligned} \quad (1.21)$$

Where  $\omega(R_1)$  is the angular velocity at  $R_1$ . Thus if the degenerate star is spinning slowly ( $\omega_{spin} \ll \omega(R_1)$ ), a luminosity equal to that of the disc will originate from a thin transition zone between the accretion disk and the compact object, in which the gas decelerates. Given that the dimensions of

this region will be approximately those of the compact object, the range of expected temperatures will be similar to those quoted above for direct accretion, and so this boundary layer will be a region of potentially strong x-ray emission.

It is important to note the conditions under which the thin-disc approximation breaks down. A test particle in the disc at  $R$  which is given a velocity component  $v_{\perp}$  perpendicular to the orbital plane, will follow a ballistic trajectory and reach a maximum height  $H \sim Rv_{\perp}/v_k$ , where  $v_k$  is the Keplerian velocity at  $R$ . A perpendicular velocity component in the gas is provided by thermal motion at about the sound speed  $c_s$ , thus the scale height of the disc is,

$$H = Rc_s/v_k = Rc_s \left( \frac{R}{GM_1 M_{\odot}} \right)^{1/2} \quad (1.22)$$

Clearly the thin disc approximation ( $H \ll R$ ) is only valid if the Keplerian velocity is highly supersonic.

It has been stated that the form of the viscosity is poorly understood. A model which was developed by Shakura and Sunyaev (1973) assumes that  $\nu$  scales with the product of sound speed ( $c_s$ ) and the scale height ( $H$ ),

$$\nu = \alpha c_s H \quad (1.23)$$

Where  $\alpha$  is a parameter of order  $\lesssim 1$ . This formulation has some advantages, in particular physical parameters of interest are not strong functions of  $\alpha$ , but it essentially translates ignorance of  $\nu$  into ignorance about  $\alpha$ . Until the viscous processes which dominate disc behaviour become better understood, the  $\alpha$ -disc model will remain a standard solution.

### 1.2.5 Components of a Physical Model

Combining the ideas of the above sections, a physical model for these systems can be described. This is summarised in figure 1.4 (a). The secondary fills its Roche lobe, mass transfer takes place through the L1 point, forming a gas stream which is incident upon the accretion disc. Matter loses angular momentum through the disc and falls to the boundary layer before settling on the white dwarf surface. The main uncertainties in a full theoretical picture are in the way in which the gas stream interacts with the disc, and in the processes which occur in what is expected to be a highly turbulent boundary layer. In eclipsing CVs there is evidence of a so-called ‘bright spot’ at the point at which the stream is expected to impact the disc. There is also evidence for substantial vertical structure in accretion discs in this vicinity, this will be discussed further in chapter 6.

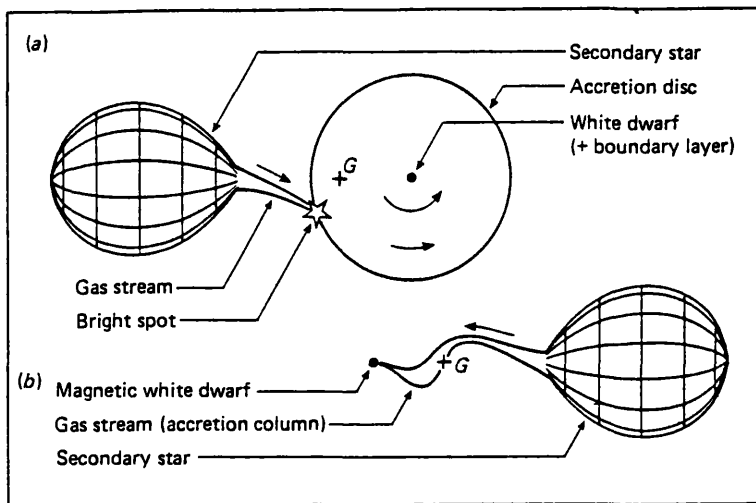


Figure 1.4: Schematic representation of: (a) Non-magnetic CVs and most LMXB systems, showing the main physical components. The system is viewed from pole-on, and the structure lies in the orbital plane of the binary. (b) A strongly magnetic (AM Her) system in which the gas stream follows the magnetic field lines. Again viewed pole-on, the gas stream will generally be deviated out of the orbital plane. From Wade and Ward (1985).

### 1.2.6 Magnetically Controlled Accretion

In the case considered above, it has been assumed that any magnetic field associated with the compact object is insufficient to alter the flow of accreting material appreciably. A perfectly conducting plasma in a magnetic field  $\mathbf{B}$ , will be subject to a pressure which acts perpendicular to the field direction. The magnitude of this pressure is given by,

$$P_{mag} = \frac{B^2}{8\pi} \quad (1.24)$$

A tension of equal magnitude also acts along the field lines. A gas of density  $\rho$ , moving with a bulk velocity  $v$ , has a ram pressure of  $P_{ram} = \rho v^2$ . If  $P_{mag} > P_{ram}$  the gas flow will be dominated by the magnetic field, and will be forced to flow along the field lines. Because the  $P_{mag}$  (for a dipole field) falls off faster than  $P_{ram}$  as a function of radius, plasma falling onto a compact object will fall freely until it reaches a radius (termed the Alfvén radius) at which  $P_{mag} \sim P_{ram}$  and thereafter it will follow the magnetic field.

A schematic illustration of a magnetic system is shown in figure 1.4 (b). The gas stream confined by the magnetic field and falls along an accretion column onto one pole of the compact object. A more detailed discussion of accretion flow in the magnetic field of a rotating star is given in the context of the x-ray pulsar 1E 2259+586, in chapter 5. CVs in which accretion is magnetically controlled can be grouped into those in which the white dwarf rotates at the orbital period (called Polars or AM Her systems), and those in which the white dwarf spins asynchronously (the Intermediate Polars). In all LMXB with strong magnetic fields the neutron star spin period is much smaller than the orbital period.

### 1.2.7 Wind Accretion

Many bright x-ray binary sources are not powered by the overflow mechanism described above, but by capture of a stellar wind by a compact object. A schematic illustration of such a system is shown in figure 1.5. Only a small fraction of the mass lost by the early type star accretes onto the compact object. There is a strong bow shock between the wind and the material which has been captured. Although none of the sources considered here fall into this category, the case of accretion from the interstellar medium which is discussed in chapter 5 is similar in many respects to this type of process.

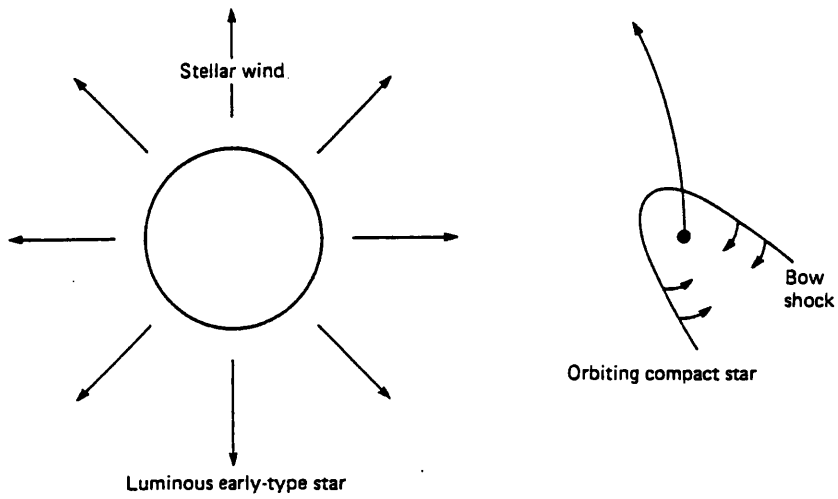


Figure 1.5: A schematic diagram of the components of a high mass x-ray binary, in which the compact star accretes from the stellar wind of an early type companion.

## Chapter 2

# Instrumentation and Data Reduction

### 2.1 INTRODUCTION

The two fundamental considerations in the design of any observatory are the sensitivity the telescope, and the suitability of the site in terms of factors which may affect visibility. The technical progress that has allowed x-ray astronomy to evolve from the simple detection of sources to its present status as an important branch of diagnostic astrophysics are basically advances in these two areas. The sensitivity of detectors used in the 1980s is approximately seven orders of magnitude greater than that of the instrument flown on a sounding rocket in 1962, with which Giacconi and collaborators first obtained evidence for a cosmic x-ray source. The absorption of x-rays by air demands that detectors must be flown above the atmosphere, thus the progression from sounding rockets and balloon flights to satellite observatories in orbits with different background radiation environments can be thought of as improvements in ‘seeing’ conditions.

The first x-ray astronomy satellite, *Uhuru*, was launched in 1970, and eventually revealed 339 discrete x-ray sources both within and outside of the Galaxy. A series of orbiting observatories followed throughout the seventies, including ANS (1974), *Ariel V* (1974), and HEAO-1 (1977). The primary instruments on these satellites were non-imaging proportional counter detectors. The launch of the *Einstein* observatory in 1978 saw the first major use of an imaging x-ray telescope,

and remains the most sensitive set of detectors yet flown. However, during its three year lifetime *Einstein* covered only a small fraction of the sky ( $\sim 3\%$ ), and operated at relatively soft x-ray wavelengths (0.5–4 keV). It was also in a low earth orbit. Such orbits, with altitudes of  $\sim 500$  km, are commonly used because they can use relatively cheap launch vehicles, but observations are typically restricted to about half an orbit due to earth occultation. Thus sources cannot be monitored continuously for more than about 50 mins before a break in the observation of similar duration.

In a narrative on the development of x-ray astronomy from an American point of view, Tucker and Giacconi (1985) look forward to the developments of the 1980s and dismiss the EXOSAT mission with one sentence, stating that a lower sensitivity than *Einstein* would restrict its use to the study of relatively nearby objects. Although it is true that EXOSAT could not make sensitive imaging observations, the observatory offered other facilities which complement those of *Einstein*, and have resulted in significant advances in most areas of x-ray astronomy. In particular, EXOSAT provided moderate resolution spectroscopy over a broad energy band of  $\sim 0.05$  to 50 keV. It also offered a large area non-imaging detector capable of operating at high (i.e. a few msec) time resolution, and its orbit allowed long, uninterrupted observations to be made.

*Ginga* in some senses can be thought of as an extension of part of the EXOSAT mission, with a large area non-imaging proportional counter experiment forming the principal scientific instrument. This detector offers moderate spectral resolution at medium (2–35 keV) x-ray energies. In the following sections these two observatories will be described briefly. More detailed overviews of the EXOSAT and *Ginga* missions have been given by White and Peacock (1988) and by Makino (1987).

## 2.2 THE EXOSAT OBSERVATORY

The European X-ray Observatory Satellite (EXOSAT) was a project developed and operated by the European Space Agency which offered observing time to the entire astronomical community. EXOSAT was launched on 1983 May 26 from the Vandenberg Air Force Base in California on a Thor-Delta rocket. After an instrumental performance verification (PV) phase, the first observation was made on June 19. Unusually, it was placed into a highly elliptical orbit with  $e \approx 0.93$ ,  $P_{orb} = 90.6$  hr and  $i = 73^\circ$ . The satellite altitude at apogee was 191,000 km with a perigee of 350 km. The original motivation for adopting this orbit was to use lunar occultation to provide positional information for the non-imaging proportional counter experiment. Between the conception of

the project in 1969 and launch, source positions became available from other missions, and so this technique was never actually utilised as planned. The orbit did however allow continuous observation for  $\sim 76$  hr per orbit. During the passage through the Earth's radiation belts (altitude  $< 50,000$  km) the scientific instruments were switched off, but for the rest of the orbit the satellite was usually visible from the ground station at Villafranca, and on-board bulk data storage was unnecessary. The satellite operated well, with only minor problems, for its expected lifetime, but eventually became inoperable on 1986 April 9, following the loss of attitude stability. It re-entered the Earth's atmosphere on 1986 May 6, having successfully completed 1780 observations.

The main components of the observatory are shown in figure 2.1. The principal detectors were two low-energy (LE) imaging telescopes, a medium energy (ME) proportional counter array and a gas scintillation proportional counter (GSPC), all of which were coaligned. The satellite was three-axis stabilised, with the attitude typically being maintained to within  $\sim 10$  arcsec and controlled by means of three gyroscopes, two star trackers and a sun sensor. Manoeuvres between sources and fine adjustment of pointing were made using a cold propane thruster system. The solar panel array was articulated, allowing a wide range of pointing directions, the main constraint being prevention of over-exposure to the star trackers from the sun, earth or moon. In practice however, it was found desirable to limit observations to a range of sun angles ( $\beta$ ) such that  $90^\circ < \beta < 130^\circ$ .

The scientific and housekeeping data were pre-processed and compressed by the on-board computer (OBC). A feature of the OBC was that data acquisition modes could be re-programmed during the course of the mission, allowing follow-up observations to concentrate on newly discovered source phenomena. The OBC modes are essentially a trade-off between temporal and spectral resolution for the ME array (see below). The data were relayed to the ground-station at a telemetry rate of 8 kbps.

Of the three main instruments, only data from the LE and ME experiments have been used for the observations presented in this thesis. The GSPC offered a higher spectral resolution than the ME, with  $\Delta E/E \sim 11(E/6 \text{ keV})^{-0.5}\%$  FWHM, but with a much smaller effective area ( $\sim 100 \text{ cm}^2$ ). A description of this detector is given by Peacock *et al.* (1981).

### 2.2.1 The Low Energy Telescope

The low-energy instruments on EXOSAT consisted of two identical telescopes and detector assemblies. The telescopes had Wolter type I grazing incidence double nested-mirrors, with a focal

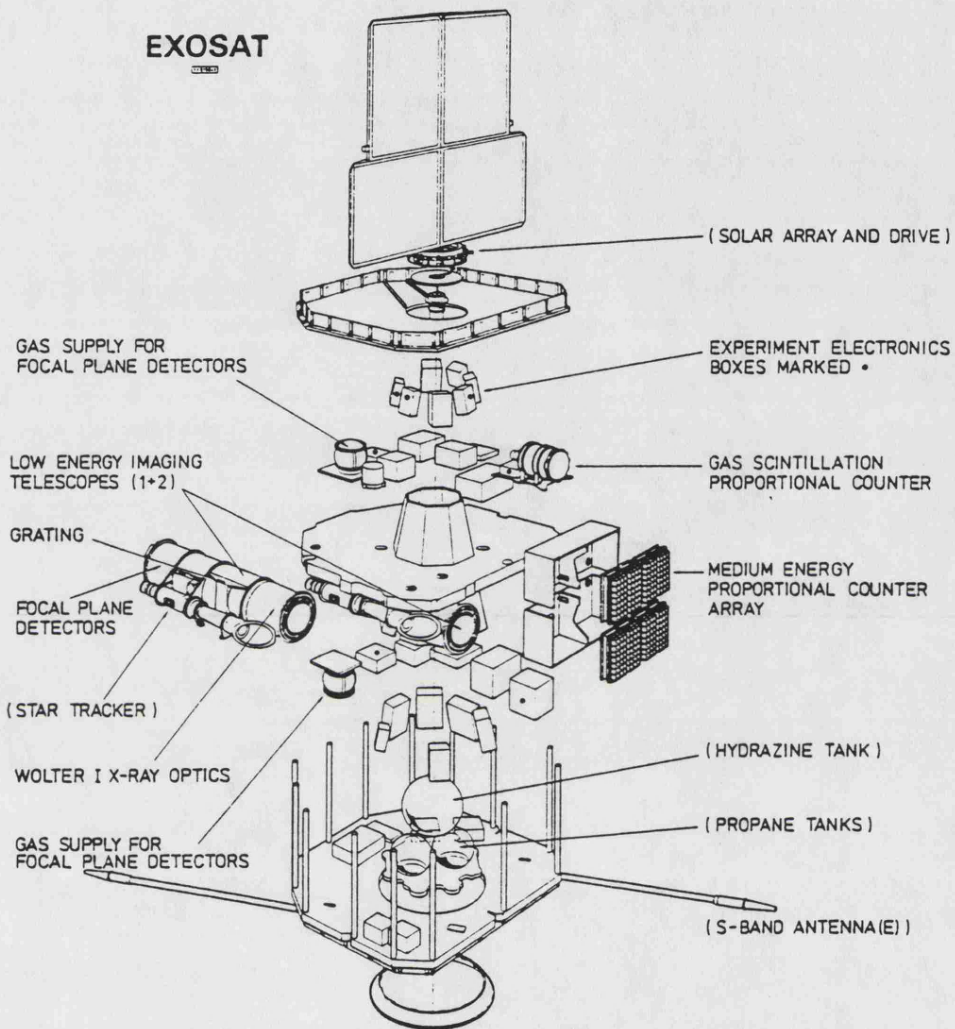


Figure 2.1: An exploded view of the EXOSAT satellite showing the scientific instruments and the principal spacecraft subsystems. From White & Peacock (1988).

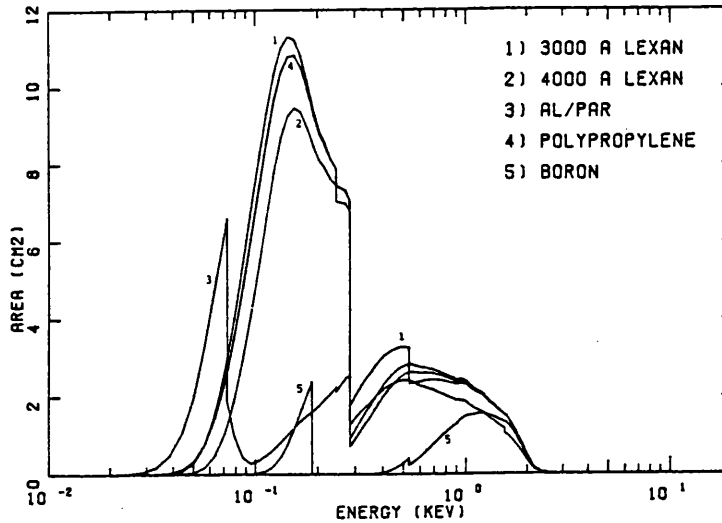


Figure 2.2: The effective area of the LE telescope with a CMA in the focal plane for each of the available filters. (From White and Peacock, 1988).

length of 1.1 m and outer diameter of 0.3 m. The mirror optics could focus x-rays with energies up to  $\approx 2$  keV. There were two interchangeable focal plane detectors, a high resolution imaging channel multiplier array (CMA) and a position sensitive proportional counter (PSD). Both PSDs failed in the PV phase and could not be used for the remainder of the mission. The CMAs had no intrinsic energy resolution. Spectra could be obtained by insertion of a transmission grating in front of the CMA. Only a few observations of this sort were made owing to the failure of the CMA on one telescope and of the grating mechanism on the other. Fortunately the remaining CMA, working in an imaging mode, remained operational until the end of the mission. Crude spectral information could be obtained by insertion of different filters in front of the focal plane. The filters used were two different thicknesses of Lexan (3000 and 4000Å), aluminium/parylene, polypropylene, and boron. Figure 2.2 shows the effective areas of the CMA as a function of energy for the available filters. The CMA was sensitive to UV photons, but by use of a selection of filters the degree of UV contamination could be estimated. Most observations not requiring spectral information were made with the thin Lexan filter since this offered the largest effective area over a wide range of energies.

The CMA had a field of view (FOV) of  $\approx 2^\circ \times 2^\circ$ . The angular resolution was limited by the telescope optics rather than detector resolution, the half energy width of the point spread function being 24 arcsec at the centre of the FOV, degrading to 4 arcmin at  $1^\circ$  off axis. The main contribution to the background arose from electrons in the solar wind. The minimum particle background

was  $\sim 8 \times 10^{-6}$  counts  $\text{sec}^{-1}$   $\text{pixel}^{-1}$ , and 90% of observations had a background of within a factor 2 of this rate. The OBC measured the position and arrival time (to an accuracy of  $2^{-17}$  sec) of each event on the CMA. Due to telemetry restrictions, intervals of high count rate could not be relayed continuously, and consequently some data were lost. In practice this resulted in gaps in the data stream of duration 0.1 to 0.5 sec with typical recurrence times of 0.5 to 1.0 sec. The overall count rates can easily be corrected for this effect for integration times greater than a few seconds. The statistical properties of the time series may however deviate strongly from the expected the Poisson distribution if sampled at a resolution of  $\lesssim 2$  s.

One minor problem with the LE telescope was that the cover of the ME array opened too far (by  $\sim 5^\circ$ ) and partially obscured the FOV of the telescopes. This resulted in a drop in effective area of this instrument of  $\sim 36\%$ .

More detailed descriptions of the LE instruments are given by de Korte *et al.* (1981). The in-flight calibration and count rate corrections are described by Giommi (1985), Giommi and Angelini (1987) and Osborne (1985).

### 2.2.2 The Medium Energy Detector Array

The ME instrument was an array of eight double cell gas proportional counters. Each detector had an area of  $\approx 200$   $\text{cm}^2$ , and the eight were arranged in pairs to form quadrants of a square array. Pivoting around a line joining opposite corners of each quadrant allowed half the array to point off-source and to monitor two separate regions of background. There were two positions to which the background monitoring quadrants could be placed, termed positive and negative offset. Alternatively all detectors could be coaligned on source. The collimators used were based on lead glass microchannel plates with a field of view of  $0.75^\circ \times 0.75^\circ$  (FWHM), with a truncated pyramidal response with a flat top of  $\approx 4$  arcmin in width.

Each detector consisted of an upper argon chamber separated by a 1.5mm beryllium window from a lower xenon chamber, with both gases mixed with carbon dioxide and at a pressure of about 2 atmospheres at 273 K. The typical range of energy sensitivities from these two layers were 1.5–20 keV and 5–50 keV for the Ar and Xe cells respectively. The detector windows were made of beryllium, with four having a thickness of  $62\mu\text{m}$ , the remainder of  $32\mu\text{m}$ . The detectors were of a multi-wire anode design, giving energy resolution of  $\Delta E/E \sim 21(E/6 \text{ keV})^{-0.5}\%$  FWHM for the Ar layer and  $\Delta E/E \sim 18(E/22 \text{ keV})^{-0.5}\%$  FWHM for the Xe layer. The particle background was

Table 2.1: Principal spectral OBC programs for the ME detector.

Program	Data Type	Time Resolution	PH Channels	Notes
HER4	Spectral	10, 5, or 2.5 s	128 (Ar) + 128 (Xe)	Separated by detector
	Intensity	250, 125, or 31 ms	1	Summed over Ar + Xe
HER5	Spectral	1 s	Selectable	Separated by half array
	Intensity	0.31 s	1	Summed over Ar

reduced using anti-coincidence and pulse rise time discriminator techniques. The background in the Xe layer was much higher than in the Ar layer, and so was only of use in studying relatively bright sources. Only data obtained from the Ar layer will be used in the analysis presented in this thesis.

The ME only suffered one major fault during the lifetime of the satellite. On 1985 August 20 detector 3 failed and remained inoperable for the remainder of the mission.

Output from the ME array was preprocessed by the OBC before being relayed to the ground. The form of the ME data was in 128 pulse height channels from each layer, the higher time resolution modes of operation of the OBC integrated the count rate over selectable sets of these channels. Observations considered here were made in either the HER4 or HER5 OBC modes, details of which are given in table 2.1. Most observations considered here had a time resolution of 10 sec.

A pre-flight specification of the ME detector array is given by Turner, Smith and Zimmermann, (1981). A post-mission analysis is provided by White and Peacock (1988).

## 2.3 THE GINGA OBSERVATORY

*Ginga* is the third in a series of x-ray astronomy satellites developed by the Japanese Institute of Space and Astronautical Science (ISAS), and follows on from the *Hakucho* and *Tenma* missions. It was launched on 1987 February 5 on a Mu-3S-II-3 rocket, from the Kagoshima Space centre. The payload comprises three main instruments, a large area proportional counter (LAC), an all sky monitor (ASM) and a gamma-ray burst detector (GBD). The satellite and its principal components

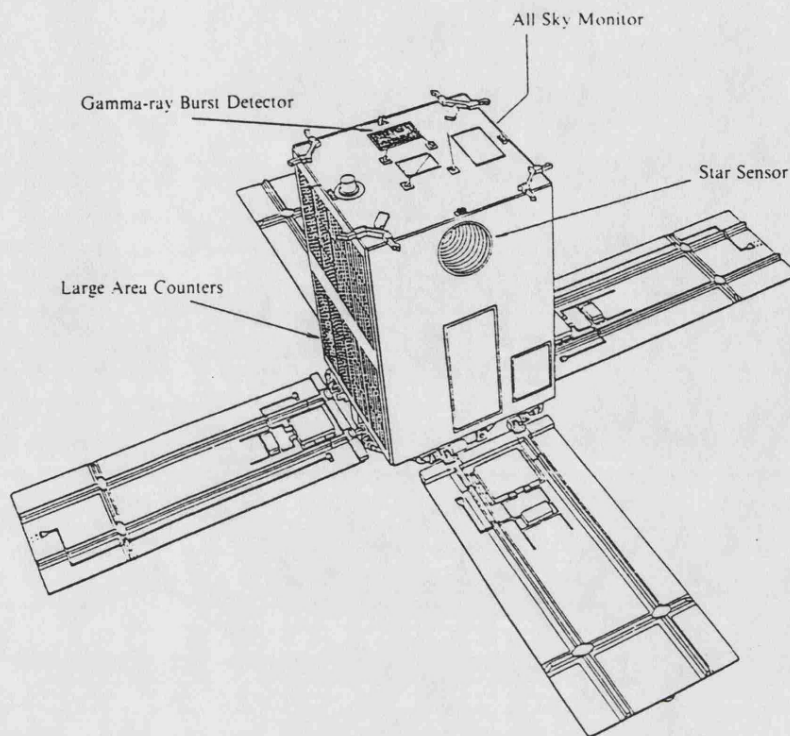


Figure 2.3: An illustration of the *Ginga* satellite x-ray observatory, showing the location of the main scientific experiments. From Turner *et al.* (1989).

are shown in figure 2.3.

The satellite is three axis stabilised, with a momentum wheel being used to slew the spacecraft around its vertical ( $Z$ ) axis at a rate of up to  $\sim 18^\circ \text{ min}^{-1}$ . The pointing of the  $Z$  axis can be altered using three magneto-torquers, allowing a change of  $\sim 3 - 4^\circ \text{ hr}^{-1}$ . Attitude stability is maintained using four gyroscopes, which are calibrated every  $\sim 100$  mins using information from the star trackers. The pre-launch expectation was for attitude stability of  $\lesssim 6$  arcmin, and attitude reconstruction to within  $\lesssim 1$  arcmin. Unfortunately an amplifier on one star tracker developed a fault soon after launch, such that it could only be utilised if a star of  $m_v \lesssim 6$  is in the field of view. This condition is not often satisfied, and so most attitude reconstruction must be performed using data from one star tracker only, which occasionally cannot provide a reliable solution.

Unlike EXOSAT, *Ginga* was launched into a low earth orbit with an orbital period of 95 mins. The orbit is elliptical, with  $e = 0.01$ , and with apogee and perigee altitudes of about 670 km and 500 km. Observations are broken by earth occultation such that continuous exposure for more than  $\sim 40$  mins is unusual. The satellite makes fifteen orbits per day of which only five allow ground

station contact. Data from remote orbits is stored in a bubble memory of 42 Mbit capacity, and the downlink rate can be either 65 or 131 kbps using UHF or S-band frequencies.

The solar panels are not manoeuvrable, and in order to maintain power the angle between the  $Z$  axis and the sun must be  $< 135^\circ$ . To avoid solar contamination in the LAC, the angle between the sun and the pointing direction must be held at  $> 90^\circ$ . These two constraints place limitations on the visibility of sources at a given time. In six months however, any point on the celestial sphere can be observed.

All observations discussed here were made using the LAC. Descriptions of the other two instruments are given by Tsunemi *et al.* (1989) and Murakami *et al.* (1989) for the ASM and GBD respectively.

### 2.3.1 The Large Area Counter

The LAC is in many respects a similar instrument to the EXOSAT ME. It consists of eight gas filled, multi-wire proportional counters. There are however important differences. The detectors are all fixed, coaligned, and offer a total collecting area of  $4000 \text{ cm}^2$ . They are of a single gas cell design, and filled with a mixture of Ar (75%), Xe (20%) and  $\text{CO}_2$  (5%), at a pressure of 1.86 atmospheres at 273 K. The detector body is made from stainless steel, with a  $62 \mu\text{m}$  beryllium foil front window. The active depth of the counters is 3.9 cm. The background is reduced by anticoincidence rejection techniques and by shielding of the detector assembly using 0.2mm of tin. The LAC detects x-rays in the energy range 1.5 to 37 keV, and has an energy resolution of  $\Delta E/E \approx 18(E/6 \text{ keV})^{-0.5}\%$ . The collimator is formed from silver coated stainless steel sheet in a regular semi-hexagonal honeycomb, giving an elliptical,  $1.1^\circ \times 2.0^\circ$ , field of view.

The OBC analyses the LAC pulse height data in 64 channels covering a range of energies from 1.5 to 37 keV. The top 32 channels are compressed by a factor of two for storage and transmission. The OBC has several data acquisition programs, which form a trade-off between spectral and temporal resolution. The highest quality spectral data is obtained in MPC1 mode, giving 48 pulse height channels, and separating the upper and middle anode layers. The highest time resolution can be obtained in PC mode which gives the flux in two selectable broad-band energy ranges at an integration time of  $\approx 1$  msec. These modes are listed in table 2.2. These programs may be run at three different rates. The major limitation to usage of high data acquisition rate is the capacity of the bubble memory. The total available recording times in the different modes are 43 min, 5 hr 42 min, and 22 h 45 min at high, medium and low bit rates respectively. Thus high time resolution

Table 2.2: Time resolution for each data mode of operation for the LAC.

Mode	PH Channels	Time Resolution			Notes
		High	Medium	Low	
MPC1	48	500 ms	4 s	16 s	8 detectors, 2 layers
MPC2	48	62.5 ms	500ms	2 s	2 groups of 4 detectors
MPC3	12	7.8 ms	62.5 ms	250 ms	1 group of 8 detectors
PC High	1	1.9 ms	15.6 ms	62.5 ms	2 groups of 4 detectors
Low	1	0.98 ms	7.8 ms	31.3 ms	2 groups of 4 detectors

data is effectively restricted to contact orbits only.

## 2.4 DATA REDUCTION

All of the data analysis presented in this thesis was performed using the Leicester node of the Starlink network or the computing facilities of Leicester University. Fortunately both systems are VAXclusters operating under the same operating system (VMS), and so duplication of x-ray data analysis software has been straightforward to implement. This arrangement allows flexibility in the choice of hardware that is required to perform specific tasks.

All analysis software was run under a locally written operating environment called QCL (quick command language) which allows easy intercommunication between analysis programs, as well as file manipulation and graphics facilities. Software was written in VAX FORTRAN rather than standard FORTRAN 77 since some of the additional features of this version were found to be convenient for handling large data files. Portability to other types of operating system is not required.

Data reduction can be divided into two stages. Initial processing, which involves manipulation of the raw data into a standard form for the second stage of more detailed analysis. Background subtraction and removal of suspect data can be considered to be part of the former process, as can a further process which is sometimes required to correct the fluxes for off-source pointing in *Ginga* observations. The scaling for this effect, termed aspect-correction, has a small energy dependence because of reflection in the collimator.

The raw data arrive in Leicester on magnetic tapes from ESTEC (EXOSAT) or ISAS (*Ginga*), which contain the most of the housekeeping and science data. The format of files on these tapes differ from each other, and a suite of software is available convert these data into a standard form.

### 2.4.1 X-ray Background Subtraction

Background flux in an astronomical x-ray detector may arise from either x-rays or from particle induced events. Sources of x-rays include the diffuse cosmic background, the sun and the bright limb of the earth. The diffuse background is thought to originate from the summed contribution of distant discrete sources, it shows some degree of spatial variability, and is commonly attributed to unresolved high luminosity active galactic nuclei (see e.g. Boldt, 1987, for a detailed discussion).

Non x-ray events are due to cosmic rays, the solar wind, and energetic particles trapped in the geomagnetic field. The majority of events in a proportional counter which are due to energetic particles rather than photo-ionisation can be rejected using anticoincidence and rise-time techniques. There are however, secondary processes which prove more difficult to discriminate against. The interaction of particles with material in the detector body and the spacecraft may directly produce gamma-rays, or may result in the formation of radioactive isotopes. Gamma-rays from both of these sources may then undergo Compton scattering within the detector gas and so contribute to the background flux. The presence of any residual radio-isotopes in the fabric of the spacecraft will have a similar effect (such as the plutonium in the ME detector casings).

The earth's magnetosphere traps energetic particles, and acts as a barrier against penetration of cosmic rays below a certain energy. Of particular importance to satellites in a low earth orbit is a region centred on 30°S 35°W, where a combination of the earth's displaced and tipped dipole and local magnetic variation give a relatively low value of  $B$  at a given altitude. The particle flux over this area, which is termed the South Atlantic Anomaly (SAA), is particularly high, and radio-isotope formation occurs predominantly as the satellite crosses this region (see e.g. Peterson, 1975).

### The LE telescope

In the case of imaging instruments it is usually straightforward to estimate the background component using a source-free region of the field of view, and this approach was used for the analysis

of LE data. Figure 2.4 shows an entire CMA field of view for the bright source SS Cygni whilst in outburst. The small diamond surrounds the so-called 'hot-spot', which has an increased count-rate due to a software bug. Note that the background increases towards the edge of the FOV. For the generation of time series presented here, the source fluxes were integrated over a small ( $3 \times 3$  arcmin<sup>2</sup>) area, and the background from the larger ( $12 \times 12$  arcmin<sup>2</sup>) box.

### **The ME array**

Prior to launch, the intention had been to use the offset quadrants to provide a background which could be subtracted from the on-source data. In practice, this approach was seldom used for two reasons. Firstly, the spectral responses of the two half arrays were found to differ significantly. Secondly, for a given source, the count rate measured by an array was found to depend on the offset position, with +ve offset giving a higher flux than the aligned position, which in turn was higher than that from a -ve offset.

During the part of the orbit that the instruments were operational it was typically found that the background did not vary appreciably. Thus background subtraction is reduced to the process of estimating the appropriate spectrum to remove from the on-source data. Data from the offset quadrants are however still required to monitor the background for intermittent activity such as solar flares. In the case where the on-source configuration is the same as during the slew manoeuvre, the slew data usually provide a good estimate of the background spectrum. In all the ME analysis presented here, this technique was applied, since most of the observations are short, in the same configuration as the slew data, and sufficient slew data exists to give a reasonable estimate of the background.

### **The LAC**

The LAC has no facility for direct monitoring of the off-source background. The approach adopted is to use a model of the background which has as its parameters the available relevant auxiliary information. At some times the background behaves in a way that cannot be predicted, but generally these intervals can be identified from the auxiliary information, and the data removed before any subsequent analysis. The quantities used for these processes are the satellite housekeeping data and parameters derived from the orbital elements of the satellite, the most important being;

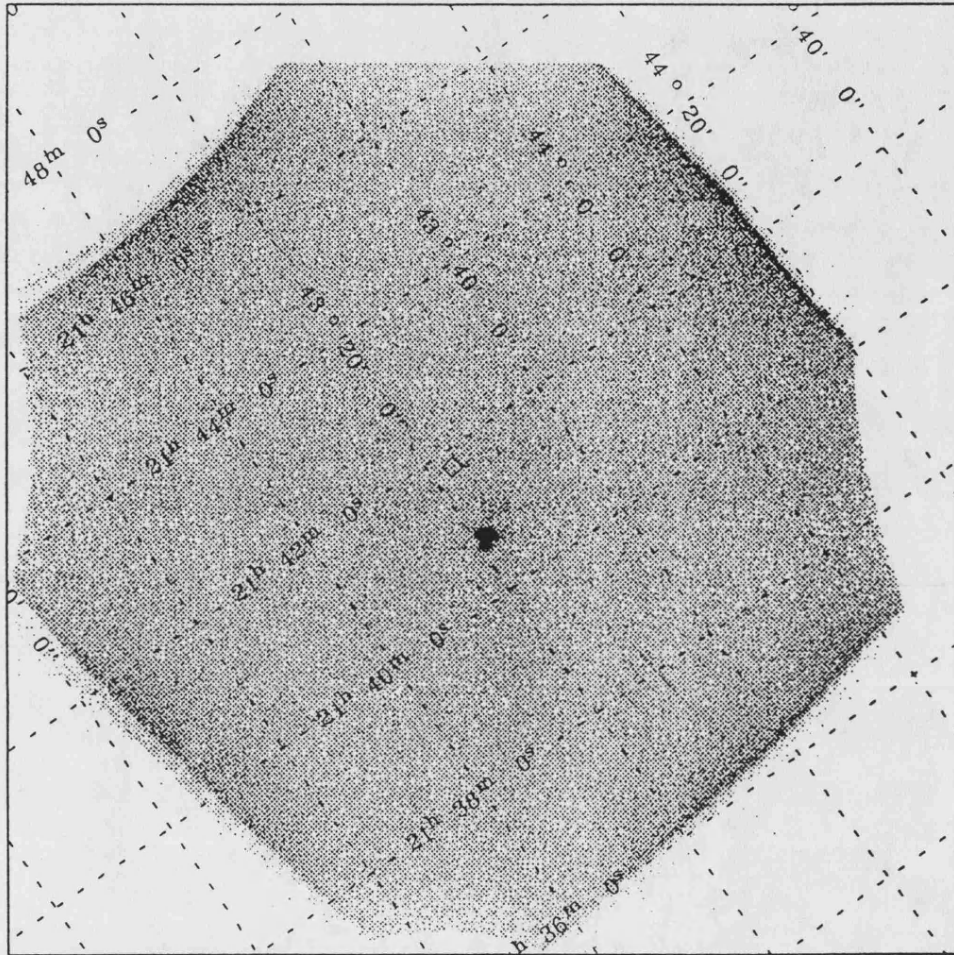


Figure 2.4: An example CMA image, in this case showing a very bright soft x-ray source, the dwarf nova SS Cygni in outburst. The grid shows celestial coordinates across the field of view. The diamond (near the centre of the image) marks the position of the spurious hotspot.

**SUD** ‘Surplus over Upper Discriminator’. This measures the number of x-ray like events with energies above an upper discriminator (24 keV). It provides a good indication of the internal background because the detection efficiency of x-rays at these energies is low. This parameter scales approximately linearly with the background rate.

**PIM** This is the count rate of LAC anode wires which are not directly illuminated via the collimator. Under normal circumstances PIM scales linearly with SUD.

**MID** The count rate from the middle anode layer of the LAC. This layer has a low detection efficiency for low energy (1–5 keV) x-rays. It provides a useful indication of the internal background component.

**SOL2** This refers to the count rate from the solid state electron detector which is used to automatically switch the LAC off as *Ginga* passes through the SAA.

**COR** The cut-off rigidity, which is a measure of the momentum per unit charge that a particle must have to be able to penetrate the magnetosphere and reach the satellite. The COR is calculated from a model of the Earth’s magnetic field and the orbit of the satellite. The background count rate is approximately inversely proportional to the COR.

A full description of the origin and behaviour of the background in the LAC and the parameterisation process is given by Hayashida *et al.* (1989).

The behaviour of the background is illustrated in figure 2.5 which shows the 2-10 keV light curve for a two day observation made on 1987 Sep 5. The count rate can be seen to vary from about 22 to 35 counts sec<sup>-1</sup> and from 8 to 14 counts sec<sup>-1</sup> in the top and mid anode layers respectively. At ~20:00 hrs UT the satellite passes through the SAA and an increase in background flux is evident.

The model used for the estimation of the background is a function of time  $t$ , and energy  $E$ ,

$$C(E, t) = F_1(E) + \sum_{n=2}^N P_n(t) \times F_n(E) \quad (2.1)$$

Where,

$C(E, t)$  = LAC count rate due to the background

$n$  = label of component being fitted

$P_n(t)$  = parameter being fitted to the data

$F_n(E)$  = coefficients determined from fit to background data

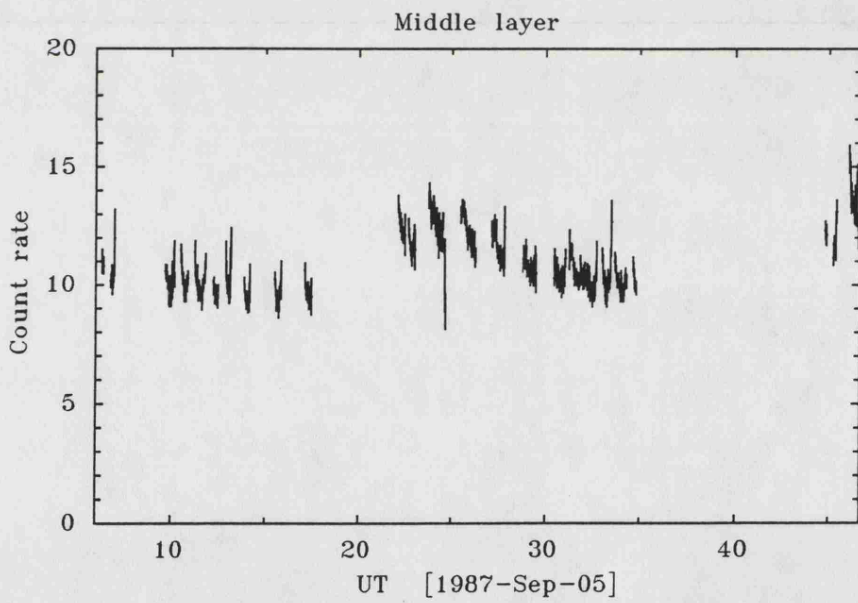
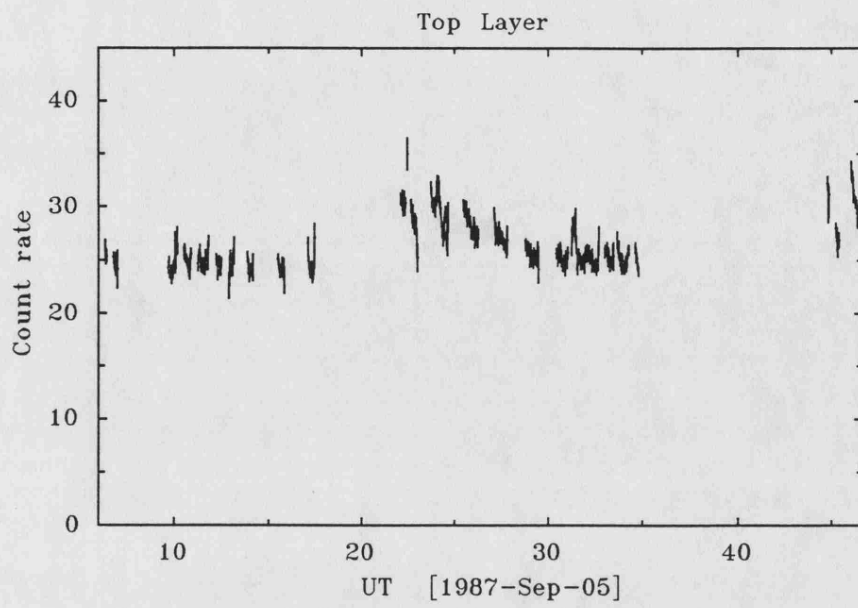


Figure 2.5: An example of the behaviour of the 2–10 keV background radiation detected by *Ginga*.

In practice, the parameters used are

- A constant component representing the diffuse x-ray background.  $F_1(E)$ .
- The SUD rate.
- Components from the decay of three radio-isotopes, with half-lives of 40 min, 80 min and 8.7 hrs, formed during passage through the SAA. The presence of another radio-isotope ( $T_{1/2} \sim$  tens of hours) has also been inferred, but is not an important contribution over the typical duration of an observation. The exponential behaviour due to radio-isotope decay ( $T_{1/2} = 80$  min, and 8.7 hrs) is evident in the background light curve shown in figure 2.5.

There are two methods of determination of the background parameters. A background observation is usually made immediately before or after most source pointings. Provided that this observation covers a sufficient interval to determine the strength of the 8 hr decay component, this is usually sufficient. In the case where there is no suitable nearby background pointing, the parameters may be determined from a data base of such observations (the so-called “Universal” background generation method). In this case it is necessary to account for a further aspect of the time variability of the background which arises from the precession of the orbit. The satellite enters the SAA at an altitude which varies with a 37 day cycle. The data base for the universal background method covers this periodicity sufficiently well to model behaviour at any part of the cycle.

The limiting sensitivity for the LAC is not determined by the accuracy to which the internal background may be estimated, but by the spatial fluctuation in the diffuse x-ray background. By comparison of a number of blank fields at high galactic latitude Hayashida *et al.* (1989) found that the 2–10 keV fluxes due to the cosmic x-ray background have a distribution of rms width  $\approx 0.86$  counts  $\text{sec}^{-1}$ . In order to be detected, a source must be significantly brighter than this limit. The quoted  $3\sigma$  limit for the LAC is  $\approx 2.6$  counts  $\text{sec}^{-1}$  in the 2–10 keV band, which corresponds to a flux of about  $6 \times 10^{-12}$  ergs  $\text{sec}^{-1} \text{cm}^{-2}$  for a spectrum similar to that of the Crab nebula (which is a common calibration standard in x-ray astronomy).

The circumstances under which reliable background modelling cannot be performed include;

- Solar contamination. A sun angle ( $\beta$ ) of less than  $90^\circ$  may result in reflection of soft (1–3 keV) solar x-rays in the collimator. Similarly, observations in which the bright limb of the earth is in the FOV must also be rejected.

- Anomalous particle events. These can be detected by high levels in the SOL2 rate and by deviation from the from a linear PIM – SUD relationship.

As a final point it should be noted that the accurate background subtraction is not always necessary for some timing applications, since techniques such as simple detrending might be sufficient. Also the estimated *Ginga* background can only model background variability on timescales greater than the rate at which the housekeeping data are collected, which is 16 sec. Investigation of source variability on much shorter timescales does not warrant detailed background modelling.

## 2.5 SPECTRAL ANALYSIS

Spectral information on source behaviour is given by pulse height data from the proportional counter experiments and the flux measured by the LE telescope. An example of a pulse height spectrum, in this case from the *Ginga* LAC is shown in figure 2.6. The method used for fitting model continua and line features to these data is as follows. The model is specified with trial values of; the set of parameters ( $S$ ) which determine the shape of the spectrum, the column density ( $N_H$ ) along the line of sight, and the normalisation ( $A$ ). The model spectrum is calculated and folded through a detector response matrix to give the expected pulse height spectrum, which is then compared to the data. The goodness of fit is measured by the  $\chi^2$  statistic, and the best fit model is found iteratively by searching for a minimum in the  $\chi^2$  surface in the parameter space of the model (see e.g. Bevington, 1969). Errors associated with parameters are determined by searching for values which will give the appropriate change in  $\chi^2$ . All errors quoted here are at the 90% confidence limit unless otherwise stated.

The form of the detector matrix for *Ginga* is essentially constant with time. For EXOSAT however, the gain of the ME varied over the course of the mission, and the detector matrix appropriate to the time of observation must be used.

The spectral model, as a function of energy  $E$  may be written as the number of photons  $dN$  in an infinitesimal energy range  $dE$ .

$$\frac{dN}{dE} = A \exp(-N_H \sigma(E)) f(S, E) \quad (2.2)$$

Where  $N_H$  is the hydrogen column density along the line of sight,  $\sigma$  is the photo-electric cross section, and  $f(S, E)$  defines the shape of the spectrum and is generally a function of a set of

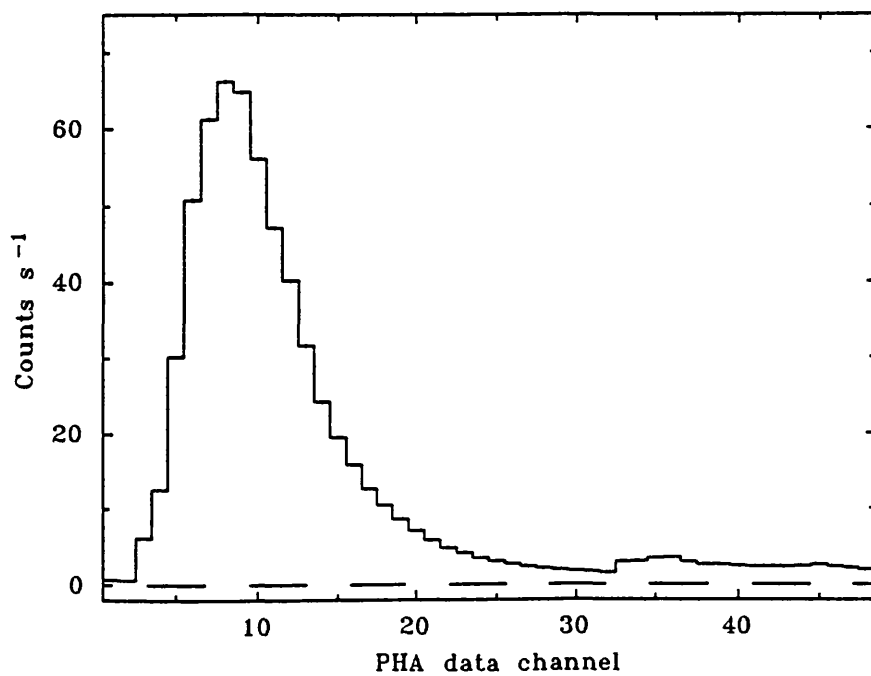


Figure 2.6: An example of a pulse height spectrum from the *Ginga* LAC instrument. The source in this case is the LMXB dip source X 1624-490. Note the 'jump' at channel number 33 due to the binning of the instrumental channels 33-64 into 16 OBC pulse height channels.

parameters  $S$ . In this work the form of  $\sigma$  is that given by Morrison and McCammon (1983). The commonly used continuum forms of  $f(S, E)$  are given below. To obtain the spectrum in terms of the energy rather than the photon distribution, these expression must be multiplied by a factor of  $E$ .

- Power law (PL).

$$f(S, E) = E^{-\alpha} \quad (2.3)$$

The parameter  $\alpha$  is the photon index, the index of the energy distribution is  $\gamma = \alpha - 1$ .

- Thermal bremsstrahlung or thin thermal emission (TB).

$$f(S, E) = g(E, kT) \exp\left(-\frac{E}{kT}\right) E^{-1} (kT)^{-1/2} \quad (2.4)$$

$T$  is the bremsstrahlung temperature.  $g(E, kT)$  is the temperature-averaged gaunt factor ( $\propto E^{0.4}$ ).

- Blackbody emission (BB).

$$f(S, E) = \frac{E^2}{\exp(E/kT) - 1} \quad (2.5)$$

$T$  is the blackbody temperature.

- Generalised thermal (GT).

$$f(S, E) = E^{-\Gamma} \exp\left(\frac{-E}{kT}\right) \quad (2.6)$$

This model was suggested as an approximation for unsaturated Comptonisation by Eardley *et al.* (1978). The expected range of  $\Gamma$  (for the photon spectrum) is -0.5 to 3, and  $kT$  is a characteristic temperature. This form of spectrum was first applied to the spectra of LMXB by White (1986).

Emission lines are modelled using a Gaussian profile centred at the line energy. The integrated area under this curve corresponds to the equivalent width of the line feature. The most prominent emission lines in x-ray spectra over the 2–10 keV range are those due to fluorescent and thermal  $K\alpha$  emission from iron, with energies of  $\approx 6.4$  and 6.7 keV (see e.g. Makishima, 1986).

## 2.6 TIME SERIES ANALYSIS

There are several standard techniques which are commonly used to search for periodic modulation or to measure timescales of variability in a source, these are described briefly below. The various

techniques have different applications dependent upon the type of variability exhibited by the source.

A useful concept in the discussion of periodic modulation is that of coherence. For an oscillation with period  $P$ , the period coherence is defined as  $Q_P = |\dot{P}|^{-1}$ , and represents the number of cycles that are required before the period changes significantly. The phase coherence,  $Q$ , is a measure of the number of cycles that elapse before the phase of the oscillation changes significantly, i.e. by about  $\pi/2$  radians. This is a much stricter constraint than the requirement of period stability and thus  $Q_P > Q$ . Modulation with very high coherence is typically associated with processes, or 'clocks,' having a large angular momentum, such as the orbital motion of the binary or of the rotation of the compact object. Examples of low coherence are provided by phenomena such as quasi-periodic oscillation (QPO) in LMXBs and quasi-coherent oscillations in CVs. The clocks driving these pulsations are generally not well understood.

In terms of non-periodic variability, it is useful to determine if there is a characteristic timescale for the process of interest. An example of this sort might arise from flaring activity, occurring randomly, but following a rise and fall which are determined by the underlying physical processes. A characteristic time, then, may be that required for the flare to decay to a certain fraction of its peak intensity. Variability may be however be self-similar, such that changes scale with the time interval that they are observed over. In these cases it is of interest to determine whether this type of behaviour breaks down above or below some timescale, which may give some limits on the underlying physical conditions.

### 2.6.1 Auto and Cross Correlation

The auto-correlation function (ACF) of a time series, or the cross-correlation function (CCF) of a pair of time series are useful diagnostics in characterising aperiodic time variability, and in measurement of the coherence of periodic oscillations (see chapter 4). The formulae for the ACF and CCF are straightforward, the definitions adopted here are that the ACF of a time series  $x_1, \dots, x_N$ , is given by ;

$$r(u) = \frac{\sum_i (x_i - \langle x \rangle)(x_{i+u} - \langle x \rangle)}{\sum_i (x_i - \langle x \rangle)^2} \quad (2.7)$$

and the CCF of two consecutive time series,  $x_1, \dots, x_N$  and  $y_1, \dots, y_N$  is given by ;

$$r(u) = \frac{\sum_i (x_i - \langle x \rangle)(y_{i+u} - \langle y \rangle)}{(\sum_i (x_i - \langle x \rangle)^2 \sum_i (y_i - \langle y \rangle)^2)^{1/2}} \quad (2.8)$$

where  $\langle x \rangle$  and  $\langle y \rangle$  are the mean values of  $x$  and  $y$  over the appropriate range of summation.

There are two points regarding correlation functions which are often overlooked. The first concerns the determination of errors associated with a correlation function. In the case where the correlation function is non-zero, then, by adopting the transformation of variables suggested by Fisher (see for instance, Spiegel, 1961),

$$Z = \frac{1}{2} \ln \frac{1+r}{1-r} \quad (2.9)$$

The statistic ( $Z$ ) can be shown to be normally distributed with mean ( $\mu_Z$ ) and standard deviation ( $\sigma_Z$ ), given by

$$\mu_Z(u) = \frac{1}{2} \ln \frac{1+r_0(u)}{1-r_0(u)} \quad (2.10)$$

$$\sigma_Z = \frac{1}{\sqrt{N-u-3}} \quad (2.11)$$

Where  $r_0$  is the best estimate of the population correlation coefficient. In all correlation functions shown here the error bars shown correspond to the  $1\sigma$  deviations unless otherwise stated.

A second point concerns the effect on the correlation function of the variance due to counting statistics in the original light curve. Weisskopf *et al.* (1975) illustrated that the effect of Poisson noise is to suppress (i.e. reduce the absolute value of) correlation functions. The correlation function may be corrected by scaling by the ratio of the total variance to the intrinsic source variance. Obviously, such a procedure will be sensitive to the reliability of the estimate of intrinsic source variance. The relationship between the calculated correlation function  $r(u)$  and that appropriate to the true source behaviour ( $r_{int}(u)$ ) is given by the following expressions for the ACF,

$$r(u=0) = 1 \quad (2.12)$$

$$r(u \neq 0) = \frac{(\sum_i (x_i - \langle x \rangle)^2 - \sum_i \sigma_x^2)}{\sum_i (x_i - \langle x \rangle)^2} r_{int}(u) \quad (2.13)$$

and the CCF,

$$r(u) = \frac{(\sum_i (x_i - \langle x \rangle)^2 - \sum_i \sigma_x^2)}{\sum_i (x_i - \langle x \rangle)^2} \frac{(\sum_i (y_i - \langle y \rangle)^2 - \sum_i \sigma_y^2)}{\sum_i (y_i - \langle y \rangle)^2} r_{int}(u) \quad (2.14)$$

As an example of this effect, figure 2.7 shows the ACF of flaring activity in the x-ray dip source X 1624-490, the dashed and solid curve represent the original and corrected auto-correlation functions respectively.

The major difference between the approach adopted by Weisskopf *et al.* and that adopted here lies in the estimate used for the average count rates. The *Uhuru* experiment was a scanning wide

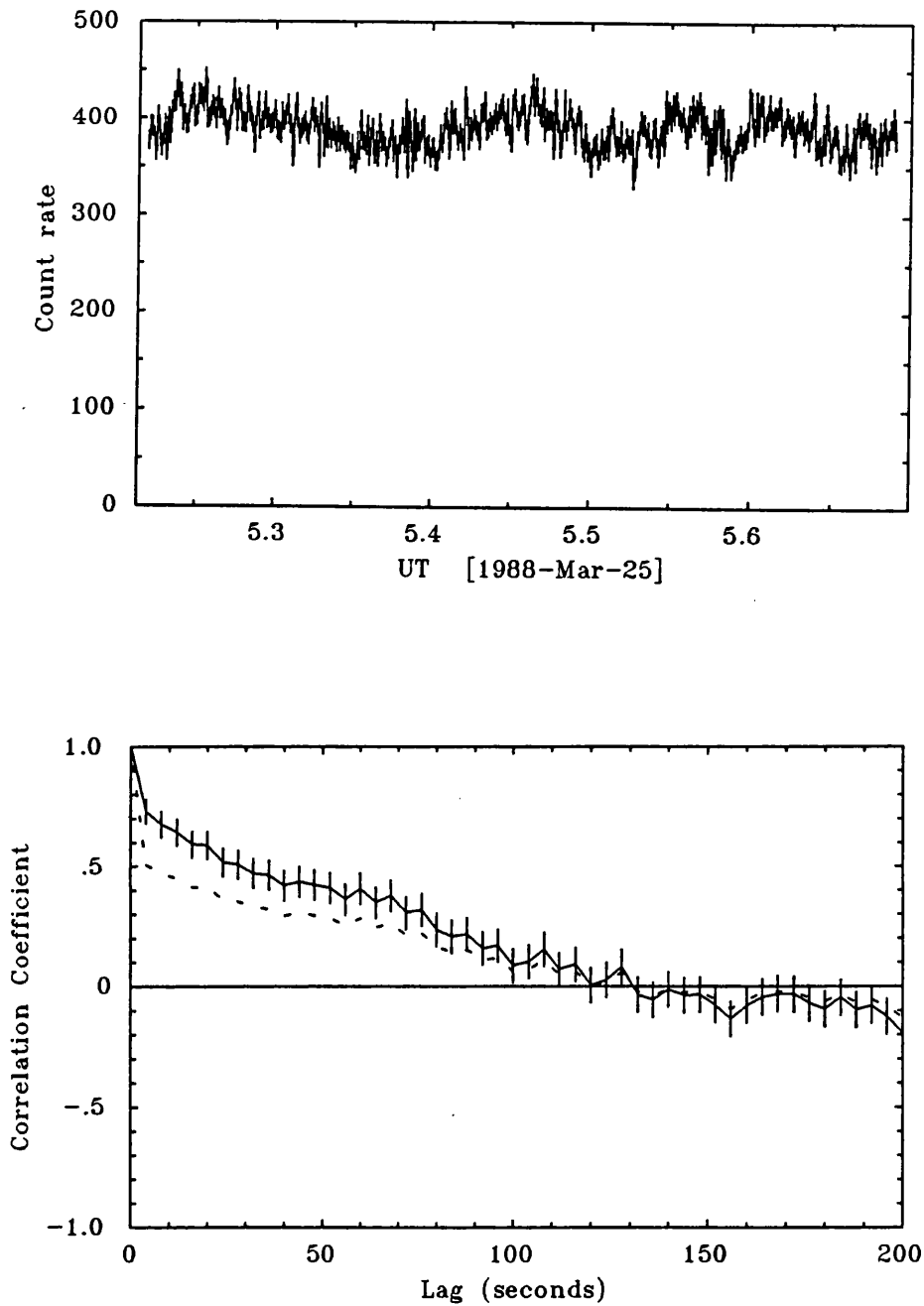


Figure 2.7: An example of the autocorrelation function. The top panel shows the 5–10 keV light curve of the the LMXB source X 1624-490. The lower panel shows the ACF corrected for the effect of counting statistics (solid line) with  $1\sigma$  error bars. The dashed curve shows the uncorrected ACF. The typical timescale for the variability in this case is 50–100 sec.

field of view proportional counter, such that the dominant variability in the raw data arose from the changes in transmission during the slew. The appropriate averages in this case are then the weighted mean count rates. In contrast, the EXOSAT and *Ginga* light curves are usually dominated by the intrinsic source variability and consequently the mean is the appropriate average.

In passing it should be noted that consideration of this correction procedure is not given by many authors. Ideally, the correction should be mentioned explicitly, and comment should be made on the reliability of the adopted correction factor. In the case of the ACF the effect of poorly determined correction is most pronounced between the first ( $u = 0$ ) and second points (since  $r(u = 0) = 1$  by definition). Without a discussion of the correction factor, the use of a large initial drop in the ACF as evidence for short timescale variability should be treated with caution.

## 2.6.2 Power Spectrum

A time series  $x_k$  ( $k = 1, \dots, N$ ) may be represented as a sum of Fourier components with frequencies  $\omega_j$  such that,

$$x_k = \frac{1}{N} \sum_j a_j e^{-i\omega_j t_k} \quad (2.15)$$

where the coefficients  $a_j$  are termed the Fourier amplitudes and are generally complex. The set of  $a_j$  form the Fourier transform of  $x_k$  and an inverse Fourier transform may be defined,

$$a_j = \sum_k x_k e^{i\omega_j t_k} \quad (2.16)$$

It is often useful to measure the moduli of  $a_j$  by forming the set of quantities  $P_j \propto a_j^* a_j \equiv |a_j|^2$ . Such a set is termed the *power spectrum* of  $x_k$ . If  $x_k$  is sinusoidally modulated at frequency  $\omega_l$  and free from noise, then it is trivial to show the  $P_j$  will be finite only for  $\omega_j = \omega_l$ . Initial applications of power spectra in x-ray astronomy approximated well to this ideal case, and little regard was paid to the statistical behaviour of  $P_j$  since strong peaks in the distribution hardly warranted this approach. One of the first correct quantitative treatments of power spectral distributions in this context was given by Leahy *et al.* (1983). The statistical properties of power spectra have become the subject of increased interest since the discovery of the QPO phenomenon.

A simple argument to obtain the distribution of  $P_j$  from a normally distributed  $x_j$  is given by van der Klis (1988) who provides an excellent review of the use of Fourier techniques in x-ray astronomy, and from which much of the following is taken. Representing the Fourier transform in

terms of the real coefficients  $A_j$  and  $B_j$  (where  $a_j = A_j + iB_j$ ) then,

$$A_j = \sum_k x_k \cos \omega_j t_k \quad (2.17)$$

$$B_j = \sum_k x_k \sin \omega_j t_k$$

$$P_j = A_j^2 + B_j^2 \quad (2.18)$$

If  $x_k$  are normally distributed then  $A_j$  and  $B_j$  must also be since both are linear combinations of  $x_k$ . It may be shown (see e.g. Freund & Walpole, 1987) that if  $A_i$  is normally distributed that  $A_i^2$  follows a  $\chi^2$  distribution with one degree of freedom (dof). From the additive property of  $\chi^2$  it follows that  $P_j$  follows a  $\chi^2$  distribution with 2 dof ( $\chi_{\nu=2}^2$ ). The scaling of the  $\chi_{\nu=2}^2$  distribution will however depend on the normalisation adopted for  $P_j$ . It was noted by van der Klis (1988) that while the above is strictly only true for normally distributed  $x_k$ , the power is  $\chi_{\nu=2}^2$  distributed for Poisson noise and most other types of noise encountered in x-ray timing measurements. A normalisation which is commonly used is that suggested by Leahy *et al.* (1983) which for a Poisson noise signal containing  $N_\gamma$  photons, gives a power spectrum which is exactly  $\chi_{\nu=2}^2$  distributed;

$$P_j = \frac{2}{N_\gamma} |a_j|^2 \quad (2.19)$$

Instrumental effects such as dead-time alter the signal noise properties and consequently alter the distribution of  $P_j$ . Although some detailed analyses of these effect have been produced (see for example Tennant, 1987, in relation to the EXOSAT ME), it was pointed out by van der Klis (1988) that usually the  $\chi_{\nu=2}^2$  property still holds, although the distribution is re-scaled. The scaling factor may be empirically determined, being the ratio of the ideal mean noise power ( $=2$ ) and the experimental mean noise power (in the absence of any signal). This approach has been adopted in the power spectra presented in this work.

There are two equivalent methods of reducing the noise in a power spectrum, both of which at the expense of the frequency resolution. One method is to simply re-bin the spectrum into coarser frequency bins, the other is to reduce the initial sampling and then to average the resultant set of power spectra. Due to the additive property of  $\chi^2$ , a spectrum formed by averaging  $M$  individual spectra, and by frequency re-binning by a factor  $R$ , will also have a  $\chi^2$  distribution. This new distribution will have  $2RM$  degrees of freedom, and, because of the averaging and the rebinning processes, the power in this distribution will be scaled by a factor of  $1/RM$ . Thus the new distribution still has a mean power of 2, but now has a variance of  $4/RM$ . The shorter sampling method has several advantages over the re-binning method. It is generally faster to compute, and

is more suited to the analysis of time-series containing many gaps. It also offers the possibility of studying the time evolution of spectral features, since the spectra may be plotted as a function of time to form a dynamic power spectrum.

Given a time series of duration  $T$  which is binned into samples of equal duration  $\delta t = T/N$ , the highest frequency that may be investigated is the Nyquist frequency  $\nu_{N/2} = N/(2T)$ . This corresponds to an oscillation with a period of  $2\delta t$ . As the frequency of a measured signal increases towards this limit, the power will be suppressed due to the binning of the time series. It may be shown that this factor is,

$$\beta(\nu) = \frac{\sin \pi\nu T/N}{\pi\nu T/N} \quad (2.20)$$

This is commonly referred to as the ‘diffraction’ term, by analogy with the expression in optics for Fraunhofer diffraction from a narrow slit. The value of  $B(\nu)$  varies from 1 at  $\nu = 0$  to  $2/\pi$  at the Nyquist frequency.

The advantage of Leahy’s normalisation lies in the simplicity of determination of the significance of any features in the power spectrum. The significance of a single power can be calculated from the appropriately scaled  $\chi^2$  distribution. If the confidence level for detection is  $\delta = (1 - \epsilon)$ , i.e. there is only a small chance,  $\epsilon$ , that the detected signal is due to noise, then confidence limit that should be determined from the  $\chi^2$  distribution must take account of the number of frequency bins in the range of interest. For a search across  $N_{trial}$  frequencies, the power at a confidence level  $\delta$  requires that the probability that the signal is due to noise in any one bin is  $\sim \epsilon/N_{trial}$ .

In the case of no detection it is useful to place upper limits on the observed power. Figure 2.8 shows the relevant quantities. The search range is from  $\nu_1$  to  $\nu_2$ , with a maximum power in this range of  $P_i$ . The detection limit, at a confidence  $\delta$ , appropriate to this search range is  $P_{detect}$ . There is a lower power limit which would be expected to be exceeded at a probability of  $\delta$ , which is labelled  $P_{exceed}$  in figure 2.8. In calculation of the upper limit to the power this level is subtracted, since it is likely to be exceeded in a noise-only spectrum,

$$P_{ul} = P_i - P_{exceed} \quad (2.21)$$

In searching for broad peaks in power spectra, the usual procedure is to increase  $RM$  and to calculate the spectrum in progressively coarser bins. Clearly, this procedure will lower  $P_{detect}$  since  $N_{trial}$  will decrease. It should be noted that the formal significance of any excess power remains constant throughout this procedure, it is only the power limit appropriate to a single bin which decreases.

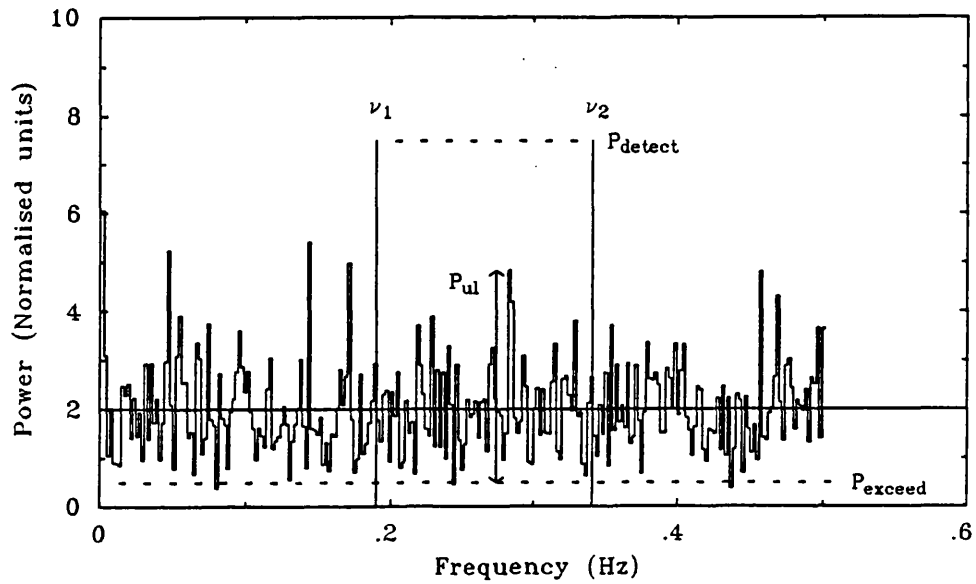


Figure 2.8: An example power spectrum using the normalisation of Leahy *et al.* (1983), showing a search range  $\nu_1$  to  $\nu_2$ , the detection limit  $P_{detect}$ , and the upper limit to any modulation  $P_{ul}$  above the level which is usually exceeded  $P_{exceed}$ .

It is useful to express power in terms of the root mean square (rms) variation. From Parseval's theorem and using the Leahy normalisation, the rms variation of a signal which causes an excess power  $P_{excess}$  (over  $P_{exceed}$ ), possibly over a range of frequency, is,

$$\mathcal{R} = \beta(\bar{\nu}) \sqrt{\left(\frac{P_{excess}}{N_{ph}}\right)} \quad (2.22)$$

Where  $\beta(\bar{\nu})$  is the diffraction term (equation 2.20) at an appropriate average frequency  $\bar{\nu}$ .

### 2.6.3 Periodogram Techniques

Whereas power spectrum techniques are sensitive in detection of periodicities in sinusoidally modulated time series, their use is limited when applied to other types of modulation. A method which is commonly used in the detection of periodicities is that of folding the time-series at a trial period and testing some statistic derived from the resultant pulse profile. The method that has been adopted here is the straightforward test of the hypothesis that the folded profile is consistent with being constant by means of a  $\chi^2$  test. The resultant periodogram is a set of  $\chi^2$  values across the range of trial periods and periodicity is indicated by a peak in the distribution. An illustration of a  $\chi^2$ -periodogram is given in figure 2.9, which shows a period search for a short (2000 sec duration) interval of an EXOSAT LE observation of the dwarf nova SS Cyg in outburst. A sharp peak at 7.8 sec indicates the presence of a strong modulation at this period.

The method has several advantages over power spectrum analysis other than the sensitivity mentioned above. Drop outs in the original time-series do not affect the final result provided that a reasonably even phase coverage is attained. Similarly the technique is insensitive to irregularly sampled time series, which is essentially the case if the original time series is transformed to a barycentric frame of reference. There are some disadvantages of the method also. The choice of  $\chi^2$  as the test statistic has the disadvantage that it selects periods at which the data are least consistent with being constant, but can be scattered. A more realistic test might discriminate in favour of smoothly modulated profiles.

### 2.6.4 Fractal Analysis

The initial application of this method in x-ray astronomy was made by McHardy & Czerny (1987) in their study of the x-ray variability of the Seyfert galaxy NGC 5506. A feature of geometric shapes that are fractal in nature, is that some property of the figure, such as a perimeter length, has

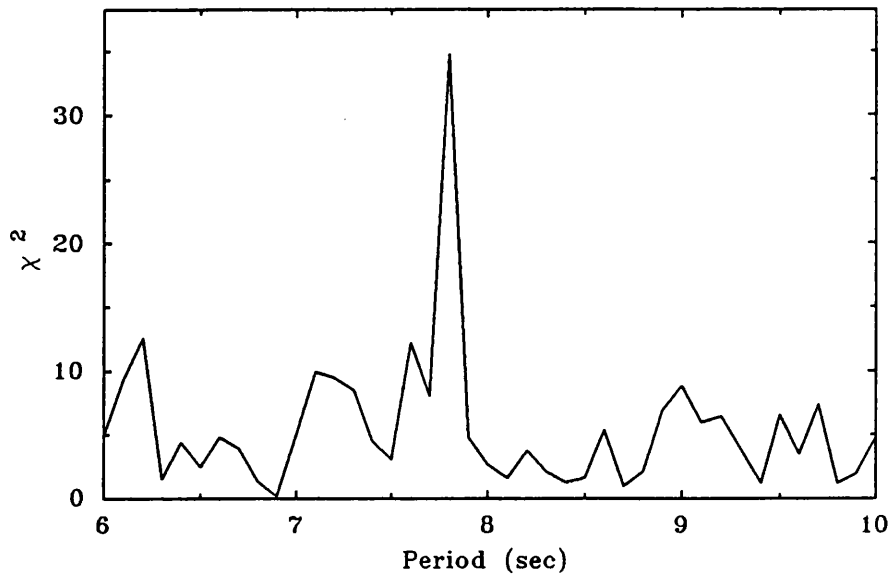


Figure 2.9: An example of a  $\chi^2$ -periodogram. A section of EXOSAT LE data from an outburst observation of the dwarf nova SS Cyg has been folded across a range of periods from 6 to 12 sec. The folded profiles have then been tested against the hypothesis that they represent a constant value by means of the  $\chi^2$  statistic. A sharp peak at 7.8 sec shows the presence of modulation at this period.

a value which is dependent on the lengthscale at which it is measured. This scaling is self-similar such that there is no preferred scale of measurement. An example which is commonly cited (e.g. Mandelbrot, 1983) is that of the length of a coastline ( $L$ ). Using a measuring lengthscale  $\epsilon$ , then two constants are required to describe  $L(\epsilon)$ , since the total length consists of  $F\epsilon^{-D}$  intervals of length  $\epsilon$

$$L(\epsilon) \sim F\epsilon^{1-D} \quad (2.23)$$

The quantity  $D$  is termed the *fractal dimension* of the coastline, it has non-integer value which is greater than the topological dimension of the figure, and describes the way in which the length scales as a function of the units of measurement.

The application of the above ideas to a light-curve requires a slight modification, since the 'length' under investigation is one dimensional, being a difference in intensity. Thus the expected value of  $D$  should lie in the range 0–1 rather in the range 1–2 obtained for the examples above. For a one-dimensional length it would be expected that,

$$L(\epsilon) \propto \epsilon^{-D} \quad (2.24)$$

The measuring lengthscale becomes a timescale  $\Delta t$ , such that for a light curve  $F(t)$  the fractal length function  $L(\Delta t)$ , and fractal dimension  $D$ , are defined by:

$$L(\Delta t) = \frac{1}{\Delta t} \int_{t_s}^{t_s+\Delta t} |F(t) - F(t_s)| dt \quad (2.25)$$

and,

$$D = -\frac{d \log L(\Delta t)}{d \log \Delta t} \quad (2.26)$$

Where  $t_s$ , and  $T$  are the start time and duration of the sample respectively. The measured value of  $L(\Delta t)$  however, contains a contribution from the noise associated with the flux measurements. It is straightforward to show that noise has the property of  $D = 1$ , and the noise contribution to  $L$  may be easily calculated. The noise is statistically independent of the signal and so may be corrected for using the relation;

$$L_{observed} = (L_{signal}^2 + L_{noise}^2)^{1/2} \quad (2.27)$$

It should be stressed that the term 'fractal analysis' does not imply that the light curves that are being studied are genuinely fractal in nature. The technique is essentially a method of determining whether or not variability is self-similar over a range of measuring timescales. If characteristic timescales do exist in the time-series, then it will not possible to measure a single fractal dimension over the entire range of  $\Delta t$ , and  $D$  will generally be a function  $D = D(\Delta t)$ .

### An example of the power of fractal analysis: The response of $L(\Delta t)$ to square shots

An application to which fractal analysis has been put in this work is in the study of the morphology of ‘dip’ light-curves from LMXB systems (chapter 7). To a first approximation, these dips may be represented as inverted top-hat functions or square shots. Although the modelling of dip-light curves presented in chapter 7 requires Monte-Carlo simulation to investigate the behaviour of  $D$  under various distributions of shot recurrence and duration, an analytic solution for  $D$  can be obtained for a simple distribution of square shots.

Consider a time series  $F(t)$  with associated signal noise  $\sigma_s$ . Individual square shots have depth (or height)  $a$  and duration  $t^*$ . If the time series contains  $n$  shots, then provided that the probability of overlap of shots is small ( $nt^* \ll T$ ), and that the shot modulation is much greater than the noise ( $a \gg \sigma_s$ ), the fractal length function and dimension can be shown to be,

$$\begin{aligned} L(\Delta t) &= \frac{\eta T}{\Delta t} + 2n(a - \eta) \quad , \Delta t < t^* \\ &= \frac{\eta T}{\Delta t} + \frac{2t^*}{\Delta t}(a - \eta) \quad , \Delta t > t^* \end{aligned} \tag{2.28}$$

and,

$$\begin{aligned} D &= 1 - \left(1 + \frac{\eta T}{2n\Delta t(a - \eta)}\right)^{-1} \quad , \Delta t < t^* \\ &= 1 \quad , \Delta t > t^* \end{aligned} \tag{2.29}$$

where  $\eta = \sigma_s / \sqrt{\pi/2}$ . This is illustrated in figure 2.10, which shows part of an artificial time series containing sparsely distributed square shots and the corresponding fractal length function. The solid line shows  $L(\Delta t)$  as predicted from equation 2.29. The discrepancy between the actual and predicted behaviour can be attributed to the simplifying assumptions made in the derivation of the equation not being met in the artificial data. The characteristic response of  $L(\Delta t)$  to square shots is that there is a well defined break at  $\Delta t = t^*$ , below this break  $D$  is not constant but is  $< 1$ , whereas for  $\Delta t > t^*$ ,  $D$  tends to the noise only value of 1.

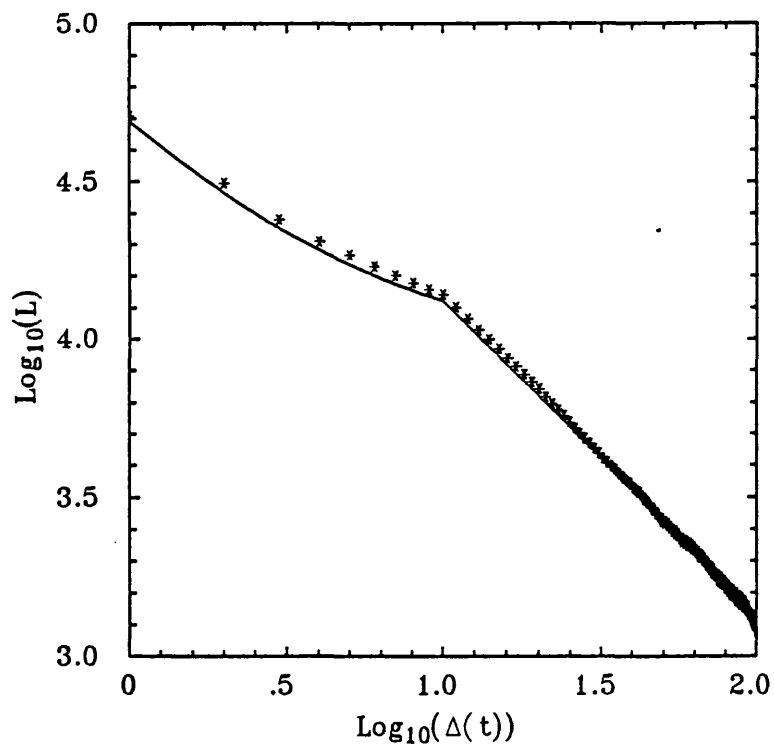
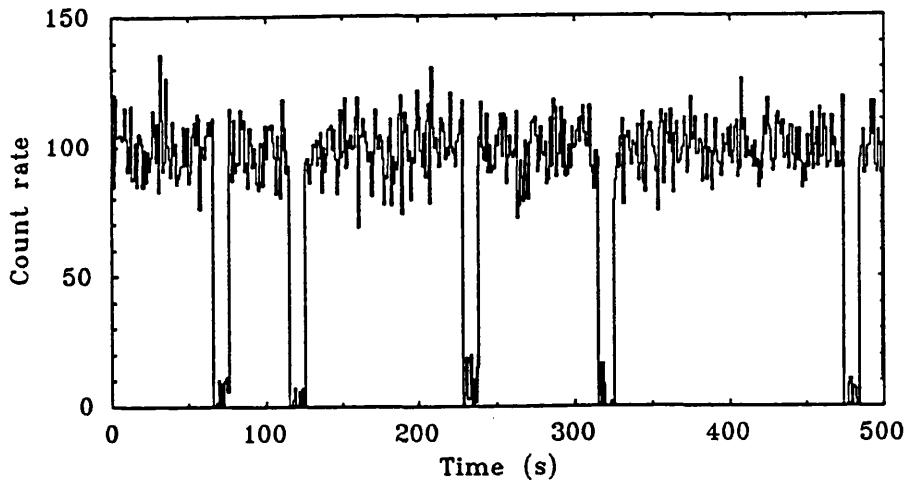


Figure 2.10: An example of the fractal length function. The top panel shows a short section ( $\sim 10\%$ ) of a simulated time series consisting of randomly occurring square shots. The lower panel shows the empirical fractal length function (\*) determined from the time series. Also shown, by the solid line, is the analytic solution for the fractal length as given by equation 2.28.

## Chapter 3

# Dwarf Nova Variables

### 3.1 INTRODUCTION

As an introduction to the EXOSAT observations of the dwarf nova SS Cygni presented in chapter 4, the observational properties of this class of cataclysmic variable are reviewed. Classification of these sources on the basis of their outburst behaviour is described, as are the spectral characteristics which suggest similarity with other types of CV. Dwarf novae are weak x-ray emitters ( $\sim 10^{33}$  ergs sec $^{-1}$ ) and show two distinct components of emission which behave in different ways during optical outburst. Theoretical models which have been proposed to describe outburst behaviour are discussed in relation to observations. A feature common to many dwarf novae in outburst, and novalike variables, is the presence of small amplitude, short period optical oscillations. X-ray observations of three dwarf novae suggest that these pulsations have a high energy origin. The known properties of these oscillations, prior to the EXOSAT observations of SS Cyg, are summarised.

### 3.2 CLASSIFICATION OF DWARF NOVAE

The optical variability of the class of stars termed the dwarf novae first drew the attention of astronomers during the second half of the last century, with the discovery of U Geminorum in 1855 (Hind, 1856, and Pogson, 1883). This variability is characterised by recurrent outbursts in which

the source brightens by 2-5 magnitudes for a period of typically a few days before returning to a quiescent state. These outbursts recur, not at a strict period but on characteristic timescales which range between tens and hundreds of days depending on the particular object. Many systems were found to be single or double lined spectroscopic binaries and by the mid-1960s it was generally accepted that all dwarf-novae are binary systems (e.g. Mumford, 1967). The orbital periods of these systems are all found to be of the order of a few hours, with one component inferred to be a late type dwarf (K-type or later) filling its Roche lobe. The other component has a characteristic blue spectrum which is now attributed to an accretion disc around a compact primary which is generally accepted to be a white dwarf. Thus the dwarf novae form a subset of the cataclysmic variables.

The brightest members of the class have  $m_v \sim 8 - 9$  while in outburst, and many have been monitored on a regular basis by amateur observers since their identification as dwarf novae. These observations, which give night to night measurements of  $m_v$  to an accuracy of typically  $\pm 0.2$  mag, form the basis of statistical studies of the properties of dwarf nova outbursts (see for example, Bailey, 1975, Szkody and Mattei, 1984). As a result of different outburst morphologies, dwarf novae are usually classed as members of one of three subgroups which are named after archetypal sources exhibiting this type of behaviour: U Gem, SU UMa and Z Cam type variables.

The U Gem type variables are characterised by outbursts of similar total luminosity. There are however different types of outburst commonly exhibited by this class, as can be seen from the light curve of SS Cyg shown in figure 3.1. Several different schemes of classification of outbursts exist. The simplest has only three categories, 'short', 'long', and 'anomalous', figure 3.1 shows the first two types and illustrates another feature common to U Gem variables in that these types of outburst tend to alternate. The anomalous outbursts occur infrequently and typically have a long duration, there is a tendency for there to be an extended quiescent interval following such an event. More detailed classification schemes are used on occasion, particularly in statistical studies of outburst properties such as rise and decay times, but will not be considered further here.

It appears that the difference between short and long outbursts becomes more pronounced as the orbital period ( $P_{orb}$ ) of the system gets shorter. For dwarf novae with periods less than  $\sim 2$  hrs the long outbursts are typically up to 1 mag brighter than the normal outbursts and are of longer duration. These events are usually termed 'superoutbursts', and may have a total outburst energy which is an order of magnitude greater than the short type (which are commonly referred to as normal outbursts in this context). The tendency for alternation of outburst type disappears, superoutbursts occur at a much lower frequency than normal outbursts. Systems of this type are

termed SU UMa variables. An example light curve of the SU UMa system VW Hyi is shown in figure 3.2, the normal outbursts occur about every 28 days or so, and the superoutbursts recur every  $\sim 180$  days.

A statistical study of 26 dwarf novae by van Paradijs (1983) supports the idea that the duration of both the short and long outbursts are positively correlated with the orbital period of the system. The dependence on  $P_{orb}$  is stronger in the case of short outbursts, and van Paradijs suggests that the extreme differences between outburst types seen in SU UMa systems is primarily due to the narrowing of short outbursts. Given the continuity of outburst type between the U Gem and SU UMa type variables, the only distinguishing characteristic of the superoutburst phenomenon is that in these events the optical emission is smoothly modulated with an amplitude of  $\sim 0.3$  mag at a period which is a few percent longer than the orbital period. This modulation is referred to as ‘superhump’ behaviour, to distinguish it from the orbital ‘humps’ seen in many dwarf novae which occur at the orbital period.

The final class of dwarf novae are the Z Cam type variables. An example light curve is shown in figure 3.3, from RX And, and illustrates a characteristic ‘standstill’ in which the source brightness remains fixed at an intermediate intensity level for an extended period of time. Z Cam itself, for example, has a outburst recurrence time of 23 days but has been observed in standstill for up to about eighteen months. The standstills always start in decline from outburst and end with a return to quiescence.

The association of dwarf novae with other classes of cataclysmic variable is based to their characteristic spectra. In quiescence the optical spectra are characterised by strong, sometimes broad, emission lines of H, He I and sometimes He II, with a flat or blue continuum. In outburst the continuum becomes bluer and the neutral hydrogen and helium lines tend to become broad absorption features. An example of these changes is shown in figure 3.4, and shows the dramatic change in continuum and line emission associated with outburst, in this case in WX Hyi (from Hassall *et al.*, 1983). Other stars which are believed to be interacting binaries in which mass transfer is taking place by Roche lobe overflow onto a white dwarf are;

- Classical novae. These stars are characterised by single outbursts in which the optical flux brightens by  $\sim 10$  mag in a few days, and declines to its quiescent level over a period of months to years. The source spectrum changes with the decline from outburst, passing through a ‘post-novae’ stage which is similar to dwarf novae in outburst, to an ‘old-novae’ state which is similar to dwarf novae in quiescence.

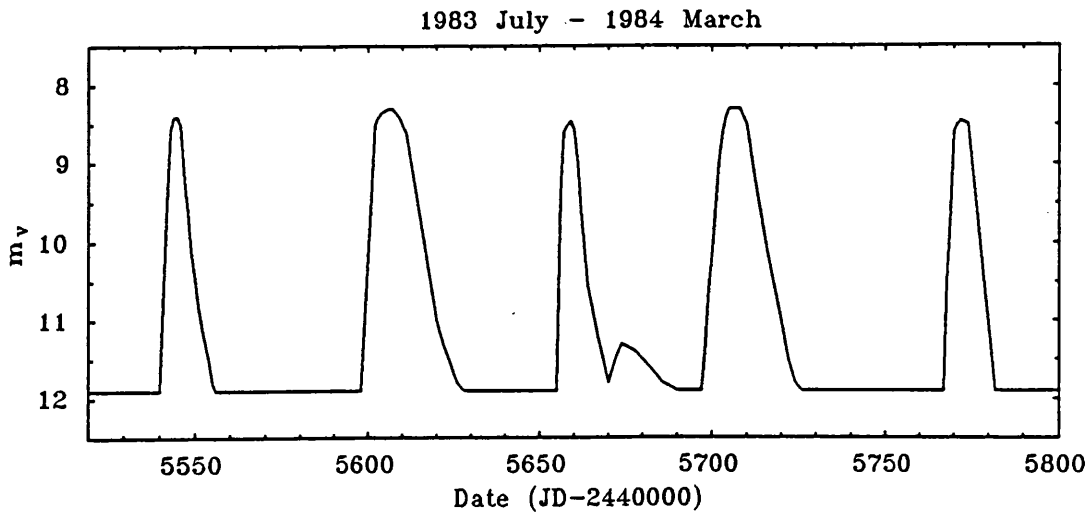


Figure 3.1: A light curve from SS Cyg showing recurrent outbursts of short and long type. From data provided by the AAVSO.

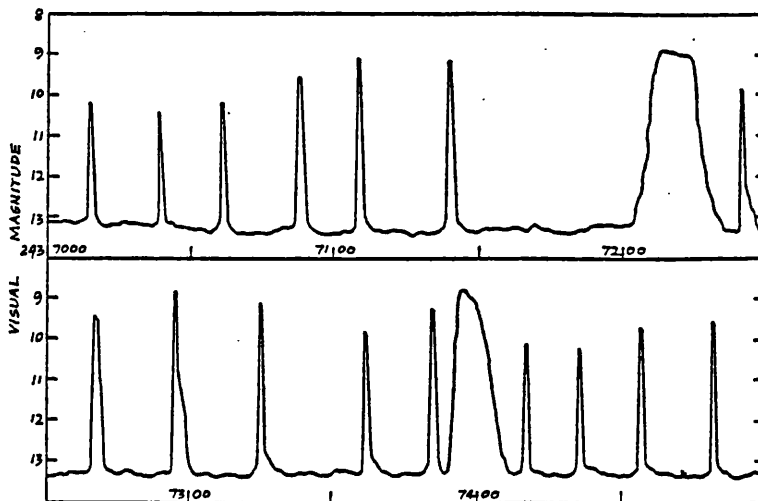


Figure 3.2: A light curve from VW Hya showing normal outbursts and superoutbursts. From Glasby (1970) (original data supplied by the variable star section of the BAA).

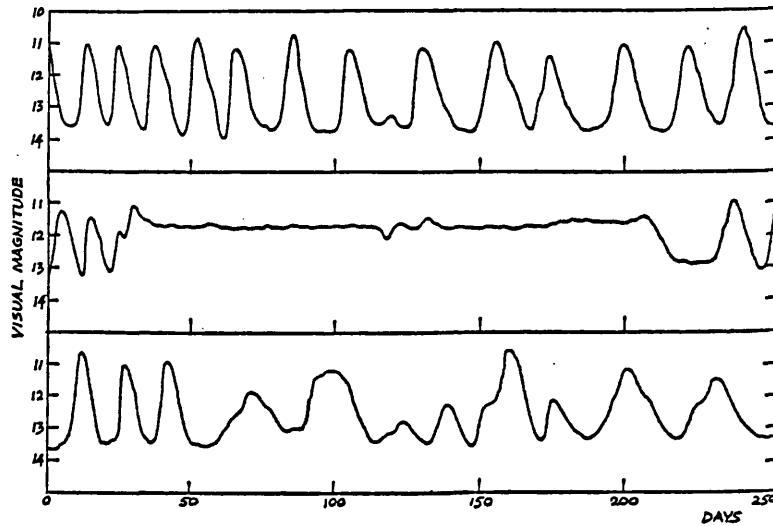


Figure 3.3: A light curve from RX And, showing a long duration standstill in the decline from outburst. From Glasby (1970) (original data supplied by the variable star section of the BAA).

- Recurrent novae, which show large amplitude outbursts similar to those seen in classical novae but which recur on a timescale of a few tens of years.
- The ‘magnetic’ CVs, in which the accretion flow is channeled onto the poles of the white dwarf by a strong magnetic field ( $B > 10^6$  G). This class includes the AM Her systems (the ‘polars’) and the intermediate polars. They are characterised by periodic changes in optical polarisation, and by coherent modulation of the x-ray emission.
- The ‘novalike’ variables. So called because of spectral similarities to novae, but have not been observed undergoing outburst. The UX UMa class have a low level of variability ( $\sim 0.5$  mag), and appear as dwarf novae in a permanent outburst state. The DY Scl types have been termed the ‘anti-dwarf novae’, and as this suggests, they are usually in what appears to be a dwarf nova outburst state, but show occasional dips into quiescence.

There are some differences between spectra of different types, in particular the post-novae and the UX UMa types may show weak emission lines of high excitation states such as He II  $\lambda 4686$  and the CIII-NIII complex at  $\lambda\lambda 4600-4650$ . Such differences have been attributed to increased mass transfer rates in these systems. The post-novae spectra are also complicated by the emission line components from the circumstellar shell which is ejected in the nova explosion.

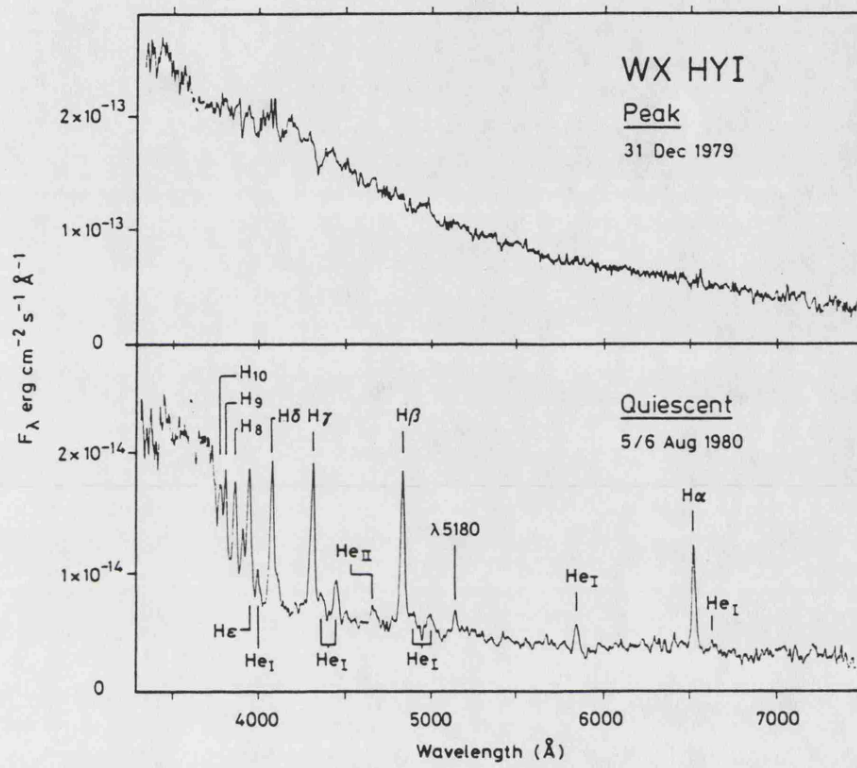


Figure 3.4: Optical spectra for the dwarf nova WX Hyi in outburst and quiescence. From Hassall *et al.* (1983).

The number of identified dwarf novae is estimated to be  $\sim 200$ , there are a few dozen UX UMa types, and only 10 or so DY Scl variables. There are however, several important selection effects inherent to the identification and classification of CVs. Misclassification is likely if the distinguishing characteristic has a relatively infrequent occurrence. A Z Cam variable would be classed as a U Gem type until a standstill is observed, a UX UMa type may reveal itself to be a VY Scl variable following the observation of a quiescent dip. Another effect is that novalike variables have no large scale variability to indicate their presence. A good example of this was provided by the novalike variable IX Vel (CPD -15° 1477), which at  $m_v \approx 9.8$  is the brightest example of the class in the sky, and yet was only identified as such in 1982 (Garrison *et al.*, 1982, 1984, and Eggen and Niemela, 1984). Another consequence of this lack of variability is that novalikes which are eclipsing binaries will be preferentially identified. Wade and Ward (1985) noted that it is uncertainties in correcting for these effects which has prevented quantitative estimates on the relative populations of types of CV from being made.

### 3.3 THEORIES OF OUTBURST

The accepted scenario for the classical novae outbursts is that a hydrogen rich layer on the surface of the white dwarf is ignited in a thermonuclear reaction (Starrfield, Sparks and Truran, 1976). Bath and Pringle (1985) argue that a similar hydrogen burning shell model for dwarf novae outbursts can be rejected for two reasons. Observations of the eclipsing U Gem variable Z Cha shows that the eclipse profile changes in outburst in such a way as to imply that the outburst luminosity arises in a disc of material which almost fills the Roche lobe of the primary. Secondly, multiwavelength studies of VW Hyi, indicate a time lag between the onset of optical and UV outburst, such a delay between spectral components cannot be reconciled to a thermonuclear burning model. It is now generally accepted that outbursts in dwarf novae have their origin in an increased rate of mass transfer through the accretion disc. Such a model is attractive since the required luminosity may easily be produced at moderate mass transfer rates (see section 3.4).

Two mechanisms have been suggested to give rise to the increased mass transfer rate. Osaki (1974) suggested that the disk itself may be subject to an unspecified type of instability. The rate of mass transfer from the secondary is constant, and the disc can accumulate matter while the disc operates under one flow regime. Following the onset of the instability, the flow changes such that the reservoir of material accretes rapidly through the disc, giving rise to the outburst. In the outline of the theory of thin accretion discs in chapter 1, it was shown that disc models describe a surface

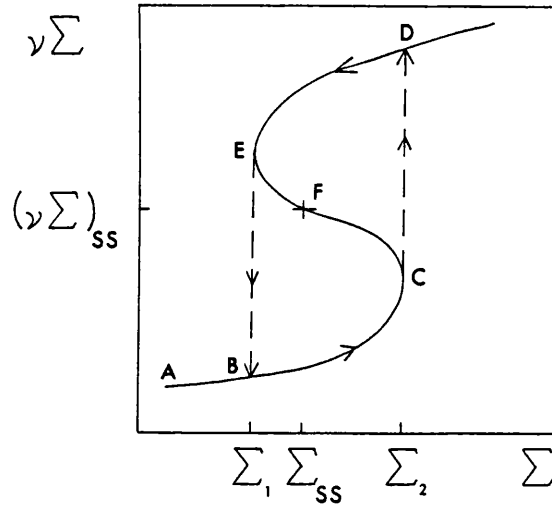


Figure 3.5: The  $\nu\Sigma - \Sigma$  plane, with kinematic viscosity  $\nu$  and surface density  $\Sigma$  in an accretion disc. Stable solutions exist only for  $\partial(\nu\Sigma)/\partial\Sigma < 0$ , a disc with steady state solution at **F** is unstable and follows the limit-cycle indicated. (From King, 1989)

density  $\Sigma$ , and evolution in a disc with viscosity  $\nu$  is given by the diffusion-like equation 1.16. Lightman and Eardley (1974) pointed out that the disc will be unstable if  $\partial(\nu\Sigma)/\partial\Sigma < 0$ . In this case the matter in the disc diffuses away from less dense areas and the disk will fragment. Bath and Pringle (1982) suggested that a limit-cycle behaviour may occur, given a form of  $\nu\Sigma$  as shown in figure 3.5. If the steady state solution of the disc (determined by  $\dot{M}$ ) lies at point **F** on an unstable part of the curve, then starting from a low density at **A**, the disc will evolve to **C**, where the disc is forced to find the only stable solution at that density  $\Sigma_2$ , and jumps to point **D**. Now the disc again tries to reach the steady state solution, but at **E** it jumps again to the lower branch of the curve. This cyclic behaviour has many of the characteristics of the viscosity changes that would be required to give an outburst. A theoretical problem noted by King (1989) is that the conditions across the disc have to be finely tuned, otherwise the instability will fail to propagate and will result in rather low amplitude variability. Meyer and Meyer-Hofmeister (1981) suggested that the dramatic change in opacity at  $T \sim 10^4$  K due to photoionisation of neutral hydrogen may give rise to the required instability. Within a certain range of temperature there are two stable density states. The low temperature regime, which has low viscosity corresponds to the branch **B - C** in figure 3.5, and the high temperature phase with high viscosity to the section **D - E**.

The alternative mechanism is one in which the mass transfer rate through the inner Lagrangian (L1) point increases during outburst. Detailed numerical studies of the effect of injecting mass in various distributions into an accretion disc have been carried out by Bath and Pringle (1981 and 1982), and indicate that the observed outburst luminosity profiles may be formed by this mechanism. An example of the type of outburst observed for an arbitrary mass injection is shown in figure 3.6, and can be seen to have similar qualitative features to observed dwarf novae outbursts, having a rapid rise time and a rather slower decline. The process which drives the mass injection is somewhat uncertain, Bath and Pringle (1981) suggest an instability in the atmosphere of the secondary. A requirement of any theory for this process is that it must explain the recurrence properties of the outbursts.

It has proved difficult to determine which model is correct. In this type of system a significant fraction of the optical luminosity originates from the hot-spot at which the gas stream from the L1 point is incident on the outer edge of the accretion disc. In principle the mass transfer through the gas stream should determine the luminosity of the hot-spot. In eclipsing systems it is possible to estimate the contribution made by this region from the changes in the light curve which occur as it is occulted by the secondary. In fact, it is the bright-spot which is believed to give rise to the orbital humps mentioned above. Paczyński and Schwarzenberg-Czerny (1980) constructed a simple model for the hot-spot emission, from which they obtained a lower limit to the mass transfer rate through the L1 point, which was found to be greater than the implied disc accretion rate. This observation then supports the disc instability type model. Similar types of study have been applied to WZ Sge and Z Cha by Patterson *et al.* (1981) and Vogt (1981) respectively. The results of these two studies suggest that the mass transfer rate through the hot-spot does increase during outburst, and so supports the mass transfer type model.

Studies of the hot-spot are not the only method of studying regions of the system which show an enhanced accretion rate. Since the spectral emission from accretion discs is reasonably well determined, it should be possible to distinguish between models in which the change in mass transfer rate propagates inwards from the edge of the disc, and those in which the instability starts at some intermediate radius. Of course both instabilities may start at the outer edge, but the mass transfer model must evolve in this way. Observations of the evolution of the 500–1200Å spectrum of SS Cyg during outburst, made using the Voyager UV spectrometer by Polidan and Holberg (1984), strongly suggest that the change in accretion rate propagates inwards from the outer edge of the disc. This view is supported by simultaneous optical–UV (IUE) observations of WX Hyi, reported by Hassall, Pringle and Verbunt (1985), who also argued that disc instability models

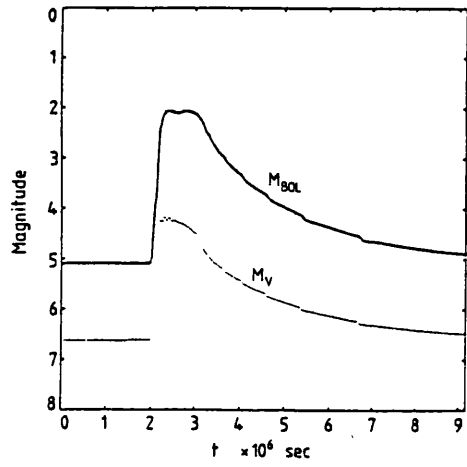
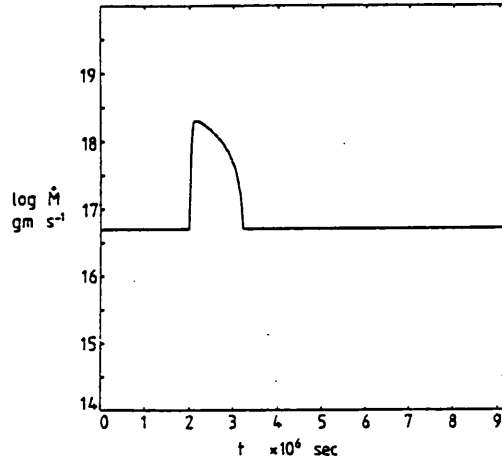


Figure 3.6: Predicted light curves for outbursts arising from the injection of an arbitrary mass function through the L1 point. From Bath and Pringle (1981).

would produce outbursts which rise simultaneously in optical and UV. The reasoning behind this argument lies in the fact that the hot phase invoked in the Meyer and Meyer-Hofmeister (1981) model would be expected to have a temperature in the range 10000 – 14000 K. Outburst only occurs by transition to this state, but gas at this temperature would emit strongly in the UV, and so the possibility of time lags is excluded. A similar result was expressed by Pringle, Verbunt and Wade (1985), who performed detailed calculations on the spectral evolution through outburst for both types of model. Their calculations using the mass injection model were found to give good agreement with observed outburst behaviour.

Observations would then seem to support the variable mass transfer rate model. However this is due, at least in part, to the additional freedom provided by the use of an arbitrary mass injection function. Until a consistent mass donor instability mechanism can be found and observationally verified it seems likely that the debate over which mechanism is appropriate will continue.

### 3.4 X-RAY PROPERTIES

The first detection of x-ray emission from a dwarf nova was made by a group from MIT using a sounding rocket experiment, scanning a region near Cyg X-2 on 1973 March 30 (Rappaport *et al.* 1974). A detector sensitive to the 0.15-0.28 keV band showed a  $5\sigma$  peak at a position coincident with SS Cyg, which was known to be in outburst at the time. A null detection in the 0.4–0.85 keV band suggested that the source was extremely soft. Since its detection in outburst, SS Cyg has been studied using several satellite-borne detectors, and much of the insight into how the x-ray properties of dwarf novae vary through outburst derive from studies of this one object.

That SS Cyg is also a hard x-ray (i.e.  $E > 1$  keV) source was established by Heise *et al.* (1978). The behaviour of this component of emission through outburst was studied by Ricketts, King and Raine (1979) following a series of scanning observations with the sky survey instrument (SSI) on *Ariel V*. It was found that the x-ray flux in the 2–18 keV band is anti-correlated with the optical emission, which implies that the mechanism for hard x-ray production is suppressed at high accretion rates. Evidence that this is the case for all non-magnetic CVs was provided by Patterson and Raymond (1985b), in an analysis of an *Einstein* IPC survey of 63 of these systems. About 70% were discovered to exhibit x-ray emission in the 0.2 to 4.0 keV band. By using emission line strength of  $H\beta$  as a diagnostic for the mass transfer rate Patterson and Raymond showed that the hard x-ray luminosity of dwarf novae and novalike variables is suppressed for accretion rates of

$$\dot{M} \gtrsim 10^{16} \text{ gs}^{-1}.$$

Further observations have provided details which confirm this general picture of x-ray behaviour. The hard component which may be characterised by a thermal bremsstrahlung continuum with  $kT \sim 10 - 20$  keV, appears to be approximately anti-correlated with the optical emission. The soft component, which has characteristic temperature  $kT \sim 30$  eV, (Córdova *et al.*, 1980), appears to follow the optical outburst behaviour closely. The maximum flux in this soft component during dwarf nova outburst in SS Cyg, integrated over all frequencies (using a blackbody model) is  $L \sim 2 \times 10^{33}$  ergs sec<sup>-1</sup>. As with the UV emission, the soft x-ray outburst is delayed from the onset of optical outburst. In the case of VW Hyi, van der Woerd, Heise and Bateson (1986) report a 2.5 day interval between the onset of optical and soft x-ray outburst, compared to the typical  $\sim 1$  day delay between the optical and the UV.

Considerable effort has gone into a theoretical description of the x-ray behaviour of dwarf novae. There are various sites within the system which may give rise x-ray emission, these being; the corona of the secondary, the hot-spot, the inner part of the accretion disc, the atmosphere of the white-dwarf, and a corona above the accretion disc. The inner regions of the accretion disc and the white dwarf atmosphere have attracted most attention as possible sites of x-ray production, since they are the only regions which can easily provide the required luminosities ( $L \sim 10^{33}$  ergs sec<sup>-1</sup>) at x-ray energies (see chapter 1).

In the absence of any coherent modulation of the x-ray emission, it is probably reasonable to assume that the magnetic field of the white dwarf has no effect on the accretion flow. Half of the maximum available accretion luminosity must be dissipated in the accretion disc, and up to this amount again may be produced in the boundary layer between the innermost Keplerian orbit and the white dwarf surface. The process which decelerates the orbiting gas is not clearly understood. Pringle and Savonije (1979) suggested a double shock mechanism. Decelerating gas is weakly shocked near the white dwarf surface, the shocked gas in turn forms a strong shock with the accreting matter. Tylenda (1981b) argued that turbulence will be the dominant effect in this region. The exact nature of the decelerating process may not be important in this context provided that it can be assumed that most of the kinetic energy at the innermost Keplerian orbit is converted into the internal energy of the gas, and that both processes would act on similar timescales.

Pringle and Savonije (1979) suggested that the mechanism by which the boundary layer luminosity is radiated depends on the efficiency of bremsstrahlung cooling with respect to the timescale on which the heated gas may expand adiabatically. Their model used a Shakura and Sunyaev  $\alpha$ -disc

prescription, for which it was shown that the ratio between the bremsstrahlung cooling time ( $t_{brem}$ ) and the adiabatic expansion time ( $t_{ad}$ ) is a function of the mass transfer rate ( $\dot{M}$ ),

$$\frac{t_{brem}}{t_{ad}} \propto \dot{M}^{-14/17} \quad (3.1)$$

The critical mass transfer rate  $\dot{M}_{crit}$ , at which  $t_{brem}/t_{ad} \sim 1$  was estimated as  $\sim 2 \times 10^{16} \text{ g sec}^{-1}$  for typical system parameters. This lies within the range expected for observable accreting CVs of  $10^{14}$  to  $10^{18} \text{ gs}^{-1}$  (see e.g. Patterson 1981).

Pringle and Savonije (1979) examined the two limiting cases in which  $t_{brem}/t_{ad}$  becomes much smaller or much larger than unity.

1.  $\dot{M} \ll \dot{M}_{crit}$ . The shocked gas expands adiabatically out of the plane of the disc and forms a hot ( $T \lesssim 2 \times 10^8 \text{ K}$ ) corona around the white dwarf. This corona then cools by bremsstrahlung emission.
2.  $\dot{M} \gg \dot{M}_{crit}$ . In this case, the distance that the shocked gas may expand before bremsstrahlung cooling is smaller than the typical thickness of the accretion disc. In escaping from the boundary layer, hard x-ray photons are likely to be absorbed or degraded by Compton recoil by cool material in the disc. Pringle and Savonije estimate that for  $\dot{M} \gtrsim 10\dot{M}_{crit}$ , essentially all of the x-rays emitted in strong shocks would be thermalised. The boundary layer emission would be expected to approximate to a blackbody spectrum with a temperature of a few tens of eV (Pringle 1977).

A schematic diagram of these two boundary layer regimes is shown in figure 3.7 (from van der Woerd, 1987b). Note the scale height ( $H$ ) associated with the hard x-ray emitting corona ( $H \sim 0.3r_{wd}$ ) and the soft x-ray emitting boundary layer ( $H \sim 0.03r_{wd}$ ). Estimation of the scale height appropriate to the boundary layer is rather difficult due to the uncertainties of conditions in the boundary layer. The figure quoted above is an estimate based on the approximate analytic formula derived by Patterson and Raymond (1985b).

A detailed study of the cooling of the hard x-ray emitting corona was made by King and Shaviv (1984), who assumed that the gas is heated by turbulence, and that it cools quasi-hydrostatically. A luminosity-temperature relation was derived, which appeared to be confirmed by EXOSAT observations of SS Cyg in quiescence (Watson, King and Heise, 1985). A detailed study of the initial conditions in the cooling corona model by King and Smith (1986) however concluded that the model was unlikely to give the observed correlation, and suggested an instrumental bias as an alternative explanation.

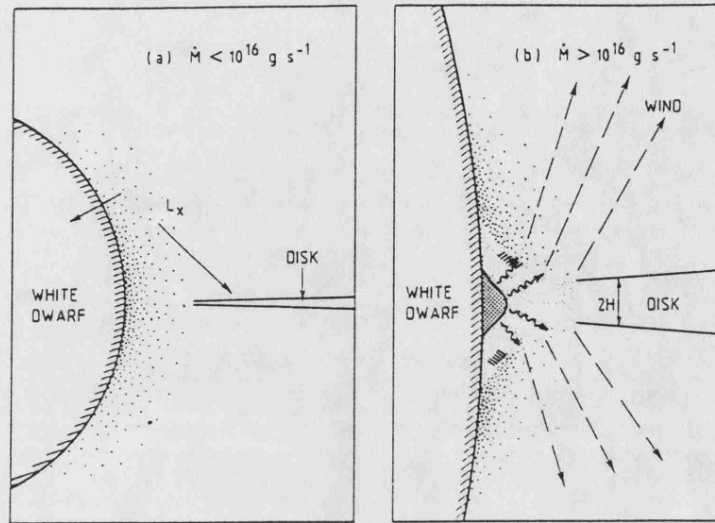


Figure 3.7: A schematic diagram of the two boundary layer regimes in non-magnetic CVs. From van der Woerd (1987b).

There is some evidence for a third x-ray component to the emission from dwarf novae. Van der Woerd (1987) reported an EXOSAT LE observation of the eclipsing dwarf nova OY Car, in which the x-ray flux was not reduced during the eclipse of the white dwarf. The luminosity of this component was  $\sim 10^{31} \text{ ergs sec}^{-1}$ , and was suggested to originate in an optically thin plasma with a temperature of  $10^6$  to  $10^7 \text{ K}$ , which forms a corona above the accretion disc while the source is in superoutburst state. In this scenario the luminous boundary layer region near the inner edge of the accretion disc is obscured by the disc itself, and so source may be analogous to the subset of the low mass x-ray binaries termed 'Accretion Disc Corona' (ADC) sources (see section 6.4).

### 3.5 SHORT PERIOD OSCILLATIONS

A remarkable feature of the soft x-ray component in some dwarf novae is that the emission is very strongly modulated at a short period ( $P \sim 10$  to  $30 \text{ sec}$ ). To date three of the brightest dwarf novae in the x-ray band have been found to exhibit such pulsations, SS Cyg, U Gem and VW Hyi, in observations reported by Córdova *et al.* (1980 and 1984), and van der Woerd *et al.* (1987) respectively. These papers will be referred to frequently and so the abbreviations C80, C84 and VDW will be adopted hereafter. In this section the properties of these pulsations will be described

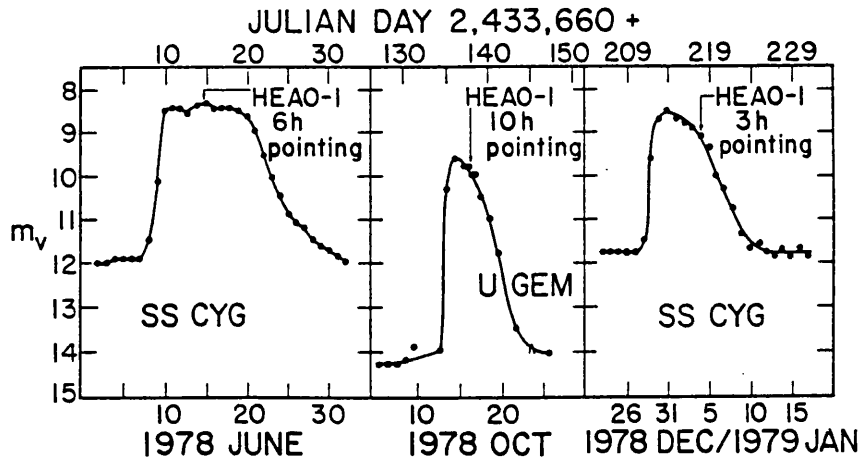


Figure 3.8: The optical light curves of SS Cyg and U Gem showing the HEAO-1 pointings. (From Córdova *et al.* (1984).

and their relationship to optical oscillations discussed.

The observations reported by C80 and C84 were made using the HEAO-1 LED-1 detector. This was a proportional counter with an energy sensitivity in the range 0.1 – 3 keV, and data were accumulated with time resolution of least 1.28 sec. SS Cyg was observed on two occasions (1978 June 14 and 1979 Jan 4) and U Gem once (1978 Oct 16), and the optical states of the sources are indicated in figure 3.8. It can be seen that the pointings were made at various stages through outburst. Oscillations in VW Hyi were detected in two observations (1983 Nov 21 and 1984 Oct 27) out of series of sixteen made using the EXOSAT observatory. The pulsations were only detected in the data from the LE telescope. During the positive detections the source was in superoutburst, although not all observations made while the source was in this state showed evidence for oscillations.

The periods of these oscillations were  $P = 8.7$  to  $10.7$ ,  $27$ , and  $14.06$  to  $14.4$  sec for SS Cyg, U Gem and VW Hyi respectively. The mean amplitude of the oscillations is between 15% and 20%, but this amplitude is clearly variable on timescales as short as a few cycles, C80 reporting variability between 0 and 100%. In two of these observations changes in period could be measured, being a spin-up of  $\dot{P} \sim -1 \times 10^{-5}$  for one of the SS Cygni observations, and one of VW Hyi showing an erratic jump in period from 14.2 to 14.4 sec. C80 and C84 made a very detailed analysis of the coherence of the pulsations in SS Cyg. The coherence will be described here in terms of the

parameter  $Q$  which is a measure of the timescale (in cycles) over which the phase of an oscillation will wander by a significant amount (i.e. enough to wash-out the pulsation, typically  $\sim \pi/2$  rad). Similarly to the case in VW Hyi, SS Cyg was seen to exhibit apparently random jumps in period in the course of a general spin-up of the oscillator. C80 proposed a model to describe the phase variability which is based on a strong random walk in the phase of the oscillation. Using this model it was found that the coherence of the oscillation varied from  $Q \sim 25$  to about 2 for the mid-outburst and decline observations of SS Cyg respectively. For U Gem, the coherence was  $\sim 1$  cycle. In contrast the observations of VW Hyi showed much higher coherences, in one case  $Q \sim 2500$  cycles.

The pulse shape was found by C80 and C84 to be sinusoidal to the limits of measurement with a typical upper limit of  $\sim 20\%$  of the power in the fundamental being allowed in the first or higher harmonics. It was suggested by C80 that such a simple pulse shape must act as a very strong constraint on the modulating mechanism. One of the observations of VW Hyi however showed a non-sinusoidal pulse shape.

Prior to the discovery of the x-ray pulsations, it was known that SS Cyg exhibits small amplitude ( $\sim 0.02\%$ ) optical oscillations with periods in the range 8.5–10.6 sec (Patterson, Robinson, & Kiplinger, 1978, and Patterson, 1979), and since the first x-ray observations the optical period has been observed at values as low as extended down to 7.3 sec (Hildebrand, Spillar and Stiening, 1981a). The similarity of the period and the period changes in the optical and the soft x-ray pulsations led C80 to suggest that both are manifestations of a single underlying mechanism.

By the mid-1970s optical photometry of the brightest dwarf novae in outburst at a resolution of  $< 1$  sec became technically feasible. This led to the discovery that dwarf novae in outburst can exhibit at least two types of oscillation on timescales of seconds to tens of seconds. The type which are related to the x-ray pulsation typically have a higher coherence, whereas the other type are characterised by broad power-spectrum peaks, which imply a rather low coherence. In a review of oscillations in dwarf novae, Patterson (1981) suggested that the term dwarf nova oscillation (DNO) should be adopted for the former case, and the term quasi-periodic oscillations for the latter. Patterson noted however that the x-ray pulsations of SS Cyg show low coherence but that these observations appear to be related to the optical DNO, implying that a classification based on coherence alone is probably unsuitable.

A total of 17 sources have documented optical DNO. A summary of these observations is given in table 3.1, which also lists the three identified x-ray DNO. The range of periods between different

objects is from  $\sim 7$  sec for SS Cyg to  $\sim 32$  sec in the novalike variable V3885 Sgr. The evidence for supposing that the soft x-ray and optical pulsations have the same origin is based on the similar periods and period variability of the oscillations in both wavebands. This is the case for SS Cyg alone. Optical QPO have been observed in both U Gem and VW Hyi, but optical pulsations near the x-ray period have not been detected.

The HEAO-1 observations showed that the soft x-ray component in SS Cyg and U Gem can be represented by a blackbody with a temperature of a few 10s of eV, and C80 showed that the optical pulsations could be produced from the low-energy tail of such a distribution. The spectral information also allowed a crude estimate of the total luminosity of the source to be made,  $L \sim 1.8 \times 10^{33} \times (d/200 \text{ pc})^2 \text{ ergs s}^{-1}$ . A characteristic area of the emitting region was calculated by C80 to be,

$$A = \frac{L}{\sigma T^4} \approx 2 \times 10^{15} \left( \frac{d}{200 \text{ pc}} \right) \left( \frac{30 \text{ eV}}{kT} \right)^4 \text{ cm}^2 \quad (3.2)$$

This it was noted, is much smaller than the area of the white dwarf ( $\sim 3 \times 10^{18} \text{ cm}^2$ ).

There was no evidence of any correlation of temperature with pulse phase in the SS Cyg observations, the  $2\sigma$  limit to any sinusoidal variation in temperature was quoted to be 70%. However in the case of VW Hyi, VDW deduce that the pulsing component is spectrally harder than the non-pulsed emission by comparing pulsation amplitudes as measured through different filters. It was cautioned however that because the filtered observations being compared had to be made at different times, this effect may be due to the secular variation in pulse amplitude.

A characteristic property of the DNO appears to be that the pulsation frequency ( $\nu$ ) varies with the source intensity ( $I$ ). A schematic illustration of the evolution of these observables through outburst is shown in figure 3.9. Following the curve A, the first detectable modulation occurs at the onset of outburst (i), the frequency and intensity are both low. Both quantities increase together, until outburst maximum is reached (ii), the frequency however continues to rise, reaching a maximum up to about two days later (iii). The frequency then drops with the declining source luminosity until oscillations are no longer detectable (iv). The locus of the oscillator in the  $I - \nu$  plane was termed a 'banana loop' by Patterson (1981), who suggested that the time delay between the maximum intensity and period may be due to a changing bolometric correction. The dashed lines in the figure represent a hypothesised closed loop, but it is not clear whether or not the oscillations continue into quiescence, since the evidence from an optical study by Hildebrand, Spillar and Stiening (1981) suggests that the coherence drops as the source returns to quiescence. Furthermore the x-ray observation of SS Cyg show a dramatic change in coherence between outburst maximum and the

Table 3.1: Summary of optical and x-ray detections of dwarf novae oscillations.

Name	Type	Orbital Period (hr)	Oscillation Period (sec)		References
			Optical	X-ray	
SS Cyg	DN	6.60	7.3 - 10.9	7.4 - 10.7	1,2,3,4,5,6
U Gem	DN	4.25	-	27	5,7
VW Hyi	DN (SU)	1.78	20 - 32	14.2 - 14.4	8,9,10,11
RU Peg	DN	8.99	11.6 - 11.8		7,12
EM Cyg	DN	6.98	14.6 - 21.2		13,14,15
Z Cam	DN (Z)	6.96	16.0 - 18.8		16,17
OY Car	DN (SU)	1.79	19.4 - 28.0		18
V436 Cen	DN (SU)	1.50	19.5 - 20.1		19
HT Cas	DN (SU)	1.77	20.2 - 20.4		14
KT Per	DN	-	22.0 - 29.2		7,20,21
SY Cnc	DN	8.1	23.3 - 33.0		14,21,22
AH Her	DN	5.93	24.0 - 38.8		14,23,24
CN Ori	DN	3.91	24.3 - 25.0		25,26,17
IX Vel	NL	4.5	24.6 - 29.1		27
TY PsA	DN (SU)	2.0	27 - 29		28
Z Cha	DN (SU)	1.79	24.8 - 27.7		28,29
WZ Sge	DN	1.36	27.87, 28.97		30,31
UX UMa	NL	4.72	28.5 - 30.0		32,17
V3885 Sgr	NL	4.94	29 - 32		33,34

Notes: DN - Dwarf Nova, SU - SU UMa type, Z - Z Cam type, NL - Novalike variable.

References : 1 - Hildebrand, Spillar & Stiening (1981a), 2 - Horne & Gomer (1980), 3 - Patterson, Robinson & Kiplinger (1978) 4 - Córdova *et al.* (1980), 5 - Córdova *et al.* (1984), 6 - This work, 7 - Robinson & Nather (1979), 8 - Warner & Brickhill (1974), 9 - Robinson & Warner (1984), 10 - Warner & Brickhill (1974), 11 - van der Woerd *et al.* (1987), 12 - Patterson, Robinson & Nather (1977), 13 - Nevo & Sadeh (1978), 14 - Patterson (1981), 15 - Stiening, Dragovan & Hildebrand (1982), 16 - Robinson (1973a), 17 - Warner & Robinson (1972), 18 - Schoembs (1986), 19 - Warner (1975), 20 - Nevo & Sadeh (1976), 21 - Robinson (1973b), 22 - Middleditch & Córdova (1982), 23 - Hildebrand, Spillar & Stiening (1981), 24 - Hildebrand *et al.* (1980), 25 - Warner & Brickhill (1978), 26 - Schoembs (1982), 27 - Warner, O'Donoghue & Allen (1985), 28 - Warner & O'Donoghue (1987), 29 - Warner (1974), 30 - Patterson (1980a), 31 - Robinson, Nather & Patterson (1978), 32 - Nather & Robinson (1974), 33 - Warner (1973), 34 - Hesser, Lasker & Osmer (1974).

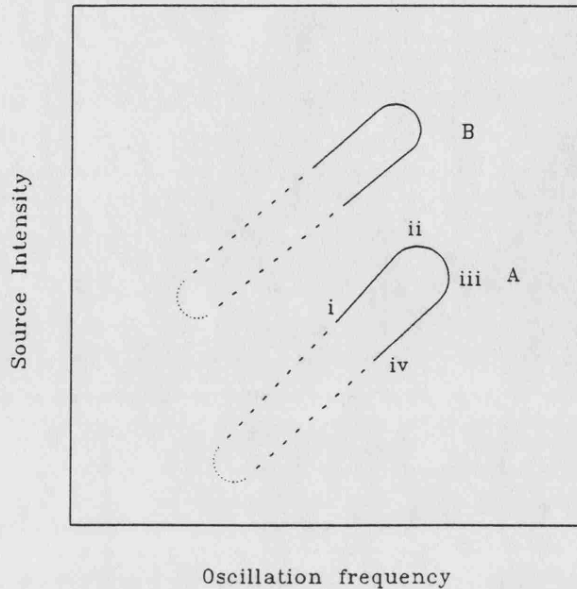


Figure 3.9: A schematic illustration of the behaviour of optical dwarf nova oscillations.

decline phase (C84). A problem in studying this behaviour is that although the banana loop is well defined for a single outburst, between observations there are considerable differences in the position and shape of the respective loops. This is illustrated schematically by the curve **B** in figure 3.9, which shows the behaviour due to a different outburst to that considered in case **A**.

### 3.6 SUMMARY

Dwarf novae show outbursts which are attributed to a change in the mass transfer rate ( $\dot{M}$ ) through the accretion disc. The origin of this change is not clear, but observations support a model in which an increase  $\dot{M}$  propagates inwards from the outer edge of the accretion disc. The processes which occur at the boundary layer are sensitive to  $\dot{M}$ . For  $\dot{M} > 10^{16}$  g sec<sup>-1</sup>, the boundary layer luminosity is emitted from a small volume with a low temperature of a few tens of eV. At lower accretion rates an extended hot ( $kT \sim 10$  keV) corona is formed.

The soft x-ray boundary layer component shows strong, sinusoidal modulation at periods of a few tens of seconds. This modulation is also seen in the optical band although at a much smaller

amplitude. The period of this oscillation changes in a way which is probably correlated with the luminosity, although this has not been shown in the x-ray band. The phase of the oscillation shows some type of random variability. The oscillations could be an important diagnostic to the physical conditions in the boundary layer between the accretion disc and the white dwarf surface.

## Chapter 4

# The EXOSAT observations of SS Cygni

### 4.1 INTRODUCTION

A series of observations of SS Cyg using *EXOSAT*, which monitored the source in outburst and quiescence are presented. The physically distinct soft and hard x-ray emitting components were spectrally resolved by the LE and ME instruments respectively, and their behaviour in relation to the optical state is described. The spectrum of the hard x-ray emission is compared to previous observations. The soft x-ray component shows large amplitude oscillations during outburst. The methods of detection and parameterisation of this modulation are discussed in detail. As yet, there is no theoretical model which satisfies all the observed properties of this pulsation. Further observations and theoretical work that might lead to an understanding of this phenomenon are suggested.

#### 4.1.1 SS Cygni

The importance of SS Cyg to the study of the x-ray properties of dwarf novae has been outlined in chapter 3. The source has a flux of up to a few  $10^{-10}$  ergs  $s^{-1}$   $cm^{-2}$  and  $\sim 5 \times 10^{-11}$  ergs  $s^{-1}$   $cm^{-2}$  in x-ray bands above and below 1 keV respectively. Since its discovery in 1896, SS Cyg has

Table 4.1: Orbital parameters for SS Cyg. From Kiplinger (1981)

Orbital Period	$P_{orb}$	= 6.60 hrs
Mass of white dwarf	$M_1$	= $1.05M_{\odot}$
Mass of red dwarf	$M_2$	= $0.80M_{\odot}$
Binary separation	$a$	= $1.5 \times 10^{11}$ cm
Inclination (assumed)	$i$	$\sim 30^{\circ}$

been subject to extensive optical studies and has been monitored on a regular basis by amateur astronomers for over sixty years. Classified as a U Gem type variable, it has a quiescent optical brightness of  $m_v = 12$  which in outburst rises to  $m_v = 8.1$ , making it the brightest dwarf nova while in this state. The outburst recurrence time is about 50 days but variation in outburst interval of between 30-70 days is not uncommon. The distance to the system has been determined by parallax at  $\approx 200$  pc (Strand, 1948). The system is non-eclipsing, but is a double-lined spectroscopic binary with orbital period  $P_{orb} = 6.60$  hrs (Stover *et al.*, 1980). A summary of the orbital parameters derived from radial velocity measurements by Kiplinger (1981) is given in table 4.1.

This chapter describes a series of observations made with EXOSAT over an interval of 11 months which covered quiescent and outburst intervals. Of particular importance were observations made over a single outburst which show in detail how the hard and soft x-ray properties vary, and the observations in which soft x-ray pulsations were detected.

As in the previous chapter, the papers reporting the HEAO-1 observations of SS Cyg in outburst by Córdova *et al.* (1980 and 1984) will be referred to as C80 and C84 respectively. The terms hard and soft x-ray will be used to describe emission at energies above and below 1 keV respectively.

## 4.2 OBSERVATIONS

SS Cygni was subject to an extensive monitoring project using EXOSAT. The source was observed on nine occasions between 1983 November 11, and 1984 September 22. Information on the optical state of SS Cyg was provided by the American Association of Variable Star Observers (AAVSO), such that short notice EXOSAT observations could be scheduled in order to observe the source during outburst. The light curves for the period of study are shown in figure 4.1, with the times

of the EXOSAT pointings indicated. The outburst of 1984 June 26 – July 10 was subject to a single  $\sim 4$  hr observation, and the outburst of 1984 September 9 – 24 was monitored by five separate observations made between September 14 and 21. Both of these outbursts are of the short type, a long outburst having occurred between July 29 and August 20. The observation of 1983 December 4 was made near the end of optical decline, although the AAVSO light curves (which have a standard error of  $\approx \pm 0.2$  mag) indicate a small (0.5 mag) anomalous rise in optical flux at the time of observation. The two other observations were made while SS Cyg was in a quiescent state, these being on 1983 November 11 and 1984 August 28–29.

A catalogue of the observations is given in table 4.2. Reference to specific observations will be made by the date given in column 2 of this table. Note that two pointings were made on Aug 28, but will be treated as a single observation here. The length of the observations varies from  $\sim 3800$  sec to  $\sim 25000$  sec. The ME array was operated in HER5 and HER4 modes, respectively giving a time resolution of 1 and 10 sec with 64 and 128 channel pulse height channel spectra from the Ar and Xe layers (see section 2.2.2). The source fluxes were too low for any useful information to be obtained from the Xe layer data. The background subtraction technique used followed that outlined in section 2.4.1, using the slew data to estimate the constant background flux. In the case of the observation of Aug 28, the offset half-array indicated a high level of background variability for the interval 18:30 – 24:00 (UT) and these data were excluded from any further analysis. For most of the observations the LE telescope was used with the 3000Å lexan filter in front of the CMA, with only the observation of Aug 28 utilising the Al/Par and Boron filters. Again, the background subtraction methods were those outlined in section 2.4.1. The source fluxes were too low to obtain any useful data from the GSPC detector.

In addition to the optical data provided by the AAVSO, about half of the observation of Jun 27 was covered by UB<sub>V</sub> photometry performed by Echevarría and co-workers (priv. comm.). The start time of this optical observation was Jun 27 02:20 (UT), and the time resolution of these data was  $\sim 5$  mins. The light-curves in UB<sub>V</sub> and soft x-ray bands are shown in figure 4.2.

### 4.3 GENERAL X-RAY BEHAVIOUR

The mean count rates for each observation are given in tables 4.3 and 4.4 for the ME and LE instruments respectively. The flux of the hard component has also been determined assuming a simple continuum fit to the ME spectrum, the quoted values are for the 2–10 keV range. These

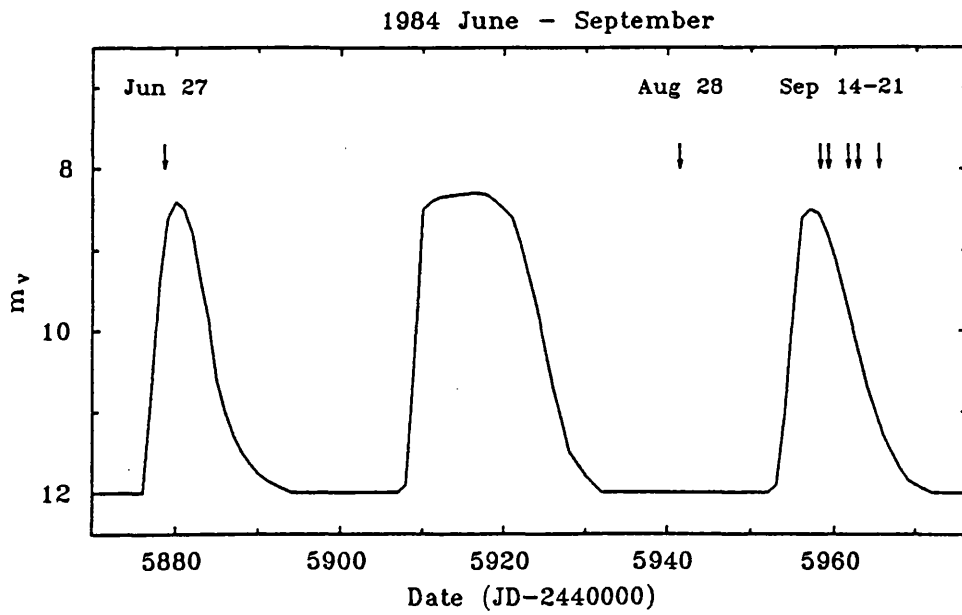
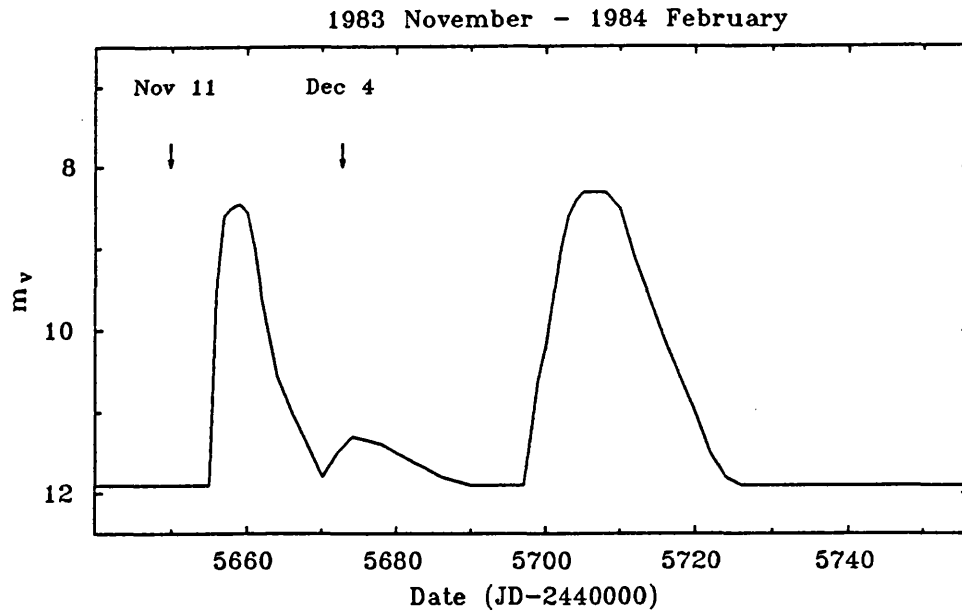


Figure 4.1: The optical light curves for SS Cyg from late 1983 and mid-1984. The times of EXOSAT observations are indicated by arrows. Note that both outbursts which were observed at x-ray wavelengths were of the short type. (From data supplied by the AAVSO).

Table 4.2: Catalogue of the EXOSAT observations of SS Cygni.

Year	Date	Time (UT)		ME Exposure (sec)	LE	
		Start	End		Filter	Exposure (sec)
1983	Nov 11	06:42	07:52	3800	3lx	3300
	Dec 4	01:49	08:25	23700	3lx	24000
1984	Jun 27	00:05	04:30	15800	3lx	15500
	Aug 28	04:35	18:00	8800	3lx	4100
					Al/Par	4400
					Boron	3500
	Aug 28	18:29	00:01 <sup>a</sup>	9200	3lx	11500
	Sep 14	14:16	21:09	25300	3lx	24000
	Sep 15	13:12	15:40	8800	3lx	8000
	Sep 18	00:31	04:59	16000	3lx	16000
	Sep 19	03:30	04:55	4200	3lx	4200
	Sep 21	21:00	23:39	9000	3lx	8700

Note: (a) - Observation ended on Aug 29.

---

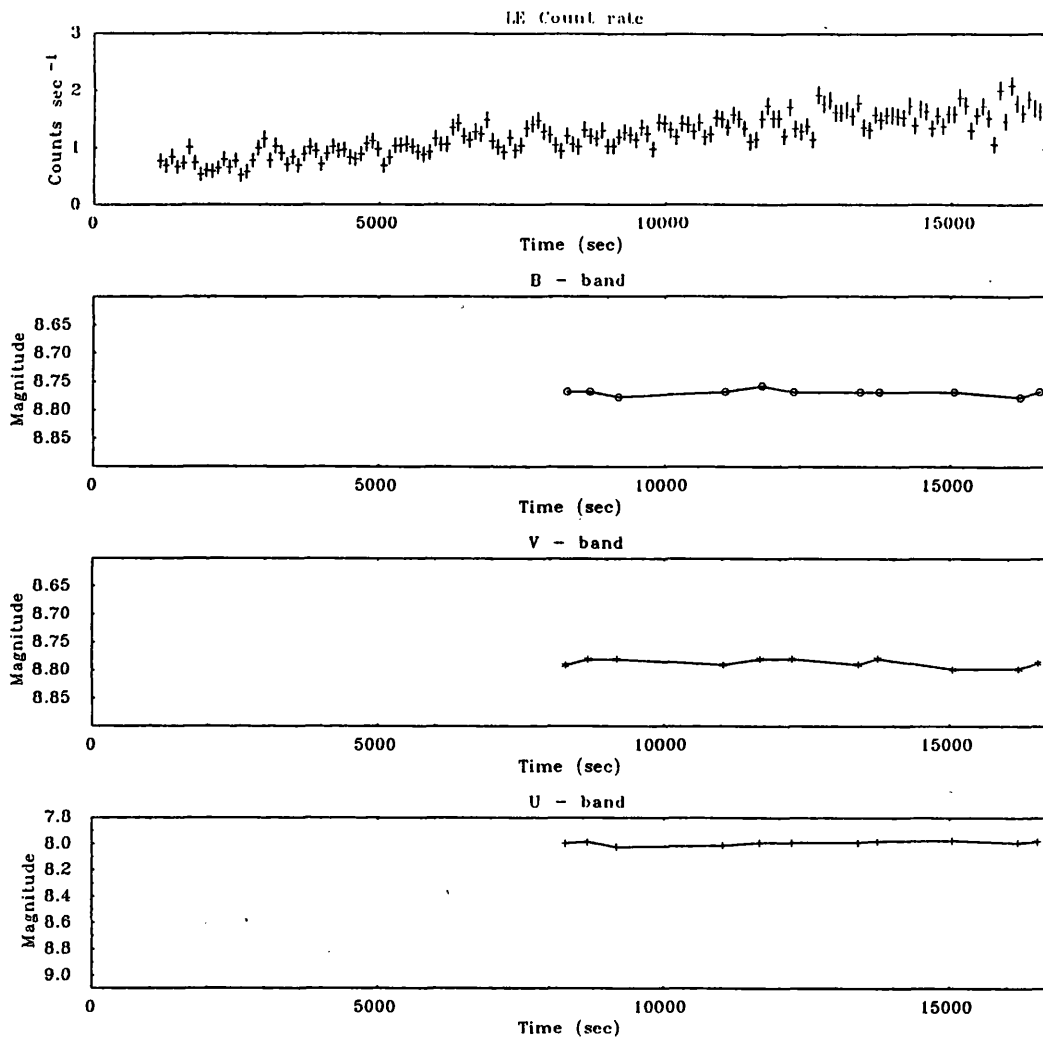


Figure 4.2: The LE (3000Å lexan filter) and UVB light curves for the Jun 27 observation of SS Cyg. (Optical data courtesy of J. Echevarría).

Table 4.3: The ME observations of SS Cygni

Year	Date	Optical state	Duration (sec)	ME count rate 1.2 - 8.5 keV	Model Flux 2 - 10 keV
1983	Nov 11	Q	3810	$4.4 \pm 0.2$	5.3
	Dec 4	Q	23730	$19.3 \pm 0.2$	25
1984	Jun 27	O	15870	$1.24 \pm 0.09$	1.4
	Aug 28	Q	6870	$2.0 \pm 0.5$	2.6
	Sep 14	O	15300	$1.75 \pm 0.10$	2.3
		O	10000	$1.50 \pm 0.10$	2.0
	Sep 15	O	8880	$1.12 \pm 0.25$	1.2
	Sep 17	D	16080	$0.95 \pm 0.04$	1.1
	Sep 19	DQ	4250	$1.58 \pm 0.09$	1.9
	Sep 21	Q	9080	$10.2 \pm 0.1$	13

Notes: The ME count rate is given in counts per second per detector, the model flux is that found for the best fit power-law spectrum, and is given in units of  $10^{-11}$  ergs  $s^{-1}$   $cm^{-2}$ . Errors quoted are at the  $1\sigma$  level. Key to optical states; Q - quiescent, O - outburst, D - decline from outburst.

fluxes are shown, along with the optical brightness, in figure 4.3 for the nine observations in chronological order. Note that the optical magnitudes are shown on a linear scale, so that a comparison may be made between the rates of change of flux in all bands.

It can be seen figure 4.3 that the fluxes from both instruments show a considerable degree of variability. The LE flux appears to be strongly correlated with the optical state, closely following the outburst behaviour. The ME flux shows more complex behaviour, being suppressed while the source is in outburst state but also showing a wide range of variability during quiescence. This behaviour is strong evidence for the existence of the two distinct components of x-ray emission, as has already been established (see chapter 3). The soft component was found by C80 to be consistent with a blackbody type spectrum at a few tens of eV, the hard emission has been reported as a

Table 4.4: The LE telescope observations of SS Cygni.

Year	Date	Optical state	Duration (sec)	L.E Count Rate (counts sec <sup>-1</sup> ) 0.04 - 2 keV .	Filter
1983	Nov 11	Q	3300	0.074 ± 0.006	3lx
	Dec 4	Q	24000	0.230 ± 0.004	3lx
1984	Jun 27	O	15500	1.19 ± 0.01	3lx
	Aug 28	Q	4100	0.062 ± 0.005	3lx
		Q	4400	0.030 ± 0.004	Al/Par
		Q	3500	0.009 ± 0.004	Boron
	Aug 29	Q	11500	0.054 ± 0.006	3lx
	Sep 14	O	24000	2.09 ± 0.01	3lx
	Sep 15	O	8000	1.93 ± 0.02	3lx
	Sep 17	D	16000	0.270 ± 0.005	3lx
	Sep 19	DQ	4200	0.077 ± 0.004	3lx
Sep 21	Q	8700	0.160 ± 0.005	3lx	

Notes: (a) - Modulation detected at 99% confidence level, amplitudes include the diffraction term. (b) - Count rate too low to allow periodicity search. Key to optical states; Q - quiescent, O - outburst, D - decline from outburst.

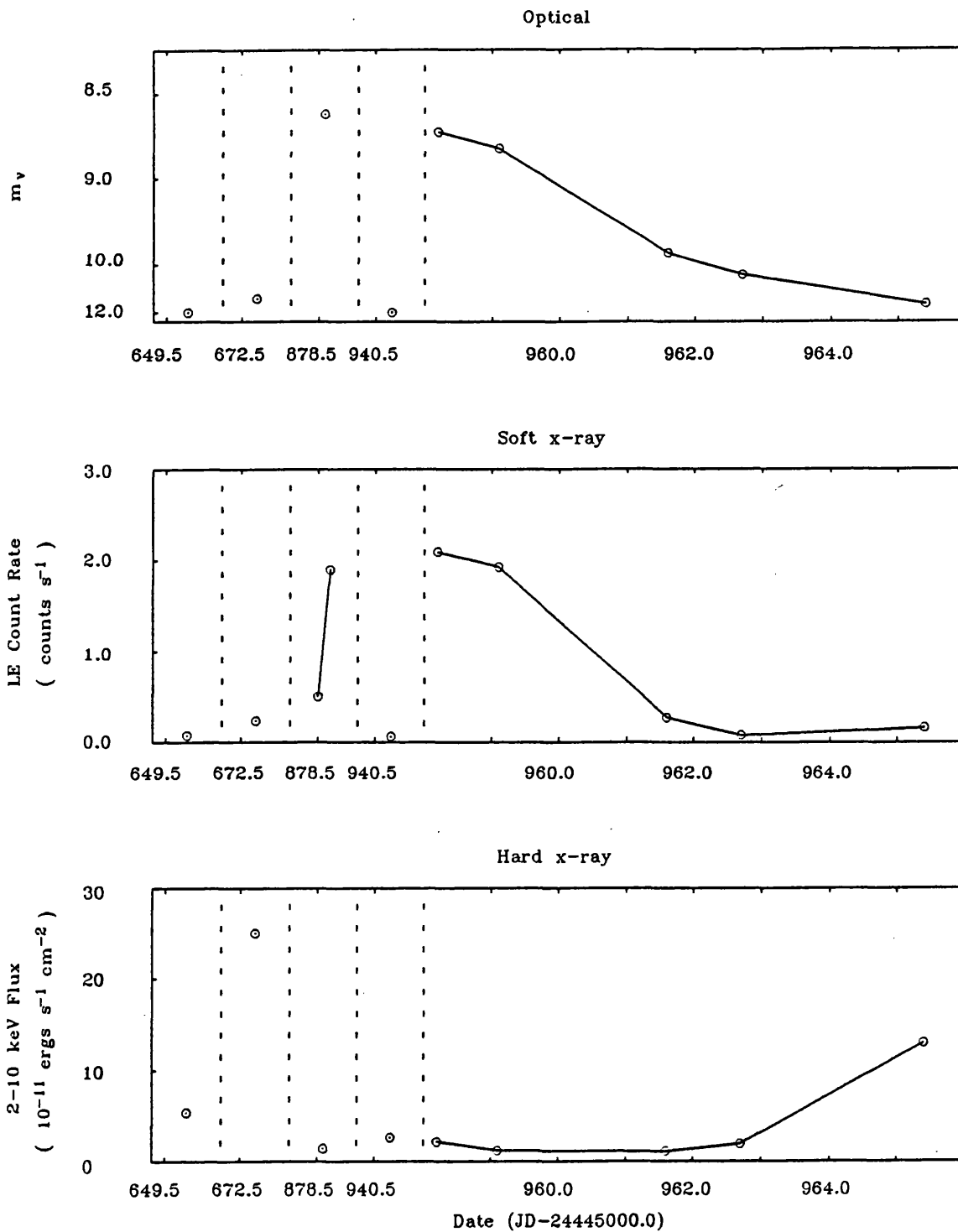


Figure 4.3: The optical, soft (0.04–2 keV) and hard (2–10 keV) x-ray fluxes curves of SS Cyg during the nine EXOSAT observations made between 1983 Nov 11 and 1984 Sep 21. The hard x-ray fluxes are those derived for the best fit spectral models. The dashed vertical lines indicate breaks in the time ordinate. The optical data were provided by the AAVSO and have a typical error of 0.2 mag. Note the linear scale adopted for these data.

thermal bremsstrahlung with a temperature of a  $\sim 10$  keV (Swank, 1979).

The energy sensitivities of the LE and ME instruments are such that these soft and hard x-ray components of emission were essentially separated between the two detectors. The soft component can only be detected by the LE telescope since the ME instrument has a low energy cut-off at  $\sim 1$  keV. The hard component however can make some contribution to the flux in the LE band ( $E \approx 0.04 - 2$  keV).

Since the hard and soft components are essentially anti-correlated, the only case in which the two components cannot be independently measured is when the hard component is bright. In this case, both components may contribute significantly to the LE flux. The contribution to the LE from the hard component can be estimated from an extrapolation to low energies of the best fit ME spectrum. It is found however, that this contribution is sensitive to the column density. For the Dec 4 observation for instance, the best fit continuum to the ME data (see section 4.3.2) has a fitted column density of  $< 3.1 \times 10^{21} \text{ cm}^{-2}$  at the 90% confidence level. The expected flux in the LE for  $N_H = 3.1 \times 10^{21} \text{ cm}^{-2}$  is  $0.06 \text{ counts sec}^{-1}$ , whereas for  $N_H = 0.1 \times 10^{21} \text{ cm}^{-2}$  the count rate would be  $0.6 \text{ counts sec}^{-1}$ . The measured flux in this case is  $0.23 \text{ counts sec}^{-1}$  and so it is concluded in this case, that the hard component must contribute at least  $\sim 25\%$  of the measured LE flux and could account for all of the observed flux. For all of the quiescent observations it was found that the LE fluxes could be attributed totally to the low-energy part of the hard component, and so no lower limit to the contribution from the soft component can be given for this state.

The lack of filtered observations in outburst prevent these data being used to give any constraints on the spectrum of the soft x-ray component. In order to check that these data were consistent with results of C80, the blackbody spectrum was determined which would give the flux quoted by C80 from the (HEAO-1) LED-1 detector near outburst maximum and the highest observed flux in the LE telescope (with thin lexan filter). These correspond to fluxes of  $4.5 \times 10^{-11} \text{ ergs s}^{-1} \text{ cm}^{-2}$  in the energy range (0.13–0.48 keV) and  $2 \text{ counts sec}^{-1}$  respectively. Assuming the column density given by C80 of  $1 \times 10^{20} \text{ cm}^{-2}$ , the blackbody temperature which satisfies this condition is  $kT \approx 20 \text{ eV}$ , and so there is no evidence of any significant difference between the soft component observed with HEAO-1 and EXOSAT.

### 4.3.1 The Soft X-ray Component

At outburst maximum the soft component shows significant variability of  $\sim 20\%$  on timescales of a few hundred seconds, as can be seen from the light-curves of Sep 14 and 15 in figures 4.4 and 4.5. No evidence was found for orbital modulation of the soft x-ray flux. On longer timescales ( $\gtrsim 1000$  sec) the flux in the Sep 14 observation can be seen to be falling slowly at a rate which is similar to that which is implied between this observation and that of Sep 15, this being  $-0.01$  counts  $\text{sec}^{-1}$   $\text{hr}^{-1}$ . In contrast, the observation of Jun 27 shows a rapid increase from 0.7 to 1.7 counts  $\text{sec}^{-1}$  over the 15000 sec duration of the observation (see figure 4.2), giving a rate of change of flux of  $0.24$  counts  $\text{sec}^{-1}$   $\text{hr}^{-1}$ . The natural interpretation of this change is that it represents the rise in the soft x-ray outburst. It should be noted however, that in the case of VW Hyi, van der Woerd (1987a) reports a soft x-ray precursor to the outburst proper. Since there is no evidence that such precursors are general features of the soft x-ray behaviour, it will be assumed that the observed change in flux is the start of the x-ray outburst.

For the Jun 27 observation the partially simultaneous UVB photometry indicates that the optical outburst had very nearly reached its peak. There was no significant change in the optical band over the interval that the LE flux varied from  $\sim 1.1$  to  $1.7$  counts  $\text{sec}^{-1}$ . It is evident then that there is a time delay between the rise in the optical and x-ray bands. The measurement of this time delay is important since it gives information on the viscous timescale in the disc. Ideally, the delay should be measured between the onset of outburst in the optical and x-ray bands respectively. This would represent the propagation time through the disc of the leading edge a pulse of increased mass transfer rate. Measurement of any other features of the outburst will depend on the way in which this pulse propagates through the disc.

Unfortunately, the time of onset of outburst in both wavebands is difficult to determine, due to the limitations of the AAVSO data, and incomplete coverage of outburst in the x-ray data. An estimate for the time delay between outbursts was however made from the time difference between the half maximum intensities in both bands. It was assumed that the peak soft x-ray intensity for the 1984 June outburst is similar to the maximum measured for the 1984 September observations,  $\approx 2$  counts  $\text{sec}^{-1}$  and at minimum is  $< 0.1$  counts  $\text{sec}^{-1}$ . The half optical intensity between  $m_v = 12$  and  $8.5$  is  $m_v \approx 9.3$ . The main source of error lies in estimation of the mid-point of the optical rise from the data provided by the AAVSO, which cannot be determined to an accuracy of better than about half a day. The mid-point of the x-ray light curve can be estimated to within a few 1000 sec. The time delay is estimated then to be between 0.5 and 1.1 days. This is somewhat

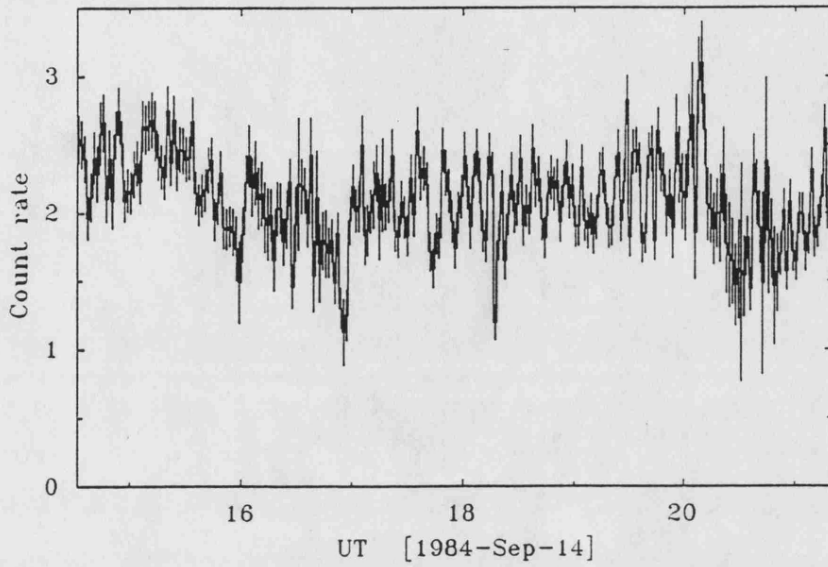


Figure 4.4: The LE (3000Å lexan filter) light curve for the Sep 14 observation of SS Cyg.

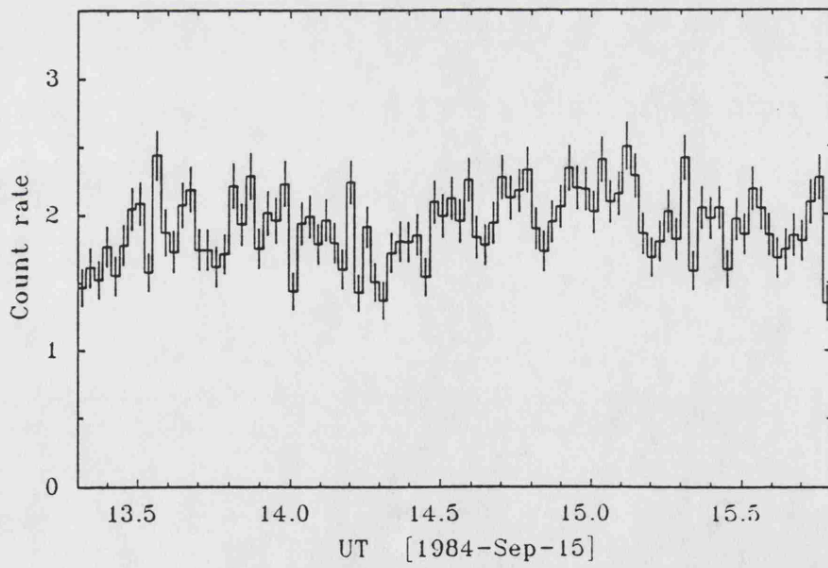


Figure 4.5: The LE (3000Å lexan filter) light curve for the Sep 15 observation of SS Cyg.

shorter than the 2.5 day delay reported by van der Woerd (1987a) for an outburst in VW Hyi. It is however comparable with the time delay of 0.5-1.0 days measured by Polidan and Holberg (1984) between the onset of optical and far UV ( $E \sim 10$  eV) outburst for SS Cyg.

The result should be treated with caution because of the assumptions made about the range of the x-ray flux, and because it is evident that the rise times in the two wavebands differ. The rate of change of intensity of the soft x-ray flux in figure 4.2 implies a transition time between the low and high states of  $\sim 8$  hrs. This is faster than the optical rise time which is  $\approx 2$  days for this outburst. If it is assumed that the intensity changes in the rise to outburst are approximately linear with time, the difference in rise times, combined with the above estimate for the delay, imply a time delay between onset of outburst in the two wavebands of 1.3-1.8 days.

Another difference between the soft x-ray and optical light curves is that the decline from outburst is more rapid in the x-ray band. This can be seen in figure 4.3: between the observations on Sep 15 and 17 the x-ray flux drops by 85% whereas the optical intensity shows only a 60% reduction, and a similar change is seen between Sep 17 and 19. Note that the increase in soft x-ray flux between Sep 19 and 21 may be attributed to the contribution from the hard x-ray component as discussed above. The implications of the time delays between the x-ray and optical bands will be discussed further in section 4.5.

### 4.3.2 The Hard X-ray Component

In quiescence this component is relatively bright and appears to show a factor  $\sim 10$  variability between observations. The five observations in outburst (as defined by the soft x-ray behaviour) all have lower fluxes than the those in quiescence and so it may be argued that the hard x-ray flux is genuinely suppressed during these intervals. The luminosity of this component can be surprisingly large, the Dec 4 observation has a luminosity across the 2-10 keV band of  $1.2 \times 10^{33}(d/200\text{pc})\text{ergs sec}^{-1}$ . This is only about 30% lower than the total luminosity for the soft component (C80) when the mass transfer rate is near maximum. This would seem to suggest that the difference in mass transfer rate between outburst and quiescence is rather small. However, inspection of the AAVSO light curve (figure 4.1) at the time of this observation shows an anomalous 'hump' in which  $m_v$  peaks at about 11.0 to 11.5 mag. This feature is probably associated with the decline from outburst and it can be argued that at that time there was a moderate enhancement of the mass transfer rate which was insufficient to suppress the hard emission. The other observation in which the luminosity of the hard x-ray component was relatively high was on Sep 21, which was

also just after the (soft x-ray) outburst. This strongly suggests that the hard x-ray component is brighter in the post-outburst interval than in quiescence. This type of behaviour was inferred by Swank (1979) from scanning observations made with HEAO-1 (A2), and from *Ariel V* data reported by Ricketts, King and Raine (1979).

The short timescale variability of the hard component is illustrated in the light curves of the brightest observations, those of Nov 11, Dec 4, and Sep 21 (see figures 4.6, 4.8 and 4.9). At a time resolution of 30 sec, all three observations show a significant excess variability, of about 25% about the mean. The light curves show flaring events, which are similar in all three observations. The characteristic timescale, determined from the  $e$ -folding time of the autocorrelation function (figure 4.7) for this flaring behaviour is  $\sim 100$  sec.

The x-ray spectra of the luminous, post-outburst stages of Dec 4 and Sep 21 were fitted using power-law, thermal bremsstrahlung and blackbody models. It was found that in both observations the power-law continuum provided the best fit, and inspection of the residuals in both cases indicated an excess near  $\sim 7$  keV. Modelling this excess by an emission line, it was found that the data are not good enough to constrain the line energy, and so models with line energies fixed at 6.4 and 6.7 keV were adopted. The improvement in  $\chi^2_\nu$  obtained by adding a line feature to the power-law model was from 1.54 to 0.61 and from 1.16 to 0.90 for the Dec 4 and Sep 21 observations respectively. An  $F$ -test shows that addition of the line component is justified at a confidence level of  $> 99.5\%$  in both cases. The best fit parameters are given in tables 4.5 and 4.6, and the spectra are illustrated in figures 4.10 and 4.11. The Dec 4 observation strongly favours a model with a 6.7 keV line, and inspection of the residuals (figure 4.10, lower panel) shows a sharp excess near 8 keV. This feature could be interpreted as the thermal  $K\beta$  iron emission line at 7.9 keV, and supports the claim that the spectrum originates in a hot optically thin region. The Sep 21 data are less clear,  $\chi^2_\nu$  is slightly lower for the 6.4 keV line, but inspection of the residuals to the best fits show no systematic trends around either line feature, suggesting that distinction cannot be made between the two line energies. Thus the Dec 4 data support a model in which iron line emission is thermal in origin, and are in this respect, in agreement with spectra obtained from the HEAO-1 A2 instrument reported by Swank (1979). The HEAO-1 spectra of SS Cyg measured at outburst maximum ( $m_v = 8.3$ ) and in late decline ( $m_v = 11$ ) were modelled as thermal bremsstrahlung continua ( $kT \approx 7$  and  $\approx 20$  keV respectively). The Dec 4 and Sep 21 observations were fitted significantly better by power-law models, but for comparison with earlier results it is useful to note that the typical temperatures of the best fit bremsstrahlung models are  $\approx 15$  and  $\approx 22$  keV respectively.

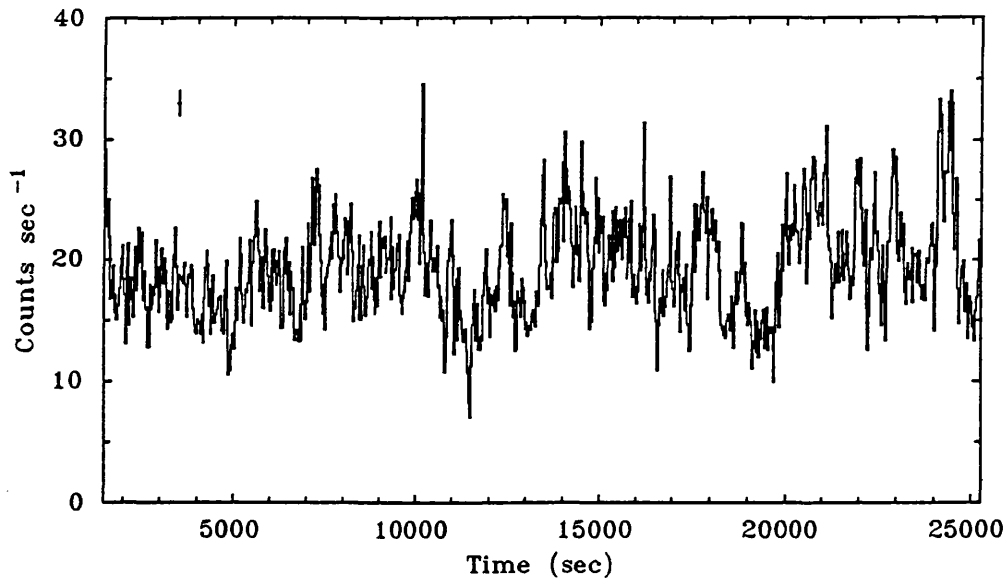


Figure 4.6: The 1.2–8.5 keV light curve of the observation of 1983 Dec 4. The time resolution is 30 sec. A typical  $1\sigma$  error bar is shown

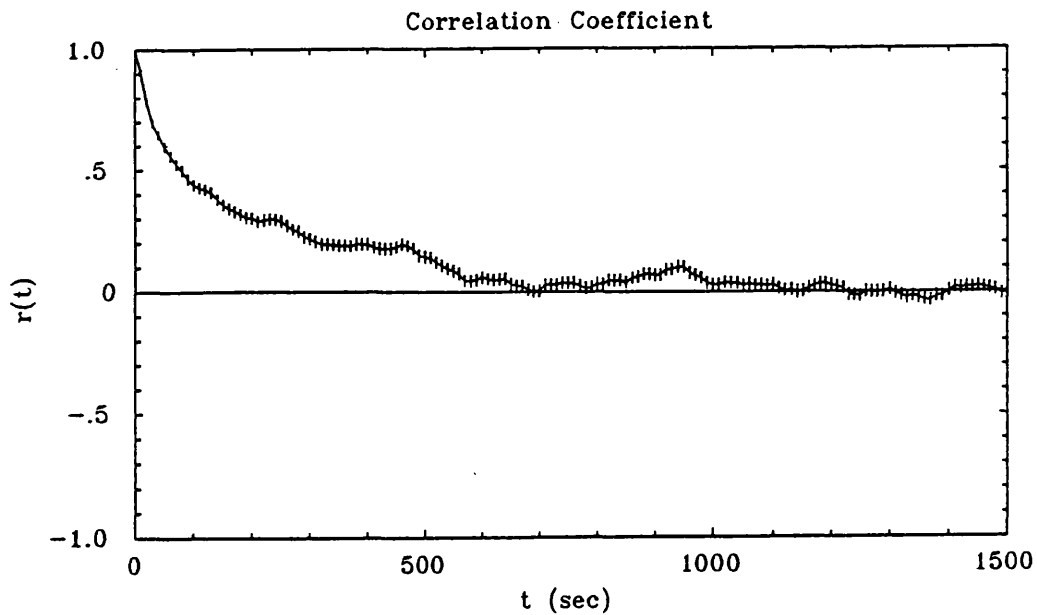


Figure 4.7: The autocorrelation function of the 10 sec resolution ME light curve from the observation of 1983 Dec 4. The error bars are at  $1\sigma$  and a counting statistics correction has been applied.

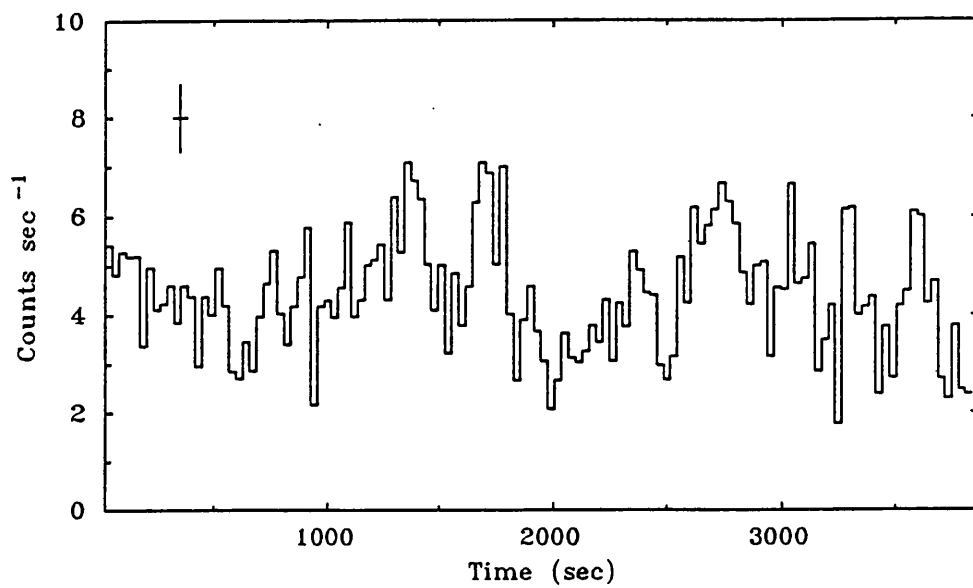


Figure 4.8: The 1.2–8.5 keV light curve of the observation of 1983 Nov 11. The time resolution is 30 sec. A typical  $1\sigma$  error bar is shown

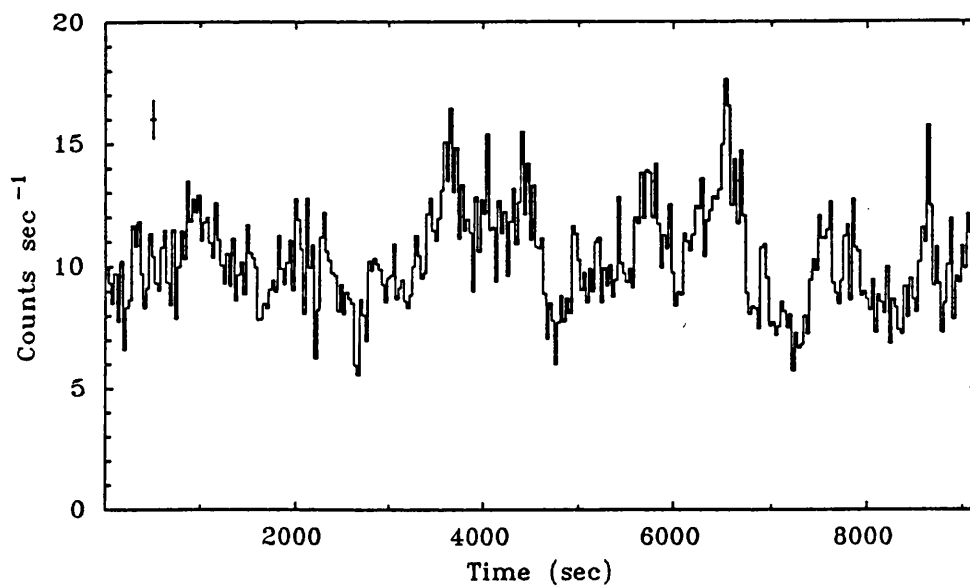


Figure 4.9: The 1.2–8.5 keV light curve of the observation of 1984 Sep 21. The time resolution is 30 sec. A typical  $1\sigma$  error bar is shown

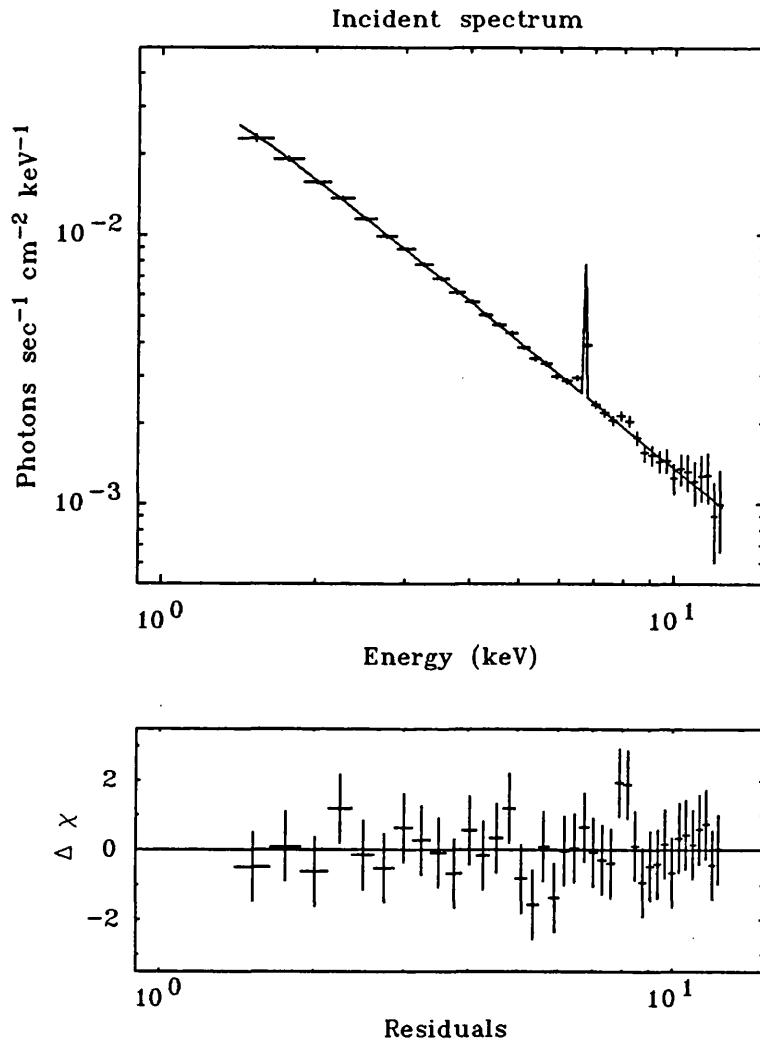


Figure 4.10: The EXOSAT ME spectrum of the observation of 1983 Dec 4. The model spectrum is a power-law with  $\alpha \approx 1.6$ , with a low column density ( $N_H < 3.1 \times 10^{21} \text{ cm}^{-2}$ ) and a fixed emission line at 6.7 keV. Note the excess near 8 keV, which may be due to thermal  $K\beta$  iron emission at 7.9 keV.

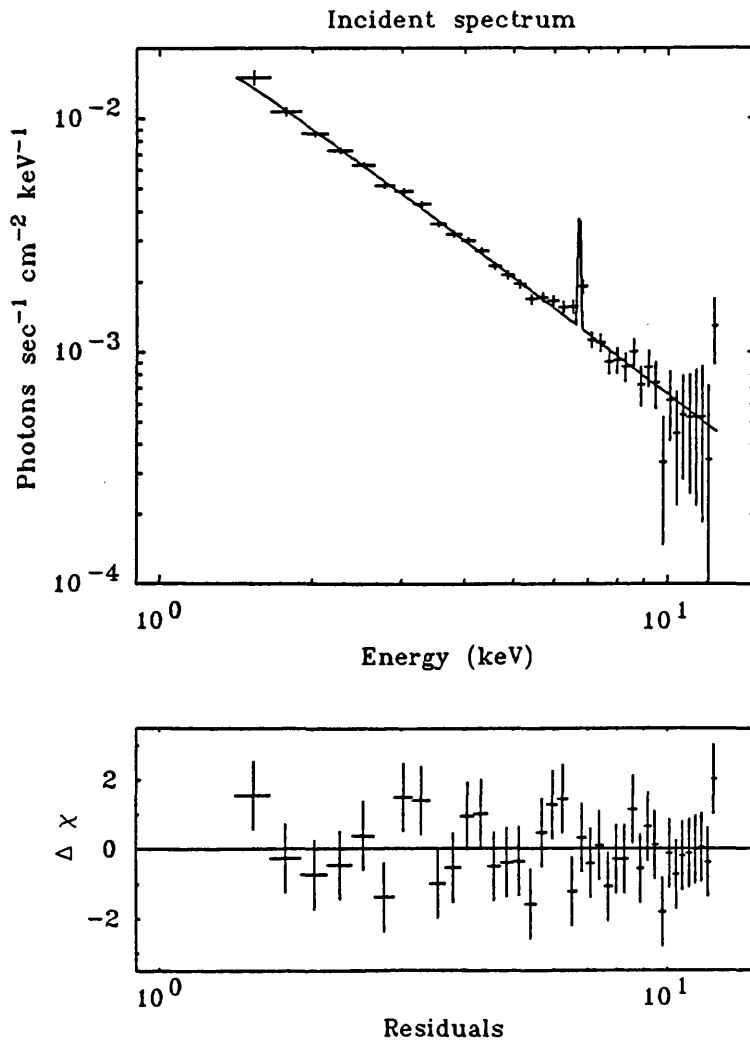


Figure 4.11: The EXOSAT ME spectrum of the observation of 1984 Sep 21. The model spectrum is a power-law with  $\alpha \approx 1.6$ , with a low column density ( $N_H < 5.5 \times 10^{21} \text{ cm}^{-2}$ ) and a fixed emission line at 6.7 keV.

Table 4.5: Best fit parameters for the power-law models of spectra from the Dec 4 and Sep 21 observations. The model includes an emission line with a fixed energy of 6.4 keV.

Model parameter	Dec 4	Sep 21
Normalisation ( $\times 10^{-1}$ photon $\text{sec}^{-1}$ $\text{cm}^{-2}$ $\text{keV}^{-1}$ )	$(0.48^{+0.06}_{-0.04})$	$(0.29^{+0.11}_{-0.03})$
Photon Index	$1.54^{+0.07}_{-0.06}$	$1.64^{+0.20}_{-0.09}$
Line Flux ( $\times 10^{-3}$ photon $\text{sec}^{-1}$ $\text{cm}^{-2}$ )	$(0.33^{+0.21}_{-0.22})$	$(0.28^{+0.29}_{-0.25})$
$N_H$ ( $\times 10^{21}$ $\text{cm}^{-2}$ )	$< 2.5$	$< 5.3$
$\chi^2_\nu$	0.92	0.90

Table 4.6: Best fit parameters for the power-law models of spectra from the Dec 4 and Sep 21 observations. The model includes an emission line with a fixed energy of 6.7 keV.

Model parameter	Dec 4	Sep 21
Normalisation ( $\times 10^{-1}$ photon $\text{sec}^{-1}$ $\text{cm}^{-2}$ $\text{keV}^{-1}$ )	$(0.49^{+0.07}_{-0.04})$	$(0.29^{+0.10}_{-0.03})$
Photon Index	$1.56^{+0.08}_{-0.06}$	$1.64^{+0.19}_{-0.09}$
Line Flux ( $\times 10^{-3}$ photon $\text{sec}^{-1}$ $\text{cm}^{-2}$ )	$(0.45^{+0.23}_{-0.23})$	$(0.28^{+0.30}_{-0.28})$
$N_H$ ( $\times 10^{21}$ $\text{cm}^{-2}$ )	$< 3.1 \times 10^{21}$	$< 5.5 \times 10^{21}$
$\chi^2_\nu$	0.61	0.95

Note: All errors quoted at the 90% confidence limit.

Unfortunately, the next two brightest hard x-ray observations, both in the quiescent state away from outburst, were subject to a certain degree of background contamination. Inspection of the data from the off-source array showed that after background subtraction, these spectra (which should be consistent with having zero flux in all channels) were contaminated. Consequently, no spectral information could be obtained from the observation of Aug 28, and the Nov 11 data had to be limited to an energy range of 1-8 keV. The best fit model was found to be a thermal bremsstrahlung with  $kT = 9.9_{-3.5}^{+4.2}$  keV,  $N_H < 5.1 \times 10^{21} \text{ cm}^{-2}$  (90% confidence), with  $\chi^2_\nu = 1.94$  (24 d.o.f.), and is shown in figure 4.12.

The data from the outburst observations were too weak to provide any strong constraints on the variation of spectral parameters. The spectra were acceptably fitted by either thermal bremsstrahlung or power-law models, with temperatures or indices consistent with the brighter state spectra. Swank (1979) claims, without quoting any upper limits, that there is no evidence for an increase in the photoelectric absorption of the spectrum when the source is in outburst. For the EXOSAT data it was found that by leaving all the spectral parameters free, the limit on the maximum column density during outburst is rather high,  $N_H < 20 \times 10^{21} \text{ cm}^{-2}$  (90% confidence). The Sep 14 to 19 data were investigated further by fixing the continuum shape to the best fit model for the bright Sep 21 observation (power-law with  $\alpha = 1.6$ ). The limit to the maximum column density found from this method was found to be  $N_H < 3 \times 10^{21} \text{ cm}^{-2}$ , and is consistent with the value obtained for the post-outburst (Sep 21) spectrum,  $N_H < 2.6 \times 10^{21} \text{ cm}^{-2}$  (power-law model without line feature). Thus it is concluded that any increase in column density during outburst must be  $< 3 \times 10^{21} \text{ cm}^{-2}$  at the 90% confidence level.

The ME data from the Dec 4 observation was analysed by King, Watson and Heise (1985), by the generation of the hardness ratio as a function of luminosity to give information on the spectral behaviour of the hard component. A similar approach was attempted for the remaining observations. It proved to be impossible to make this study because it was found that this method, when applied to data with a low signal/noise ratio, is subject to a very strong bias which leads to a spurious hardness-intensity correlation.

#### 4.4 SOFT X-RAY PULSATIONS

The properties of the large amplitude x-ray pulsations seen in SS Cyg and U Gem in outburst (C80 and C84) were reviewed in section 3.5. The search for, and parameterisation of, these oscillations

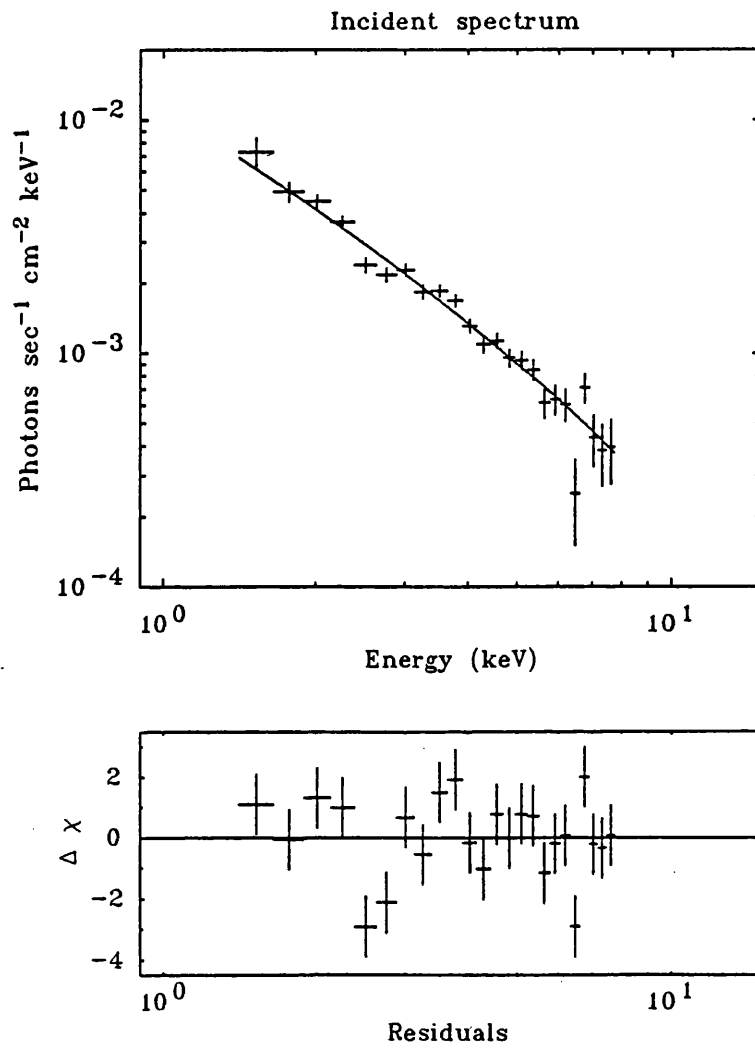


Figure 4.12: The EXOSAT ME spectrum of the observation of 1983 Nov 11. The model spectrum is a thermal bremsstrahlung with  $kT = 10$  keV, and a column density  $N_H < 5 \times 10^{21} \text{ cm}^{-2}$ .

in the data from the EXOSAT observations of SS Cyg will be presented here.

#### 4.4.1 The Search for Oscillations

A search for modulation was performed on the data from the LE telescope only. Since the majority of the ME observations were made at 10 sec resolution, or had too low a count rate to give useful limits to modulation. The pulse profile was shown by C80 to be sinusoidal to the limits of measurement of the HEAO-1 LED-1 data. Since it also known that the pulsations may have a low phase coherence, the search for oscillations was thus made using a power-spectrum method.

The frequency range used for the search corresponds to the interval of period of 6-12 sec. This covers the known range of observed periods for both optical and x-ray oscillations. The criterion adopted for a positive detection was that the excess power should be significant at the 99% confidence level. Careful consideration was made of the noise properties of the time series. In a power-spectral analysis of EXOSAT LE observations of VW Hyi, van der Woerd *et al.* (1987) noted that integration times in the time series of less than  $\approx 1.5$  sec will give large deviations from Poisson statistics due to the presence of dead-time gaps in the data stream (see section 2.2.1). The effect of the dead-time on the power-spectrum distribution may be evaluated by generation of a time series using a background area of the CMA image (van der Woerd *et al.*, 1987), since the dead-time in this and the on-source data streams are identical. By choosing the integration area of the off-source data to give a count-rate similar to that obtained from the source, the noise properties in both time series will be similar. The power spectrum of the off-source data thus gives a good estimate on the effect of dead-time in the on-source data. It was found that even at a time resolution of 1.5 sec, the mean power was not 2 as would be expected for a time series which is dominated by Poisson noise (the power spectrum normalisation used in all cases is that described in section 2.6.2). However, in all cases the power was found to be  $\chi^2$  distributed, and by using the scaling technique described in section 2.6.2, the confidence levels of detection could be calculated.

The power spectra were formed by addition of the individual power spectra of consecutive samples of 768 sec duration of the light curves. The spectra have a frequency resolution of 0.0013 Hz. The upper limits to the fractional rms variation were calculated by the methods described in section 2.6.2, and are at the 99% confidence level. Three observations were found to have strong peaks, these being at periods of 9.5, 7.4 and 7.8 sec on June 26, Sep 14, and Sep 15 respectively. These power spectra are shown in figures 4.13 and 4.14, the 99% confidence intervals are also shown. The lower dashed lines in all power spectra presented represents the power that would be expected

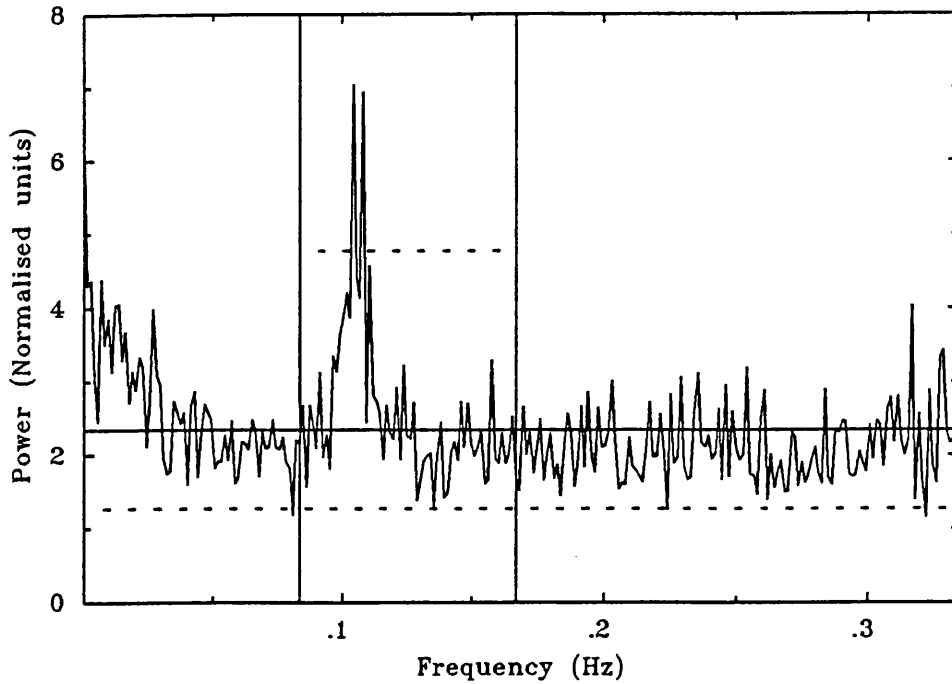


Figure 4.13: Power spectrum of the LE light curve from the Jun 27 observation. Dashed lines indicate  $P_{exceed}$  and  $P_{detect}$  power levels at the 99% confidence limit. The vertical lines indicate the range of frequencies searched.

to be exceeded ( $P_{exceed}$ ) at the same confidence level as the detection limit (see section 2.6.2). The 99% confidence limits and the measured rms powers for the LE observations are given in table 4.7. These limits have not been corrected for the “diffraction” term, which is found to be typically  $\sim 5\text{--}10\%$  over the frequency range of interest.

In a power-spectral search for a line feature with width  $\gamma_\nu$ , the optimum frequency resolution is  $\delta\nu \sim \gamma_\nu$ . Although the exact shape of the power spectral peak is dependent on the form of the oscillation, it is in general true that a decrease in the coherence (section 2.6) of the oscillator will result in a broadening of this peak. In order to search for low coherence oscillations, the frequency resolution of the power-spectrum was progressively degraded by decreasing the sampling length ( $\Delta t$ ). Using this technique, the observation of 1984 Sep 17 was also found to be significantly modulated in addition to the three cases mentioned above. At  $\Delta t = 192$  sec ( $\delta\nu \approx 0.005$  Hz), a broad peak can be seen in the power spectrum which is significant at the 85% confidence level (figure 4.15). By reducing  $\Delta t$  to 96 sec ( $\delta\nu \approx 0.01$  Hz) the peak becomes significant at the 99%

Table 4.7: The LE telescope observations of SS Cygni with measured or upper limits to the RMS amplitude of any pulsation in the range of period 6–12 sec.

Year	Date	Optical state	Duration (sec)	L.E Count Rate (counts sec <sup>-1</sup> ) 0.04 – 2 keV	Filter	RMS Amplitude (or limit)
1983	Nov 11	Q	3300	0.074 ± 0.006	3lx	0.27
	Dec 4	Q	24000	0.230 ± 0.004	3lx	0.12
1984	Jun 27	O	15500	1.19 ± 0.01	3lx	0.11 <sup>(a)</sup>
	Aug 28	Q	4100	0.062 ± 0.005	3lx	— <sup>(b)</sup>
		Q	4400	0.030 ± 0.004	Al/Par	— <sup>(b)</sup>
		Q	3500	0.009 ± 0.004	Boron	— <sup>(b)</sup>
	Aug 29	Q	11500	0.054 ± 0.006	3lx	— <sup>(b)</sup>
	Sep 14	O	24000	2.09 ± 0.01	3lx	0.13 <sup>(a)</sup>
	Sep 15	O	8000	1.93 ± 0.02	3lx	0.19 <sup>(a)</sup>
	Sep 17	D	16000	0.270 ± 0.005	3lx	0.10 <sup>(a)</sup>
	Sep 19	DQ	4200	0.077 ± 0.004	3lx	0.27
	Sep 21	Q	8700	0.160 ± 0.005	3lx	0.14

Notes: (a) - Modulation detected at 99% confidence level, amplitudes include the diffraction term. (b) - Count rate too low to allow periodicity search. Key to optical states; Q - quiescent, O - outburst, D - decline from outburst.

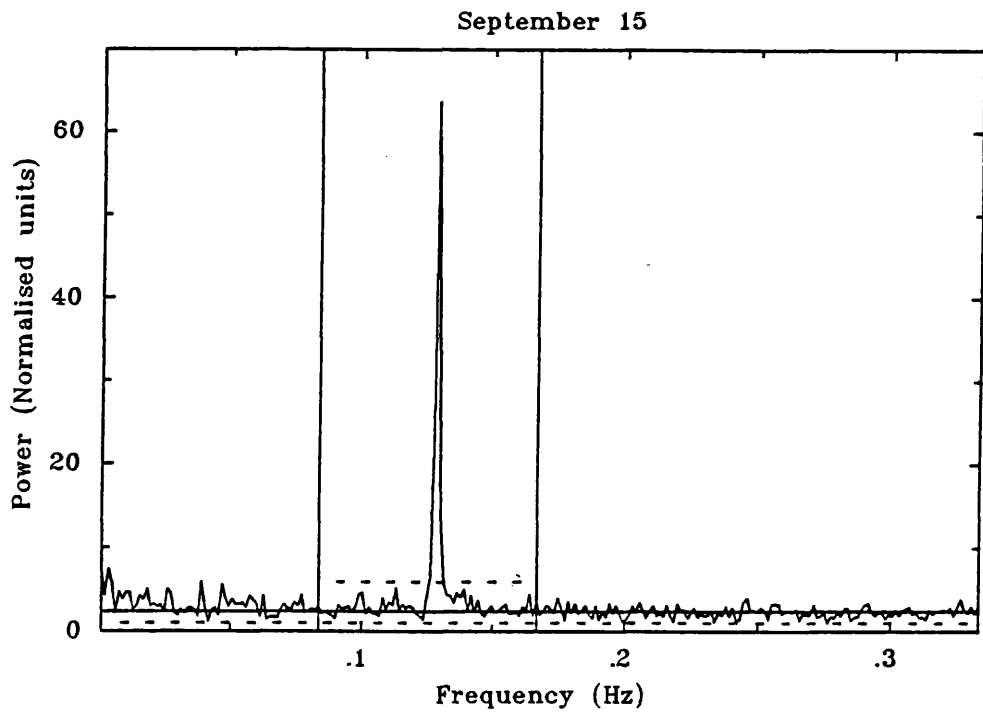
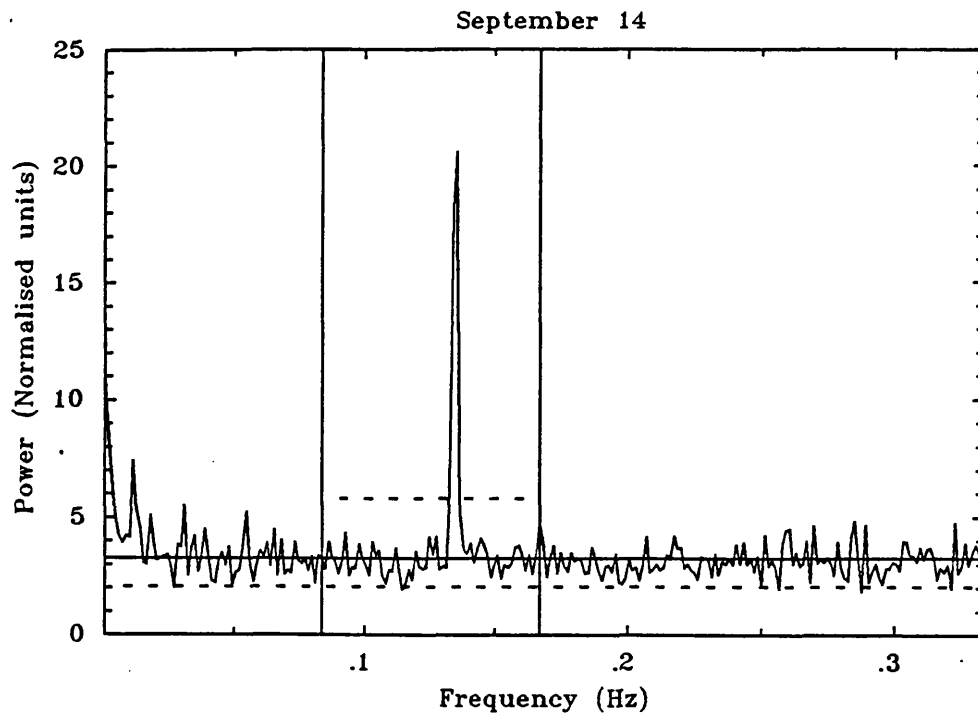


Figure 4.14: Power spectra of the LE light curves from the Sep 14 and 15 observations. Dashed lines indicate  $P_{exceed}$  and  $P_{detect}$  power levels at the 99% confidence limit. The vertical lines indicate the range of frequencies searched.

confidence level. Both these power-spectra are shown in figure 4.15, the best fit Lorentzian for the higher resolution power-spectrum has a peak frequency of  $\nu_{peak} = 0.096 \pm 0.006$  Hz ( $P = 10.4 \pm 0.6$  sec) and a width (half-width at half maximum) of  $\gamma_\nu \approx 0.008$  Hz.

#### 4.4.2 Detailed Analysis of the Pulsations

Having established the existence of a significant modulation, the properties of the oscillation, such as period, amplitude and phase coherence may be measured. The techniques adopted to measure these quantities depend on both the signal/noise of the data and on the coherence of any oscillations that are present. In the ideal case, each pulse would be directly visible in the light-curve; the pulse amplitude and arrival time would form a complete description of the oscillation from which the above quantities could be calculated. In these data however, even the strongest oscillations are difficult to discern in the raw data as individual pulses, and measurement of individual pulse arrival times is not possible.

##### Dynamic Power Spectra

The variation of pulse period and amplitude with time may be investigated by the formation of a time resolved, or 'dynamic' power spectrum (see section 2.6.2). In order for this to be effective it is necessary that the feature to be studied has a reasonably strong signal each sample transform. This condition was met for the observations of June 26, and Sep 14 and 15. The sampling length used was 384 seconds, which gives a reasonable compromise between time and frequency resolution ( $\delta\nu = 0.0026$  Hz). The dynamic power-spectra for all three observations are shown in figures 4.16 and 4.17 and have been smoothed using a 2-D Gaussian mask with width 0.0016 Hz and 576 sec in frequency and time respectively. The most striking feature of these spectra is the change in frequency in the Jun 27 observation which appears to be strongly correlated with the change in source intensity. The associated change in period is from 10.2 to 8.9 sec, while the flux increases from 0.7 to 1.7 counts  $\text{sec}^{-1}$ . These changes occur in  $\approx 15000$  sec, giving  $\dot{P} = -(8.7 \pm 1.3) \times 10^{-5}$ . Changes in period are also evident in the other two observations, but are much smaller and at the limit of the frequency resolution of the spectra. It can be seen however that the oscillator is spinning down between the two observations at a rate of  $\dot{P} \sim 5 \times 10^{-6}$ . Another feature that is evident in these spectra is the variable strength of the oscillation, with factor of two changes in power occurring on timescales of a few hundred seconds.

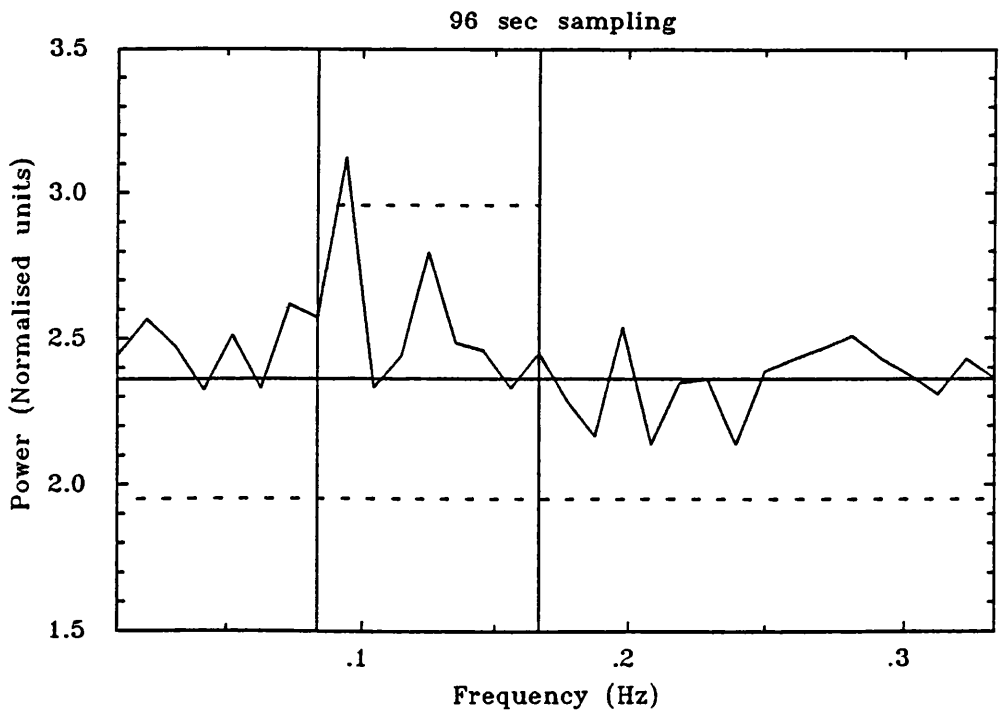
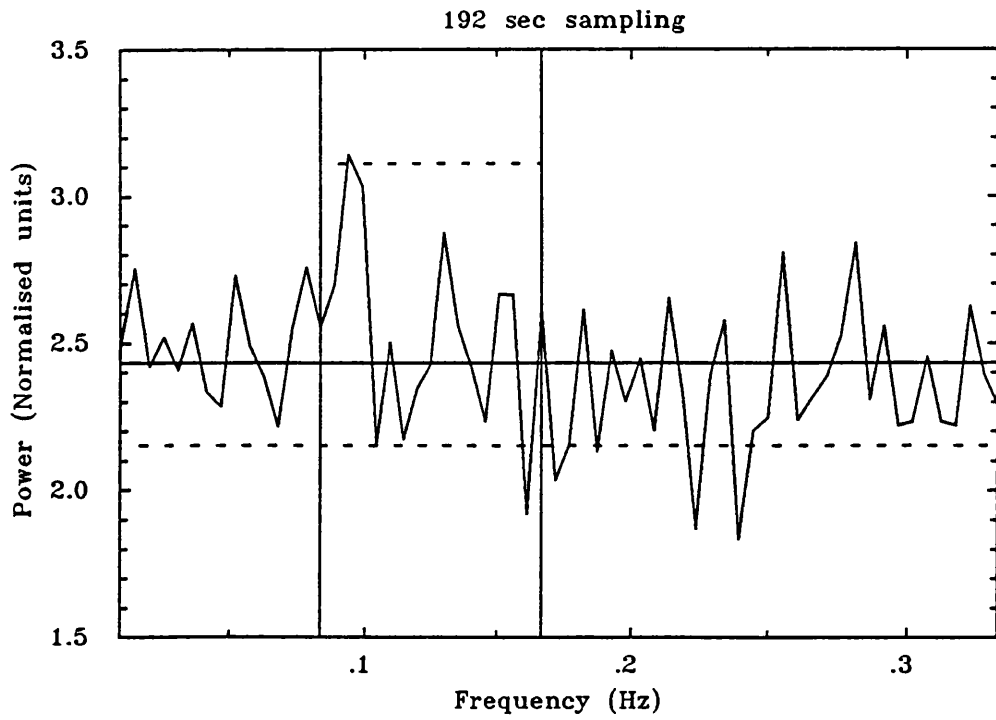


Figure 4.15: Power spectra of the LE light curve from the Sep 17 observation. The upper panel shows the spectrum obtained with a sampling length of 192 sec, and the lower is that obtained with sampling of 96 sec. The dashed lines indicate detection levels at the 85% and 99% confidence limits respectively.

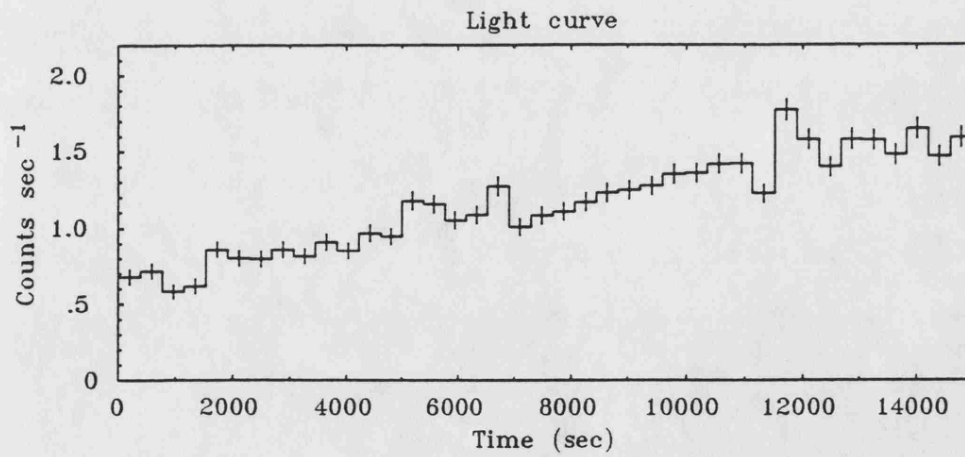
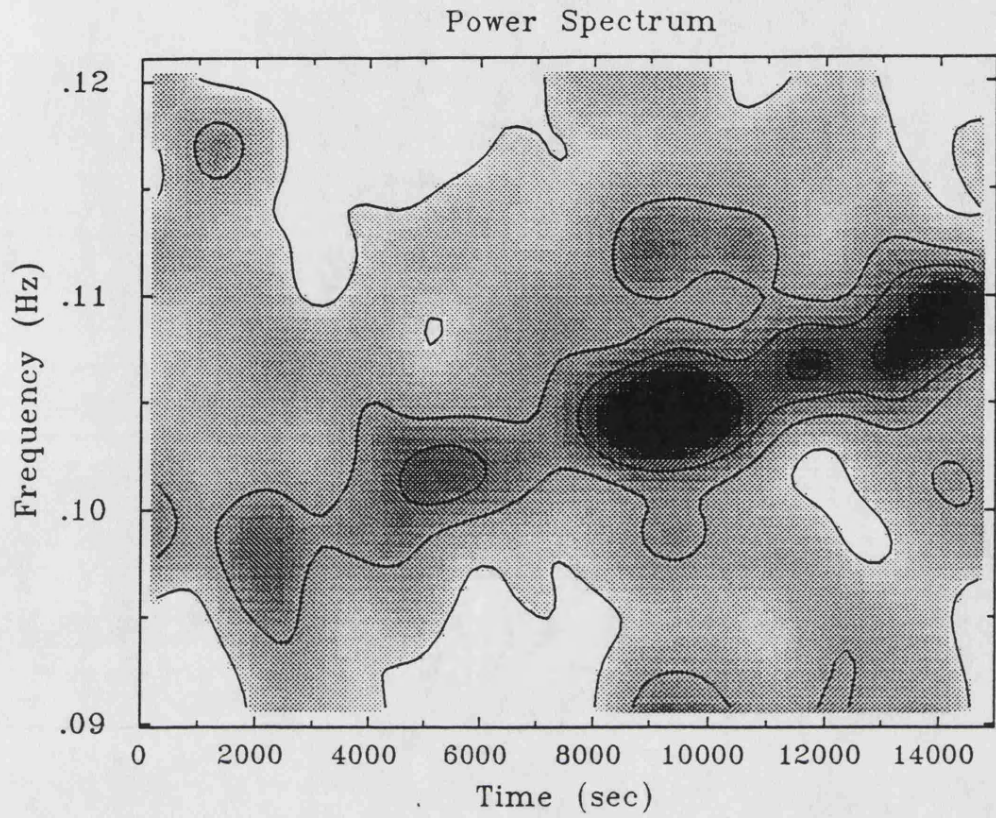


Figure 4.16: The dynamic power spectrum and light curve of the LE observation of Jun 27. The sampling length is 384 sec. The spectrum has been smoothed using a 2-D Gaussian mask. The grey scale shows power above the mean noise level, the contour interval is 2 normalised units. Note the strong correlation of the oscillation frequency with the source intensity.

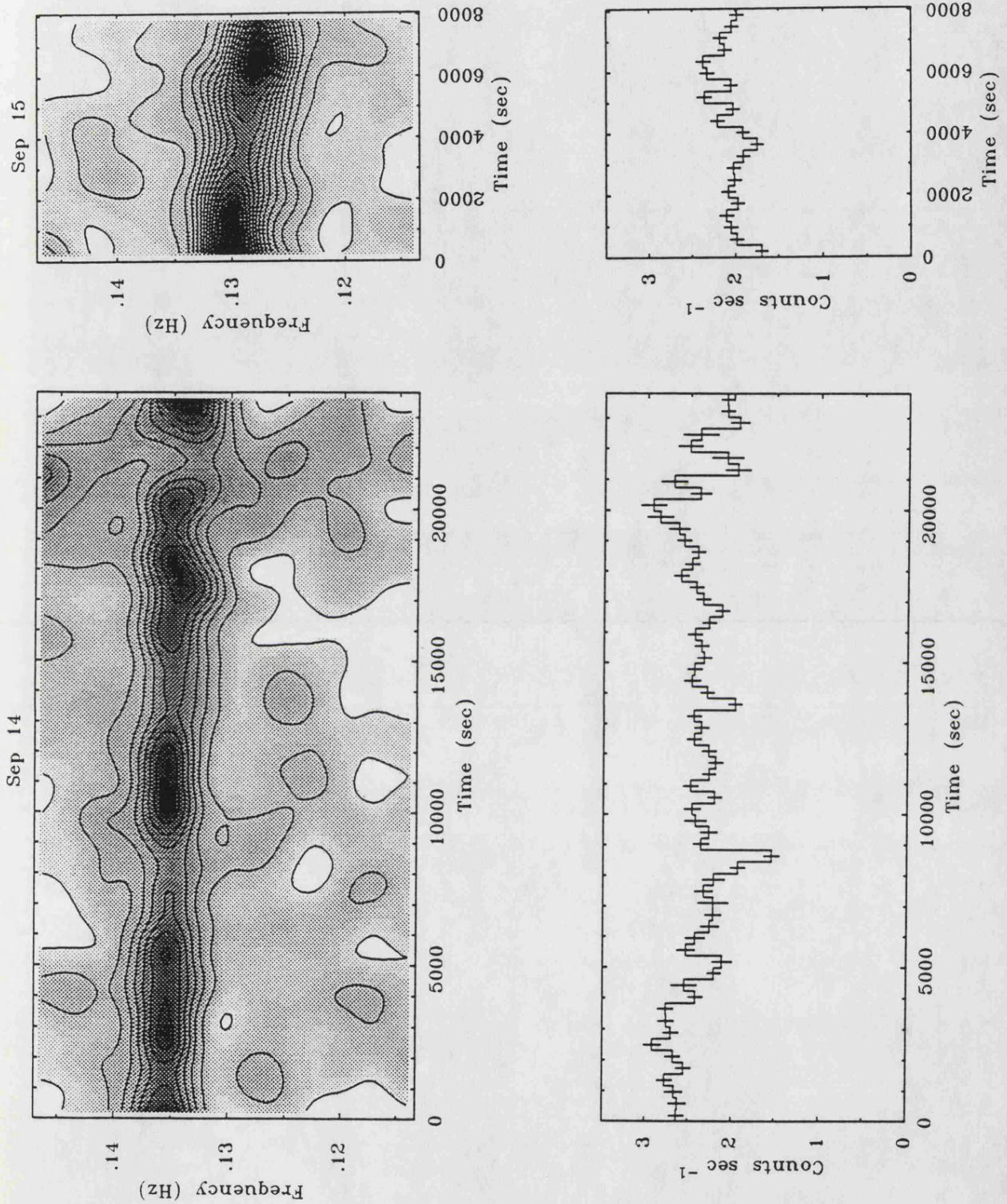


Figure 4.17: The dynamic power spectra and light curves of the LE observations of Sep 14 and 15. The spectrum has been smoothed using a 2-D Gaussian mask. The grey scale shows power above the mean noise level, the contour interval is 2 normalised units (see text). Note the peak amplitude variability on timescales of  $\sim 5000$  sec.

## Phase and Amplitude Evolution

To study the observations in which the rate of change of period is small (Sep 14 and 15), a pulse fitting technique was used. The method adopted is similar to that used by C80. The mean pulsation period is derived from the peak of the power spectrum. Samples consisting of a whole number of cycles duration were selected from the light curve. The samples were then folded at the trial period and these data were then fitted by a master pulse profile. Since the power spectra of both of these observations showed no detectable power in the first (or higher) harmonic, a sinusoidal template was adopted for the pulse profile. Fitting this to the data yields an amplitude and a pulse phase appropriate to the time interval covered by the sample. The amplitudes are expressed here such that for an oscillation  $f(t) = A + B \cos \omega t$ , the pulsed fraction ( $\mathcal{A}$ ) is  $B/A$ , as opposed to the alternative definition  $B / \langle A \rangle$  (where  $\langle A \rangle$  is the mean of  $A$  over the duration of the observation).

By sampling the entire light curve with suitable choice of sample length and overlap between consecutive samples the time evolution of the phase of the oscillator may be determined. C80 used this technique with independent samples of four cycles duration. Due to the poorer signal/noise of the LE data, sample lengths of 10 and 15 cycles were adopted for Sep 14 and 15 respectively. In the phase evolution diagrams presented here there is an overlap between samples is 90%. It is stressed then that adjacent points are therefore not independent, and that variability on timescales of less than  $\sim 100$  sec will be smoothed out.

A criterion adopted by C80 was that a fitted section should only be accepted if the amplitude determined for that section was significant at a high enough level that the number of spurious fits occurring in a given data set should be less than one. The significance level adopted in that case was 99%. Application of such a stringent condition to the LE data resulted in the rejection of most of the fitted sections. Consequently the acceptance threshold was reduced until a reasonable representation of the phase evolution was obtained. The confidence levels adopted were 95% and 68% for the Sep 14 and 15 observations respectively, and so some spurious phase points will be accepted in this process. This is nevertheless acceptable in the context of obtaining an overall picture of behaviour of the oscillation. Unlike C84, the more detailed study of the phase behaviour considered below is not based on this phase fitting technique.

The resultant phase-time diagrams for the Sep 14 and 15 observations are shown in figures 4.18 and 4.19. In interpreting this type of diagram it is important to note that if the trial period ( $P_{trial}$ ) is larger than the true oscillation period ( $P_{true}$ ) by some amount  $\Delta P$ , the fitted phases ( $\phi$ ) will

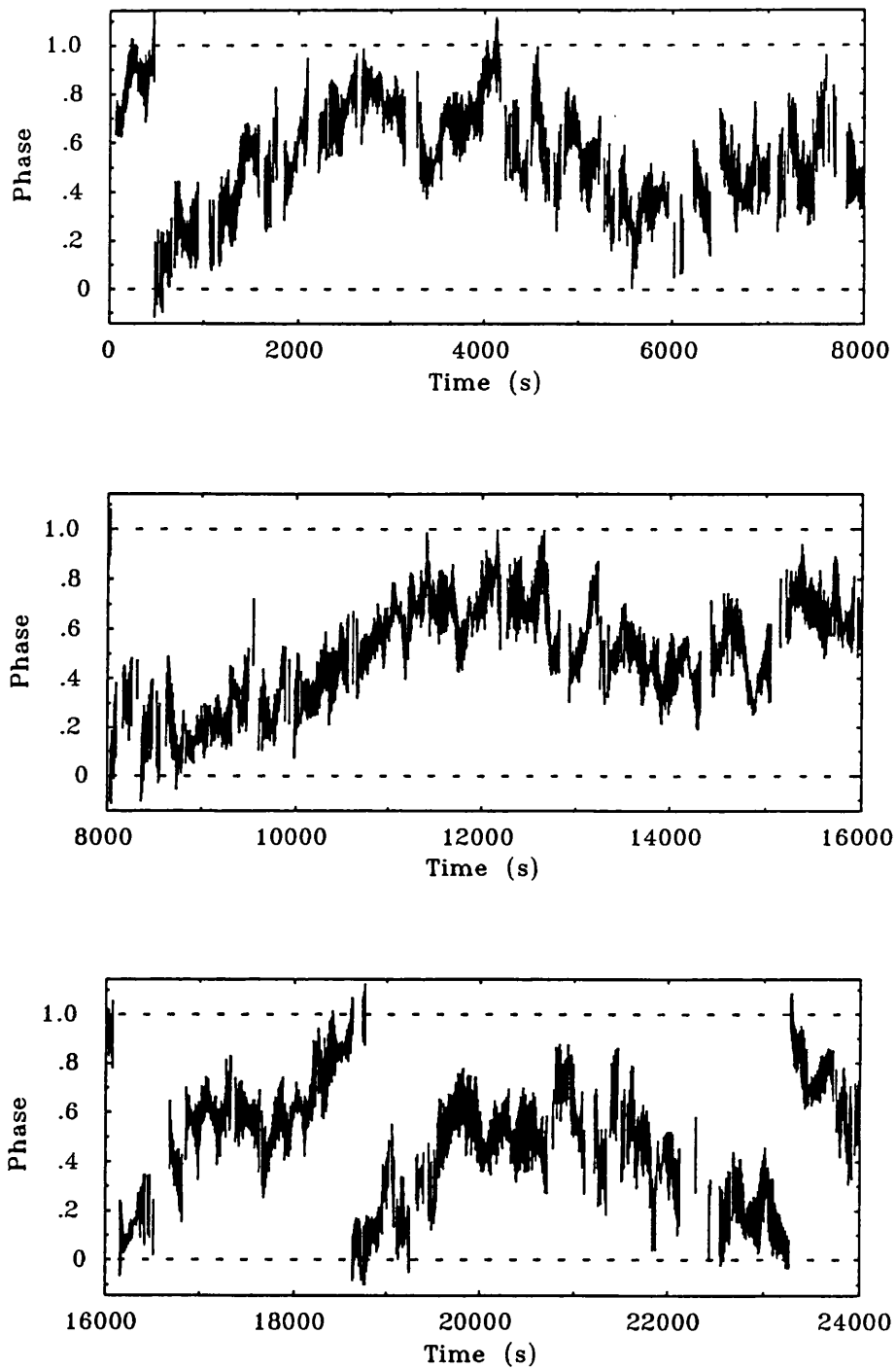


Figure 4.18: A phase-time diagram for the pulsations detected in the Sep 14 observation. The trial periods adopted were 7.396 (upper panel), 7.424 (middle panel) and 7.457 sec (lower panel). The sample length is fifteen cycles and there is a 90% overlap between consecutive cycles. The fitted phases are shown with  $1\sigma$  error bars.

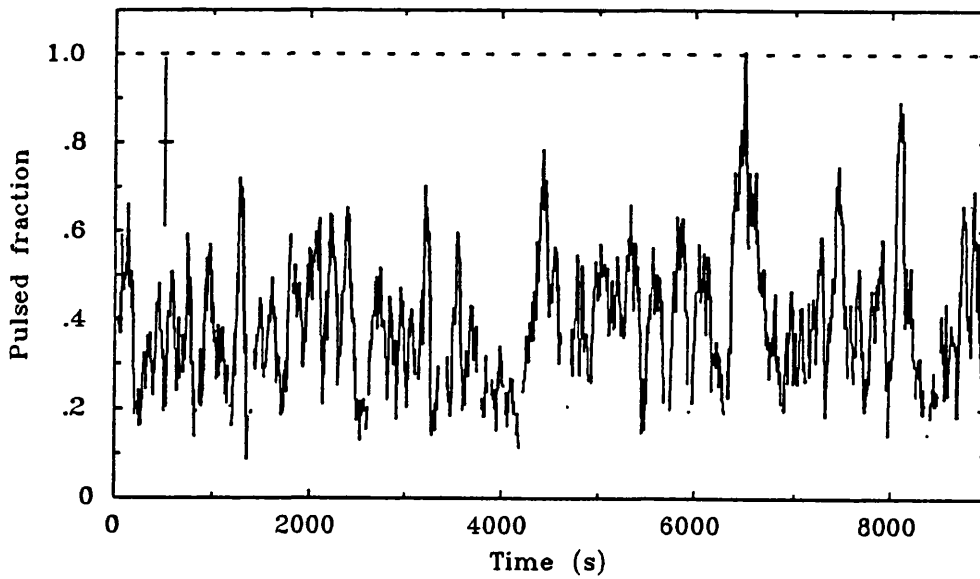
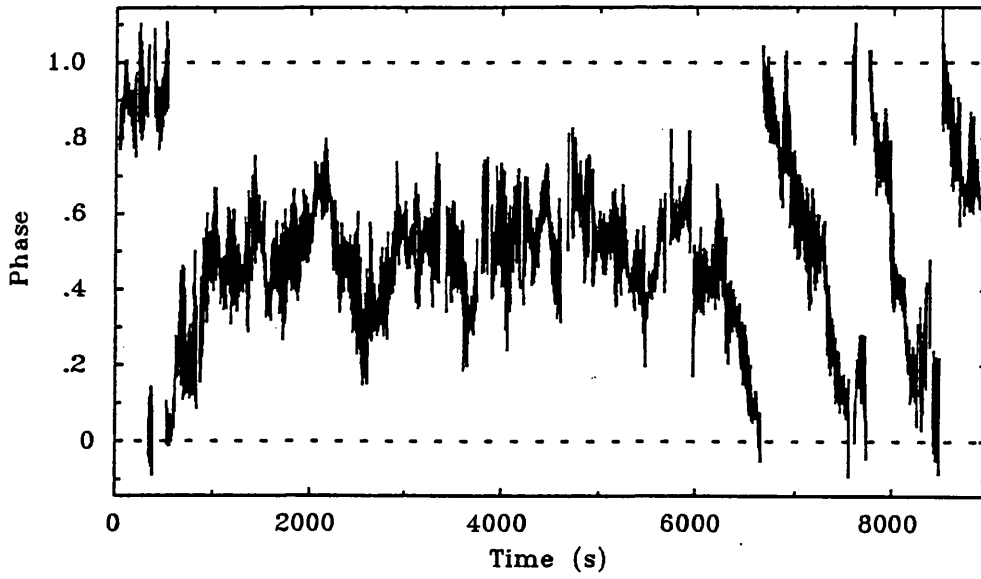


Figure 4.19: Upper panel: the phase amplitude diagram for the pulsations detected in the Sep 15 observation. The trial period used is 7.747 sec, the sample length is ten cycles and there is an overlap of 90% between consecutive samples. The phase points are shown with  $1\sigma$  error bars. Lower panel: the fitted amplitudes for the pulsations in the Sep 15 observation. A representative  $1\sigma$  error bar is shown.

have a linear trend given by,

$$\phi(t) \approx \frac{\Delta P_{true}}{2\pi P^2} t \quad (4.1)$$

from which the true period may be established. A value of  $P_{trial} = 7.747$  sec was used in the fitting shown in figure 4.19, and it can be seen that for the section between  $t = 1000-6000$  sec this is a good estimate of the pulsation period. At  $t \approx 6000$  sec however there is a sharp jump in the period, and using equation 4.1 the period appropriate for  $t = 6000-9000$  sec is  $P = 7.813$  sec. There is also a suggestion of a period jump at  $t \approx 1000$  sec, the period during the first part of the observation being 7.722 sec.

It was found that the ‘stable’ period sections in this observation are subject to significant variations in phase on timescales of a few hundred seconds, as illustrated by the  $t = 1000-6000$  sec section of figure 4.19. Although phase noise is evident, the phase seems to vary in a continuous fashion, and there are very few jumps in the phase. The phase behaviour is similar to that reported by C80, and as a comparison, the phase evolution results from that work are shown in figure 4.20.

Inspection of the phase-time diagrams for Sep 14 show a similar behaviour, with period jumps of  $\approx 0.01$  sec occurring on timescales of a few 1000 sec. It should be noted however that on short timescales, it is not possible to separate apparent period jumps from the phase noise. The jumps are however distinct features on long timescales since they represent reasonably large period shifts which are always in the same sense. This is illustrated in figure 4.21, which shows the periods of the stable period sections of the observations of Sep 14 and 15. It may be seen that the spin-down rate ( $\dot{P}$ ) defined by the period variation on Sep 14 is in good agreement with the spin down rate implied over both days of observation, for which  $\dot{P} = 4.6 \times 10^{-6}$ . Thus it appears that although the spin-down rate is not well defined on timescales of order  $\sim 10^3$  sec, it is well defined for timescales  $> 10^4$  sec and is slowly varying at this stage of the outburst.

There appear then to be two aspects to the phase behaviour, the short term (few 100 sec) phase noise, and the longer term (few 1000 sec) period jumps. The existence of period jumps has already been inferred by C80, C84 and by van der Woerd *et al.* (1987) in the case of VW Hyi. These observations show that phase jumps are a common occurrence and that they are the mechanism by which the period changes over long timescales. It is also evident that the phase of the oscillation varies continuously through these period changes.

The amplitudes of the folded sections were also determined in the fitting process, and figure 4.19 shows the evolution of the amplitude through the observation of Sep 15. Due to the rather low signal/noise of these data it is difficult to determine if there is any correlation between amplitude

and the changes in phase or period. C80 report that there is no such correlation, but it is interesting to note that the period change which occurs at  $t \approx 6000$  sec is coincident with a large peak in the amplitude distribution. Unfortunately the amplitudes determined from the Sep 14 observation have even larger associated error and little information can be obtained from them.

The mean pulsed fractions ( $\mathcal{A}$ ) were calculated to provide estimates of amplitude measured in a fashion consistent with those given by C80 and C84. This is however a rather poor estimate of the amplitude of the oscillation. If an amplitude discriminator is used in the fitting process then obviously  $\mathcal{A}$  will be biased towards an overestimate of the real pulsed fraction. Without a discriminator there will be a contribution to  $\mathcal{A}$  from the amplitudes due to the noise in the time series, and will again be an over-estimate, this however was the technique employed by C80 and values quoted here include the noise component. For the Sep 14 observation  $\mathcal{A} \approx 28\%$  and for Sep 15  $\mathcal{A} \approx 37\%$ . The rms amplitudes ( $\mathcal{R}$ ), (table 4.4) which have been derived from the power spectra imply values of  $\mathcal{A}$  of 15% and 19% for Sep 14 and Sep 15 respectively. The large discrepancy between the two estimates can be attributed to the biasing described above. Since the rms amplitudes represent an excess above the noise level it would appear that they form a more reliable estimate of the pulsed fraction than the pulse fitted amplitudes.

It should be noted that the data used were not corrected for heliocentric, satellite or binary motion. The maximum change in time delay over the duration of a  $2 \times 10^4$  sec observation from these effects is expected to be 0.5, 0.6 and 1.5 sec respectively. Modulation from any of these sources is of too low an amplitude to be detected in the large and rapid phase variations measured for the oscillator.

### Measurement of Phase Coherence

Although the fitting technique described above gives a representation of the behaviour of the oscillator, it would be useful if a mathematical model could be found to describe the phase behaviour using a small number of parameters. It might also be hoped that such a model may give some clues to the physical mechanism responsible for the pulsations. Note that for convenience, the angular frequency  $\omega$  will be used instead of the frequency ( $\nu$ ) in most of the following discussion.

A description of the phase behaviour that could be made from the examination of the phase-time evolution is that the oscillator undergoes jumps in period of magnitude of up to  $\sim 0.05$  sec on timescales of a few 100 to a few 1000 seconds. In the intervening 'stable' period sections the phase shows apparently random variability. This 'model' would be improved if the distribution of the

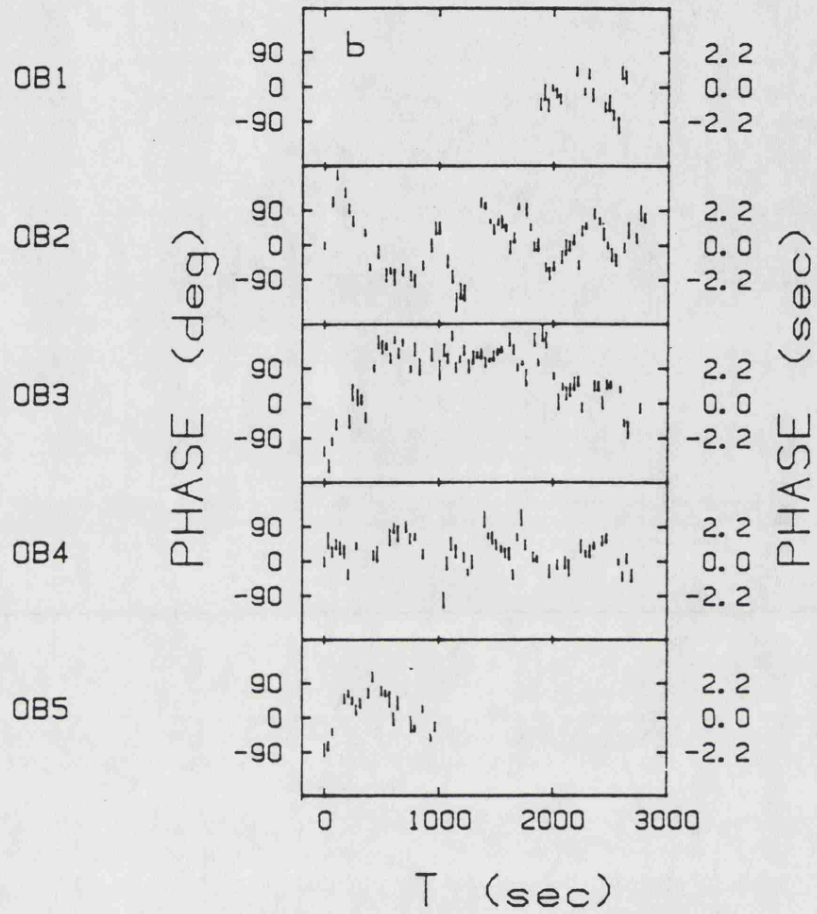


Figure 4.20: The phase of pulse arrival times for every set of four pulses, for five orbits of the HEAO-1 satellite, for the 1978 June outburst of SS Cyg. The pulsation periods adopted were 8.893, 8.876, 8.785, 8.757 and 8.745 sec for orbits OB1 to OB5 respectively. (From Córdova *et al.*, 1980).

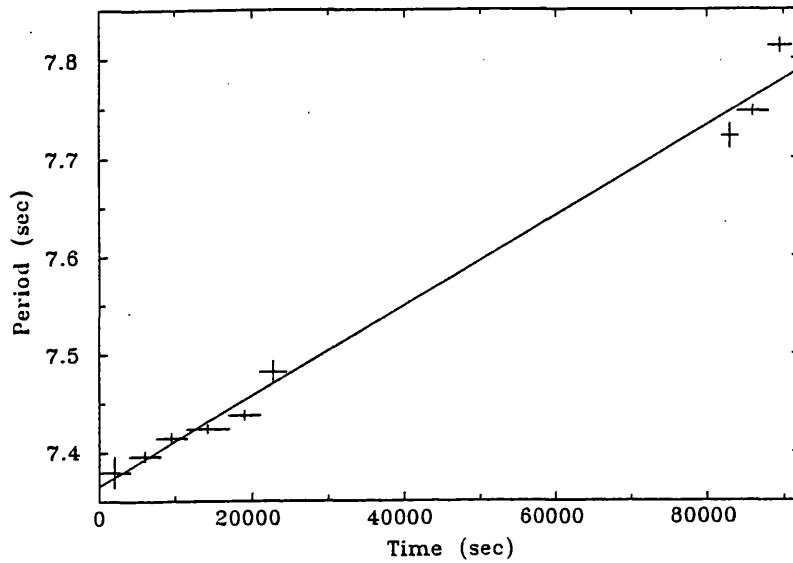


Figure 4.21: Period as a function of time for the observations of Sep 14 and 15. The error bars on the periods are at the  $1\sigma$  level, and on the time ordinate show the duration of that period. The straight line shows the best fit spin-down rate of  $\dot{P} = 4.6 \times 10^{-6}$ .

period jumps could be estimated, and if the random phase behaviour could be parameterised.

A mathematical description of the phase behaviour was put forward by C80 and C84, who suggested that the oscillator shows a random walk in phase, such that the arrival time ( $T$ ) of the  $n^{\text{th}}$  pulse is given by,  $T_n = T_{n-1} + (P_0 + P_1 x)$ , where  $P_0$  and  $P_1$  are constants, and  $x$  is a random variable with Gaussian distribution of zero mean and unit standard deviation. The strength ( $S_\phi$ ) of the random walk is given by the product of the mean square phase step ( $\langle \delta\phi^2 \rangle$ ) and the step rate ( $R$ ),

$$S_\phi = R \langle \delta\phi^2 \rangle = \frac{1}{P_0} \left( \frac{2\pi P_1}{P_0} \right)^2 \quad (4.2)$$

In principle it should be possible to measure  $S_\phi$  directly from the phase coherence of the oscillation. Coherences will be expressed here in terms of the parameter  $Q$  which represents the number of cycles before the oscillation phase has shifted by a significant amount ( $\sim \pi/2$  radians, see section 2.6).

The HEAO-1 data were interrupted by Earth occultation, allowing continuous monitoring of the phase of oscillation for intervals of less than  $\sim 3000$  sec. It is evident that period changes similar to those seen in the EXOSAT measurements (figure 4.19) would be difficult to detect in a data segment of this length. If one occurred in the observation interval, it would probably be interpreted as being due to the phase noise, since the existence of relatively stable period sections is only evident on timescales greater than a few 1000 sec. It is possible, for instance, that the linear change phase at the start of OB2 in figure 4.20 represents a period jump. It is of interest then to measure the coherences in an analogous fashion to the previous studies, and to investigate the effect of period changes on phase noise models. The phase variability of stable period sections will also be considered.

The technique used by C84 to study the phase behaviour was as follows. For each pulse an arrival time was determined. A composite pulse train  $F(\tau)$  was then formed by the superposition of the entire light curve with itself, with each arrival time acting once as the centre of superposition. For a pulse profile  $g(\omega\tau)$  with a randomly varying phase  $\phi_t$ , it was shown that the expected composite profile would have the form,

$$F(\tau) = e^{-\langle \cos \phi_t^2 \rangle / 2} g(\omega\tau) \quad (4.3)$$

So for a pulse profile  $g(\omega\tau) = A \cos \omega\tau$ ,

$$F(\tau) = A e^{-\langle \cos \phi_t^2 \rangle / 2} \cos \omega\tau \quad (4.4)$$

Counting noise introduces an error into the estimates of the pulse arrival times, such that  $F(\tau)$  increases for  $\tau = 0$  but is suppressed elsewhere. In practice  $F(\tau)$  also contains a constant term

representing the mean count rate. The behaviour of the envelope of this function gives information on the phase variability, which may arise from a random walk in phase itself or in its higher derivatives. Cordes (1980) shows that the variance of the phase in random walk models have the following dependences on time;

$$\langle \phi_\tau^2 \rangle = \begin{cases} R \langle \delta\phi^2 \rangle t & = S_\phi t & \text{random walk in phase} \\ \frac{1}{3} R \langle \delta\omega^2 \rangle t^3 & = \frac{1}{3} S_\omega t^3 & \text{random walk in frequency} \end{cases} \quad (4.5)$$

and  $\langle \phi_\tau^2 \rangle \propto t^5$  for a random walk in the time derivative of frequency. The strength of the random walk process is described by the strength  $S$  which is the product of the step rate  $R$  and the relevant root mean step amplitude  $\delta\phi$  or  $\delta\omega$ . Having calculated  $F(\tau)$  from the data, a general function of the form,

$$F(\tau) = Ae^{-S\tau^\alpha} \cos \omega\tau \quad (4.6)$$

could in principle be fitted, although in practice only a comparison between models with different fixed values of  $\alpha$  could be performed. It was claimed that the data supported the  $\alpha = 1$  model. Consequently the data were then fitted to a model of the form,

$$F(\tau) = Ae^{-S_\phi \tau^{1/2}} \cos \omega\tau \quad (4.7)$$

It was noted by C84 that the auto-correlation function (ACF) of data which have a random walk in phase were similar to those obtained by Robinson and Nather (1979) for an autoregressive (AR) type process, for which

$$r(\tau) = e^{-\gamma\omega\tau} \cos \omega\tau \quad (4.8)$$

The mechanical analogue of an AR process is a driven damped harmonic oscillator,  $\gamma\omega^{-1}$  being the damping time of the system. Another important characteristic of an AR process is that its power spectrum is a Lorentzian peak at frequency  $\omega_0$ , with half width at half maximum  $\gamma\omega$ ,

$$P(\omega) \propto \frac{\omega_0^2}{(\omega - \omega_0)^2 + \gamma\omega^2} \quad (4.9)$$

Note that a peak in a power spectrum which is given in terms of frequency  $\nu$  has a half width of  $\gamma\nu = \gamma\omega/2\pi$ . In an AR model the phase is likely to be coherent for  $\sim Q$  cycles before an oscillation at an arbitrary phase is excited. In the observed type of oscillation however, the phase appears to vary in an approximately continuous manner, ruling out an AR type mechanism. By comparison with equation 4.7 it can be seen that  $\gamma\omega = S_\phi/2$ . That the pulse superposition method and the ACF are identical for the two types of noise behaviour was shown by C84 by use of simulated data. Provided that a sinusoidal pulse shape is assumed, the equivalence of the two techniques can however be shown analytically by the following argument.

Consider a noise free time series of a pulse train  $g(\omega t)$ , then using the standard form of the ACF (equation 2.7),

$$r(\tau) = \frac{\langle (g(t) - \langle g(t) \rangle)(g(t + \tau) - \langle g(t) \rangle) \rangle}{\langle g(t)^2 \rangle} \quad (4.10)$$

If the pulse shape is given by  $g(\omega t) = \cos \omega t$ , then the pulse at time lag  $\tau$  will be  $g(\omega t) = \cos(\omega(t + \tau) + \phi_t)$ , where  $\phi_t$  is the phase shift due to a general noise process.

$$r(\tau) = 2 \langle \cos \omega t \cos(\omega(t + \tau) + \phi_t) \rangle \quad (4.11)$$

This may be expanded,

$$\begin{aligned} r(\tau) = & 2(\cos \omega \tau \langle \cos^2 \omega t \cos \phi_t \rangle - \sin \omega \tau \langle \cos \omega t \sin \omega t \cos \phi_t \rangle \\ & - \cos \omega \tau \langle \cos \omega t \sin \omega t \sin \phi_t \rangle - \sin \omega \tau \langle \cos^2 \omega t \sin \phi_t \rangle) \end{aligned} \quad (4.12)$$

If the phase varies according to a random walk process as described above, then provided that the steps occur on a timescale which is small in comparison to the oscillation period, then  $\phi_t$  will be normally distributed. Because  $\phi_t$  is not correlated with  $t$ ,

$$\langle \cos^2 \omega t \cos \phi_t \rangle = \langle \cos^2 \omega t \rangle \langle \cos \phi_t \rangle \quad (4.13)$$

and similarly for the other terms. Since  $\phi_t$  is normally distributed, and may be assumed to have a zero mean,  $\langle \sin \phi_t \rangle = 0$ , but

$$\langle \cos \phi_t \rangle = \sqrt{\frac{2}{\pi \langle \phi_t^2 \rangle}} \int_0^\infty \cos \phi_t e^{-\phi_t^2 / (2 \langle \phi_t^2 \rangle)} d\phi_t \quad (4.14)$$

$$= e^{-\langle \phi_t^2 \rangle / 2} \quad (4.15)$$

(The integral being non-analytic, see e.g. Spiegel, 1968) Thus only the first term in equation 4.12 is non-vanishing, and the ACF becomes,

$$r(\tau) = e^{-\langle \cos \phi_t^2 \rangle / 2} \cos \omega \tau \quad (4.16)$$

which is identical (apart from normalisation) to the pulse-superposition function  $F(\tau)$  in equation 4.4. The effect of noise on an ACF has already been considered in section 2.6.1, where it was shown that  $r(\tau \neq 0)$  is suppressed. This is again similar to the case in the pulse superposition method. Note that the equivalence of the two techniques is independent of the type of random walk process, and so in principle the envelope of the ACF may also be fitted to a general model as in equation 4.6.

There are two points that require further consideration in implementation of this technique. Although the counting statistics correction can be estimated in the manner outlined in section 2.6.1,

it was found to be unreliable in application to the data considered here. This is illustrated in figure 4.22, which shows the ACF of the 1.5 sec light curve from the Sep 15 observation, where there is a large initial drop in  $r(\tau)$ . Consequently the initial point of the ACF was ignored and a normalisation factor was allowed as a free parameter in the fitting of the envelope function. Secondly, trends in the light curve must be removed since they will otherwise distort the ACF from the expected profile. This was done by subtraction from the data of the best fit cubic spline using a knot-spacing of  $\sim 50$  sec.

The envelope profiles were obtained by division of the ACF by  $\cos \omega \tau$ , using the mean oscillation frequency appropriate to the data section (as determined from the peak in the power spectrum). Only points with  $\cos \omega \tau > 0.5$  were used in the fitting process. In practice it was found that the data cannot reasonably constrain the general model, and so the case with  $\alpha = 1$  has been adopted for all results quoted here. The parameter used here to measure coherence is  $Q$ ,

$$Q = \frac{\text{decay time}}{\text{period}} = \frac{1}{\gamma_\omega P} = \frac{2}{S_\phi P} \quad (4.17)$$

The coherences determined for the observations of Jun 27, and Sep 14 and 15, by this method were  $Q \approx 2 - 3$ ,  $Q = 68 \pm 8$ , and  $Q = 44 \pm 2$  cycles respectively. These values do not however take the changes in period into account. It is evident from phase-time plots such as in figure 4.19, that a major contribution to the decay of an exponential envelope will arise from period shifts. The exact form of the envelope depends on the way in which the period changes with time. A crude estimate of the magnitude of this effect can be determined by consideration of the simple case of a time series with sinusoidal modulation of duration  $T$ ; for the interval 0 to  $T/2$  the oscillation frequency is  $\omega + \delta\omega$ , and for  $T/2$  to  $T$  is at  $\omega - \delta\omega$ . Provided  $T \gg 2\pi/\omega$  and discussion is limited to small lags ( $\tau \ll T$ ), then to a reasonable approximation,

$$\begin{aligned} r(\tau) &\approx \frac{1}{2} \cos(\omega\tau + \delta\omega\tau) \cos(\omega\tau - \delta\omega\tau) \\ &= \cos \omega\tau \cos \delta\omega\tau \end{aligned} \quad (4.18)$$

i.e. the envelope is modulated at the beat frequency. Additional frequencies will tend to suppress the envelope at phases  $\phi > \pi/4$ . Approximating the period changes in the observation of Sep 15 to a sharp jump in period of  $\sim 0.05$  sec, the beat period  $\sim 1000$  sec, and so the envelope would decay to  $1/e$  in about 200 sec or 25 cycles. Clearly this is a crude argument but it illustrates that period shifts can easily dominate in the measurement of the oscillator coherence by this method. More generally, the  $e$ -folding time will depend on the magnitude  $\dot{P}$  and the duration of the observation

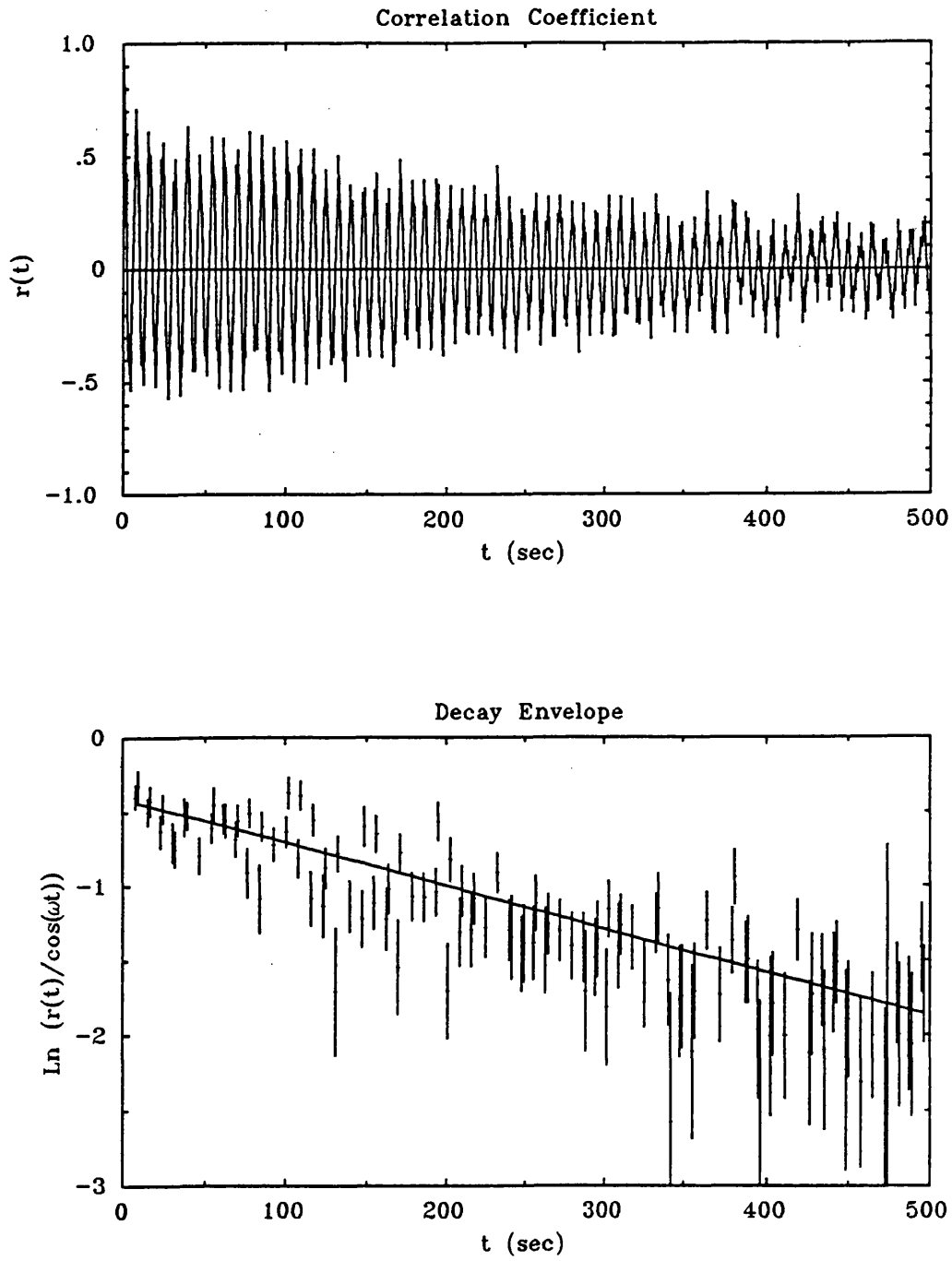


Figure 4.22: The ACF of the 1.5 sec resolution light-curve of the Sep 15 observation. A counting statistics correction has been applied but can be seen to be unreliable. The lower panel shows the envelope of the ACF, from which the coherence is found to be  $Q = 44 \pm 2$  cycles.

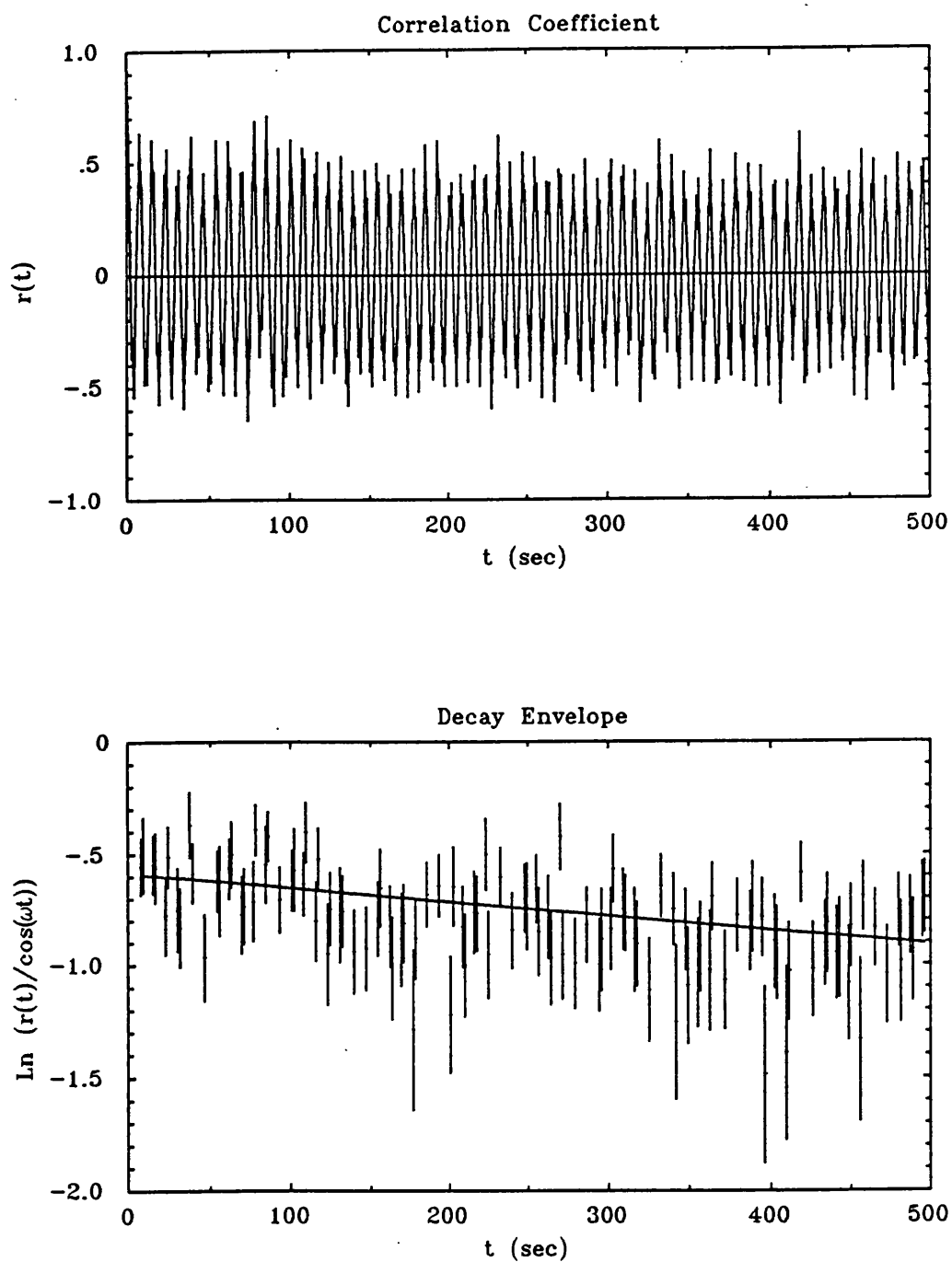


Figure 4.23: The ACF of a stable period section of the 1.5 sec resolution light-curve of the Sep 15 observation. The lower panel shows the envelope of the ACF, which can be seen to have a much longer decay time than obtained for the total observation (figure 4.22),  $Q = 201 \pm 36$  cycles.

$T$ , so that the coherence due to *period* changes is,

$$Q \sim \frac{P}{PT} \quad (4.19)$$

All the coherences determined above for the EXOSAT observations can be explained in terms of the previously determined changes in period.

In an attempt to compare the EXOSAT results with those obtained from HEAO-1, the coherences were measured on similar timescales to the duration of those observations ( $\sim$  few 1000 sec). This is however, a similar timescale to that on which the period jumps occur, and the measured coherences depend strongly on whether or not the sample contains such a jump. For the stable period sections of the Sep 14 and 15 observations, coherences were found to range from  $\sim$  100 to 500 cycles. For sections containing abrupt period changes the coherences were typically lower, with a range of  $Q \sim$  50 to 100 cycles. An illustration of the variability in the measured values of  $Q$  comes from two overlapping 3000 sec duration samples of data from the observation on Sep 15, in which  $Q = 201 \pm 36$  (figure 4.23) and  $60 \pm 5$  ( $1\sigma$  errors) respectively. The probability of these two values representing a single value of  $Q$  is less than 0.1%. However, such variability in  $Q$  is commonplace, and can even be seen in the data presented by C84 (see the plot of the parameter  $S$  in their figure 8). The important conclusion that can be drawn from the EXOSAT data however, is that the estimated value of  $Q$  varies in a random manner on timescales shorter than are required to perform the measurements.

This large random variability in  $Q$  puts into question the validity of the random walk in phase model. The model may reproduce phase behaviour which is similar to that seen in the real data, but would require arbitrarily varying coherences to do so. The model fails the requirement of the mathematical model since the variability cannot be parameterised by an easily measurable quantity. It is also unlikely to give any insight to the physical processes responsible for the phase behaviour since the implied erratic changes in the strength of the random walk process itself would require a model of variability.

The measurement of oscillator coherence is still however important. Although single values of  $Q$  are not well defined for the oscillation, it is useful to consider to range of values that may be measured at a certain time. It has been shown that the period jumps can give coherences as low as  $\sim$  50 cycles for the Sep 14 and 15 observations. In order to obtain an upper limit to  $Q$ , coherences were measured over the stable period sections, and values of up to several hundred cycles could be obtained (i.e. the oscillation is essentially coherent over a typical measuring interval). At this stage of outburst then, it seems that the range of  $Q$  that might be measured in a single observation

of a few 1000 sec duration would be from  $\sim 50$  to a few 100 cycles.

There is evidence from the 1978 Dec outburst that the oscillation coherence drops dramatically towards the end of outburst. C84 used the width of the peak in the power spectrum to estimate  $Q$ . Some caution was expressed about using this approach since it assumes that the phase variability is described by an AR process, which has been shown not to be the case. The coherence of the oscillation of frequency  $\nu$  and with half-width  $\gamma_\nu$  is, (equation 4.17)

$$Q = \frac{1}{\gamma_\omega P} = \frac{\nu}{2\pi\gamma_\nu} \quad (4.20)$$

The coherence measured in this way for the 1978 Dec observation was  $\approx 2$  cycles. A similar approach may be adopted here for the Sep 17 observation. The Lorentzian half-width was estimated to be  $\gamma_\nu \approx 0.004$  Hz, at a frequency of 0.096 Hz, giving  $Q \approx 4$  cycles. Note that for this observation the coherence due to period changes (equation 4.19) is  $\sim 50$  cycles. Thus this observation supports the claim (C84) that the oscillation coherence does drop towards the end of outburst.

Measurements of the optical coherence have been given by Hildebrand, Spillar & Stiening (1981). Near outburst maximum the coherences, measured from the Lorentzian half-widths, were found to be  $\sim 400$  cycles (at  $P = 7.3$  to  $7.5$  sec), dropping to  $\sim 50$  cycles as the outburst declined ( $P = 9$  sec). These ranges of coherence are also found for the x-ray pulsation, although the repeated measurements of  $Q > 400$  cycles would only be obtained from the x-ray data if the number of period jumps was small at that time. Clearly simultaneous x-ray and optical observations are required to confirm that the pulsations have the same phase properties in these two bands.

### 4.4.3 Summary of Pulsation Properties

In combination with the HEAO-1 results, the EXOSAT data can now be used to build up a picture of the way in which the pulsations evolve through outburst. In the absence of evidence to the contrary, it is assumed that the oscillator behaves in a similar way during different outbursts. Of the four separate outbursts monitored, three have been of the short type, with only that of June 1978 (C80) being a long type. The properties considered are the period, the rate of change of period and the oscillation amplitude, expressed as the pulsed fraction ( $\mathcal{A}$ ) (including the noise contribution), and as rms variation ( $\mathcal{R}$ ) for the EXOSAT observations. Note that the rms amplitude has been scaled by  $\sqrt{2}$  for comparison between  $\mathcal{R}$  and  $\mathcal{A}$ .

These properties are listed in table 4.8 in order of outburst phase. It can be seen that the period starts at  $P \approx 10$  sec, with a rapid spin up of  $\dot{P} \approx -8 \times 10^{-5}$ . By the time the period has reached of

Table 4.8: Summary of the evolution of the oscillator through outburst.

Outburst Phase	Date of observation	Period (sec)	$\dot{P}$ (sec/sec)	Pulsed Fraction		Coherence (cycles)
				$\mathcal{A}$	$\sqrt{2}\mathcal{R}$	
Onset	26 June 1984	10.1-9.2	$-8 \times 10^{-5}$	30%	16%	> 50
Maximum	June 1978 (H)	8.8	$-1 \times 10^{-5}$	30%	—	16 - 42
Maximum	14 Sept. 1984	7.4	$4.6 \times 10^{-6}$ $1.3 \times 10^{-5}$	28%	18%	> 50
Early decline	15 Sept. 1984	7.8		37%	27%	> 50
Late decline	17 Sept. 1984	10.4		—	14%	~ 4
Late decline	Dec 1978 (H)	10.7	—	18%	—	~ 2

Note: H indicates a HEAO-1 observation, results are taken from Córdoba *et al.* (1984).

8.8 sec the spin-up rate has dropped by a factor of  $\sim 8$ . Presumably the oscillator must continue to spin-up, since the minimum observed period is 7.4 sec. At this stage  $\dot{P}$  is small, being  $\approx 5 \times 10^{-6}$ , and is then seen to increase to a value of  $\approx 1 \times 10^{-5}$ , with period changing between 7.8 and 10.4 sec in an interval of  $\sim 2$  days. The observation which is apparently the latest in outburst phase is from 1978 Dec shows the period at 10.7 sec. The rms amplitude ( $\mathcal{R}$ ) of the oscillation varies  $\sim 10\%$  at onset of outburst, reaching a maximum of  $\sim 30\%$  some time after the peak in intensity, and drops back to the initial value on decline. The range of coherences also varies, the typical values of  $Q$  that might be measured are  $> 50$  cycles for most of the outburst. The rather low range of  $Q = 16 - 42$  obtained by C84 has not been found from other observations. In decline there is a fall in the oscillator coherence to  $\sim$  a few cycles. It has been suggested by C84 that at the end of outburst the oscillation coherence becomes so poor that the variability is then seen as random flickering.

## Intensity - Frequency Correlations

The study of the correlation of oscillation frequency with source luminosity indirectly provides a method of determining the effect of a changing mass transfer rate on the pulsation mechanism. The fact that the pulsations are primarily a soft x-ray phenomenon suggests that this correlation should be studied using an estimate of the mass transfer rate at the site of x-ray production. In the case of the optical  $I - \nu$  studies it is likely that the observed behaviour is complicated by the fact that the optical intensity gives an indication of the mass transfer rate not at the boundary layer, but at some region further out in accretion disc. This may explain why the optical banana loops are observed to wander around the  $I - \nu$  plane between outbursts; the x-ray banana loops may be fixed, but changes in the time taken for matter to propagate from the optically emitting region to the boundary layer would displace the optical banana loops. It is suggested then that the x-ray banana loops are in fact constant. Although there is little observational evidence to support this claim, the variability of the optical loops form only a weak argument against it.

The data used to study the  $I - \nu$  relationship are from the observations of Jun 27 and Sep 14, 15 and 17. In order to compare the x-ray results with the published optical results for SS Cyg it is convenient to deal with the pulsation frequency ( $\nu$ ) rather than period. The first three observations allow some degree of time resolution, the oscillation frequency was determined by fitting Gaussian profiles to the peaks in power spectra, the intensity is the mean for the sample of time series used. Peaks with an amplitude significant at the  $2\sigma$  level were accepted for plotting the behaviour in the  $I - \nu$  plane. Figure 4.24 shows the  $I - \nu$  points determined from the 768 sec sampled dynamic power spectra of observations of Jun 27, Sep 14 and Sep 15. Also indicated is the single  $I - \nu$  point obtained from the detection of oscillation in the Sep 17 observation. The observation of Jun 27 shows a strong spin-up associated with the increase in intensity, those of Sep 14 and 15 show little correlation of frequency with intensity. As a comparison with the optical behaviour, figure 4.25 shows the  $I - \nu$  curve obtained for a single outburst of SS Cyg (in October 1979) by Hildebrand, Spillar and Stiening (1981a). There is an obvious similarity in the loci traced out in both bands.

The x-ray banana loop covers a greater range in both frequency and intensity than the optical loops. Unfortunately, because the x-ray data come from different observations it is not possible determine the duration of the cycle, but there is no discrepancy between the two wavebands in the time taken to decay from maximum. There are no optical observations corresponding to the rapid rise in the x-ray loop.

The x-ray data are not complete enough to indicate whether the  $I - \nu$  relation has a loop type

behaviour or is a single valued function. Patterson (1981) suggested that the optical loop, and in particular the delay between maximum intensity and peak frequency may arise from a changing bolometric correction. There is no evidence that the x-ray flux and oscillation frequency peak at different times. Further observations are needed to confirm this behaviour and to determine the positions of the rising and falling branches on the x-ray banana loop.

Assuming that mass transfer rate increases with soft x-ray luminosity, the qualitative features of the oscillator behaviour are as follows. At the onset of outburst the oscillator shows a rapid spin-up, and the data suggest that  $d \ln \nu / d \ln I$  is increasing at this stage. At the highest measured frequency however, the frequency appears to show little variation for significant changes in intensity. A day later, the mean frequency has dropped, but is again insensitive to intensity changes. Two days after this the oscillator has returned to the frequency seen at onset, but now at a much reduced amplitude. The rising frequency phase then suggests a strong dependence on  $\dot{M}$ . The maximum intensity points suggest that the oscillator is near some equilibrium condition. These observations will be discussed in terms of simple physical models in section 4.5.3.

## 4.5 DISCUSSION AND SUMMARY

### 4.5.1 General X-ray Behaviour

The EXOSAT observations support the overall pattern of x-ray behaviour through outburst that is illustrated in figure 4.26. After the onset of the optical outburst ( $t_1$ ), there is a short delay before there is a flaring of the hard x-ray component ( $t_2$ ). Although this was not observed in the EXOSAT observations, this behaviour was reported by Swank (1979) from HEAO-1 (A2) data, and inferred by the *Ariel V* observations (Ricketts, King and Raine 1979). This flare ends with the onset of soft x-ray outburst ( $t_3$ ), and the hard x-ray emission becomes suppressed below its quiescent level. At the peak of optical outburst, the soft x-ray emission follows the optical behaviour closely, but on decline falls away quickly to the quiescent level ( $t_4$ ). This is then followed by a brightening of the hard x-ray component, which decays to a quiescent level on a slightly longer timescale than the optical decline. In quiescence the hard x-ray emission is illustrated as being reasonably constant, however the scanning *Ariel V* observations (Ricketts, King and Raine, 1979) indicate that large scale (factor of  $\sim 5$ ) variability may be present. The coverage of genuine quiescent intervals in the EXOSAT observation is limited to two observations of rather low flux, and so no conclusions can be drawn about this state.

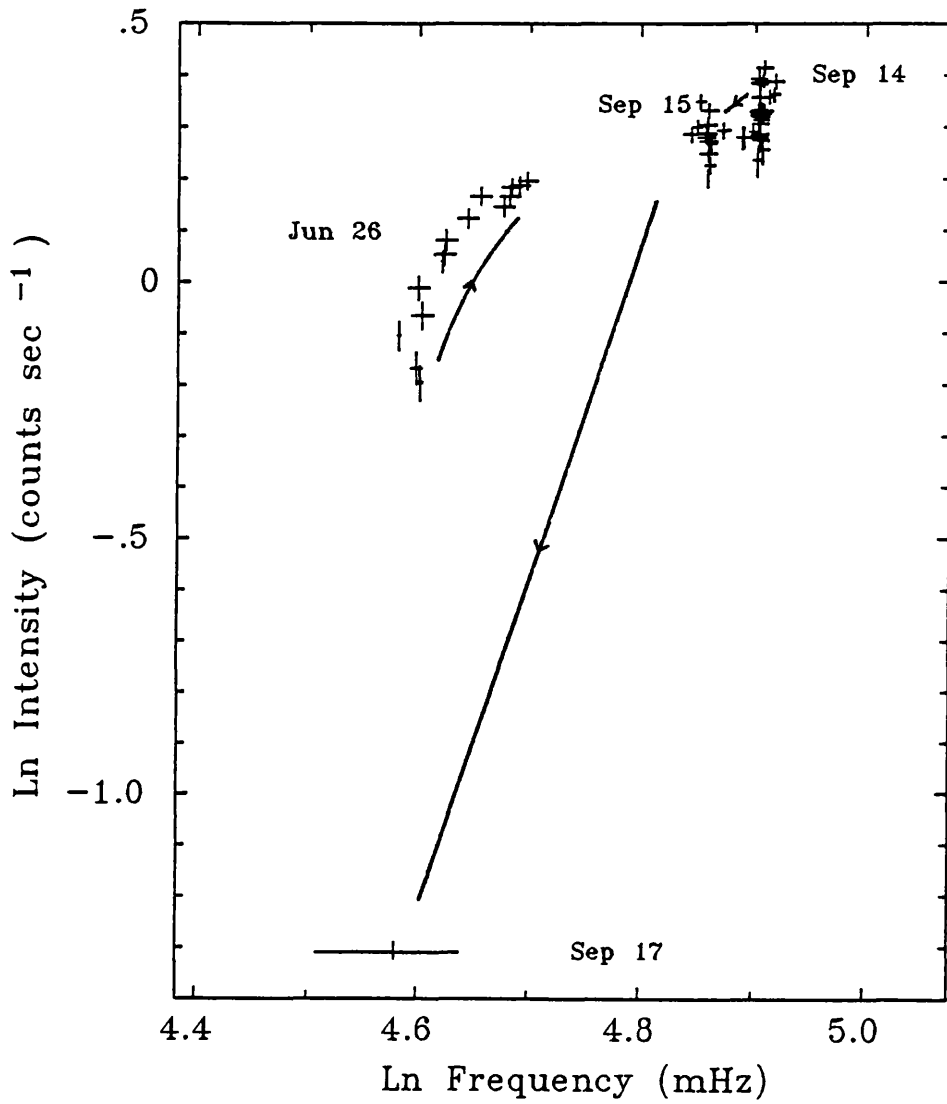


Figure 4.24: Variations of the soft x-ray count rate with oscillator frequency for the outbursts of 1984 June and September.

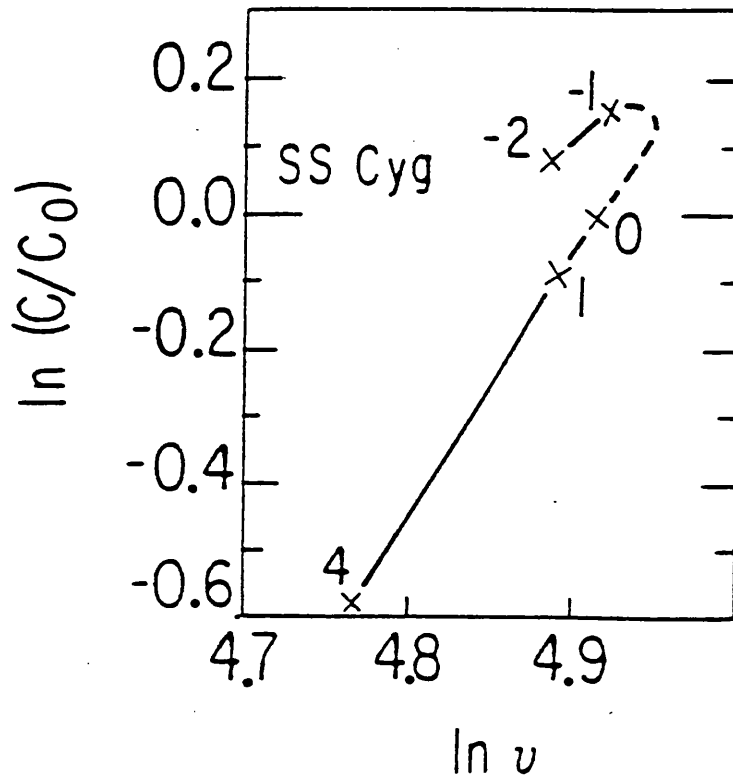


Figure 4.25: The variations of optical count rate  $C$  with frequency  $\nu$  for the 1979 October outburst of SS Cyg. The count rate has been normalised to 1.0 on the date that it was first observed to decrease. The numbers show the number of days before (-) or after that date. (From Hildebrand, Spillar, & Stiening, 1981a).

This pattern of behaviour can be explained in qualitative terms at least, by a model in which the accretion luminosity from the boundary layer is emitted as hard x-rays or soft x-rays depending on the mass accretion rate ( $\dot{M}$ ). As was discussed in chapter 3, theoretical models for this behaviour have been postulated. These models can at present only give crude estimates of how the x-ray emission varies with  $\dot{M}$ . Below a critical accretion rate  $\dot{M}_{crit}$ , the boundary layer gas forms an extended hot corona. Above  $\dot{M}_{crit}$ , the luminosity is thermalised in a small boundary layer region. The sum of the total luminosities from both components must follow the mass accretion rate at the boundary layer. The time delay between the onset of optical outburst and the hard x-ray flare arises due to the time taken for the enhancement in  $\dot{M}$  to travel through the accretion disc. Clearly the duration of this flare will depend on the rate of change of  $\dot{M}$  at the boundary layer since once it reaches  $\dot{M}_{crit}$  the accretion luminosity switches to being radiated by the soft component. This also explains the rapid rise in the soft x-ray outburst, since it probably represents the timescale for transition between the two regimes of emission rather than on the form of  $\dot{M}(t)$  itself. In peak optical outburst the soft x-ray component follows the optical behaviour because it is the only mechanism available for the dissipation of the boundary layer energy. However, once the accretion rate has dropped below  $\dot{M}_{crit}$  the soft x-ray emission will decline on the timescale for transition from soft to hard emission processes. The boundary layer luminosity is then radiated by the hard component. This hard x-ray emission then falls back to the quiescent value as  $\dot{M}$  at the boundary layer decays.

There are two further points to be made about this qualitative model. The EXOSAT data showed that the soft emission dropped significantly before the rise in the hard x-ray band. It is suggested then that in order to maintain a smoothly varying boundary layer luminosity, the temperature of the soft component must also fall during this decline stage. Also, the decline of the hard component may be expected to lag that in optical due to the propagation time through the disc. It is probable that the rate of decline in the hard x-ray band is also somewhat slower than in optical, since numerical studies of the propagation of increased mass transfer rates (see e.g. Bath and Pringle, 1981) show that impulses of  $\dot{M}$  become ‘smeared out’ as they propagate through the accretion disc.

## 4.5.2 Hard X-ray Spectrum

The bright, post-outburst, hard x-ray emission has been shown to be well modelled by a power-law continuum with  $\alpha \approx 1.6$ . The brightest observation (Dec 4) shows a strong emission line at

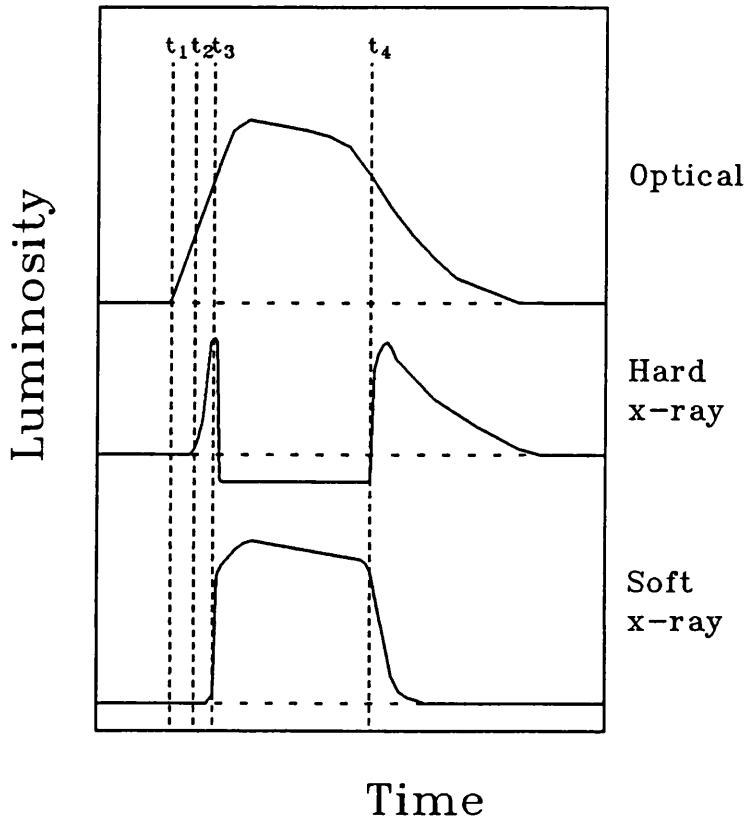


Figure 4.26: A schematic illustration of the behaviour of the optical and the soft ( $E < 0.5$  keV) and hard ( $E > 1$  keV) x-ray components of emission through outburst. Optical outburst ( $t_1$ ) is followed after a short delay by the onset of the hard x-ray outburst ( $t_2$ ). The hard x-ray emission begins to rise until a critical mass accretion rate ( $\dot{M}_{crit}$ ) is reached and this component is suppressed to a level below the quiescent flux ( $t_3$ ). At  $\dot{M}_{crit}$  the soft x-ray component rises rapidly and follows the optical behaviour until  $\dot{M}_{crit}$  is reached again on the declining phase ( $t_4$ ). At this point the soft x-ray emission declines rapidly, and the hard x-ray emission increases again. The optical and hard x-ray emission then fall back to their quiescent level. The decay in optical is possibly faster than in the hard x-ray band.

6.7 keV, indicating thermal excitation of iron in an optically thin region. The case for thermal emission is supported by evidence for line emission near 7.9 keV, which could be attributed to the thermal iron  $K\beta$  line. The line energy for the Sep 21 observation is not well determined, and it would be unwise to claim that the marginally better fit obtained with a 6.4 keV emission line is evidence for fluorescence. Given the large amplitude flaring of the hard state, it seems probable that the power-law continuum arises from the superposition of many bremsstrahlung components, with a range of temperatures (typically around 20 keV) and emission measures.

### 4.5.3 Physical Models for Soft X-ray Pulsations

Any physical model for the soft x-ray pulsations must account for the following properties, which have been established from the optical and x-ray observations of dwarf novae:

1. Large amplitude modulation.
2. A pulse profile which is very nearly sinusoidal.
3. A period history which shows a rapid spin-up at the onset of outburst and a gradual spin-down after reaching a well defined minimum period.
4. A spin-down mechanism which gives apparent jumps in period on timescales of a few thousand seconds, but which conserves the phase of the oscillation.
5. A phase coherence during the stable period sections of  $\sim$  few 100 cycles.

Two of the requirements of the modulation mechanism listed above may in fact not be as severe as at first appears. The condition of sinusoidal modulation may be relaxed to a certain degree, C84 found that the first and higher harmonic terms are suppressed in the power spectrum of an oscillation with appreciable phase noise. Furthermore, van der Woerd *et al.* (1987) found evidence for a non-sinusoidal pulse in part of the observation of VW Hyi. The other point regards the amplitude of the modulation. C80 state that such a large amplitude implies that the modulation must be inherent to the x-ray production mechanism. However as van der Woerd *et al.* (1987) point out, the modulation process may, for instance, involve a difference in optical depths over a small lengthscale, and need not be considered as being fundamental to the emission process.

The problem of finding a realistic model may be divided into two requirements; firstly for a suitable modulation mechanism, and secondly for an underlying 'clock' to drive the modulator. Both

requirements may be met in a single process but this need not necessarily be the case. To date, none of the models proposed successfully describe all of the observed properties of DNO. The processes which have been considered as having a potentially important role in the clock or modulation mechanism are reviewed critically below.

### White Dwarf Rotation

The power required to spin-up a body with moment of inertia  $I$ , and period  $P$  at a rate  $\dot{P}$  is,

$$L \approx I\omega\dot{\omega} = -4\pi^2 I\dot{P}/P^3 \quad (4.21)$$

For a  $1M_{\odot}$  white dwarf with radius  $\sim 7 \times 10^8$  cm, it would be expected that  $I \sim 10^{50}$  g cm<sup>2</sup>. Using the observed values, of  $\dot{P} \sim -10^{-5}$  with  $P = 10$  sec, for SS Cyg, the power required to spin up a  $1M_{\odot}$  is found to be  $> 10^{43}$  ergs sec<sup>-1</sup>. This is a factor of  $10^{10}$  greater than the outburst luminosity, and so this type of model may be rejected.

### Keplerian Orbits

It was first pointed out by Bath (1973) that the range of periods exhibited in dwarf nova oscillations strongly suggest an association with the minimum Keplerian period around a white dwarf. In the case of SS Cyg  $M_{wd} = 1.05M_{\odot}$ , assuming the mass-radius relationship from equation 1.8 gives  $R_{wd} = 5 \times 10^8$  cm, and so the Keplerian period ( $P_{min}$ ) at the white dwarf surface is 5.9 sec. Within the uncertainties of estimating  $M_{wd}$  and  $R_{wd}$ ,  $P_{min}$  is consistent with the observed minimum period of 7.3 sec (Hildebrand, Spillar and Stiening, 1981). Attributing the clock to an orbit near the white dwarf surface is attractive not only because of the magnitude of the expected period, but also because such a mechanism offers a natural limit to the period, which must always exceed the Keplerian period at the surface of the white dwarf.

Figure 4.27 shows the observed minimum oscillation periods for 10 dwarf novae and novalike variables, together with the minimum values expected on the basis of the mass radius relationship. It can be seen that all systems are consistent with this model.

In this scenario, the changes in period are due to variation of the radius of the orbit at which the modulation mechanism acts. For a  $1M_{\odot}$  mass white dwarf, the radius ( $r$ ) corresponding to a period  $P$  (in sec) is given by Kepler's law,

$$r = 1.50 \times 10^8 P^{2/3} \text{ cm} \quad (4.22)$$

Thus for SS Cyg, variation in radius implied by the full range of observed periods of 7.2 to 10.9 sec is  $r = 5.6$  to  $7.4 \times 10^8$  cm, (which corresponds to a 30% change).

This ‘model’ only describes the underlying clock mechanism, and does not offer any explanation for the modulation itself. At any one time, the modulation process must be restricted to a narrow range of radii, otherwise differential rotation would soon smear out the pulsation. An estimate may be made on the maximum radial extent of the modulation region given the condition that the pulsation must be coherent to the observed value of up to  $\sim 100$  cycles. This implies that the maximum value of any relative change in Keplerian frequency is  $\Delta\omega/\omega \lesssim 100$ . Small changes in radius ( $\Delta R$ ) are related to the change in Keplerian frequency by,

$$\Delta r \approx -2/3(\Delta\omega/\omega)r \quad (4.23)$$

and so for SS Cyg,  $\Delta r \sim 5 \times 10^6$  cm. A similar result for the maximum radial extent of the modulating orbits was given by Bath (1973) for the optical period changes seen in CN Ori.

### Loosely Coupled Surface Layer

In this scenario, the accreting material forms a surface layer which is only weakly coupled to the rotation of the white dwarf. While the accretion rate is high, this layer may be spun-up to a frequency which again is limited by the Keplerian frequency at the surface of the white dwarf. When the accretion rate falls, the layer loses angular momentum through the coupling to the white dwarf surface. This type of model was originally proposed by Paczyński (1978)

A crude estimate of the moment of inertia (and hence mass) of this layer can be made using a similar line of reasoning to that which excludes white dwarf rotation, i.e. by equating observed luminosity with the rate of change of angular kinetic energy, ( $L = I\omega\dot{\omega}$ ). This gives the mass of a surface layer (at  $r \sim 5 \times 10^8$  cm) as  $\sim 10^{23}$  g, which is approximately the mass accreted in an outburst interval.

This model provides a clock mechanism and offers a natural limiting frequency, but the form of the modulation mechanism is again unknown. King (1985) suggests that transient magnetic fields may play an important role in this context (see below). It is also unclear how the structure of such a layer might be sustained.

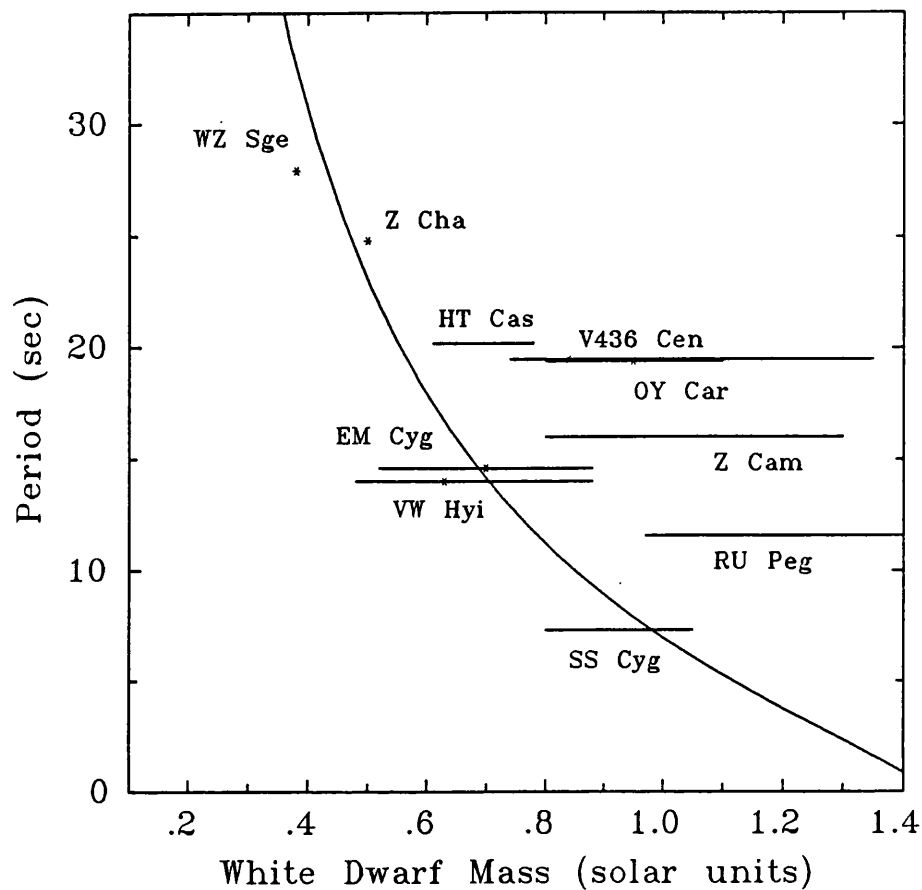


Figure 4.27: Minimum observed oscillation period against white dwarf mass for 10 dwarf novae and novalike variables. The curve represents the minimum Keplerian period as a function of mass, assuming the mass-radius relationship from equation 1.8. The masses are shown either as the range of quoted values, or as a single value (\*) with error bars if provided by the original authors. References for mass estimates: SS Cyg - Kiplinger (1979a), Robinson (1976); RU Peg - Robinson (1976), Stover (1981); VW Hyi - Schoembs & Vogt (1981); EM Cyg - Robinson (1976); Z Cam - Robinson (1976 and 1984); OY Car - Vogt *et al.* (1981); V436 Cen - Gilliland (1982); HT Cas - Patterson (1981); Z Cha - Smak (1979); WZ Sge - Robinson, Nather & Patterson (1978). Figure after Patterson (1981).

## White Dwarf Pulsations

Another class of model involves modes of vibration of the white dwarf itself. In isolated stars, the two types of oscillation which have received most attention are those in which the restoring force is provided either by the pressure, or by the buoyancy of the perturbed gas, these are termed p-mode and g-mode pulsations respectively. Radial or non-radial p-modes were soon discounted as being a viable mechanism, since the implied range of period for a  $1M_{\odot}$  white dwarf is 1 to 10 sec (Chanmugam, 1972), which although might be acceptable for SS Cyg, is too low for the majority of dwarf novae. Consequently, the g-modes were supported by several authors because the typical period range from this mechanism is 10 to 40 sec (Brickhill, 1975, Osaki and Hansen, 1974) In order to prevent this oscillation being washed out in the intensity integrated over the surface of the star, it was suggested it must have a low (orbital) wavenumber,  $l = 2$ .

Severe objections to these models were raised by Papaloizou and Pringle (1978), who argued that the observed period changes exclude g-mode oscillations of the entire star. It was suggested that a model of this type, which has a spectrum of frequencies separated by a factor of  $\sim 1/l$ , could give the required small changes in period, provided that  $l$  were high enough. Apart from the problem of the pulsation being washed out, the excitation of a single mode at any given time was considered to be rather unphysical. The actual model frequencies can only vary if there is a gross change in the properties of the gas involved in the pulsation, this was shown to effectively limit the mass of the oscillating region or layer to  $10^{23} - 10^{25}$  g. This is essentially the same as the surface layer mass estimate given above, and so the angular momentum of this layer becomes important. Papaloizou and Pringle investigated pulsations (which they termed  $r$ -modes) in this region and found that period changes arise mainly from a change in the rotation of the layer.

The important conclusion then is that even pulsational models require some type of weakly coupled rotating surface layer, and this can be considered to form the underlying clock mechanism. It should be noted however, that the rotation period of this layer may not be the same as the observed oscillation.

## Magnetic Modulation

The interaction of the accretion flow with a magnetic field has been invoked by several authors as a modulation mechanism. Such schemes are attractive because of the relative ease with which large amplitude oscillations with a simple pulse shape could be generated. A feature of such models is

that the modulation will be at the period of rotation of the magnetic field, and a problem arises in association of the magnetic field with a structure of sufficiently low angular momentum to give the observed period and phase behaviour.

Clearly, the field cannot be that of the white dwarf itself. Bath (1973) suggested a model in which blobs are formed by an unspecified process at the Alfvén surface, but that they would continue to have a Keplerian orbit. Such a hypothesis is self-contradictory, the Alfvén surface is defined as the region where the magnetic field becomes the dominant effect on the gas flow, any blobs would follow the field lines and modulate the emission at the spin period of the white dwarf.

King (1985) noted that weak magnetic fields which are insufficient to dynamically control the accretion flow, could still play an important role in determining a preferred direction for thermal conduction in the gas. Even so, the modulation would be at the spin period of the white dwarf, and so it was suggested that transient magnetic fields may be produced by dynamo action in a weakly coupled surface layer. Magnetic flux tubes formed in this layer would be expelled and could form hot-spots on the surface. Observationally this model is unsatisfactory because it predicts loops which have a lifetime of a few thousand seconds before reconnection takes place. Rapidly changing periods could be accounted for by loops appearing at different latitudes in a differentially rotating layer, but this would require only one loop at a time to be visible. Furthermore the appearance of unconnected loops cannot be reconciled to the observed phase continuity.

### **Fluid Instabilities**

Fluid dynamical instabilities may offer both clock and modulation mechanisms. Unfortunately, very little is known about the gas flow in the boundary layer. The difference in rotation rates between the innermost Keplerian orbit and the white dwarf surface will probably result in strong shear flow, and the region may be extremely turbulent. Papaloizou and Pringle (1978) suggest that the boundary layer may be subject to a Kelvin-Helmholtz instability which may be quasi-coherent in nature. Another process utilises the shocks that were inferred by Papaloizou and Pringle (1978) as the deceleration mechanism (see chapter 3). These shocks would have to be non-radial to modulate the emission and might be expected to be short lived and so give rise to the phase incoherence. It was also noted that the boundary layer itself may be unstable to radial pulsations, these could be excited by a weak interaction with the magnetic field of the white dwarf, provided that the spin and magnetic axes of the star are not aligned.

At present, fluid instability mechanisms are extremely speculative. The fact that instabilities exist in flows which have some similar physical characteristics to that expected in the boundary layer suggest that they may be important. Quantitative predictions on this type of process would require extensive numerical modelling, but may be feasible.

## 4.6 SUMMARY AND FUTURE PROSPECTS

The results of the analysis of the EXOSAT observations of SS Cyg presented in this chapter can be summarised as follows;

- In support of previous observations, it was found that there are two components to the x-ray emission, one typically with  $E > 1$  keV, the other with  $E < 1$  keV.
- The soft x-ray component is correlated with the optical emission through outburst, although onset of outburst is delayed by an interval of up to  $\sim 1$  day. Evidence that the rate of change of soft x-ray flux is faster than the corresponding changes in optical light has been presented, this applies to both outburst and decline.
- The hard x-ray emission is variable in optical quiescence, and is suppressed at outburst maximum. There is evidence that this component is bright in the post-outburst interval.
- The hard x-ray emission shows flaring of  $\pm 25\%$  on timescales of  $\sim 100$  sec. This variability is present in both the bright post outburst state and in quiescence.
- The spectrum of the post-outburst state is well modelled by a power-law continuum with photon index  $\approx 1.6$ . The presence of strong thermal emission lines of iron at 6.7 and 7.9 keV indicates that the x-ray production occurs in an optically thin medium with temperature  $kT \sim 10$  keV. It is likely that the power-law spectrum arises from a superposition of thermal bremsstrahlung components with a range of temperatures an emission measures.
- The soft x-ray component is strongly modulated at a period which decreases rapidly at the onset of outburst from  $\approx 11$  sec to limiting value at  $\approx 7$  sec, with  $\dot{P} \sim -10^{-4}$ . On the decline from outburst the  $\dot{P}$  increases from  $\sim$  a few  $10^{-6}$  up to  $\sim 10^{-5}$ . There is a strong negative correlation between the source flux and the oscillation period.
- The pulsed fraction of the oscillations varies from  $\sim 15\%$  at onset to a maximum of  $\sim 30\%$  which occurs after outburst maximum, returning to  $\sim 15\%$  again near the end of outburst.

- The phase behaviour of the oscillator suggests that the period jumps by discrete amounts of  $\Delta P \sim 0.01$  sec on timescales of a few  $10^3$  sec. The phase of oscillation is conserved in these jumps. During the stable period sections the phase wanders with  $Q \sim 50$  to a few 100.
- The model put forward by Córdova *et al.* (1984) is a poor representation of the phase behaviour. That model describes the random variability of the phase by a single parameter. To model the observed phase behaviour this parameter itself would have to vary at random, and so adoption of this model does not lead to a simplified description of the data.
- The cause of dwarf nova oscillations is still unclear. The evolution of period through outburst strongly suggests an association with a Keplerian orbit close to the white dwarf surface, but the nature of the modulating mechanism is unknown.

These observations also highlight the gaps in our knowledge of the behaviour of dwarf novae, and future observations should address the following questions:

- Are the soft x-ray pulsations common to all dwarf novae in outburst? Are they present in novalike variables? A survey at low x-ray energies at high time resolution is required.
- What is the relation between the optical and x-ray pulsations? Is the optical pulsation the tail end of a soft x-ray blackbody or is it reprocessed? Simultaneous optical/x-ray observations should allow phase shifts due to reprocessing to be measured. An interesting opportunity would be provided if UX UMa were found to be a soft x-ray pulsator. The optical pulsation undergoes a  $360^\circ$  phase shift through eclipse (Nather and Robinson, 1974) simultaneous observations could constrain the geometry of the reprocessing region strongly.
- A long term study of the hard x-ray component, combined with optical monitoring at a level slightly better than available through the AAVSO, should show whether the quiescent variability (which was not well monitored with EXOSAT) is associated with low level optical fluctuations. If not then it may be necessary to model the quiescent hard variability by accretion instabilities which are confined to the inner regions of the disc.
- Is there an x-ray banana loop? The present data give an incomplete picture of the frequency – intensity relationship. It is not clear if the maximum of the soft x-ray outburst coincides with the highest frequency, neither is it known if the declining and rising branches are separated.
- How does the phase of the oscillation vary in decline from outburst? The crude estimates of the coherence from the width of power spectrum peaks at the end of outburst suggest

an increase in the phase variability. More detailed observations are required to follow the oscillator behaviour before it reaches this stage.

- What is the spectrum of the soft component? The HEAO-1 spectra from which the 'black-body' model was derived was poorly determined. Further spectral measurements are essential in the EUV band.

There are still many unanswered questions about the properties of dwarf novae. It is clear that x-ray observations provide a valuable diagnostic of the accretion processes which occur in region where the accretion disc meets the white dwarf. The gross properties of this region are thought to be understood in terms of the dominant physical processes at different values of the accretion rate. The details have yet to be considered theoretically since the problems of understanding the gas dynamics in what is probably a highly turbulent boundary layer are formidable. The pulsation properties are tantalising, the idea of surface layers which are loosely coupled to the white dwarf or of a hypothetical modulation mechanism in a variable radius Keplerian orbit are easy to visualise. However, the transformation of these essentially rigid mechanical structures into self-consistent models of the gas flow has yet to be realised.

## Chapter 5

# The X-ray Pulsar 1E 2259+586

### 5.1 INTRODUCTION

In the study of low mass x-ray binaries it is difficult to estimate the age of the system with any degree of certainty. It is of particular interest then, if an LMXB is found within the remnant of the supernova which created the neutron star, since the time that has elapsed since the supernova explosion can be reasonably well determined. There are several cases in which the association of an isolated neutron star (observed as a radio pulsar) with a supernova remnant (SNR) is clear, the Crab nebula and pulsar perhaps being the best studied example. However, until 1983 there was only one unambiguous identification of a compact binary system with an associated SNR, this being the enigmatic x-ray source SS433 and the remnant W50 (see for example Begelman *et al.*, 1980, Watson *et al.*, 1983). In 1980, Gregory and Fahlman reported the discovery of a hemispherical SNR from an *Einstein* IPC image, designated G101.1-1.0, containing a point like x-ray source which was later named 1E 2259+586. At about the same time as these x-ray observations, Hughes *et al.* (1981) mapped the entire SNR at radio wavelengths (49 cm), although the northern part of the remnant had been detected previously as the non-thermal radio source CTB109 by Bolton and Wilson (1960).

A contour map of the IPC image is shown in figure 5.1, the eastern half of the remnant and the point source are clearly visible, whereas the western half appears to be missing. It was not initially clear if this morphology was intrinsic to the source or due to obscuration by clouds in the intervening interstellar medium. Also evident in the IPC image is a 'jet' of enhanced x-ray

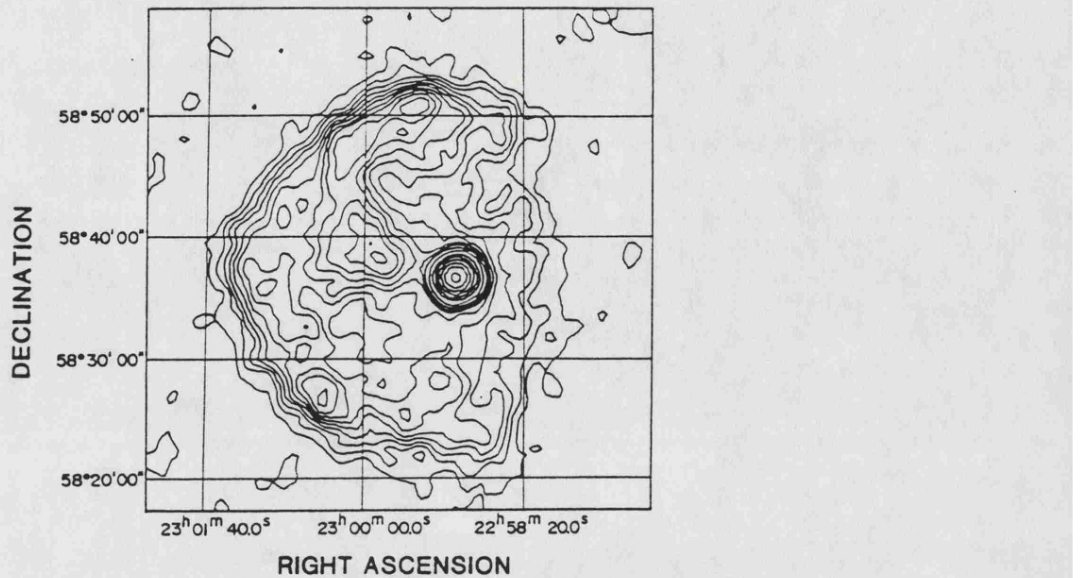


Figure 5.1: The *Einstein* IPC image of G109.1-1.0, from Gregory *et al.*, 1983.

emission which curves north-eastwards from the point source to the edge of the SNR shell. As a result a further *Einstein* observation, 1E 2259+586 was found to be a pulsar (Fahlman and Gregory, 1981), and an orbital period of 2300 sec was claimed by Fahlman and Gregory (1983). The pulse period was initially thought to be  $\approx 3.5$  sec, but after a more detailed analysis of the same data, Fahlman and Gregory (1983) showed that the pulse profile is double peaked with a true period of  $\approx 7$  sec. A *Tenma* observation made in 1983 revealed the pulsar to be slowing down at a rate  $\dot{P} \approx -5 \times 10^{-13}$  (Koyama *et al.*, 1987). Middleditch *et al.* (1983) reported a peak in the power spectrum of the light curve of a candidate IR counterpart to 1E 2259+586 at a frequency 1 mHz below the frequency of the second harmonic of the x-ray pulsation. This was attributed to reprocessing of x-rays by the secondary, with the period shift being consistent with that expected from the 2300 sec orbital period of the system. An orbital period of this magnitude would be of interest because it would be the second shortest measured for an LMXB, after 4U 1820-30 (Stella, Friedhorsky and White, 1987).

The orbital parameters given by Fahlman and Gregory (1983), were;

Orbital Period	$P_{orb} = 2300 \pm 90$ sec
Projected semi-major axis	$a_x \sin i = 190_{-30}^{+20}$ lt-msec
Eccentricity	$e = 0.30_{-0.15}^{+0.25}$

The SNR is also visible at centimetre radio wavelengths. The distance was estimated by Gregory and Fahlman (1980) and by Hughes *et al.* (1981) using the radio surface brightness arguments (see for instance Clark and Caswell, 1976), giving values of 3.7 and 4.7 kpc respectively. Gregory and Fahlman (1980) estimated the x-ray luminosity of the remnant at  $4.9 \times 10^{35}$  ergs  $s^{-1}$  and by applying a 'standard' theory of adiabatic shock waves (see for example Gorenstein and Tucker, 1976) estimated the age ( $\tau_{snr}$ ) of the SNR as  $\approx 1.2 \times 10^4$  yr, and explosion energy ( $E$ ) at  $3.8 \times 10^{50}$  ergs. Hughes *et al.* (1981) obtained values of  $\tau_{snr} \approx 1.7 \times 10^4$  yr and  $E \approx 7 \times 10^{50}$  ergs. A study of optical filaments in the SNR by Blair and Kirshner (1981) gave a significantly higher estimate of explosion energy  $E \approx 2.9 \times 10^{51}$  ergs. The 6 cm radio map of the region is shown in figure 5.2 with the IPC image overlaid. Also shown are the contours of  $C^{12}O$  emission given by Israel (1980), which indicate the presence to the west of 1E 2259+586 of a large molecular cloud complex. Interaction with these clouds was suggested by Heydari-Malayeri *et al.* (1981) as the reason for the hemispherical shape of the remnant. Recently, evidence for a physical interaction between the remnant and these clouds has come from a study of the IRAS maps of the region by Coe *et al.* 1989.

The most detailed study, to date, of the x-ray spectrum of 1E 2259+586 is that reporting an extended EXOSAT observation by Morini *et al.* (1988). The source has at least three distinct spectral components; the point-like pulsar, the diffuse SNR emission, and the jet feature. Morini *et al.* (1988) found that the combination of the SNR and jet emission could be reasonably well modelled by a thermal bremsstrahlung spectrum with  $kT \approx 0.9$  keV. Although these two components could not be separated in the EXOSAT ME data, it was concluded from LE observations using different filters that the jet emission is significantly softer than that from other parts of the SNR.

Unfortunately, the claimed orbital period of 1E 2259+586 has not been substantiated by further observations. As a result of the long EXOSAT observation, Hanson *et al.* (1988) found no evidence for orbital modulation in the pulse arrival times, and derived an upper limit ( $3\sigma$ ) of 170 lt-msec for  $a_x \sin i$  for  $2200 \text{ sec} < P_{orb} < 2300 \text{ sec}$ . Morini *et al.* (1988) using the same data, obtained a similar upper limit of 170 lt-msec, but at the  $2\sigma$  confidence level. A further search for photometric

modulation of candidate IR counterparts was conducted by Davies *et al.* (1989), who concluded that the result of Middleditch *et al.* (1983) was spurious.

This chapter reports an observation of 1E 2259+586 using the *Ginga* LAC, which had three objectives;

- The determination of pulse period ( $P$ ) at the present epoch to find  $\dot{P}$ .
- To search for orbital modulation in pulse arrival times.
- To study the energy spectrum of the mean and pulsed components of the source emission.

Given the lack of identifiable orbital period, the evidence for 1E 2259+586 being a binary system is reviewed.

## 5.2 OBSERVATION

The source was observed with *Ginga* during the P.V. phase of the mission, between 1987 June 21 09:46 and June 23 10:04 UT. The LAC was operated in all three spectral modes at both high and medium bit rates. Only the data used in the spectral analysis have been subject to full background modelling as described in section 2.4.1. In terms of the broad band behaviour, a reasonable estimate of the background for the entire observation has been produced by collaborators at ISAS, and the aspect corrected 1.0–4.6 keV and 4.6–9.3 keV light curves are shown in figure 5.3. The source variability is dominated by the pulse modulation, which is energy dependent and has a maximum value of  $\sim 40\%$ . On longer timescales the source shows relatively little variability, with changes of flux of  $\lesssim 10\%$  over a few hours (as can be seen in figure 5.3).

## 5.3 THE PULSE PROFILE

The mean pulse profile shows two asymmetric peaks separated by  $\sim 150^\circ$  in phase. At the time of the *Ginga* observation the peaks were of different amplitude. A mean pulse profile for the 1.8–3.5 keV range is shown in figure 5.4. The profile is similar to that observed with EXOSAT, *Tenma* and the second *Einstein* observation. The only evidence for a different pulse morphology comes from the first *Einstein* observation, in which the double peaks appear to be of similar height (see

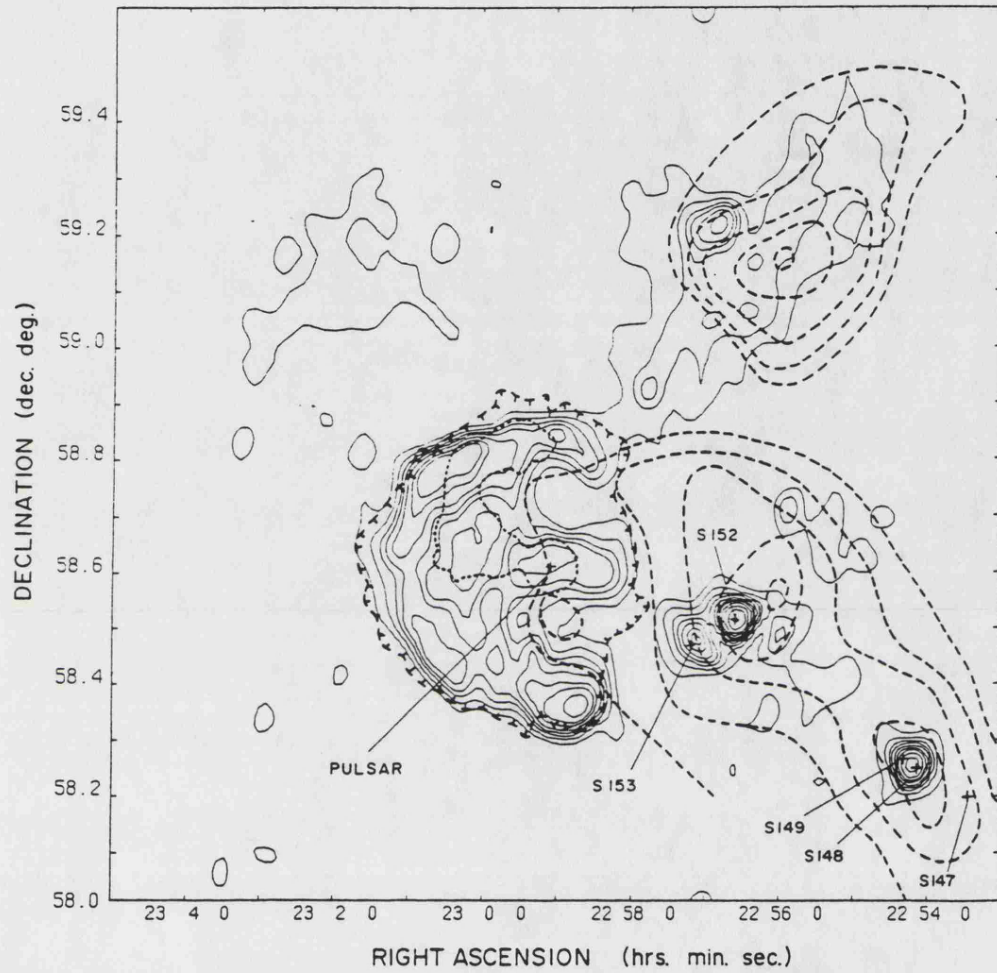


Figure 5.2: The 6-cm radio map of G109.1-1.0, with superposed x-ray (TTT and - - -) and CO emission contours (- - -) shown by dashed lines. From Gregory *et al.*, 1983.

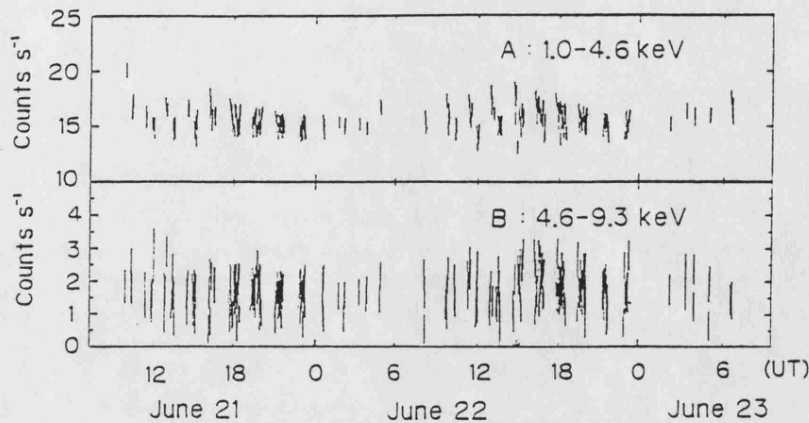


Figure 5.3: X-ray light curves of 1E 2259+586 from the *Ginga* observation of 1987 June 21–23.

Fahlman and Gregory, 1983, figure 1). The amplitude of the modulation is energy dependent, (see figure 5.5) rising from  $\sim 20\%$  at 1 keV to  $\sim 40\%$  at 5 keV.

## 5.4 THE ENERGY SPECTRUM

In order to obtain a background estimate at the level of accuracy required for spectral analysis, it was found necessary to select the data by more stringent background conditions than normally adopted. The data used were from the MPC1 and MPC2 spectral modes, and the cut-off threshold adopted for the SUD and COR parameters was lower than is normally adopted (see section 2.4.1), this gave  $\sim 9000$  sec of reliable spectral data from a total observation exposure time of  $\sim 36000$  sec. The pulsed component was isolated by subtraction of the phase minimum spectrum from that at phase maximum. Both spectra are shown in figure 5.6 in a PHA channel representation.

The most striking feature of the spectrum is that it is extremely soft, the best fit single power law has a photon index  $\alpha \approx 4.4$ , with column density  $N_H \approx 7 \times 10^{21} \text{ cm}^{-2}$ . The estimated 1–10 keV and 2–10 keV mean fluxes are estimated at  $\approx 7 \times 10^{-11} \text{ ergs s}^{-1} \text{ cm}^{-2}$  and  $\approx 2.4 \times 10^{-11} \text{ ergs s}^{-1} \text{ cm}^{-2}$  respectively. From the range of continuum models consisting of power law, thermal bremsstrahlung, blackbody, and exponential type spectra, all one and two component combinations were fitted to the data. The *Einstein* observations (Fahlman & Gregory, 1980) resolved separate emission components from the SNR and the pulsar, the former being significantly softer than the latter. Since the field of view of the LAC covers both regions it would be expected that at least

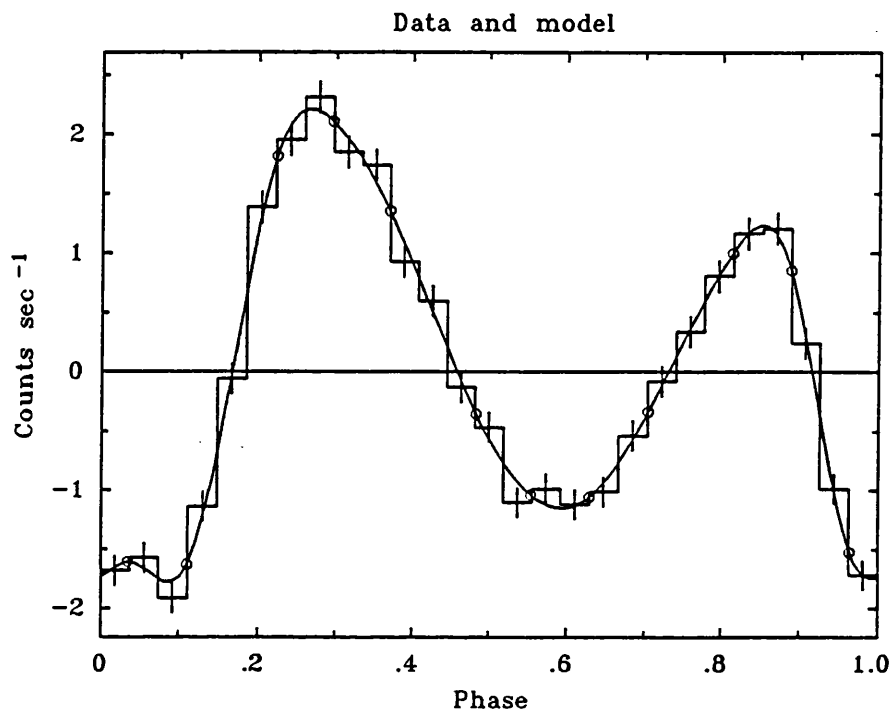


Figure 5.4: Pulse profile folded at the best fit heliocentric period with the fitted spline template (see text).

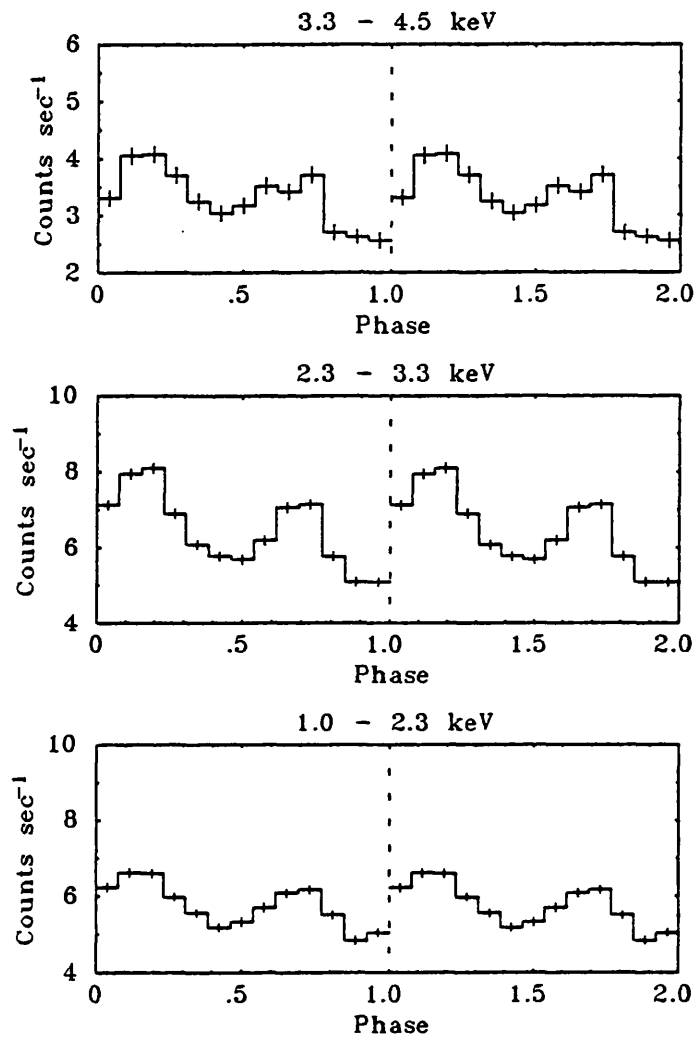


Figure 5.5: The pulse profile at three energy ranges. The profile is repeated once for clarity.

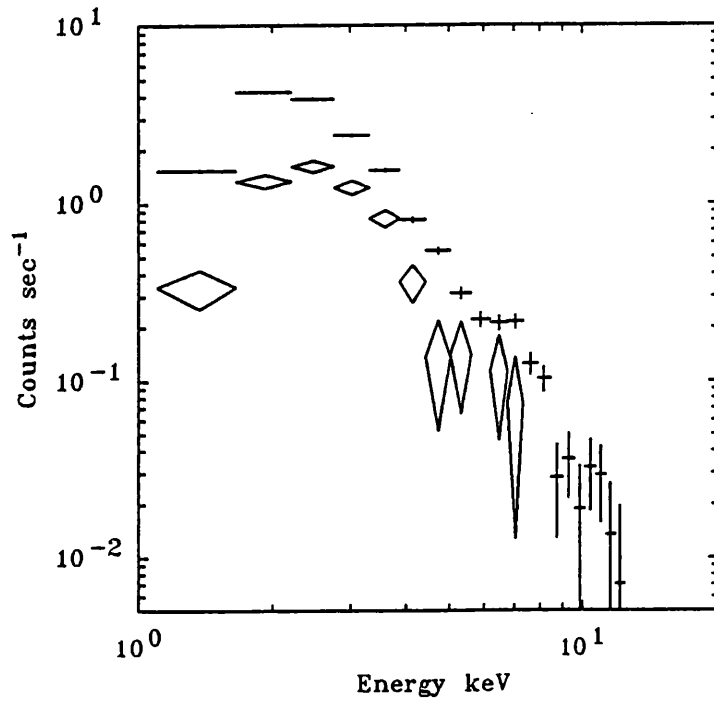


Figure 5.6: The pulse height spectra for the mean (error bars) and pulsed (diamonds) components.

a two component representation of the data would be necessary. It was found that no single or double component model provides a formally acceptable fit to the data ( $\chi^2_\nu > 6$ ) across the energy range 1–15 keV. However it was found that several models provide a similar, though formally unacceptable values of  $\chi^2_\nu$ . All of these cases reveal the presence of a broad ‘hump’ at  $\sim 7$  keV. Even taking this feature into account the fits are still unacceptable and inspection of the residual patterns indicate a large scatter from the best fit continuum rather than any systematic trends.

In order to parameterise the properties of the ‘hump’ feature, a restricted part of the spectrum (3–11 keV) was modelled using a power law and a Gaussian line. The best fit obtained has line energy, flux and width ( $\sigma$ ) of  $7.2 \pm 0.2$  keV,  $(1.1^{+2.3}_{-0.06}) \times 10^{-4}$  photons  $\text{cm}^{-2}\text{sec}^{-1}$  and  $0.6^{+0.8}_{-0.6}$  keV respectively (90% confidence limits), and is shown in figure 5.7. Although the model was formally unacceptable with  $\chi^2_\nu \approx 3$  (6 d.o.f.) it allows an estimate to be placed on the energy at which the feature occurs, from which it seems unlikely that the line is associated with  $K\alpha$  iron emission.

An acceptable fit ( $\chi^2_\nu \approx 1$ ) to the pulsed component spectrum can be obtained using any of the standard continuum models. The model parameters are not well constrained due to the relatively poor signal/noise of this spectrum. An example fit is illustrated in figure 5.8, which shows a thermal bremsstrahlung model. It is not clear if the 7.2 keV hump is present in the pulsed spectrum, although in all continuum fits there is evidence of an excess above 7 keV, this is only of marginal significance. The fluxes in the pulsed component are  $1.6 \times 10^{-11}$  ergs  $\text{s}^{-1} \text{cm}^{-2}$  and  $1.0 \times 10^{-11}$  ergs  $\text{s}^{-1} \text{cm}^{-2}$  in the 1–10 keV and 2–10 keV bands respectively.

As suggested by the pulse profiles in figure 5.5, the modulation depth is a function of energy. Inspection of the ratio of pulsed to mean spectrum, shows that the maximum modulation of about 40% occurs near 5 keV. The contribution of the SNR emission at low energies is at least in part responsible for the energy dependence of the modulation.

## 5.5 PULSE TIMING MEASUREMENT

The data that were used for the pulse timing analysis presented here were those obtained in the MPC2 spectral mode at high bit rate, and in the MPC3 mode at high and medium bit rate, giving time resolutions of 7.8 and 62.5 msec respectively. The energy range for these light curves was 1.8 to 3.5 keV, and the time series were accumulated at a resolution of 125 msec. The study of rapid time variability does not warrant the detailed background modelling described in section 2.4.1.

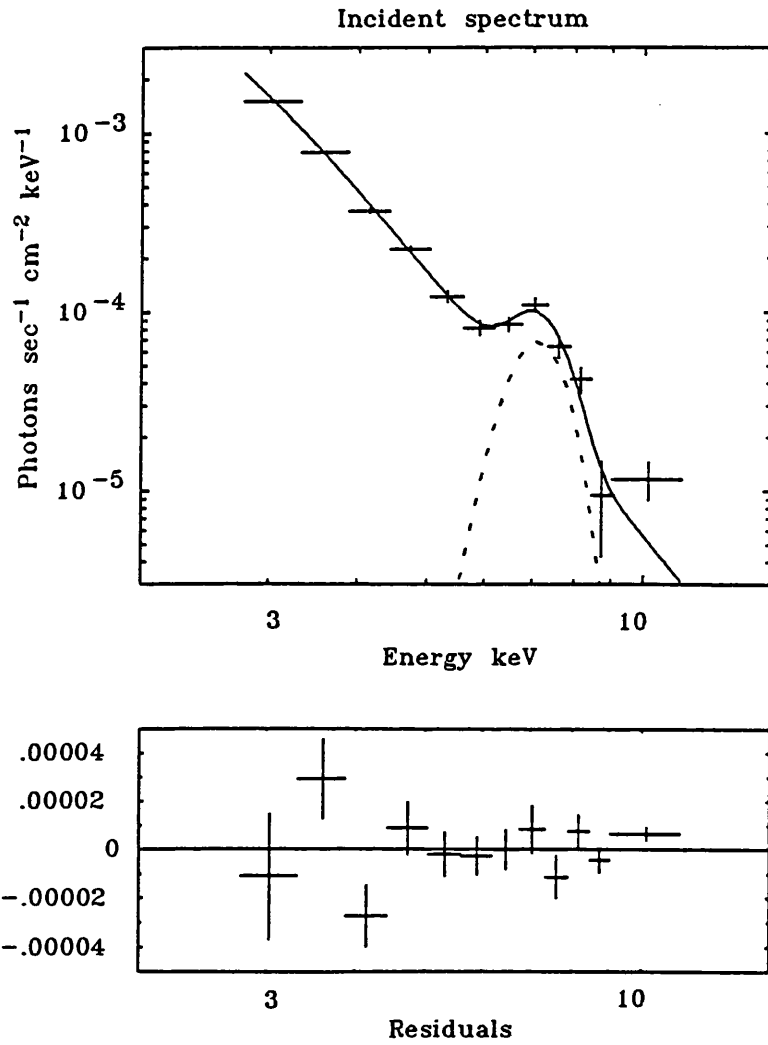


Figure 5.7: The best fit Gaussian model to the 7.2 keV feature, the continuum is represented by a power law ( $\alpha = 5.0^{+0.3}_{-1.2}$ ).

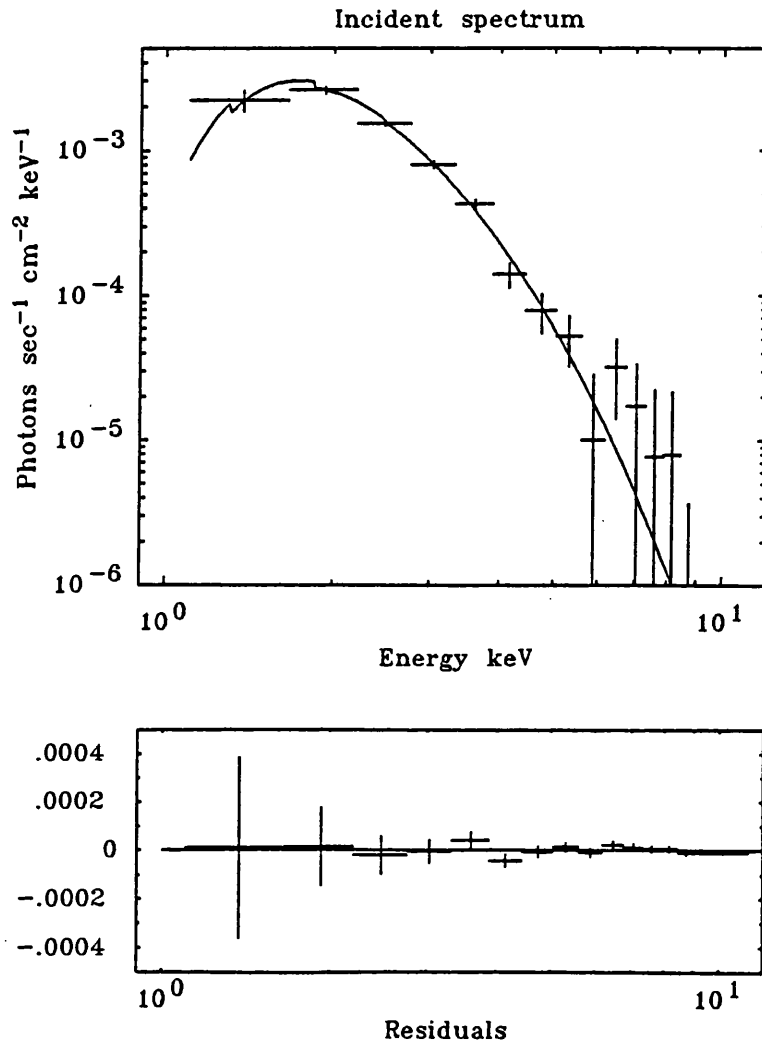


Figure 5.8: The best fit thermal bremsstrahlung model for the pulsed component of the emission. The best fit parameters are  $kT = (0.94^{+0.30}_{-0.23})$  keV and  $N_H = (20^{+16}_{-13}) \times 10^{21} \text{ cm}^{-2}$  and give  $\chi^2_\nu = 0.93$  for 12 d.o.f.

The initial analysis used the light-curve without any background subtraction, with the intention of detrending the data set on timescales longer than the pulse period, once the software for pulse timing measurement had been tested. For the non-detrended data, large flux changes were removed by applying an upper cut-off of 96 counts sec<sup>-1</sup> ( $\equiv$  12 counts per time bin). About 80% of the data were successfully detrended (using a cubic-spline fitting routine), but little difference could be discerned in the final results between the original and detrended data sets. It is the analysis of the non-detrended data which is presented here.

### 5.5.1 Period Determination

The initial estimate of period was made using the simple  $\chi^2$ -periodogram method on data in the satellite frame of reference. The time series was corrected to a heliocentric frame of reference, and consecutive short sections ( $\sim$  200 sec) of data were folded at the trial period. The resultant profile was fit by two independent sinusoids. This method gives two estimates of the arrival time (represented as a phase  $\phi_a$ ) for each section. It was found that due to the difference in peak heights that one set of arrival times had a smaller associated error than the other. From the resultant time series ( $\phi_a(t)$ ), the difference between trial and true period can be estimated using the approximation;

$$P_{true} \approx P_{trial} - 2\pi P_{true}^2 (\Delta\phi/\Delta t) \quad (5.1)$$

This approximation was repeated until  $\Delta\phi/\Delta t$  was consistent with being zero. Figure 5.9 illustrates this process, showing the better determined set of arrival times for a trial period and the best estimate of period, this being, with  $1\sigma$  error,

$$P = 6.978760 \pm 0.000003$$

This result forms the fifth measurement of period over a baseline of seven years. The pulse period history is summarised in table 5.1 and illustrated in figure 5.10. The best fit spin-down rate is  $\dot{P} = (-6.3 \pm 0.5) \times 10^{-13}$ . This is smaller than the value of  $(-7.4 \pm 0.5) \times 10^{-13}$  obtained by Hanson *et al.* (1988). The reduced  $\chi^2$  for the linear fit to  $P(t)$  is 1.96 for 3 d.o.f. and so the inclusion of a quadratic term is not justified by these data.

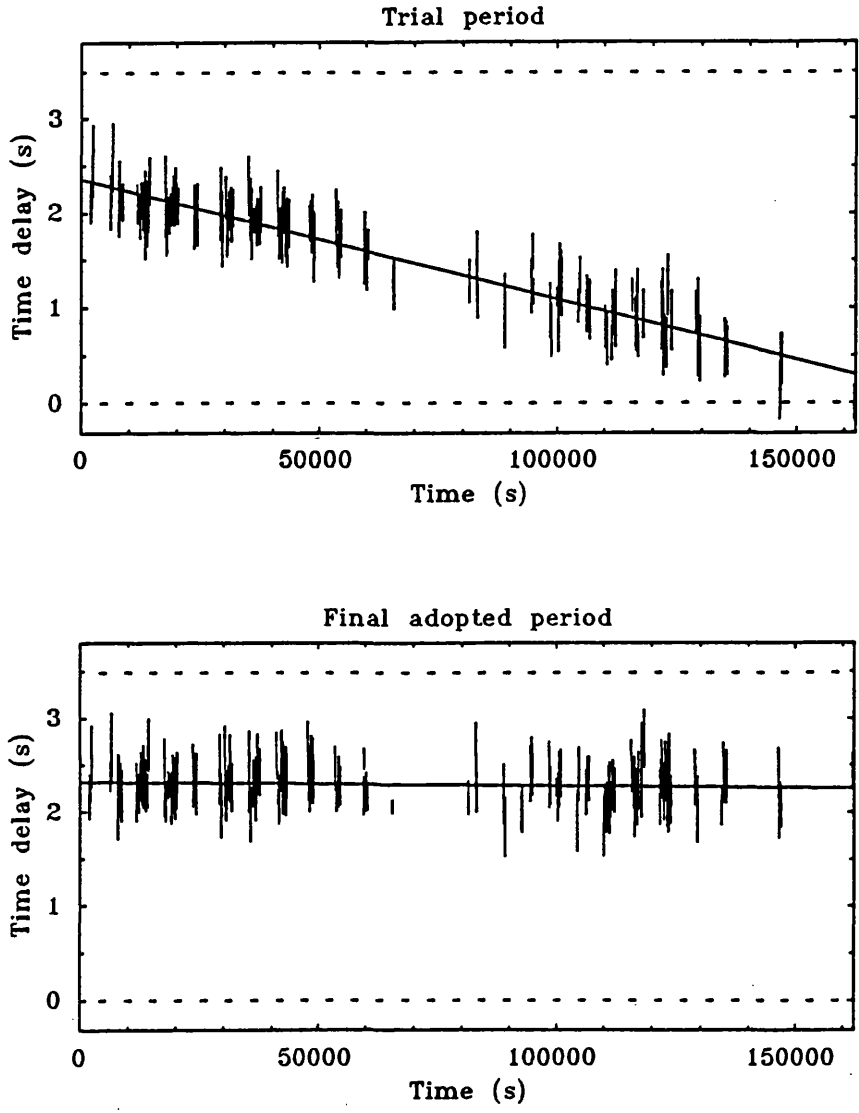


Figure 5.9: An example of the technique used for period determination. The upper panel shows the resultant set of pulse arrival times for a trial period, the lower panel shows the set at the final adopted period.

Table 5.1: Pulse period measurements for 1E 2259+586.

Date	Epoch JD - 2440000	Heliocentric Pulse period (sec)	Reference
1980 July 7	4398.5	$6.97864 \pm 0.00003$	1
1981 January 21-25	4629.0	$6.978620 \pm 0.000014$	1
1983 October 11-14	5620.0	$6.978675 \pm 0.000010$	2
1984 December 1-2	6036.0	$6.978720 \pm 0.000006$	3
1987 June 21-23	6968.9	$6.978760 \pm 0.000003$	4

References: 1 - Fahlman and Gregory 1983; 2 - Koyama, Hoshi and Inoue 1987; 3 - Hanson *et al.* 1988; 4 - This work.

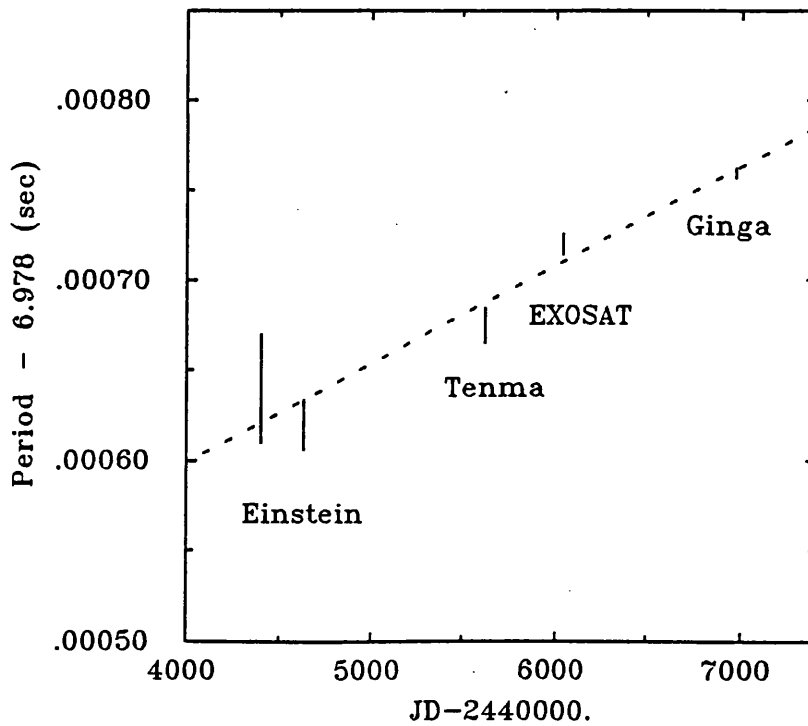


Figure 5.10: The pulse period history of 1E 2259+586.

### 5.5.2 The Search for Orbital Modulation

In searching the set of arrival times ( $\phi_a(t)$ ) for evidence of any orbital modulation the method of determining  $\phi_a(t)$  was improved over that described in section 5.5.1. Short sections of data, with duration  $\sim 120$  sec, were folded at the trial period and fitted to a master pulse profile. This technique has the advantage of being a much better representation of the pulse profile than a sinusoid, and utilises data from all phases of the fold rather than being restricted to half the phase, range which was the case in the above method.

The template profile was formed by folding the entire data set at the pulse period. The folded data were then fitted to a cubic spline to give a smooth representation of the pulse profile. The master pulse profile and the adopted spline fit are shown in figure 5.4. Note that the knot spacing is not uniform, but was chosen to obtain a good fit to the data at all phases using relatively few knots. Ideally the template function should be cyclic such that it has identical values at phase 0 and 1. Failure to satisfy this condition within the expected errors in the folded data could lead to systematic error in  $\phi_a(t)$ . The folded data were repeated over the phase range -1 to 2 before fitting the spline curve, but the template function accessed by the fitting routine used values only from the phase range 0-1. This approach gave a difference between the function at phases 0 and 1 which was smaller than the random error associated with a phase bin in a folded section by a factor  $> 100$ . In the fitting procedure the normalisation and phase of the template function were allowed to be free parameters, and only fits in which the normalisation was positive and significant at the  $2\sigma$  level were accepted in forming  $\phi_a(t)$ .

In application to the data, this process yielded 304 arrival times. To search for orbital modulation these arrival times were folded into five orbital phase bins. The choice of number of phase bins is somewhat arbitrary, being a trade-off between orbital resolution and signal/noise in the individual bins. However by adopting five phase bins a direct comparison may be made between these results and those given by Hanson *et al.* (1988). The data were folded across a trial period range of  $10^3$  to  $10^4$  sec, with the search being conducted in increments of half the separation of statistically independent periods (see section 2.6.3). Again similarly to Hanson *et al.* (1988) the trial folds were fitted to a sinusoidal function in order to estimate the projected semi-major axis  $a_x \sin i$ . Out of  $\sim 600$  trial periods about 60 appeared to be significant at the  $3\sigma$  level, much more than would be expected from a random distribution. On closer inspection however, it appeared that these periods correspond to cases in which the error in  $a_x \sin i$  ( $\sigma_a$ ) is particularly low ( $\sim 10$  msec), rather than  $a_x \sin i$  being particularly large. The distribution of  $\sigma_a$  is difficult to quantify, but it would seem

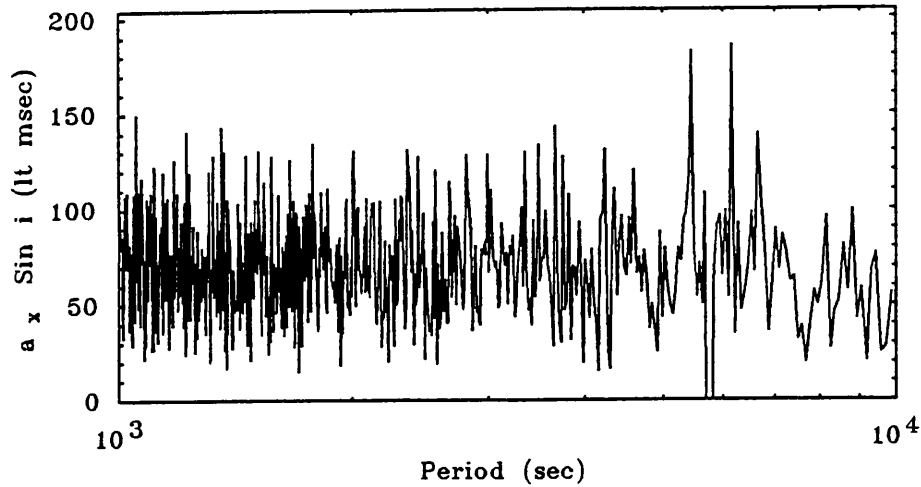


Figure 5.11: The  $3\sigma$  upper limit to  $a_x \sin i$  as determined from the *Ginga* data.

unwise to claim significance of any modulation which does not exceed the  $3\bar{\sigma}_a$  limit ( $\bar{\sigma}_a$  being the mean of  $\sigma_a$ , which is  $\approx 25$  msec in this case).

Given the lack of detectable orbital period, the  $3\sigma$  limit to  $a_x \sin i$  was calculated for the tested periods, this is illustrated in figure 5.11. In the range 1000–5000 sec the upper limit to modulation is  $\sim 150$  light msec. The gap and the large upper limits near 6000 sec are due to incomplete and poor phase coverage respectively, of periods near the satellite orbital period, and the  $3\sigma$  limit for the range 5000–10000 sec is  $\sim 200$  lt-msec. Of particular interest is the period range 2200–2400 sec which should contain the orbital period claimed by Fahlman and Gregory (1983) at  $P = 2300$  sec and  $a_x \sin i = 190$  lt-msec. This region of the periodogram is illustrated in figure 5.12. It can be seen that the  $3\sigma$  upper limit to modulation over this range is  $\sim 140$  lt-msec (c.f. the 170 lt-msec limit obtained by Hanson *et al.*, 1988). The lower limit to the semi-amplitude quoted by Fahlman and Gregory (1983) of 160 lt-msec, is excluded by these data at a confidence of  $> 99.95\%$ . A similar result was obtained by Hanson *et al.* (1988) although at a lower confidence limit. It would seem then that the claimed orbital period cannot be confirmed in later observations.

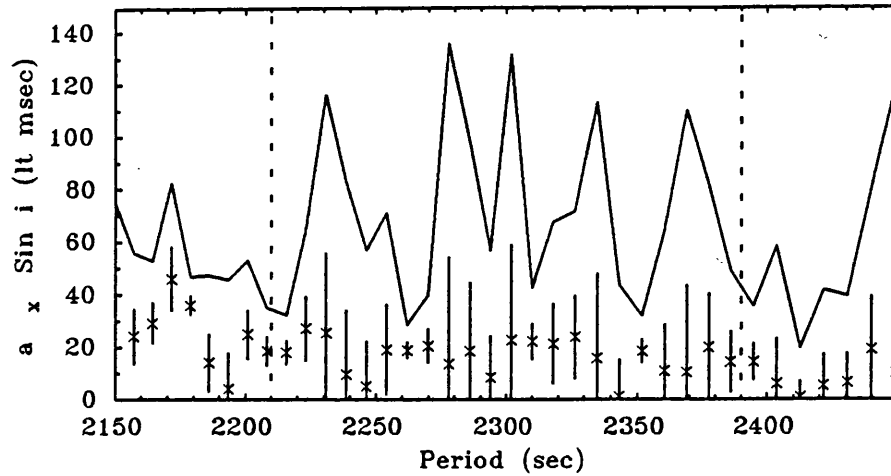


Figure 5.12: The fitted  $a_x \sin i$  values for the range covering the period claimed by Fahlman and Gregory (1983) of  $P_{orb} = 2300 \pm 90$  sec. The solid line indicates the  $3\sigma$  upper limit to the projected semi-amplitude.

## 5.6 DISCUSSION

There are three mechanisms which are commonly cited as being possible sources for the x-ray luminosity of 1E 2259+586, these being:

- a) Loss of rotational energy.
- b) Accretion from the local interstellar medium.
- c) Accretion from a binary companion.

Assuming that the distance to 1E 2259+586 is 3.7 kpc, the luminosities over the 1–10 keV range are  $1.1 \times 10^{35}$  ergs  $s^{-1}$  and  $2.5 \times 10^{34}$  ergs  $s^{-1}$  for the mean and pulsed components respectively.

In case (a) the maximum available luminosity is  $L_{rot} = 1/2 d(I\omega^2)/dt \approx I\omega\dot{\omega}$ . Given the above pulsed luminosity and the measure values of  $\omega$  and  $\dot{\omega}$ , the moment of inertia required by the compact star is,

$$I = \frac{L_{rot}}{\omega\dot{\omega}} \approx 3.6 \times 10^{47} \text{ g cm}^2 \quad (5.2)$$

The order of magnitude estimate for the moment of inertia of a  $1M_{\odot}$  neutron star is  $I \sim 10^{45} \text{ g cm}^2$ , and so is too small to provide the required luminosity. A  $1M_{\odot}$  white dwarf however has  $I \sim 10^{50} \text{ g cm}^2$ , and from this point of view is a viable mechanism. Morini *et al.* (1988) suggested this possibility, but stated that it would be unlikely that a white dwarf would be stable at such a high rotation rate.

The problem of determining the accretion rate onto a star from the local interstellar medium was discussed by Hoyle and Lyttleton (1939), and by Bondi (1952). A star of mass  $M$  which has a velocity  $v$  relative to a medium of density  $\rho$  will accrete mass from an approximately cylindrical volume of radius  $r_{acc}$  given by,

$$r_{acc} = \frac{2GM}{v^2 + c_s^2} \quad (5.3)$$

where  $c_s$  is the sound speed through the medium. The accretion rate is given by Bondi (1952) as;

$$\dot{M} \approx \frac{2\pi\alpha(GM)^2\rho}{(v^2 + c_s^2)^{3/2}} \quad (5.4)$$

where  $\alpha$  is a factor near unity. The accretion luminosity from a compact object of radius  $r$  is then;

$$L = \frac{2\pi(GM)^3\rho}{r(v^2 + c_s^2)^{3/2}} \quad (5.5)$$

It is convenient to express this in terms of the number density  $n$ ,

$$n \approx 2.9 \left[ \left( \frac{v}{\text{km s}^{-1}} \right)^2 + \left( \frac{c_s}{\text{km s}^{-1}} \right)^2 \right]^{3/2} r_6 M_1^{-3} L_{35} \quad (5.6)$$

It can be seen that the density required to give a specified luminosity will be a strong function of the greater of  $v$  or  $c_s$ . There are three cases of isolated accretion to be considered:

1. Accretion inside the SNR. In this case the dominant term in equation 5.6 will be the sound speed. Since the remnant shows x-ray emission at about 1 keV, the gas temperature is  $T \sim 10^7 \text{ K}$ . Using the relation  $c_s \sim 10(T/10^4\text{K}) \text{ km sec}^{-1}$  (Frank, King and Raine, 1985), the sound speed in the interior of the SNR is  $c_s \sim 300 \text{ km s}^{-1}$ . The density required to obtain the observed accretion luminosity is  $n \sim 10^8 \text{ cm}^{-3}$ , which is unrealistic for this environment, and this scenario may be rejected.
2. Accretion outside the visible shell of the SNR. Given that a recoil velocity may be imparted to the neutron star, this case assumes that the neutron star has managed to overtake the shock front. This scenario was originally investigated by Fahlman *et al.* (1982). The IPC image shows the remnant has a radius of  $\approx 15 \text{ pc}$  ( $d = 3.7 \text{ kpc}$ ). For an age of  $10^4 \text{ yr}$ , the required velocity is  $1500 \text{ km s}^{-1}$ . Not only is this a factor of three higher than the highest

observed random velocities in isolated pulsars (Manchester and Taylor, 1977), equation 5.6 implies  $n > 10^{10} \text{ cm}^{-3}$ , which again is implausibly large. A geometrical argument against this scenario is that the x-ray source is geometrically close to the centre of curvature of the remnant (see figure 5.1). There is only a 3% chance that the pulsar would have been scattered into the narrow range of solid angle required to give this projection.

3. Accretion outside an asymmetric SNR. Fahlman *et al.* (1982) noted that two observed features of the SNR may modify the above model; SNR is not spherically symmetric, and that there is evidence (Heydari-Malayeri *et al.*, 1981) that a molecular cloud complex may be penetrating the supernova cavity. The scenario in which the supernova exploded at the edge of a dense molecular cloud was implied, but not studied in any detail. This model will be considered further here.

Theoretical descriptions of the behaviour of a supernova explosion in a dense medium have been given by Shull (1980) and by Wheeler *et al.* (1980). The ‘standard’ theory of SNR expansion at typical interstellar densities is given by several authors, see for instance, Gorenstein and Tucker (1976). The major difference between the standard and high density models are that it is not clear if the latter evolves through an adiabatic expansion phase before reaching the so-called snowplough phase. Otherwise the predictions are similar. The shell radius is sensitive to the density of the medium, from Shull (1980);

$$r_{snr}(t) \approx 0.62 E_{51}^{3/14} n_5^{-2/7} t_4^{2/7} \text{ pc} \quad (5.7)$$

where  $t_4$  is the age of the SNR in units of  $10^4$  yr, and  $E_{51}$  is the supernova energy in units of  $10^{51}$  ergs.

To a first approximation a supernova occurring close to the edge of a molecular cloud could be treated using the standard solution for the expansion away from the cloud and the results of Shull (1980) to provide an estimate on the distance that the shock may propagate into the cloud. Thus from the standard theory, the age of  $10^4$  yr and energy of  $10^{51}$  ergs are still valid. It must also be assumed that the pulsar is ejected towards the cloud. Thus to overtake the shock front  $v_p > v_{crit}$ , where,

$$v_{crit} = r_{snr} t^{-1} = 60 t_4^{-9/4} E_{51}^{3/14} n_5^{-2/7} \text{ km s}^{-1} \quad (5.8)$$

Using equation 5.5 and noting that for a molecular cloud at  $T \sim 10$  K,  $c_s < 1 \text{ km s}^{-1}$ , the minimum density is then,

$$n_5 = 2.7 L_{35}^{7/13} E_{51}^{63/52} r_6^{7/3} M_1^{-21/13} t_4^{-15/13} \quad (5.9)$$

Given the uncertainties in the parameters then it seems plausible to obtain the required accretion luminosity by this mechanism provided that  $n \sim 10^5 \text{ cm}^{-3}$ .

There are of course observational constraints to this model. Although dense molecular clouds exist near to the pulsar (see figure 5.2), it is not clear if the density in the cloud behind the pulsar would reach the minimum required value. However the above scenario only demands that the cloud in which the supernova was embedded is of order of a few times larger than the typical distance that the shock front could travel into a dense medium, which is  $\sim$  a few parsec. Such cloud structure could easily be below the resolution of the CO maps of the region, which are at 8 arcmin resolution (Israel, 1980), which corresponds to  $\approx 9 \text{ pc}$  at  $d=3.7 \text{ kpc}$ . A further condition that must be satisfied is that the column density to the pulsar must be  $< 10^{22} \text{ cm}^{-2}$ . The maximum path length through a  $n = 10^5 \text{ cm}^{-3}$  region that the pulsar could have travelled is  $\sim 0.1 \text{ pc}$ . This would imply that the source escaped the SNR in about the last 500 yr.

As a final speculative note, Shull (1980) notes that a characteristic of SNR which occur close to the edge of clouds and at some point burst through the cloud boundary, will be the formation of a jet of hot gas collimated by the expansion of the remnant through a region of decreasing density. It is possible that the observed x-ray jet in 1E 2259+586 is the remnant of this feature.

It is not surprising that interacting binary model has gained general acceptance. As discussed in section 1.2.3 accretion luminosities of up to  $\sim 10^{38} \text{ ergs s}^{-1}$  can be produced by mass transfer in binaries containing a neutron star. There is no firmly identified optical counterpart to 1E 2259+586, the limiting magnitude is  $B \approx 21.3$  (Fahlman *et al.*, 1982). Adopting an interstellar reddening of  $A_B \approx 5$  (Fahlman *et al.*, 1982), and a distance of  $d = 3.7 \text{ kpc}$  (Fahlman and Gregory 1980) the absolute magnitude of any counterpart is  $M_B > 4$ . Thus a high mass binary scenario can be rejected, as can a low mass binary model in which the mass donor has evolved off the main-sequence. The limit on an optical counterpart suggests that the accretion disc (which is the dominant source of optical light in a LMXB) is very faint. Koyama *et al.* (1987) suggest that some models predict optically thin accretion discs at the mass transfer rates appropriate to this system ( $\dot{M} \sim 2 \times 10^{14} \text{ g s}^{-1}$ ).

If it is assumed that the neutron star mass  $\sim 1M_\odot$ , then in order for a low mass ( $< 1M_\odot$ ) main-sequence star to fill its Roche lobe, the orbital period must be less than  $\sim 12 \text{ hrs}$ . The period range  $10^3$  to  $4 \times 10^4 \text{ sec}$  (i.e. 0.3 to 11 hrs) has been searched to give a  $3\sigma$  limit on  $a_x \sin i$  of  $< 170 \text{ lt-msec}$  (this work and Hanson *et al.* 1988). Figure 5.13 shows the expected semi-major

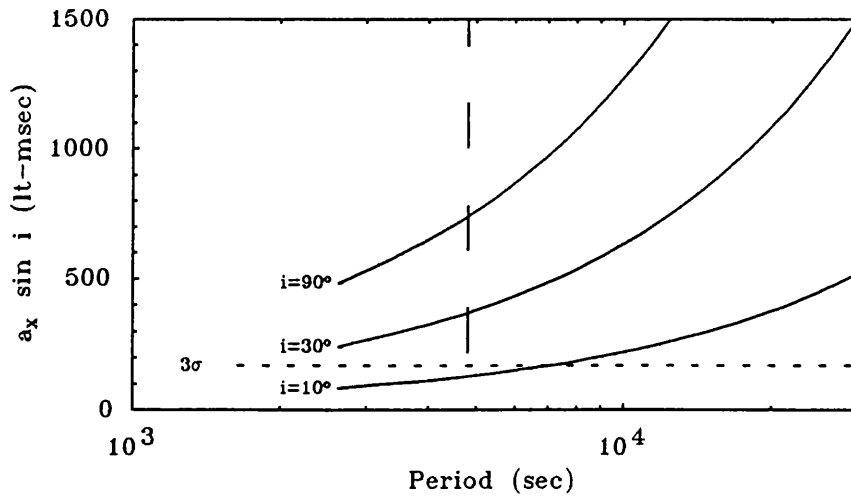


Figure 5.13: The expected projected semi-major amplitude for systems in which the mass donor is a main sequence star, assuming a  $1M_{\odot}$  neutron star, see text.

axis as a function of period for main sequence mass donors at three values of system inclination ( $i$ ). It can be seen that  $a_x \sin i$  increases with  $P_{orb}$ . The vertical dashed line indicates what has been argued is the minimum period for this type of system (see Paczyński and Sienkiewicz, 1981, and Rappaport *et al.*, 1983). The period of  $\sim 80$  mins represents the point at which the mass of the secondary becomes insufficient to sustain core hydrogen burning. Following any further loss of angular momentum, the secondary contracts to a degenerate configuration and mass transfer is terminated. At this minimum period a main sequence model for 1E 2259+586 would require that  $i < 14^\circ$ , a system orientation which has an *a priori* probability of occurrence of  $\sim 3\%$ .

The limit to  $a_x \sin i$  does not however, provide any useful constraint on the model in which the mass donor is a degenerate dwarf. Not only are the expected semi-amplitudes below 100 lt-msec, the expected orbital periods would be below the 1000 sec lower limit used here.

Other types of companion have been the object of much study, since it was believed that the system had an orbital period of  $\sim 2300$  sec, which is too large for a Roche lobe filling white dwarf. Two suggestions that have been considered in detail are a hydrogen deficient star (Nelson *et al.*, 1986), and a helium burning helium star (Savonije *et al.*, 1986). The periods at which core switch-off occurs in these models are  $\approx 50$  and  $\approx 10$  minutes respectively. These models have

found application to another LMXB containing a pulsar, 4U 1627-67 by Levine *et al.* (1988), in which case it was concluded that the hydrogen deficient star model seems more probable, since the helium burning star is expected to have an optical luminosity of  $\sim 30L_{\odot}$ . This constraint would almost certainly apply to 1E 2259+586 if the period is found to be in the range 10–80 minutes.

The present knowledge of the spin history of 1E 2259+586 can be summarised by stating that  $P \sim 7$  sec,  $\dot{P} \sim 6 \times 10^{-13}$  and that over the seven years of observation there is no evidence for a change in  $\dot{P}$ . The loss of angular momentum through dipole radiation is generally accepted to be the mechanism by which isolated pulsars spin down. From Gunn and Ostriker (1969) the spin down rate can be written as,

$$\dot{P}_{dipole} = \frac{8\pi\mu^2 \sin^2 \theta}{3Ic^3 P^2} \quad (5.10)$$

Where  $\mu$  is the magnetic moment of the neutron star, and  $\theta$  is the angle between the rotation and magnetic axes. Note that for a dipole field then,  $\mu = (1/2)Br^3$ , where  $B$  is the mean field strength at a radius  $r$ , Using the measured value of  $\dot{P}$  and reasonable estimates for other parameters, the implied magnetic moment is  $\mu \sim 3 \times 10^{32}$  g cm<sup>3</sup>. This is an order of magnitude higher than might be expected, but more significantly the pulsar would be expected to be a strong radio source, whereas in fact no radio pulsar counterpart exists (Fahlman and Gregory, 1981). Note that there is no need to assume the age of the pulsar or an initial pulse period, unlike the argument given by Koyama *et al.* (1987).

X-ray observations of pulsars in interacting binaries reveal more varied spin histories than those in isolated cases. Spin-up as well as spin-down can occur, and in some cases  $\dot{P}$  has been observed to change markedly on timescales of a few years. A theoretical understanding of secular variation in pulse period requires a knowledge of the mass transfer history and in particular the conditions at the point at which the accreting matter couples to the neutron star. Fortunately in the case relevant to 1E 2259+586, that of accretion through a disc is somewhat better understood than that in which the neutron star is fed by a stellar wind. By adopting a theoretical model for the interaction of the accreting matter with the magnetic field, the measured value of  $\dot{P}$  may be used to constrain the magnetic moment for the neutron star. The major uncertainties in the calculation are in the validity of the model and its sensitivity to the assumed neutron star parameters of mass, radius and moment of inertia. The methods used by Koyama *et al.* (1987) and Hanson *et al.* (1988) will be reviewed although no improved estimate of  $\mu$  over those previously published can be given.

If ionised gas falls, initially freely, onto a magnetised star, it will reach a region at which the magnetic pressure ( $P_{mag} \propto r^{-6}$ , for a dipole field) will exceed the ram pressure of that gas ( $P_{ram} \propto$

$r^{-5/2}$ ). Around the entire star these regions form the so called Alfvén surface, which approximately follows the field pattern. Restricting the discussion to regions away from the poles, this surface has a characteristic radius ( $r_A$ , the Alfvén radius), which is derived by equating  $P_{mag} = P_{ram}$ ,

$$\frac{4\pi\mu^2}{\mu_o 8\pi r_A^6} = \frac{(2GM)^{1/2} \dot{M}}{4\pi r_A^{5/2}} \quad (5.11)$$

where  $\mu$  is the magnetic moment of the star of mass  $M$  with accretion rate  $\dot{M}$ . Assuming the luminosity – accretion rate relation (equation 1.10), the Alfvén radius is more conveniently expressed as,

$$r_A = 2.9 \times 10^8 M_1^{1/7} R_6^{-2/7} L_{37}^{-2/7} \mu_{30}^{4/7} \text{ cm} \quad (5.12)$$

Since the Alfvén surface rotates with the star, the coupling between the compact object and the accretion disc will depend strongly on the velocity of the accreting gas relative to that of the surface itself. This is stated quantitatively as the ‘fastness parameter’  $\omega_s$  (Elsner and Lamb, 1979), which is defined as the ratio between the angular velocity of the star and the Keplerian angular velocity  $r_A$ . The co-rotation radius is that at which the Keplerian angular velocity is equal to that of the neutron star, it is given by,

$$r_{co} = \left( \frac{G}{2\pi^2} \right)^{1/3} P^{2/3} M^{1/3} = 1.89 \times 10^8 P_1^{2/3} M_1^{1/3} \text{ cm} \quad (5.13)$$

The fastness parameter may be expressed as,

$$\omega_s = \left( \frac{r_A}{r_{co}} \right)^{3/2} = 1.9 M_1^{-2/7} P^{-1} r_6^{-3/7} L_{37}^{-3/7} \mu_{30}^{6/7} \quad (5.14)$$

To a first approximation it may be expected that no torque acts on the magnetosphere when

$$r_a \sim r_{co} \quad (5.15)$$

This approach was adopted by Koyama *et al.* (1987), who suggested that since  $|\dot{P}|$  is small in comparison with other systems, 1E 2259+586 must be close to equilibrium. Combining equations 5.12 and 5.13 gives,

$$\mu_{30} = 0.48 P_1^{7/6} M_1^{1/3} R_6^{1/2} L_{37}^{1/2} \quad (5.16)$$

For the parameters appropriate for 1E 2259+586 it is found that  $\mu_{30} = 0.47$  ( $B_s = 5 \times 10^{11}$  G).

A more detailed theoretical study of the disc magnetosphere interaction was provided by Ghosh and Lamb (1978 and 1979a,b). A summary of these papers was given by Heinrichs (1983), from which much of the following was adapted. The torque at the Alfvén surface, which in the simple case is,

$$I\dot{\Omega} = \dot{M}l \equiv N_0 \quad (5.17)$$

where  $\Omega$  is the angular velocity of the Alfvén surface and  $l$  is the specific angular momentum of accreting material, is now modified by a dimensionless torque  $n$  which is a function of the fastness parameter, such that

$$I\dot{\Omega} = N_0 n(\omega_s) \quad (5.18)$$

The form of  $n(\omega_s)$  is determined by the model adopted for the system. Ghosh and Lamb (1979) produced a numerical solution to  $n(\omega_s)$  for a Shakura–Sunyaev type disc but including magnetic coupling. The rate of change of period in this model is (Heinrichs, 1983),

$$-\dot{P} = 1.86 \times 10^{-12} \mu_{30}^{2/7} M_1^{-3/7} R_6^{6/7} I_{45}^{-1} P^2 L_{37}^{6/7} n(\omega_s) \quad (5.19)$$

The numerical solution for  $n(\omega)$  is illustrated in figure 5.14. The system is in equilibrium when the net torque on the magnetosphere is zero and the period is constant. It can be seen that in this case an equilibrium condition exists ( $n(\omega_s) = 0$ ), and that this occurs at the critical value of fastness parameter  $\omega_c \approx 0.35$ . Hanson *et al.* (1988) applied the Ghosh and Lamb model to 1E 2259+586 by solving equations 5.14 and 5.19 for  $\mu$  and  $r_A$  using the numerical form of  $n(\omega_s)$ . It was found that for assumed values of  $M_1 = 1.3$  and  $r_6 = 1.5$ , that  $\mu_{30} = 0.5$  ( $B = 2.5 \times 10^{12}$  G) and that for  $M_1 = 1.0$ ,  $r_6 = 1.0$ , that  $\mu_{30} = 1.3$  ( $B = 6.4 \times 10^{11}$  G). The sensitivity to the adopted model was also discussed by Hanson *et al.* (1988), and as a comparison they calculated the field strengths implied by an analysis of the magnetosphere interaction provided by Wang (1987). In this case it was found that  $\mu_{30} = 1.5$  to 4.0 ( $B = 7.6$  to  $20 \times 10^{11}$  G) for the same range of neutron star parameters as adopted above.

Returning briefly to the isolated pulsar model, the detailed spin history of the pulsar would be difficult to determine since it could depend strongly on the coupling with the magnetosphere in the polar regions. However, unlike the case of wind accretion in a high mass system, the isolated case can only undergo spin-down.

The spectrum of 1E 2259+586 is softer than that seen in any other x-ray pulsar (see White *et al.*, 1983) for a review. The evidence from the EXOSAT observation reported by Morini *et al.* (1988), is that the SNR emits as an optically thin plasma with a temperature of  $\lesssim 1$  keV, and so is unlikely to give rise to the excess observed near 7 keV. This implies that the ‘hump’ is actually associated with emission from the compact object, although it should be admitted that evidence for its existence in the pulsed component is marginal. Such features have been observed in other four other pulsars. Her X-1 (Trümper *et al.*, 1978, and Voges *et al.* 1982), shows narrow features at energies of between 40–60 keV and around 110 keV on a steep continuum. The accepted interpretation is that the features are the fundamental and first harmonic of the cyclotron line.

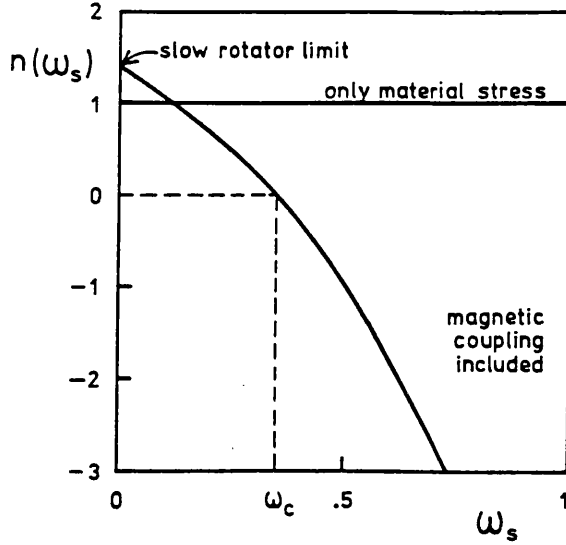


Figure 5.14: The dimensionless torque  $n(\omega_s)$  as a function of the fastness parameter  $\omega_s$ . The net torque on the magnetosphere is zero when  $n(\omega_s) = 0$ . This occurs at a critical fastness  $\omega_c$ , which, in the Ghosh and Lamb model for disk-magnetosphere interaction is  $\approx 0.35$ . From Heinrichs (1983).

Determining whether the lines are in absorption or emission has not been possible in Her X-1 since the continuum is not well defined. Another case is 4U 0115+63 (Wheaton *et al.*, 1978, and White *et al.* 1983), which shows features at 11.5 and 23 keV which are pulse phase dependent. Recent results from *Ginga* observations reported by Nagase (1989), have revealed cyclotron features in the spectra of two further sources, 4U 1538-52 and V 0332+53.

The characteristic frequency of electrons spiraling in a magnetic field is  $\nu_{cyc} = eB/2\pi m_e c$ , such that the photon energy is,

$$h\nu_{cyc} = E_{cyc} \approx 12 B_{12} \text{ keV} \quad (5.20)$$

The distribution between power in successive harmonics is  $P_{n+1}/P_n \approx (v/c)^2$ , where  $v$  is the electron velocity, and so the fundamental will dominate the cyclotron features in the spectrum. Similarly to the case in Her X-1, the steep continuum in the vicinity of the feature results in an ambiguity determining whether the line is in emission at  $\sim 7$  keV or absorption at  $\sim 6$  keV. Although it seems likely that the observed feature lies at the fundamental cyclotron frequency, it is possible that the fundamental could be masked by the steep continuum, and that the observed line is in fact at the first harmonic of the cyclotron frequency, in which case  $E_c \sim 3-3.5$  keV. Assuming that the 7.2 keV line is the fundamental, the field strengths implied by equation 5.20

are  $B \approx 5 \times 10^{11}$  and  $6 \times 10^{11}$  G for interpretation as emission and absorption respectively, and half these values if the feature is the first harmonic.

Variation of the pulse profile with energy is seen below  $E_c$ , the cyclotron energy, in Her X-1 (Trümper *et al.*, 1978) and 4U 0115+63 (Wheaton *et al.*, 1978). Numerical studies of this effect (e.g. Nagel 1981, Kii *et al.* 1986) reveal that pulse changes occur well below the cyclotron energy at about 0.1 to 0.25  $E_c$ . The fact that 1E 2259+586 shows no such profile changes over the range 1–15 keV is then consistent with a value of  $E_c \sim 7$  keV. Even if the 7 keV feature does not prove to be related to cyclotron emission, the simple nature and energy independence of the pulse profile suggest that the neutron star has a weaker magnetic field than is typical for x-ray pulsars (White *et al.* 1983).

The evolutionary scenario of 1E 2259+586 is as yet unclear, and remains a matter for speculation until the mass donor can be identified. Since the binary model for 1E 2259+586 is generally accepted, most evolutionary schemes to date have included accretion induced collapse of a white dwarf as the mechanism for the supernova. Fahlman and Gregory (1983) argued that the orbital separation would increase after the explosion, and as the present orbital configuration is too small to contain a high mass star, then the pre-supernova binary could not contain one either.

Any valid model must explain how the pulsar has the properties observed, given that any changes must have occurred over a period of  $\sim 10^4$  yr. The magnitude of the period is much larger than the 0.1–0.01 sec currently thought to be appropriate for young pulsars. At these very short rotation periods the magnetosphere-disc interaction model would predict that the magnitude of the spin-down would be much greater than at present. Lipunov and Postnov (1986) argue that the time scale for this process is  $\sim 10^5$  yr. As an alternative they propose that the progenitor of the system may have been an AM Her type system, such that the spin angular momentum of the white dwarf was much lower than would normally be expected. Koyama *et al.* (1987) pointed out that this model is unlikely since it assumes that the white dwarf has a moment of inertia of two orders of magnitude less than typically expected. It is not clear if the inferred low magnetic field is anomalous for a young pulsar. Field decay is thought to take place on timescales  $\sim 10^7$  yr (Lyne *et al.*, 1985), and would seem unlikely to have occurred in this object.

Another timescale problem that has received little attention is that of circularisation of the orbit. It is generally accepted that the binary orbit will become eccentric after the explosion. If the orbit is presently eccentric, then it is likely that the mass transfer rate would vary dramatically with orbital phase. As yet no evidence for large variations in luminosity have been observed on timescales from

the pulsar period up to several years. An eccentric orbit scenario could be viable however, if the mass transport time through the accretion disc is much longer than the orbital period, such that the modulation becomes smoothed out by viscous processes in the disc. The alternative model is one in which the orbit has circularised on a short timescale ( $\sim 10^4$  yr). Measurement of the orbital parameters of the system may show which of these models is correct and allow estimates to be made on either the viscous or the circularisation timescales.

## 5.7 SUMMARY

Direct evidence for 1E 2259+586 being a component of a binary system has not been found. The orbital parameters given by Fahlman and Gregory (1983) can be rejected with a confidence level of  $> 99.95\%$ . Circumstantial evidence would seem to support the binary hypothesis, although given certain conditions the source luminosity and observed spin-down could be explained by accretion onto an isolated pulsar. The magnetic field would appear to be  $B \sim \text{few } 10^{11}$  G, based on the pulse profile behaviour with energy and the tentative identification of a cyclotron feature in the pulsar spectrum. The pulse period is consistent with being near the equilibrium value for a neutron star with this magnitude magnetic field. The binary companion is unlikely to be a main sequence dwarf, but no other constraints on the nature of the star exist at present.

## Chapter 6

# Vertical Structure in Accretion Discs

### 6.1 INTRODUCTION

As an introduction to the observations of the LMXB sources to be presented in chapter 7, the nature of orbital modulation, and in particular so-called dipping behaviour, in this class of object is reviewed. Along with the accretion disc corona (ADC) sources, the dipping LMXB (or dip sources) provide evidence for non-axisymmetric vertical structure in accretion discs. The ADC sources allow the global structure of these systems to be determined, although at present, theoretical models for thickened discs are not well developed. The dip sources provide a means of investigating the properties of material in this vertical structure.

### 6.2 ORBITAL MODULATION IN LMXB SYSTEMS

A problem which was addressed by Milgrom in 1978 concerned the lack of eclipses in the bright galactic x-ray sources. Given a simple interacting binary model in which mass transfer takes place by Roche lobe overflow, forming a thin accretion disc around the neutron star, it would be expected (for binary components of equal mass) that about 15% of such systems would be eclipsing. This model clearly could not be supported by observation, and Milgrom suggested that

the lack of eclipses arises from the accretion disc having sufficient vertical (i.e. out of the orbital plane of the binary) extent to shield the secondary from the x-ray emission. The relative number of eclipsing systems then depends on the angle subtended by a thickened disc at the neutron star, and obviously, for thick enough discs none would ever be detected.

Not only were there no detections of eclipses (apart from the pulsar system Her X-1), there was little other direct evidence for these systems being binaries. By the early 1980s however, the advent of CCD detectors for faint optical photometry and the launch of sensitive x-ray observatories such as *Einstein* and EXOSAT saw several discoveries of orbital modulation in LMXB. Typically the optical modulation was found to be quasi-sinusoidal with full amplitude  $\sim 1$  mag. Examples of this modulation for three LMXB are given in figure 6.1. Note that the minima are V shaped and that there is a tendency for the profiles to be asymmetric.

The x-ray modulation falls into three categories; erratic dips in intensity, quasi-sinusoidal variability, and eclipses. Both partial and total eclipses were expected signatures, but neither are observed without one of the two other types of modulation. Dip modulation is characterised by recurrent intervals during which the source flux can decline rapidly and erratically (see figure 6.2), suggesting the occultation of a compact x-ray source by an irregular distribution of matter. The smooth modulation (see figure 6.3), which has only been unambiguously observed in a three sources (X 1822-371, XBT 2129-470, and X 0921-630, see e.g. Mason, 1989) suggests partial occultation or changing aspect of an extended x-ray source. The two forms of modulation appear to be mutually exclusive, furthermore the eclipses in dip sources are total, whereas in the smoothly modulated cases the eclipses are partial, which again supports the notion that different size x-ray regions are involved.

The model that has gained general acceptance is one which attributes both types of modulation to non-axisymmetric azimuthal structure associated with the accretion disc or accretion flow situated above the plane of binary. The difference between dips and smooth modulation arises from the angle of inclination at which the system is viewed, as is illustrated in figure 6.4. At very high inclination the compact x-ray source is completely hidden from direct view by the finite thickness of the accretion disc. X-rays are however scattered into the line of sight by an extended corona around the compact object, this is termed an accretion disc corona (ADC). The emission from the ADC is smoothly modulated by the azimuthal disc structure, as well being partially eclipsed by the primary. When viewed from a slightly lower inclination the point-like x-ray source becomes directly visible, and the modulation is erratic, now being sensitive to fine structure in the obscuring medium. At these inclinations eclipses need not necessarily be visible if the azimuthal disc structure

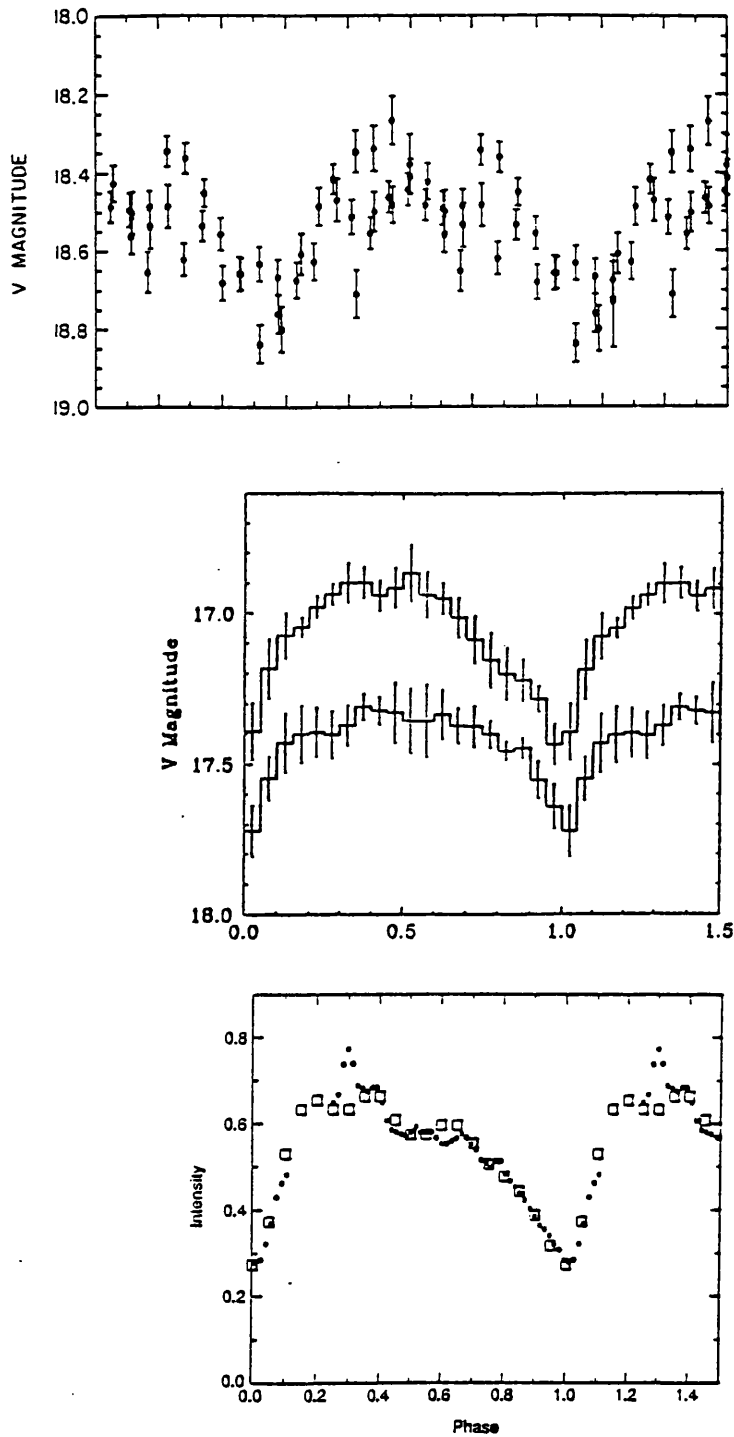


Figure 6.1: The folded optical light curves for three LMXB sources. The top and middle panels are from dip sources (X 1755-338 and XBT 0748-676 respectively) and the lower panel is from an ADC source (X 1822-371) and can be seen to have similar features. Note the asymmetric profile and the V shaped minima. From Mason, Parmar and White (1985), Motch *et al.* (1989) and Hellier and Mason (1989).

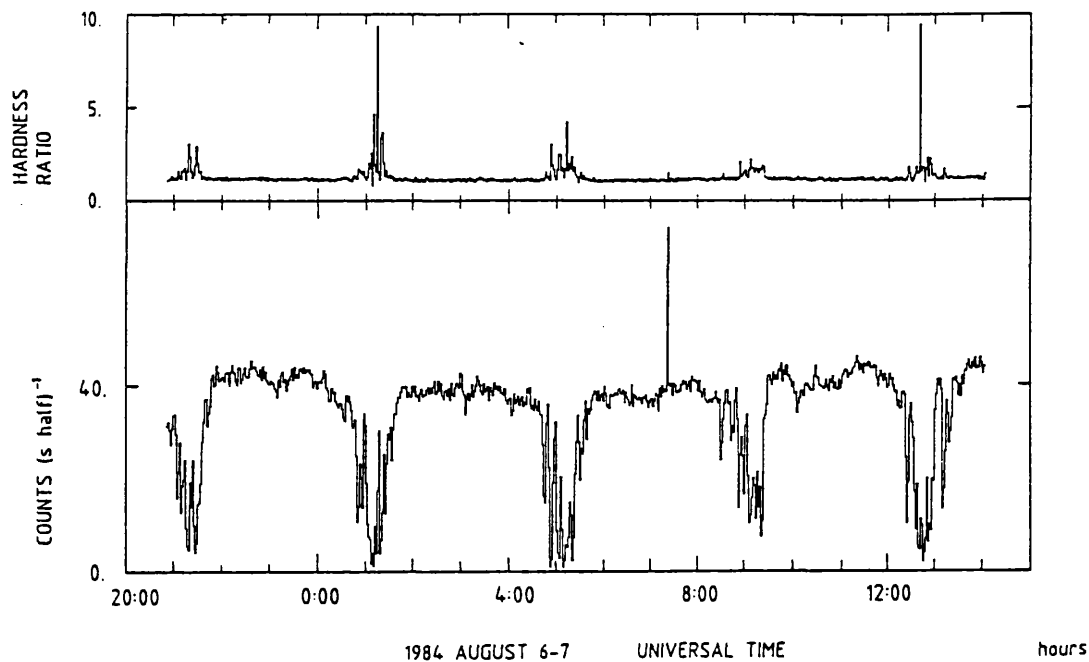


Figure 6.2: The EXOSAT ME (1–10 keV) light curve of the dip source XB 1254-690, with the hardness ratio ((3.5-10 keV)/(1-3.5 keV)) plotted at a time resolution of 2 mins. The dips are separated by  $3.88 \pm 0.15$  hr but do not repeat exactly from cycle to cycle. The source does not show eclipses. A burst can be seen at 07:22 UT. From Courvoisier *et al.* (1986).

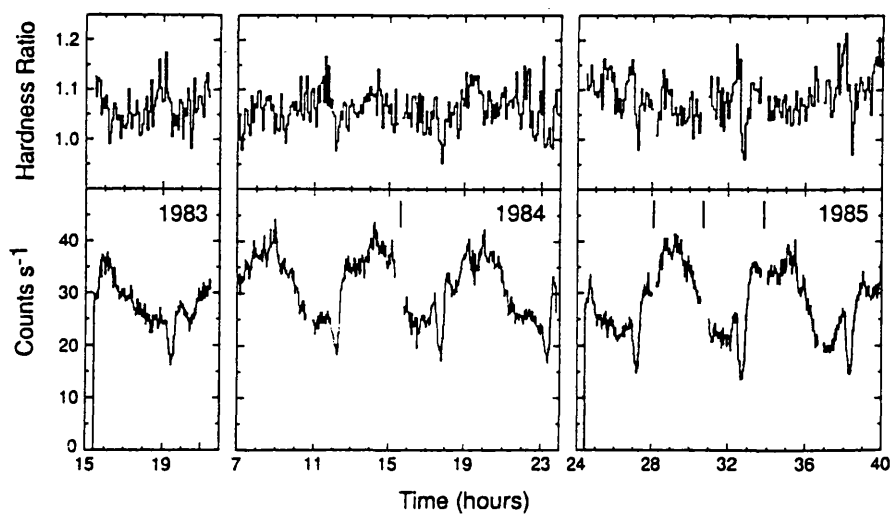


Figure 6.3: The EXOSAT light curves of the ADC source X 1822-371. The smooth, quasi-sinusoidal modulation is evident along with partial eclipses. The orbital period of this system is 5.57 hr. From Hellier and Mason (1989).

has a greater angular extent than the companion star. Support for this interpretation comes from the ratio of x-ray to optical fluxes for the two classes of object. If the ADC is optically thin then the x-ray luminosity of these sources will be much lower than those in which the x-ray source is viewed directly. However, the optical luminosity of both types of object is likely to be similar because the visible emission comes primarily from the heated surfaces of the accretion disc and the secondary. Observationally it has been found that  $L_x/L_{opt} \sim 1 - 20$  for ADC sources, but is  $\sim 100 - 1000$  for dip sources (Mason 1986).

The possibility that some sources may undergo transition between ADC and dip types has been suggested by several authors (e.g. Parmar *et al.*, 1985, Vrtilik *et al.*, 1986, Cominsky and Wood, 1989) to explain the transient nature of some sources. Such a transition would involve a change on the disc structure which need not necessarily be large. Given that the mechanism behind vertical structure in discs is so poorly understood there are no severe objections to this type of change. The best observational evidence for such transitions is in the periodic high and low state behaviour of Her X-1. During an extended low state in 1983, the source modulation was found to have changed from the characteristic dip variability of the high state to a smooth ADC like modulation (Parmar *et al.*, 1985).

### 6.3 DIP SOURCES

The first measurement of an orbital period from the recurrence of dips in an x-ray light curve was reported by White and Swank (1982) for *Einstein* and *OSO-8* observations of XB 1916-053. Since then, seven confirmed and two suspected dip sources have been found. Of these ten sources, three are eclipsing and seven have optical counterparts which show photometric modulation.

Dip activity varies considerably between sources. The maximum depth of dips ranges from  $\sim 20\%$  to  $\sim 100\%$  of the 2-6 keV flux. The duty cycle of the dips varies from  $< 10\%$  to  $> 50\%$  of the orbital period. As well as the differences between sources there is considerable intrinsic variability in dip morphology, with duty cycle and maximum depth varying on timescales as short as one orbital period. In addition to the main period of dip activity (the primary dips), two sources exhibit so-called secondary dips which are  $\sim 180^\circ$  out of phase with the primary dips.

In general, the dips are associated with a spectral hardening which is broadly consistent with the idea that the dips arise from photo-electric absorption by the intervening medium, although, as

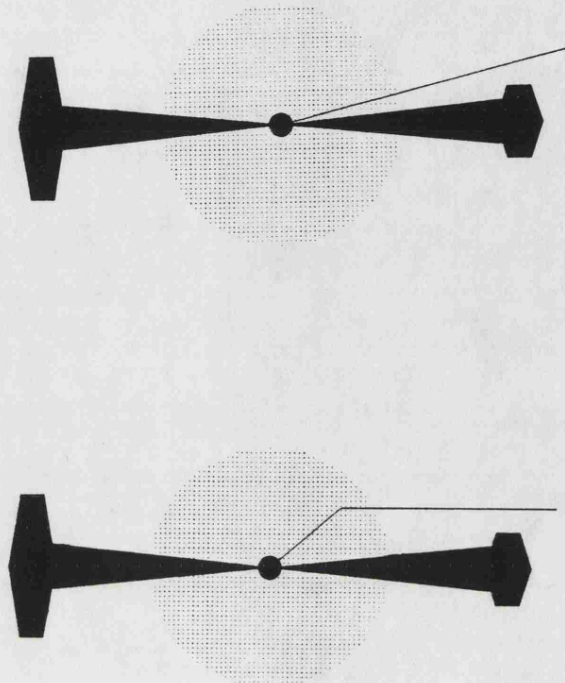


Figure 6.4: Schematic illustration of a cross section through dip (upper) and ADC (lower) sources. The systems are identical in structure, both having a thickened accretion disc and a corona around the central x-ray source. Dips are caused by occultation of the compact source by the vertical structure. In the ADC source only x-rays scattered into the line of sight are seen. The smooth modulation arises from the partial obscuration of this extended region of emission. Note that the mass donating star has been omitted for clarity.

will be discussed in chapter 7, the spectral changes are not well modelled by simple absorption of the source spectrum. Analysis of the spectral changes associated with dip activity allows an estimate to be made of the metal abundance associated with dip transitions. Again a wide range of metallicities has been reported, with most sources having near solar abundances, but two cases show lower limits to metal abundance of being  $< 1/100$  that of solar composition material.

As there are relatively few dip sources it is worthwhile to review them individually in order illustrate the range of properties exhibited by this class of object. Of particular interest however are the three sources which are the subject of chapter 7, these being XB 1915-053, XBT 0748-676, and X 1624-490. Previous reviews of this type have been given by Mason (1986) and by Parmar and White (1989). A summary of the properties of all reported dip sources is provided in table 6.1. Note that in most cases the convention that has been adopted for source names is the co-ordinate name prefixed by X, then B for sources showing type I bursts, and T for transient sources. Throughout the following work, the term 'quiescent' will be used to describe the non-dipping non-bursting state of emission.

#### **XB 1916-053 P=0.83 hr**

With a short orbital period of  $\sim 50$  mins (White & Swank, 1982), changes in dip morphology on timescales as short as a few orbital cycles are readily apparent in this source. Within intervals of dip activity, the maximum observed dip modulation can change from  $\sim 20\%$  to  $100\%$  in a few hours, and secondary dips are sometimes present. The source was the subject of three EXOSAT observations, these have been reported in detail by Smale *et al.* (1988). For those observations the 2-10 keV flux was typically  $\sim 6 \times 10^{-10}$  ergs sec $^{-1}$  cm $^{-2}$ , and the spectrum over this range was well modelled by a power law with  $\alpha \approx 1.9$  and  $N_H \sim 2 \times 10^{21}$  cm $^{-2}$ . Analysis of the type I bursts suggest a distance of 8.4-10.8 kpc and so  $L_x \sim 0.8 \times 10^{37}(d/10.8\text{kpc})^2$ . The metal abundance was given as a factor  $3 \pm 2$  (90% confidence) below solar. There is some evidence for a long term variability in data from the *Vela 5b* satellite, Priedhorsky and Terrell (1984) report a 198.6 day modulation. However as Smale *et al.* (1988) point out, mean flux measurements which integrate over dip intervals (as in *Vela* data) will be sensitive to gross changes in the dip morphology and may not reflect variability in the quiescent intensity.

The source has an optical counterpart (Grindlay and Cohn, 1987) with  $m_v \approx 21$ , which shows photometric modulation at a period of  $50.459 \pm 0.003$  mins, significantly different from that determined from x-ray dip recurrence, which is  $50.05 \pm 0.08$  mins (Smale *et al.*, 1989a). Recently, Grindlay (1989) has proposed a hierarchical triple model to explain this

Table 6.1: Summary of the properties of dip sources.

Source	Period (hrs)	Dips		Eclipses	Abundance deficiency	References	
		Primary					Secondary
		Duty cycle	Depth				
XB 1916-053	0.83	10-50%	20-100%	Yes	No	$3 \pm 2$	1,2,3,4,5
XB 1323-619	2.93	30%	50%	No	No	15-0.5	6,7
XBT 0748-676	3.82	40%	80%	Yes	Yes	2-7	8,9,10,11
XB 1254-690	3.88	20%	20-100%	No	No	4-0.5	12,13
X 1755-338	4.4	10%	40%	No	No	> 600	14,15
XB 1746-371	5	30%	15%	No	No	> 150	16
XB 1658-298	7.1	25%	100%	No	Yes	—	17,18,19
X 1624-490	21	30%	75%	No	No	0.8-1.3	20,21
Her X-1	40.8	20%	100%	Yes	Yes	~ 1	22,23
Cyg X-2	236	—	< 30%	Yes	No	100 <sup>a</sup>	24,25

Note:(a) - Attributed to ionisation rather than metal abundance, see text.

References: 1-Walter *et al.* (1982); 2-White & Swank (1982); 3-Grindlay & Cohn (1987); 4-Smale *et al.* 1988; 5-Smale *et al.* 1989a,b; 6-van der Klis *et al.* (1985); 7-Parmar *et al.* (1988); 8-Pedersen *et al.* (1985); 9-Wade *et al.* (1985); 10-Parmar *et al.* (1986); 11-Motch *et al.* (1989); 12-Courvoisier *et al.* (1986); 13-Motch *et al.* (1987); 14-White *et al.* (1984); 15-Mason, Parmar & White (1985); 16-Parmar, Stella & Giommi (1989) 17-Cominsky, Ossmann & Lewin (1983); 18-Cominsky & Wood (1984); 19-Cominsky & Wood (1989); 20-Watson *et al.* (1985a,b); 21-Bredon (1989); 22-Tananbaum *et al.* (1972); 23-Voges *et al.* (1985); 24-Cowley, Crampton & Hutchings (1979); 25-Vrtilek *et al.* (1986)

discrepancy.

#### **XB 1323-619 P=2.9 hr**

This source was detected at  $F_{2-10} \sim 7 \times 10^{-11}$  ergs sec $^{-1}$  cm $^{-2}$  with *Uhuru* (4U 1323-62, Forman *et al.*, 1978) and also with *Ariel V* (3A 1323-616, Warwick *et al.*, 1981). It was not reported in the HEAO-1 catalogue and this maybe an indication of transient behaviour. There were two EXOSAT observations of the source, the first of 4 hrs duration showed a type I burst and a single  $\sim 1$  hr duration 60% dip (van der Klis *et al.*, 1985). A follow-up observation by Parmar *et al.* (1988), of 30 hrs duration revealed the periodic nature of the dips. The quiescent spectrum was found to be well modelled by a simple power-law ( $\alpha \approx 1.5$ ) with a considerable column density ( $N_H = 40 \times 10^{21}$  cm $^{-2}$ ). From an analysis of the bursts the distance was found to be between 10 and 20 kpc. There is no identified optical counterpart.

#### **XBT 0748-676 P=3.8 hr**

First detected as serendipitous EXOSAT source, XBT 0748-676 has become the archetypal dip source as it exhibits eclipses and secondary dips, as well as having a photometrically modulated optical counterpart with  $m_v = 17$  (Pedersen and Mayor, 1985). The system shows type I bursts, the luminosity of which imply a distance of  $\sim 10$  kpc (Gottwald *et al.*, 1986) The transient nature of XBT 0748-676 is evident from the null detections in the *Uhuru*, *Ariel V*, and *HEAO-1* all sky catalogues (Forman *et al.*, 1978, Warwick *et al.*, 1981, and Wood *et al.*, 1984, respectively), which places an upper limit to the 2-10 keV flux at  $\sim 5 \times 10^{-12}$  ergs sec $^{-1}$  cm $^{-2}$ . The source was the subject of eight observations using EXOSAT, the eclipses and dips are discussed in detail by Parmar *et al.* (1984), who also examined archival *Einstein* IPC data and found XBT 0748-676 as a serendipitous source with flux of  $\sim 6.3 \times 10^{-13}$  ergs sec $^{-1}$  cm $^{-2}$ . At the time of the EXOSAT observations the non-dipping, non-bursting flux (1-20 keV) was up to  $\sim 15 \times 10^{-10}$  ergs sec $^{-1}$  cm $^{-2}$ . There was significant variability in the quiescent spectrum between observations, but typically a generalised thermal model was found to be an acceptable fit.

The eclipses in XBT 0748-676 reveal two important facts about the dip behaviour. They confirm that dips recur at the orbital period of the system. They also allow the phase of maximum dip activity to be established, which is found to be around  $\phi = 0.9$  for the primary dips, and at  $\phi \sim 0.65$  for the secondary. The optical modulation has a minimum centred on the x-ray eclipse (i.e.  $\phi = 0$ ). Parmar *et al.* (1986) note that the primary dips are consistent with the vertical structure being at the point of intersection of the accretion stream and

the disc. It was also suggested that the 4% residual emission in the eclipse flux would be consistent with emission from an extended ADC.

#### **XB 1254-690 P=3.9 hr**

First seen with *Uhuru* (Forman *et al.*, 1978), XB 1254-690 was optically identified by Griffiths *et al.* (1978) with a 19th mag object. The four EXOSAT observations, one of which had partially simultaneous optical coverage, have been reported by Courvoisier *et al.* (1986). The optical counterpart has been studied extensively by Motch *et al.* (1987). The optical spectrum shows a blue continuum with superposed weak excitation lines of the CIII-NIII blend at  $\lambda\lambda 4640-4650$ , He II  $\lambda 4686$  and  $H\alpha$ . No spectroscopic modulation was detected with an upper limit to radial velocity of  $\sim 300$  km sec $^{-1}$ . Photometrically the source exhibits a quasi-sinusoidal modulation at the dip-recurrence period of 3.88 hr. Dip activity has duration of 0.8 hr per cycle and a modulation of up to  $\sim 95\%$ . The simultaneous observation showed that optical minimum occurs  $\sim 0.15$  in phase after dip minimum. Courvoisier *et al.* (1986) report that the x-ray spectrum is best fit by a generalised thermal spectrum, with typical parameters  $\Gamma \sim 1$ ,  $kT_{char} \sim 5$  keV and  $N_H < 6 \times 10^{21}$  cm $^{-2}$ , the source flux at the time of these observations being  $F_{2-10} \approx 6 \times 10^{-11}$  ergs sec $^{-1}$  cm $^{-2}$ . The estimated distance from an analysis of two type I bursts was given as  $\sim 10$  kpc.

#### **X 1755-338 P=4.4 hr**

Although situated in the general direction of the galactic centre, the existence of a 19th magnitude optical counterpart (McClintock, Canizares and Hiltner, 1978) and the low x-ray absorption ( $N_H \sim 10^{21}$  cm $^{-2}$ ) led White *et al.* (1984) to suggest that the distance to X 1755-338 is  $\sim 3$  kpc. Two observations were made using EXOSAT, the first, of 9.5 hrs duration, established the 4.4 hr period (White *et al.*, 1984). The second observation had partially simultaneous optical coverage and was reported by Mason, Parmar and White (1985). The optical counterpart has a mean magnitude  $m_v \approx 18$  and as in the case of XB1254-690, the optical minimum occurs  $\sim 0.15$  later in phase than the centre of the dip. White *et al.* (1986) report that the x-ray spectrum is unusually soft and can be described by a generalised thermal model with  $\Gamma \sim 0.3$  and  $kT_{char} \sim 2$  keV. The quiescent 2-10 keV flux is  $\sim 10^{-9}$  ergs sec $^{-1}$  cm $^{-2}$ . A remarkable feature of the dips exhibited by this source is that they appear to be energy independent, suggesting a very low metallicity ( $< 1/600$  solar abundance) or that the obscuring medium is significantly ionised.

#### **XB 1746-371 P=5 hr?**

As a result of a search for orbital modulation in five luminous globular cluster sources in

EXOSAT archival data, Parmar, Stella and Giommi (1989) report the detection of two energy independent dips in the 1-10 keV light curve of XB1746-371 (in NGC 6641). These dips are separated by  $\sim 5$  hrs, and from the lack of associated spectral variability it was concluded that obscuring material is underabundant by a factor of  $> 150$ . NGC 6641 is however a globular cluster for which the metal abundance has been determined, being  $\sim 4-10$  times less than solar (Pilachowski, 1984). The source exhibits type I bursts, an analysis by Sztajno *et al.* (1987) suggests that the source distance is in the range 6.8 to 11.1 kpc. The source flux is  $F_{2-10} \sim 4 - 6 \times 10^{-11}$  ergs sec $^{-1}$  cm $^{-2}$ .

There is however some doubt as to the origin of the dips in the EXOSAT observations since both observations of this source were subject to unpredictable background contamination and Parmar *et al.* (1989) express caution about their result. However the detection of other examples of energy independent dips, apart from X 1755-338, would be an important result and clearly further observations are required.

#### **XBT 1658-298 P=7.1 hr**

The source is a highly variable transient and although relatively bright ( $F_{2-10} \sim 10^{-10}$  ergs sec $^{-1}$  cm $^2$ ) in the late 1970s, the source was not detectable at the time of the EXOSAT mission. Observations made using SAS 3 and HEAO-1 (A-1 scanning experiment) have been reported by Cominsky and Wood (1984 and 1989). The source shows dips for 25% of the 7.11 hr period, a stable dip feature at the end of the duty cycle was interpreted as an eclipse with a duration of  $\sim 15$  mins. No metal abundances have been measured for this source due to the poor spectral resolution of the SAS 3 and HEAO-1 (A1) experiments. The source shows bursts and has a highly variable optical counterpart (Cominsky and Wood, 1989).

#### **XB 1837+049 P=13 hr?**

Mason (1986) reports a claim of low level ( $\sim 15\%$ ) energy independent dip activity for this source (Ser X-1) by Ilovaisky and Chevalier from a 15 hr EXOSAT observation. The results of this observation have not been published.

#### **X 1624-490 P=21 hr**

A bright, optically unidentified source situated within  $0.5^\circ$  of the galactic plane and  $\sim 25^\circ$  from the galactic centre, X 1624-490 was observed with 2-10 keV fluxes of 1.2, 1.1 and  $0.4 \times 10^{-9}$  ergs s $^{-1}$  cm $^{-2}$  by *Uhuru*, *Ariel V* and *HEAO-1* respectively (Forman *et al.*, 1978, Warwick *et al.*, 1981, and Wood *et al.*, 1984). The first evidence for dip activity came from a short ( $\sim 2000$  sec) *Einstein* observation, and confirmed by a 6.3 hr duration EXOSAT

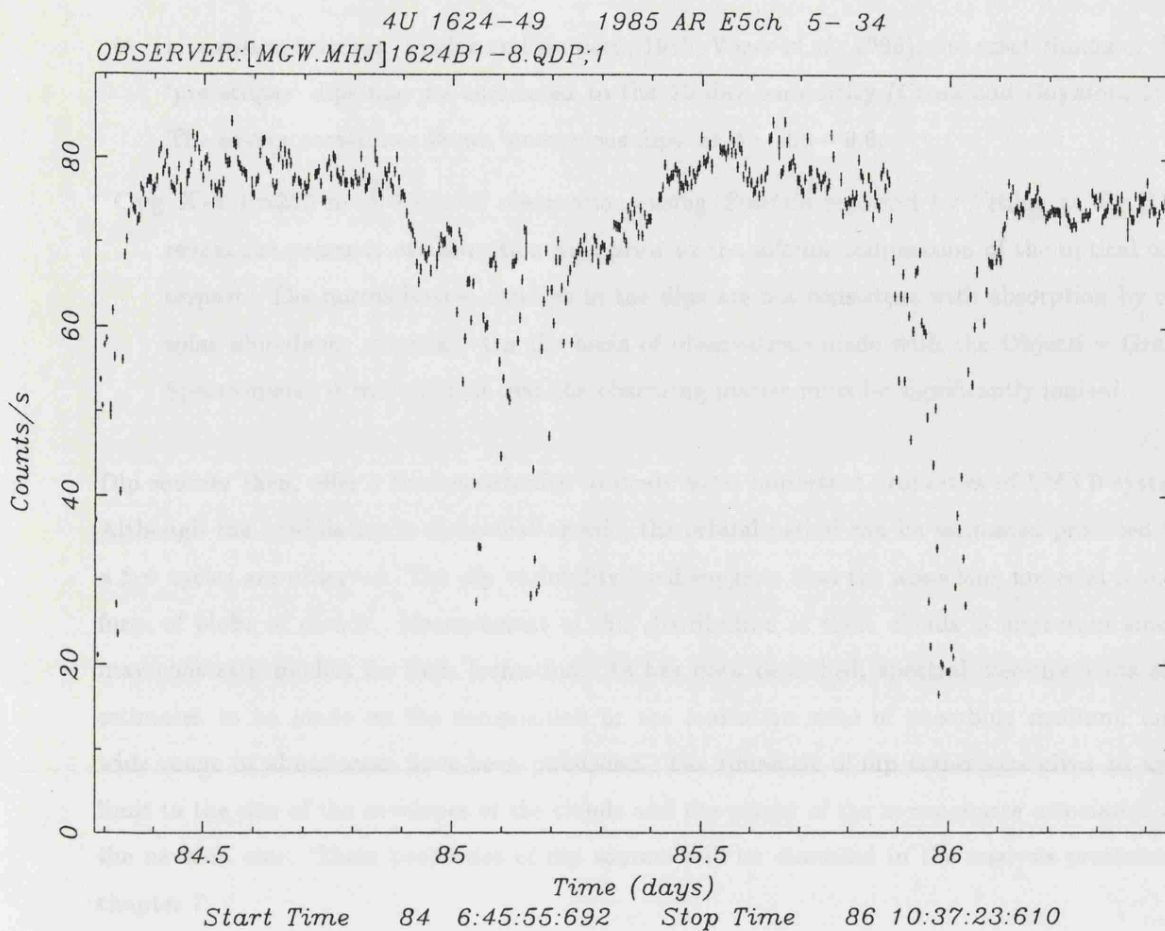


Figure 6.5: The EXOSAT ME 2-8 keV light curve of X 1624-490. The 21 hr orbital period is evident in this extended observation.

observation (Watson *et al.*, 1985b). The source was subject to a long ( $\sim 56$  hr) EXOSAT observation in 1985 which revealed the 21 hr period and  $\sim 6$  hr duty cycle of the dips (see figure 6.5). A unique feature of this source is that the maximum dip modulation is well defined, and the residual component is spectrally softer than that which is absorbed in the dip events. Watson *et al.* (1985b) speculate that this may be emission from an ADC. The *Ginga* observations of this source are described in chapter 7.

**Her X-1 (HZ Her) P= 40.8 hr** Once considered an archetypal LMXB, Her X-1 shows a wealth of periodic phenomena which sets it apart from other members of this class. Apart from eclipses, the emission is modulated at the spin period of the neutron star (1.24 sec) and shows a poorly understood 35 day cycle of variability. Prior to eclipse the source shows

absorption features (Vrtilek and Halpern, 1985, Voges *et al.*, 1985), the exact timing of these ‘pre-eclipse’ dips may be correlated to the 35 day periodicity (Crosa and Boynton, 1980). The source sometimes shows ‘anomalous dips’ at  $\phi \sim 0.3 - 0.6$ .

Cyg X-2 P=235 hr A series of observations using *Einstein* reported by Vrtilek *et al.* (1986) reveal the presence of absorption dips prior to the inferior conjunction of the optical counterpart. The normalisation changes in the dips are not consistent with absorption by cold, solar abundance material. On the basis of observations made with the Objective Grating Spectrometer it was claimed that the obscuring matter must be significantly ionised.

Dip sources then, offer a the opportunity to study some important properties of LMXB systems. Although the modulation is somewhat erratic, the orbital period can be estimated provided that a few cycles are observed. The dip variability itself suggests that the absorbing material is in the form of blobs or clouds. Measurement of this distribution of these clouds is important since it may constrain models for their formation. As has been described, spectral measurements allow estimates to be made on the composition or the ionisation state of absorbing medium, and a wide range of abundances have been published. The timescale of dip transitions gives an upper limit to the size of the envelopes of the clouds and the extent of the x-ray source associated with the neutron star. These properties of dip sources will be discussed in the analysis presented in chapter 7.

Evidence for absorption dips has also been found in some cataclysmic variables, the most striking case being in the soft x-ray emission from U Gem in outburst (see chapter 3) reported by Mason *et al.* (1988). In a series of EXOSAT observations dips corresponding to an absorption column density of  $3 \times 10^{20} \text{ cm}^{-2}$  were observed at  $\phi = 0.15$  and  $0.7$ , with large changes in profile over a few orbital cycles. Future observations of dips in CV systems are important because they should illustrate whether or not the presence of a luminous central x-ray source, as is found in LMXBs but not in CVs, is a major factor in determining the vertical structure in the disc.

## 6.4 ADC SOURCES

Whereas dip sources with their point-like x-ray sources give information on the density profile of a slice though the vertical structure around an accretion disc, the smoothly modulated ADC sources offer the possibility of building up a global picture of this azimuthal structure. In a review of orbital modulation by Parmar and White (1988), seven ADC sources are listed, of which four

are only tentatively identified as being members of this class. Of the three well determined ADC sources, most attention has been paid to X 1822-371, which is considered to be the archetypal ADC source. The source was been observed using HEAO-1, *Einstein*, (see Mason and Córdova, 1982, and White and Holt, 1982) and EXOSAT (see Hellier and Mason, 1989, hereafter HM). The results given by HM are consistent with those from the earlier missions, although the data set used to constrain the adopted model is of better quality, having full coverage over several orbital cycles.

The model used to fit these data has the geometric structure shown in figure 6.4. The ADC is spherical, homogeneous and centred on the compact x-ray source. The disc is structured at the outer rim, the simple prescription adopted by HM consisting of linear changes in height between nodes on this rim. To model the optical behaviour of the system, assumptions must be made about the emissivity of components of the system. White and Holt (1982) managed to model the optical light curve reasonably well using only a contribution from the inner surfaces of the accretion disc. A further component included by HM is the contribution from the outer edge of the disc but with a different emissivity, as would be expected for regions which are exposed and shielded from the central x-ray source. A component to account for reprocessing on the face of the primary was also included. An example of the models fitted by HM is shown in figure 6.6. Note that in this example, two bulges on the disc rim are required, the larger one is at the expected point of impact of the accretion disc with the disc ( $\phi \sim 0.8$ ) and the smaller one at  $\phi \sim 0.2$ .

The modelling of X 1822-371 by HM places strict constraints on the size of the ADC and on the location of the obscuring bulges within the system, based on the x-ray results alone. Typically it is found that the radius of the ADC is approximately half that of the accretion disc, being  $\sim 3 \times 10^{10}$  cm and  $\sim 7 \times 10^{10}$  cm respectively. The bulges are tightly constrained to lie near the outer edge of this accretion disc. The idea that ADC sources and dip sources have identical structures, but are viewed from different angle is supported by the modelling of HM. It was not a prerequisite that the compact source should be obscured at all times (this was to allow for the possibility that the ADC could be optically thick), but it was found that the best fit model was one in which the compact source is never directly visible.

At present, data from other ADC sources does not allow modelling of the type performed by HM for X 1822-371. Of the two other confirmed ADC sources, the transient XBT 2129+470 was too weak during the EXOSAT era for detailed observations to be made (Pietsch *et al.*, 1986). The other, X 0921-630 has too long an orbital period (9 days) to allow observation across an entire orbital cycle. However, as Mason (1989) points out, the similarity between the known modulation of this source and that of X 1822-371, implies that although the scale of these systems differs by

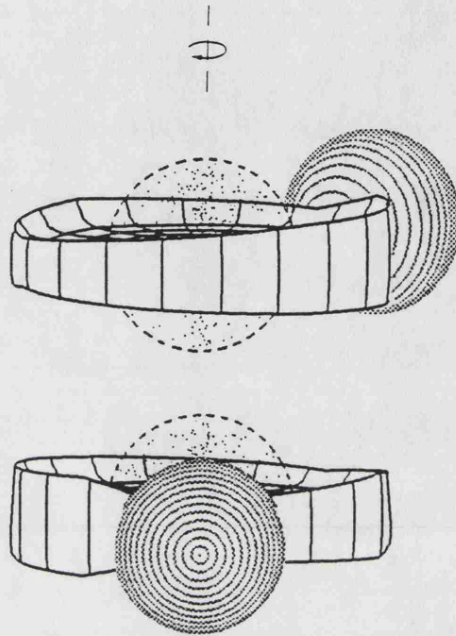


Figure 6.6: A three dimensional view of the ADC source X 1822-371. The geometric model shown has been constrained by simultaneous fitting to optical and x-ray light curves. The smooth modulation shown in figure 6.3 is produced by partial obscuration of the ADC by the variable height rim. Optical emission is from the inner and outer surfaces of the disc, the smooth modulation (figure 6.1) arises from the changing projected areas of these two components as the system rotates. From Hellier and Mason (1989).

a factor of 10, their structure must be almost identical. This scaling property must be a strong constraint on any valid physical model for this structure.

## 6.5 THEORIES OF THICKENED DISCS

The model of thin accretion discs outlined in chapter 1 clearly needs to be modified in order to reproduce the geometric structure that has been inferred from observation. As discussed above, there appears to be an association between the maximum vertical extent of the disc and the point of impact of the gas stream from the L1 point. However, Mason (1989) considers it unlikely that the energy of the incident stream would be sufficient to maintain the thickening of the disc that would be required. A model in which the stream is stopped at the outer edge of the disc can only produce vertical structure at around  $\phi \sim 0.8$ , and cannot account for secondary dips or the bulge at  $\phi = 0.2$  in the HM model.

Attempts to produce structure at other phases have utilised the properties of an overshooting gas stream. Lubow and Shu (1976) show that the stream thickness can be appreciably larger than the thin disc scale height, and so some of the accreting material may continue in a trajectory above and below the plane of the disc. The properties of this stream have been investigated by Lubow (1989) and Frank, King and Lasota (1987) (hereafter FKL). In both models it is assumed that the gas stream continues in an essentially ballistic trajectory. Lubow (1989) argues that dips arise from density enhancements both at the impact at the outer edge of the disc and at the point at which the overflowing gas stream converges on the disc (at  $\phi \sim 0.6$ ). Thus this model can only account for dip variability in phases 0.6-1.0. The FKL model assumes that a thickened ring forms at the circularisation radius ( $r_{circ}$ , see section 1.2.4) and that a shock forms at the point of impact of the ballistic stream with this ring. The shocked gas is subject to a two-phase instability due to the intense ionising flux from the neutron star, and forms cool dense clouds ( $T \sim 10^4$  K) in a hot ( $T \sim 10^7$  K) medium (see figure 6.7). These clouds again follow an approximate ballistic trajectory and may cause dips to occur as early as 0.3 in phase. This model is attractive as it provides a thickened region in the disc, a hot medium which is suggested forms the accretion disc corona, and can produce dips at almost all required phases. There are however objections to this model. From a theoretical point of view Lubow (1989) argues that the interaction of the gas stream with the disc at the circularisation radius is unlikely to lead to a thickened ring at this location. An observational constraint on this model is provided by the modelling of HM, who show that the vertical structure must be at a greater radius than  $r_{circ}$  for X 1822-371.

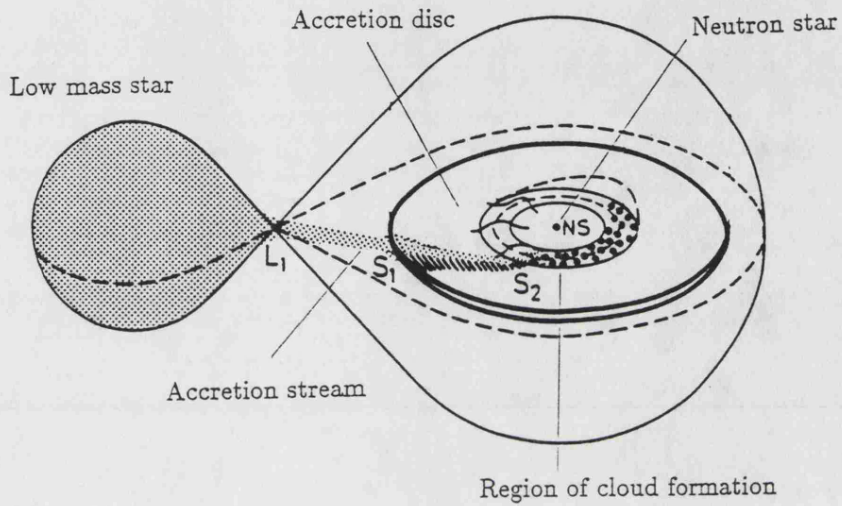


Figure 6.7: A view of the model LMXB proposed by Frank, King, & Lasota (1987). The gas stream from the L<sub>1</sub> point is incident on the outer edge of the disc at S<sub>1</sub>. A fraction of the stream overshoots the disc and impacts a thickened ring at the circularisation radius, where a shock is formed at S<sub>2</sub>. The post-shock gas forms a two phase medium of dense, cool clouds in a hot tenuous intercloud gas. From Frank, King, and Lasota (1987).

Mason (1989) speculates that the disc thickening may arise from structures unconnected with the stream-disc interaction and, as an example refers to the two dimensional numerical simulations by Sawada, Matsuda and Hachisu (1986). In those models it was found that two spiral shaped shock waves may form on the accretion disc. That series of calculations however covered a small range of sound speeds at the surface of secondary over which the mass transfer mechanism changes from Roche lobe overflow to being wind driven. The shocks seem to require interaction with a substantial stellar wind (see section 1.2.7) even though most of the mass transfer occurs by overflow. It is not clear that these conditions would be appropriate for the LMXB systems considered here, but this type of result illustrates the need for full three dimensional calculations of disc behaviour.

## 6.6 SUMMARY

In this chapter then, the following important features of the structure in accretion discs in LMXB systems have been discussed:

- Eclipses are rare because accretion discs are thickened and so shield the secondary from the compact x-ray source.
- X-ray orbital modulation is of two types: erratic dip variability, which may also be seen with total eclipses ; or, smooth quasi-sinusoidal variability which is always seen with partial eclipses. Both types of modulation can be explained in terms of non-axisymmetric vertical structure in the accretion disc.
- Dip events are caused by the occultation of a compact x-ray source by clouds of material situated above the plane of the accretion disc.
- The smooth modulation is due to partial obscuration of an extended accretion disc corona which scatters x-rays from the obscured central source into the line of sight.
- Geometric models for vertical structure in accretion discs are reasonably well constrained by observation. Consistent physical models are yet to be developed.

## Chapter 7

# Observations of Dip Sources

### 7.1 INTRODUCTION

In this chapter the *Ginga* observations of three dipping low mass x-ray binary sources, XB 1915-053, XBT 0748-676 and X 1624-490 will be presented. All were subject to earlier observations using EXOSAT, and estimates for orbital parameters and descriptions of spectral behaviour have been given by Smale *et al.* (1988), Parmar *et al.* (1986) and by Breedon (1989) for the three sources respectively. The analysis presented here uses data obtained with the *Ginga* LAC to provide further information on aspects of source behaviour studied with the EXOSAT ME. This can be divided into measurement of minimum timescales for dip events, and a study of the time variability of the spectrum. Of particular interest are the spectral changes associated with the dip events. Other aspects of the *Ginga* observations of XB 1916-053 and XBT 0748-676, such as period determination, have been published elsewhere (Smale *et al.*, 1989a,b).

The observations of X 1624-490 made with the EXOSAT ME which were reported by Watson *et al.* (1985a) and Breedon (1989), are re-analysed. A method based on the behaviour of the fractal dimension of the light curve is used to characterise the dip variability in the long uninterrupted coverage provided by these observations.

### 7.1.1 System Parameters

For all three sources, estimates for the binary parameters can only be made following assumptions about the nature of the components. The only information available is the orbital period, and in the case of XBT 0748-676 the duration of the eclipse. It is common to assume that the mass of the neutron star is  $\sim 1.4M_{\odot}$ . The mass of the secondary can then be estimated if the mass-radius relationship is known, since this star can be assumed to fill its Roche lobe. In the absence of eclipses, an upper limit may be found to the inclination ( $i$ ) of the binary, which implies a lower limit of  $90^{\circ} - i$  to the angle subtended by the vertical disc structure at the neutron star. The system parameters of XB 1916-053 and XBT 0748-676 have been discussed by Smale *et al.* (1988) and Parmar *et al.* (1986), and are reviewed below. Orbital parameters for X 1624-490 were given by Breedon (1989), but are reconsidered here and somewhat different values are derived.

#### **XB 1916-053**

The short orbital period of 51 mins is below the limit of  $\sim 80$  mins for main-sequence secondaries discussed in chapter 5. Smale *et al.* (1988) suggested that it is likely that the mass donor is a non-degenerate hydrogen-deficient star, and used numerical results given by Nelson, Rappaport and Joss (1986) to estimate the range of mass as  $0.11 \leq M_2 \leq 0.15$ , and radius  $0.09 \leq R_2 \leq 0.11$ , assuming a  $1.4M_{\odot}$  neutron star. The binary separation of this system is  $0.51 - 0.52R_{\odot}$ , and so the angle subtended by the secondary at the neutron star is  $\approx 11^{\circ}$ . The absence of eclipses implies that  $i < 79^{\circ}$  and so the vertical disc structure must have an extent of  $> 11^{\circ}$ .

#### **XBT 0748-676**

Of the three sources considered here, XBT 0748-676 is the only one in which the secondary is likely to be a main sequence star. Parmar *et al.* (1986) showed that the period and eclipse timing are consistent with the secondary being an M-dwarf with  $M_2 \approx 0.45M_{\odot}$ , for  $M_1 = 1.4$ . In this case the system inclination is  $\approx 74^{\circ}$ . The possibility was also suggested that it could be a very low mass ( $M_2 = 0.085M_{\odot}$ ) degenerate star, in which case  $i = 82^{\circ}$ .

## X 1624-490

Given the orbital period of 21 hr (Watson *et al.*, 1985a) and assuming a mass for the primary, the radius ( $R_L$ ) of the Roche lobe of the secondary can be calculated as a function of  $M_2$  using equation 1.6. Figure 7.1 shows this function for two values of secondary mass,  $M_2 = 1M_\odot$  and  $3M_\odot$ . Note that for low secondary masses  $R_L$  is insensitive to the primary mass. The dashed curve shows an estimated mass-radius relationship for the zero-age main sequence from Whyte and Eggleton (1980). It can be seen that a main sequence companion to X 1624-490 would have  $M_2 \gtrsim 4M_\odot$ , which corresponds to a late B type star. Observationally, it is not possible to rule out this scenario, since the optical counterpart is yet to be established. A strong argument against a main-sequence secondary however, arises from the spectral types of main-sequence mass donors in CVs, which are found to be of type G0 or later (Patterson, 1984). Since the evolution of binary systems to the stage at which the mass donor becomes Roche lobe filling is likely to be independent of whether the compact object is a neutron star or a white dwarf, it may be argued for X 1624-490, as for all LMXB that  $M_2 \lesssim 1.5M_\odot$ . Thus the secondary must have evolved off the main sequence, and consequently there is no unique mass-radius relationship. However, the mass of the secondary must be sufficient to allow the star to evolve off the main-sequence in the lifetime of the system, and so it may be expected that  $M \gtrsim 1M_\odot$ . For the purposes of discussion below, it will be assumed that  $M_1 \approx M_2 \approx 1.4M_\odot$ . A complicating factor however, is that  $M_2$  may have varied as a result of mass transfer over the lifetime of the system. Since this possibility cannot be treated quantitatively with any certainty, it will not be considered further. With this assumption for the masses, the orbital separation is  $a = 3.8 \times 10^{11}$  cm and the Roche lobe radius is  $1.4 \times 10^{11}$  cm. The absence of eclipses implies an inclination  $i < 69^\circ$ , and thus the vertical extent of structure in the accretion disc is  $> 21^\circ$ .

### Overview of System Parameters

A summary of the orbital parameters for all three systems is given in table 7.1. The three sources represent a wide range of orbital period, and there is an order of magnitude difference in secondary mass and binary separation between XB 1916-053 and X 1624-490. The minimum extent of the vertical structure is  $> 10^\circ$  for all systems, suggesting that actual height of this structure must scale in some way with the binary separation.

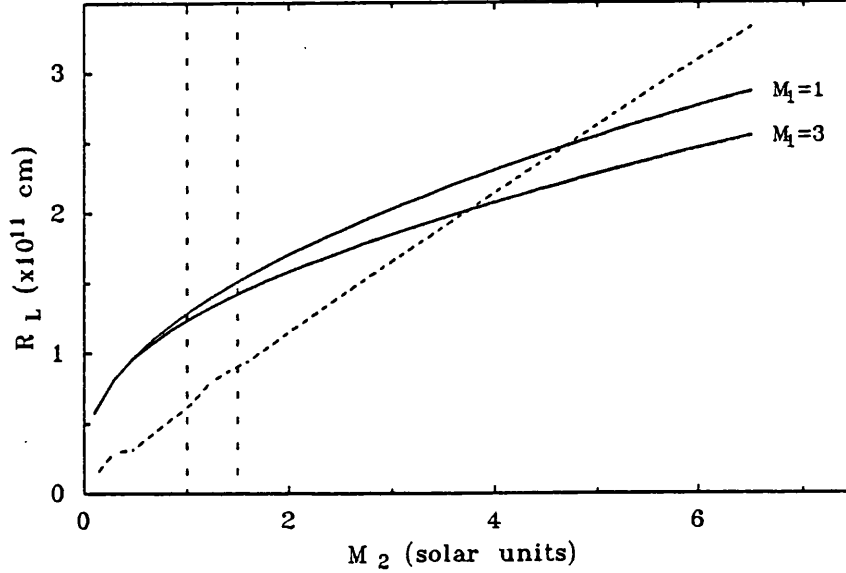


Figure 7.1: The Roche lobe radius as a function of secondary mass for two assumed neutron star masses ( $M_1$ ), using equation 1.6 (Eggleton, 1983). The dashed curve shows an approximation to ZAMS given by Whyte and Eggleton (1980). The vertical dashed lines indicate the expected range of secondary mass in X 1624-490, see text.

Table 7.1: A summary of the orbital parameters of the dip sources, XB 1916-053, XBT 0748-676, X 1624-490.

Source	$P_{orb}$ (hr)	$M_1$ ( $M_\odot$ )	$M_2$ ( $M_\odot$ )	$a$ ( $\times 10^{10}$ cm)	$R_L$	$i$
XB 1916-053	0.83	1.4	0.12	3.6	0.7	$< 89^\circ$
XBT 0748-676	3.82	1.4	0.45	11	3.1	$\approx 74^\circ$
X 1624-490	21	1.4	1.4	38	14	$< 69^\circ$

Table 7.2: Summary of observations of dip sources.

Observation	Date			Duration (hrs)	Flux (2-10 keV)
	Year	Start	End		
<b>X 1624-490</b>					
E1	1984	Mar 5 12:32	Mar 5 17:49	5.3	110
E2	1985	Mar 25 07:09	Mar 27 15:00	56	110
G1	1987	Oct 18 03:31	Oct 19 07:02	20.5	120
G2	1988	Mar 23 22:00	Mar 25 22:00	48	90
<b>XB 1916-053</b>					
G1	1987	May 15 06:00	May 16 06:00	12	-
G2a	1987	Sep 15 02:09	Sep 15 08:04	5.9	20
G2b	1987	Sep 16 00:35	Sep 16 06:15	5.7	18
G2c	1987	Sep 17 00:41	Sep 17 06:36	5.9	18
G2d	1987	Sep 18 02:59	Sep 18 07:23	4.4	19
G3	1988	Sep 9 10:51	Sep 11 22:19	60	27
<b>XBT 0748-676</b>					
G1	1989	Mar 24 17:30	Mar 26 04:20	30	49

**Notes:** The duration of observation refers to the hours spent with on-source pointing. For the EXOSAT observations the exposure time is  $\approx 100\%$  of the quoted duration, for the *Ginga* observations the exposures are typically 30%. The 2–10 keV fluxes are given in units of  $10^{-11}$  ergs  $s^{-1}$   $cm^{-2}$ , and are quoted for the best fit continuum models (see section 7.6).

## 7.2 OBSERVATIONS

### 7.2.1 XB 1916-053

The short period dip source XB 1916-053 was observed on three occasions using *Ginga*. The first observation (G1) was made in the P.V. phase of the mission. Dip coverage during this observation was poor, furthermore, a reliable estimate of the background behaviour could not be made for most of the on-source time. Consequently this observation has been excluded from the analysis presented here.

The second observation (G2) consisted of 4 separate on-source pointings, each of  $\sim 7$  hrs duration, made on consecutive days from 1987 September 15 to 18. The LAC was operated in the MPC2 spectral mode throughout, giving a time resolution of  $\leq 2$  sec. The attitude determination for these pointings indicate offsets of up to  $\approx 0.5^\circ$ , but with little change in offset over the duration of each pointing. The data were corrected for off-source pointing, but no significant spectral changes were induced by the correction procedure. The background subtraction for these observations was calculated using a blank-sky pointing of  $\sim 35$  hrs duration made on 1987 September 18–20. The background subtracted, attitude corrected 2–10 keV light curves are shown in figure 7.2. Note that a single burst was detected in observation G2b, and these data have been removed from the data used for spectral analysis.

The third observation (G3) was made on 1988 September 9–11 of  $\approx 60$  hrs duration. The LAC was operated in MPC1 mode and the time resolution of data varies between 4 and 16 sec. The calculated aspect solution was clearly in error. Since the LAC count rate is similar to observation G2 it has been assumed that any spectral changes caused by the offset pointing are negligible and consequently no attitude correction has been applied to these data. The lack of attitude solution however prevents interpretation of the gross source flux as intrinsic variability since such changes could be induced by a change in offset. Due to insufficient local background observation, the ‘universal’ background generation technique was adopted, this is expected to give a reasonably good result for MPC1 data. The 2–10 keV light curve is shown in figure 7.3. The dashed vertical lines indicate the  $\approx 14000$  sec of the data which are at 4 sec resolution, and only these data have been used for the spectral analysis discussed below. Three bursts were detected in this observation, and are visible in the light curve.

### 7.2.2 XBT 0748-676

The transient dip source XBT 0748-676 was observed once using *Ginga*. The observation was made on 1989 March 24–26, with a break of  $\approx 5$  hrs duration from March 25 07:20. The LAC was operated in MPC2 mode from the start of the observation until March 25 20:00 UT and thereafter in MPC1 mode at low bit rate. The satellite pointing was particularly poor from the start of the observation until March 25 18:00 UT, with an offset of  $\approx 1.0^\circ$  over this interval, and of  $\approx 0.25^\circ$  for the remainder of the observation. An aspect correction was applied to the data and a reasonable estimate for the broad-band flux was obtained for the entire observation. However the data up until March 20:00 UT has been excluded from spectral analysis due to the uncertainties in spectral correction at such

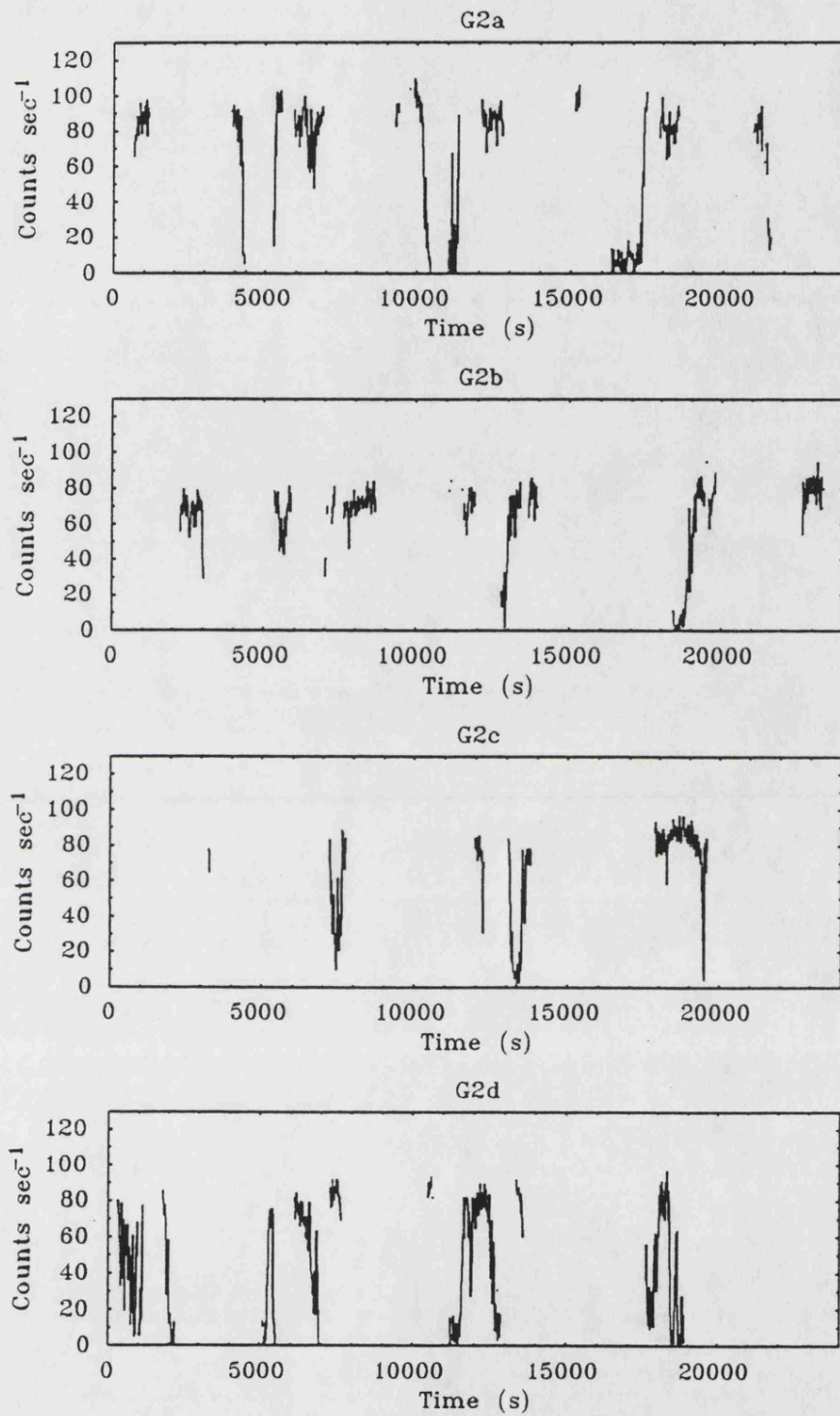


Figure 7.2: The 2–10 keV light curves from the observations of 1987 Sep 15–18 of XB 1916-053

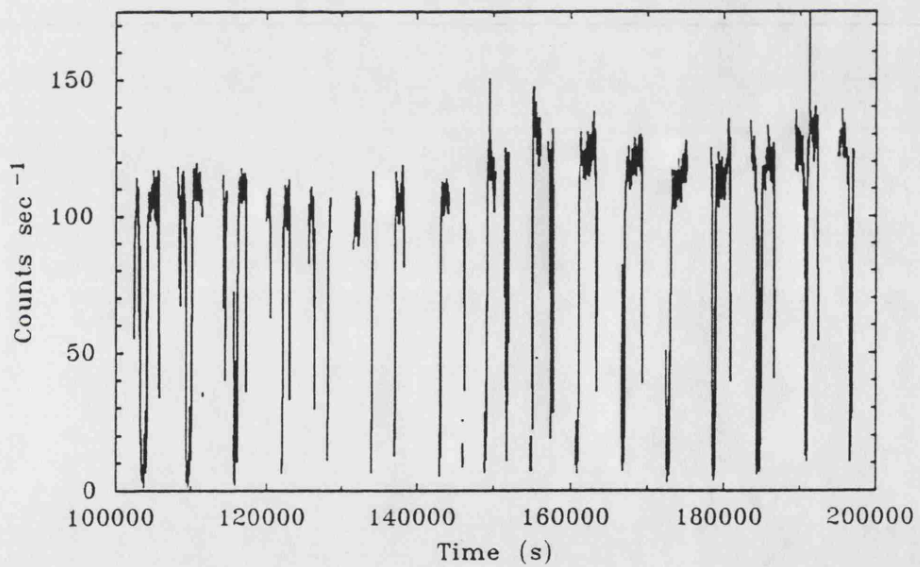
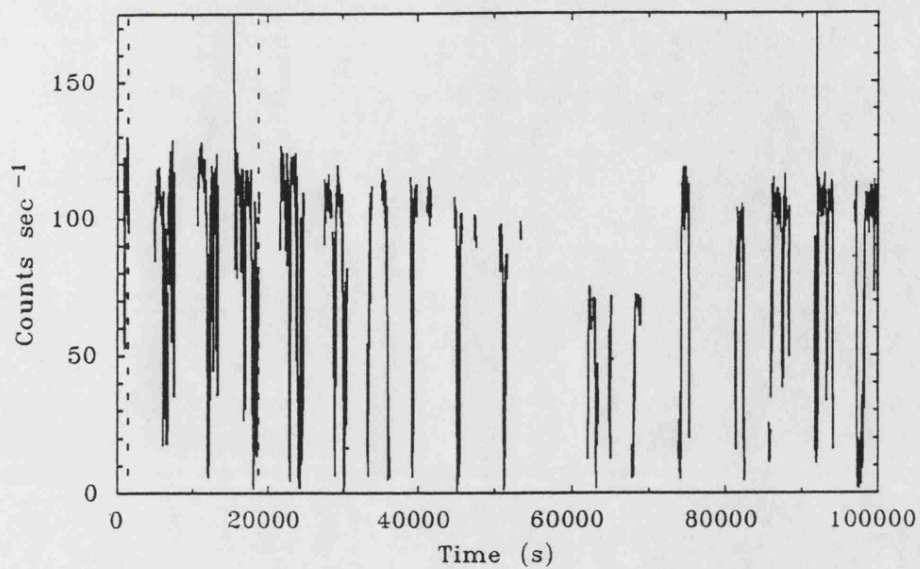


Figure 7.3: The 2-10 keV light curve from the observation of 1988 Sep 9 of XB 1916-053

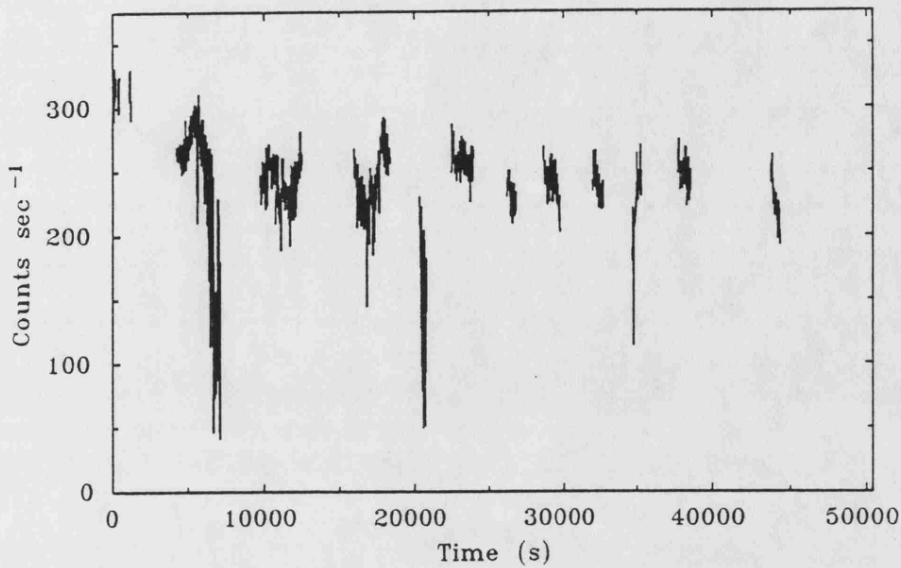


Figure 7.4: The 2–9.5 keV light curve of the MPC1 mode data from the *Ginga* observation of XBT 0748-676.

large offset, and because of the unreliability of the ‘universal’ background subtraction technique for the short section of on-source MPC2 data. Figure 7.4 shows the background subtracted, aspect-corrected light curve of the data considered in the spectral analysis. It can be seen that the total amount of dip coverage is poor, amounting in total to  $\sim 1000$  sec. The minimum time resolution of these data is 16 sec which places further restriction on spectral analysis of the dips.

### 7.2.3 X 1624-490

Four observations of X 1624-490 have been used in the analysis presented here. Two of these were made using the EXOSAT ME detector array on 1984 March 5 and 1985 March 25–27. The other two observations were made using *Ginga* on 1987 October 18-19 and 1988 March 23–25. A summary of all four observations is given in table 7.2, and the 2-10 keV light-curves for the *Ginga* observations are shown in figures 7.5 and 7.6, a 2–6 keV light curve for the 1985 March 25 observation has already been given in figure 6.5.

The EXOSAT observations were made in HER5 mode, giving a minimum time resolution of 1 sec.

Background subtraction was performed using slew data as described in section 2.4.1. The *Ginga* observations were both made using MPC2 mode at a variety of telemetry rates, with most data being at a time resolution of 2 sec. The background parameterisations for observations G1 and G2 were determined from blank-sky observations of 16 and 24 hrs duration respectively. It can be seen from figure 7.5 that the dip coverage in observation G1 was poor, 25000 sec of coverage was lost as the ground station had to be shut down due to local weather conditions, and this interval corresponds to the expected period of maximum dip activity. Consequently a second *Ginga* observation (G2) was made. Dip coverage in this observation amounts to  $\sim 3500$  sec.

## 7.3 GENERAL X-RAY PROPERTIES

### 7.3.1 XB 1916-053

The *Ginga* observations of XB 1916-053 reveal no major differences to the x-ray properties determined from previous observations. The mean non-dipping, non-bursting (quiescent) 2–10 keV flux varies over a range of  $18$  to  $27 \times 10^{-11}$  ergs  $s^{-1}$   $cm^{-2}$  between observations G1 and G2. Changes in the flux in G2 suggest that variations in flux of  $\sim 10\%$  occur on timescales of a few hours. Note however that the apparent flux changes of  $\sim 15\%$  in G3 cannot be attributed to intrinsic source variability due to the uncertainty in the aspect-solution for this observation.

The breaks in coverage due to earth occultation result in many active dip periods being only partially observed. However the presence of primary and secondary dips is evident in the data. The period of dip recurrence has been determined by Smale *et al.* (1989a,b), giving best fit periods of  $3005.0 \pm 6.6$  sec and  $3000 \pm 5$  sec for observations G2 and G3 respectively. Defining phase 0.0 at the minimum of the folded light curve, the secondary dips occur at  $\phi \approx 0.55$ – $0.65$ . The secondary dips show slow migration in phase, changing by 0.05 in  $\sim 10$  cycles (Smale *et al.* 1989b).

The spectrum hardens considerably during dip events, with primary and secondary dips appearing equivalent. The deepest dips appear total, with no evidence for any residual component. The EXOSAT observations showed that modulation depth shows considerable variability and dip profiles can change considerably from one orbit to the next. In the *Ginga* observations most of the well covered dip periods show modulation  $\gtrsim 90\%$ . The secondary dips ranged in depth from 0–100%.

The source exhibits bursts with a ratio of time-averaged quiescent flux to time-averaged burst flux

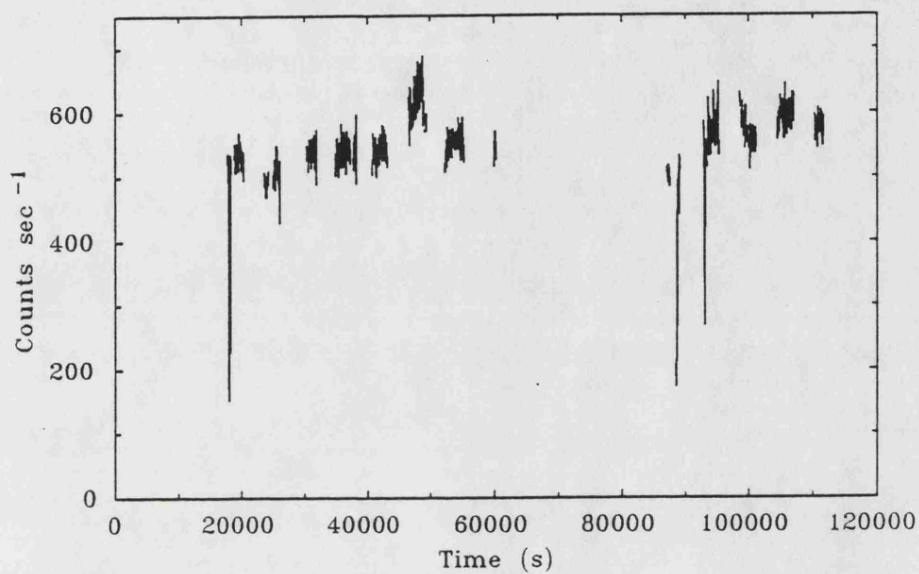


Figure 7.5: The 2-10 keV light curve of observation G1 of X 1624-490.

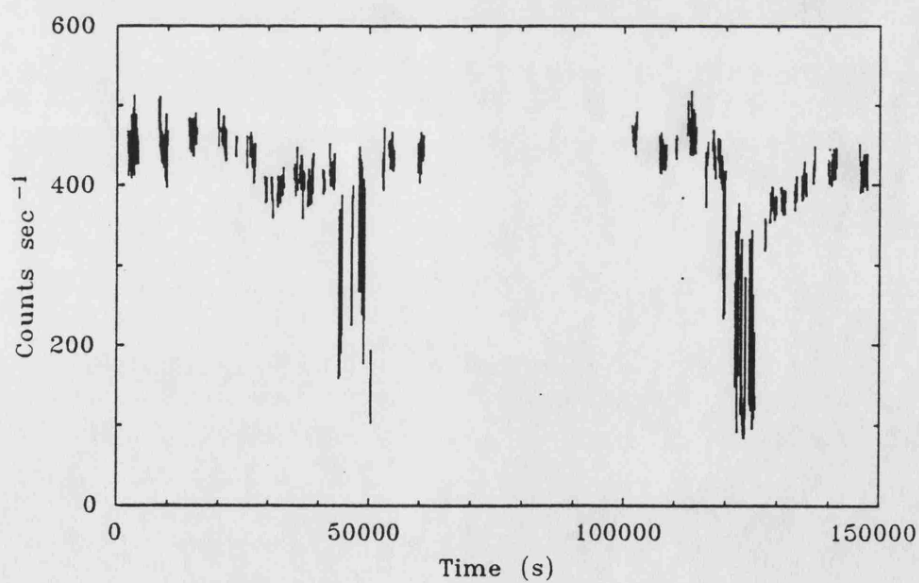


Figure 7.6: The 2-10 keV light curve of observation G2 of X 1624-490.

of  $\alpha = 170 \pm 50$  (Smale *et al.*, 1988). A single burst was observed in observation G2 and three were seen in G3. One of the bursts in G3 occurs during an interval of dip activity, although the time resolution of 16 sec is not high enough to determine whether or not the burst actually occurs in a dip.

### 7.3.2 XBT 0748-676

The source is unique amongst dip sources in that it is an eclipsing system which allows period to be determined precisely. At the time of the *Ginga* observation,  $P = 3.82410682 \pm 0.00000043$  hrs, and  $\dot{P} = -(1.72 \pm 0.28) \times 10^{-7} \text{ yr}^{-1}$  (Smale *et al.*, 1989b). The source was bright during the *Ginga* observation, having a 2–10 keV flux of  $\sim 50 \times 10^{-11} \text{ ergs s}^{-1} \text{ cm}^{-2}$ . In the quiescent state the x-ray flux varies by  $\sim 25\%$  on timescales of a few 1000 sec, but shows little associated spectral variability. Similarly to most other sources, the dips are characterised by a spectral hardening. The system exhibits primary and secondary dips at phase 0.8–0.2 and  $\approx 0.65$  respectively (defining phase 0.0 at mid-eclipse). The maximum modulation depth of primary dips in the *Ginga* observations was similar to that seen with EXOSAT, being  $\sim 80\%$ .

Gottwald *et al.* (1986) found that the burst recurrence rate is a function of the persistent flux, with  $\alpha$  varying between 20 and 300. For the flux level seen in the *Ginga* observation, the mean burst recurrence time would be expected to be  $\sim 10^4$  sec. Observation G1 has 38,500 sec of exposure, but no bursts were seen. However, given the broken coverage and the uncertainty in the recurrence rate, there is no evidence to suggest that the burst behaviour is different to that seen in previous observations.

### 7.3.3 X 1624-490

The x-ray properties of X 1624-490 seem to be similar in all four observations. The mean 2–10 keV flux outside the dips shows a variation of about 30% between observations. The mean source luminosities are in the range  $1.1\text{--}1.4 \times 10^{37} \text{ ergs sec}^{-1}$ , assuming a source distance of 10 kpc. The minimum flux level observed during dip intervals is consistent with being constant between observations E1, E2 and G2, with a 2–10 keV flux of  $2 \times 10^{-10} \text{ ergs sec}^{-1} \text{ cm}^{-2}$ . No well-defined minimum could be determined for G1 due to the poor dip coverage. A feature of the light curve is the flaring of the non-dip state, which shows intermittent variability of up to about 30% of the 2–10 keV flux.

The main features of the spectral variability of X 1624-490 are apparent in the simple representation of hard and soft fluxes in observation G2 given in figure 7.7, which shows on a grey scale, the density of fluxes in the 1.8-4.5 keV and 4.5-14 keV bands, at a time resolution of the data of 16 sec. In interpreting such a diagram it should be noted that a spectrally invariant source which undergoes flux changes would have a locus of a straight line passing through the origin. The spectral ratio associated with the non-dipping state is shown by the dashed line in in figure 7.7). The features of the two-band behaviour are:

- Data points lie on a single branch in the hard–soft plane.
- There are two types of behaviour in the non-dip state ( $\alpha + \beta$ ). In  $\alpha$  the flux changes are spectrally invariant. In  $\beta$  however, changes in flux are predominately due to variability in the hard x-ray band.
- As the source enters the dip state ( $\gamma$ ) there is an initial hardening of the spectrum. As the dips get deeper however, the spectrum softens again, such that at dip maximum a soft residual component ( $\delta$ ) remains.

At least two physically distinct components of emission are required to model this type of behaviour, one of which is subject to dip modulation, the other being constant. These components will be termed **B** and **A** respectively. Component **A**, which dominates the emission during the deepest dips, is clearly softer than **B**. The initial increase of hardness seen at the start of dip events is broadly consistent with photoelectric absorption of component **B**. The softening of the spectrum towards dip maximum arises as component **A** begins to dominate.

The hard variability, which appears as the vertical spread in the distribution in figure 7.7 near maximum flux appears to be a feature of component **B**. Inspection of the light curves shows this is an intermittent phenomenon, but does not occur during the deep dip intervals.

## 7.4 MINIMUM TIMESCALES

The estimation of a minimum time ( $\delta t$ ) associated with dip transitions allows an upper limit to be made of the minimum linear dimensions of either the compact x-ray source, or the envelopes of the absorbing clouds. The geometry of these two extreme cases is illustrated schematically in figure 7.8. In case a the source is essentially point-like but the cloud column density changes over a

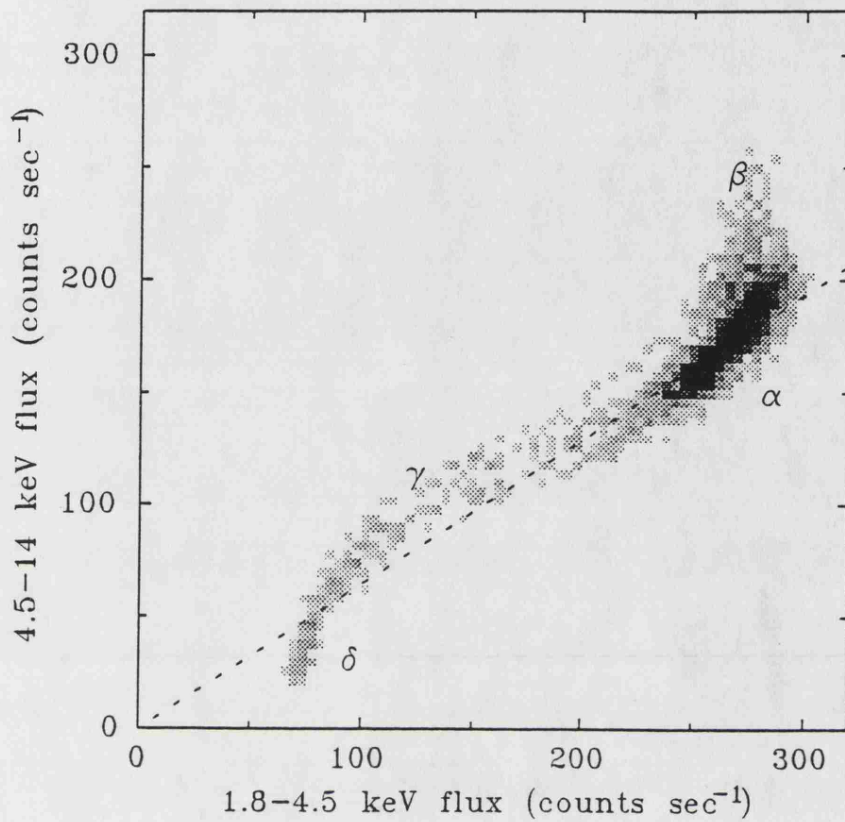


Figure 7.7: Grey-scale representation of the density soft (1.8–4.5 keV) and hard (4.5–14 keV) fluxes for observation G2 of X 1624-490. The fluxes were accumulated at an integration time of 16 sec. The non-dip state shows a spectrally invariant state ( $\alpha$ ) and some degree of variability which is restricted to the hard flux only ( $\beta$ ). As the source undergoes dip events, the spectrum hardens ( $\gamma$ ) before reaching the deepest dip state ( $\delta$ ) which is dominated by a component which is softer than the quiescent ( $\alpha$ ) state.

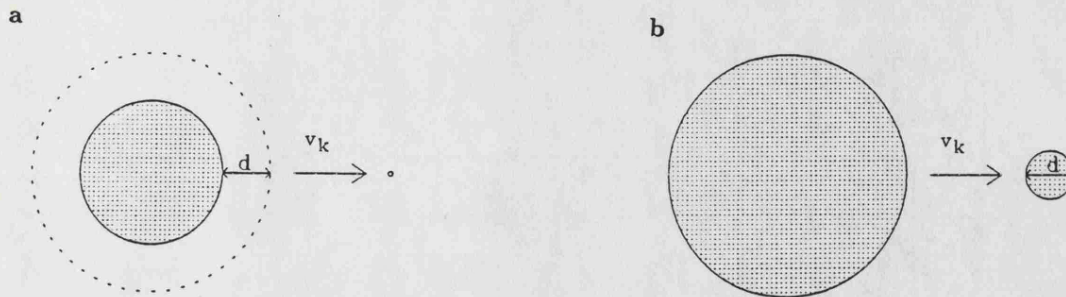


Figure 7.8: A schematic diagram showing the two extreme cases of cloud and source geometry which give rise to finite dip transition times. The clouds move across the source at the Keplerian velocity  $v_k$ . In case a the source is essentially point-like but the cloud has an envelope of thickness  $d$ . In case b the cloud envelope is small but now the source has a linear extent of  $d$ .

length  $d$ . In case b the cloud envelope is small but now the source has an extent  $d$ . An intermediate case in which the cloud envelopes and the source have similar dimensions is also possible, and  $d$  corresponds to the sum of these lengths.

The problem of measurement of minimum timescales has received little attention by previous workers. Parmar *et al.* (1986) constructed the ACF of the ME light curve for XBT 0748-676, and concluded that a characteristic dip timescale was 15 sec, and claimed evidence for significant variability on timescales down to the instrumental integration time of 1 sec. With a collecting area a factor  $\sim 5$  greater than the ME, the LAC offered the potential to reduce minimum timescales substantially. In practice this potential was not realised to the full because of the relatively poor time resolution of the MPC1 and MPC2 spectral modes. For the three sources studied, the highest time resolution available during dip events were as follows; 62.5 msec for X 1624-490, 500 msec for XB 1916-053, and 16 sec for XBT 0748-676. Although higher time resolution data were available for XBT 0748-676, the LAC offset at that time was large and the count rate was approximately half that obtained during the EXOSAT observation, and thus could not be used to study variability on the timescales of interest.

In order to obtain reasonable sensitivity to the dips, the energy range used for the light curves

was 2–6 keV. An example of a rapid dip transition in X 1624–490 is shown in figure 7.9. It is not clear that the ACF is particularly useful in this context since what is required is an estimate of the minimum timescales rather than a mean dip transition time. The procedure adopted here was to estimate the shortest observed times for significant changes in flux. The definition of a significant change adopted here is that a transition must occur between two flux levels separated at the  $3\sigma$  level, and that the change must be persistent, i.e. the count rates immediately before and after the transition must be consistent with the respective flux levels. Using this definition, minimum times  $\delta t \approx 0.5$  and 1 sec were measured for X 1624–490 and XB 1916–053 respectively.

To give a linear dimension, a cloud velocity must be assumed. It is difficult to envisage a scenario in which the clouds are not at least approximately in a Keplerian orbit. The linear dimension is  $d \sim v_k \delta t$ , where  $v_k \approx 1.4 \times 10^{13} r^{-1/2} \text{cm s}^{-1}$  is the Keplerian velocity at a distance  $r$  from the neutron star with an assumed mass of  $1.4M_\odot$ . It is not clear what an appropriate value for  $r$  should be. To date, two sites of cloud formation have been suggested, the outer edge of the accretion disc ( $r = r_{outer}$ ) (e.g. White and Mason, 1985), and the circularisation radius ( $r = r_{circ}$ ) (Frank, King and Lasota, 1987, hereafter FKL). Using the expression for  $r_{circ}$  (equation 1.15) and the approximation that  $r_{outer} \sim 3r_{circ}$ , given by FKL, values of  $r_{circ} \sim 3.5 \times 10^{10}$  cm and  $r_{outer} \sim 1 \times 10^{11}$  cm have been adopted for X 1624–490. Using  $\delta t \sim 500$  ms, values of  $d \sim 4 \times 10^7$  cm and  $d \sim 2 \times 10^7$  cm are obtained for clouds at  $r_{circ}$  and  $r_{outer}$  respectively. The corresponding values for XB 1916–053 are  $r_{circ} \sim 4.1 \times 10^9$  cm and  $r_{outer} \sim 1.2 \times 10^{10}$  cm, and using  $\delta t \approx 1$  sec, values of  $d \sim 2.2 \times 10^8$  cm and  $d \sim 1.3 \times 10^8$  cm are obtained.

Thus the long period system, X 1624–490 gives better constraints on the maximum dimensions that can be associated with the cloud envelopes or the source size than the shorter period system, XB 1916–053. In the former case, the approximate range is  $\sim 200$  to  $\sim 400$  km.

## 7.5 CHARACTERISTIC TIMESCALES

In order to measure the timescales associated with entire dip events (rather than dip transitions), and to attempt to constrain simple models for dip variability, a technique based on the study of the behaviour of the fractal dimension of the dip light curves has been employed. The concept and working definition of the fractal length function ( $L(\Delta T)$ ) and fractal dimension ( $D$ ) as applied to time-series were discussed in section 2.6.4. It was shown that the fractal length function is sensitive to a time series of randomly occurring square shots, and it is the similarity of that analytic case

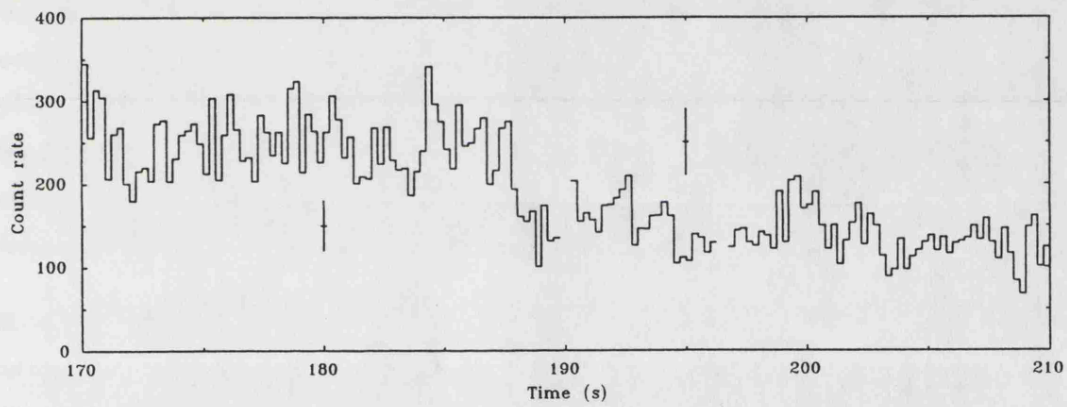
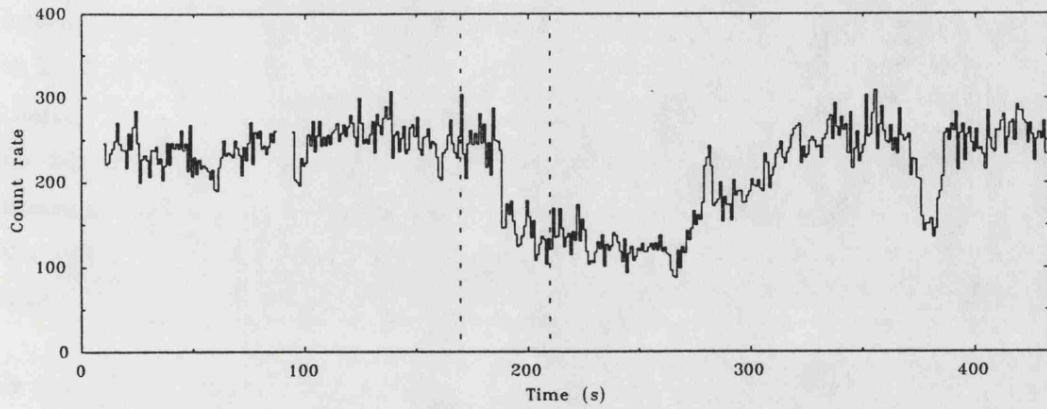


Figure 7.9: An example of a resolved, rapid dip transition, in this case from observation G1 of X 1624-490. The top panel shows the light curve at a resolution of 2 sec. The lower curve shows the dashed region from the top panel at a time resolution of 0.25 sec. Representative  $1\sigma$  error bars are shown for the high and low flux states respectively. It can be seen that a transition occurs in two bins which corresponds to 0.5 sec.

to real dip light curves which provided the motivation behind adopting this technique.

The data best suited to the study of the evolution of the morphology of the light curve through an interval of dip activity, are those in which this interval has a long duration. It is also advantageous to have an uninterrupted observation, since the effects of data gaps on the technique used to characterise the variability need not be considered. Consequently the data used here were from the EXOSAT observations of the long period source X 1624-490 (E1 and E2). As in the minimum timescale study, a high sensitivity to dip events is required, and so the 2-6 keV band was used for the light curves discussed here, and in this case the time-resolution was 4 sec. The light curves used are shown in figure 7.10.

In order to study the changes in variability through a period of dip activity (of typical duration  $\sim 2 \times 10^4$  sec) sections of 2000 sec duration were sampled with a 50% overlap between consecutive samples. This gave 45 (non-independent) sections of data. For each section, the fractal length function  $L(\Delta t)$  was calculated and inspected. It was found that for periods of intermediate dip activity, there is an apparent break in  $\log L(\Delta t)$  at  $\Delta t \sim 120$  sec. Figure 7.12 shows a typical plot of  $L(\Delta t)$ , calculated for the section of dip light curve shown in figure 7.11. The gradient of  $\log L(\Delta t)$  appears to be constant below  $\log(\Delta t) \sim 2.1$ , with a value of  $D \approx 0.65$ . Above the break at  $\log(\Delta t) \sim 2.1$  ( $\Delta t \sim 120$  sec),  $D$  tends to the noise only value of 1. The values of  $D$  calculated from the data were from those defined by the range  $\Delta t = 4 - 120$  sec.

It was found that the measured values of  $D$  are correlated with the level of dip activity. This is as might be expected, since  $D$  is likely to depend on the relative contribution to the variability in the light curve arising from dips, and that from other sources (counting noise and intrinsic source variability). Thus the characterisation of the dip morphology requires that the level of dip activity is quantified. This then allows the behaviour of  $D$  to be studied as a function of the dip activity parameter. One method of quantifying the level of dip activity is to measure the fraction of time the source spends in a dip state. Thus a parameter  $f_{low} = t_{low}/t_{tot}$  was defined, where  $t_{low}$  is the time spent below a certain flux threshold out of a total sample time  $t_{tot}$ . The threshold used in this case was half the mean maximum dip depth, and corresponds to a count rate of 25 counts  $\text{sec}^{-1}$  for both of the EXOSAT observations presented here.

The values of  $f_{low}$  and  $D$  were calculated for each data section and are shown in figure 7.13. It can be seen that for periods of low and very intense dip activity, i.e.  $f_{low} \approx 0$  and  $f_{low} \approx 1$  respectively, that the fractal dimension  $D \rightarrow 1$ . This behaviour is as expected for a time series in which is dominated by Poisson noise, which is the case for these two extremes. For intermediate

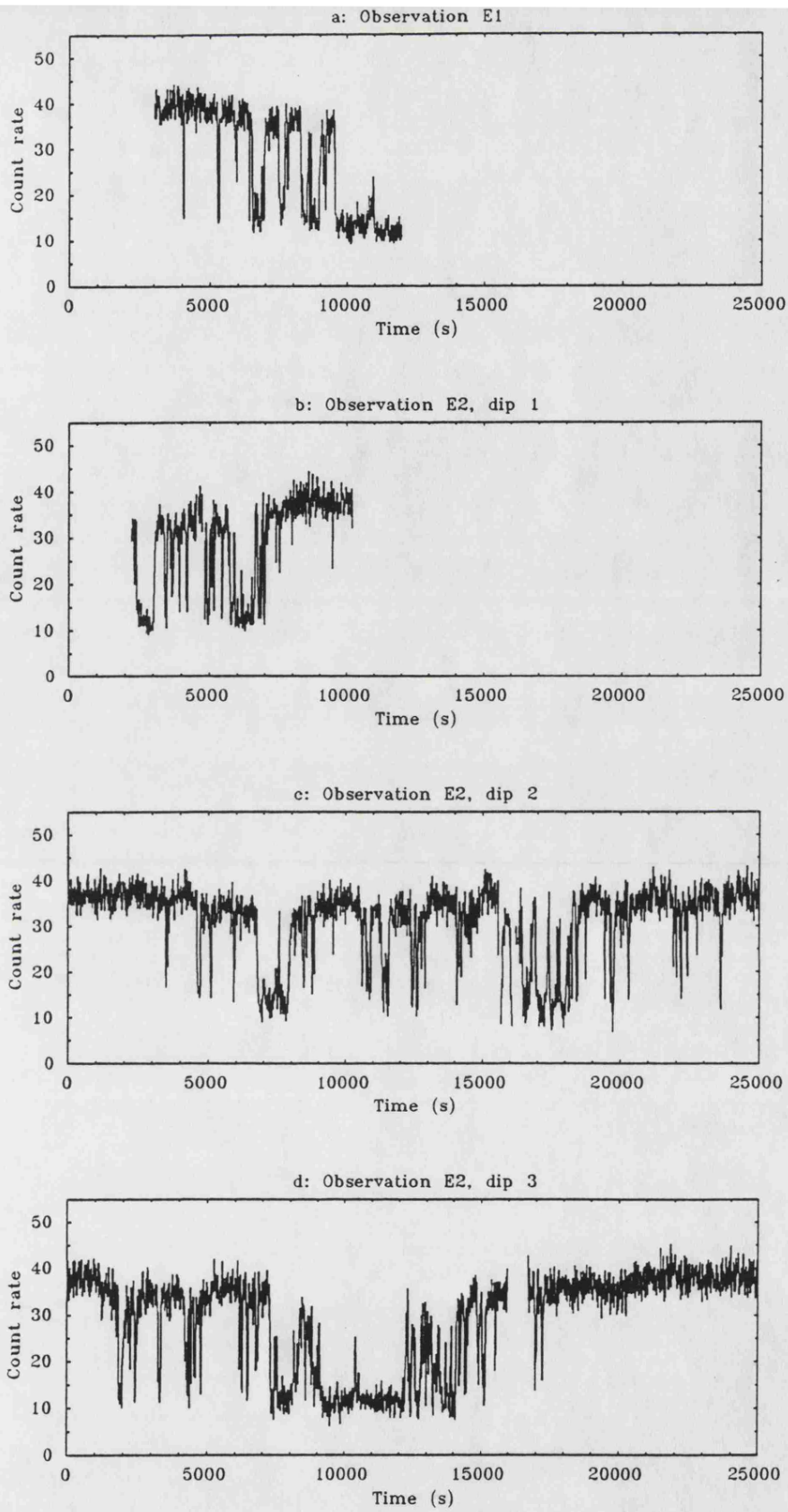


Figure 7.10: The 2-6 keV light curves from the EXOSAT observations of X 1624-490.

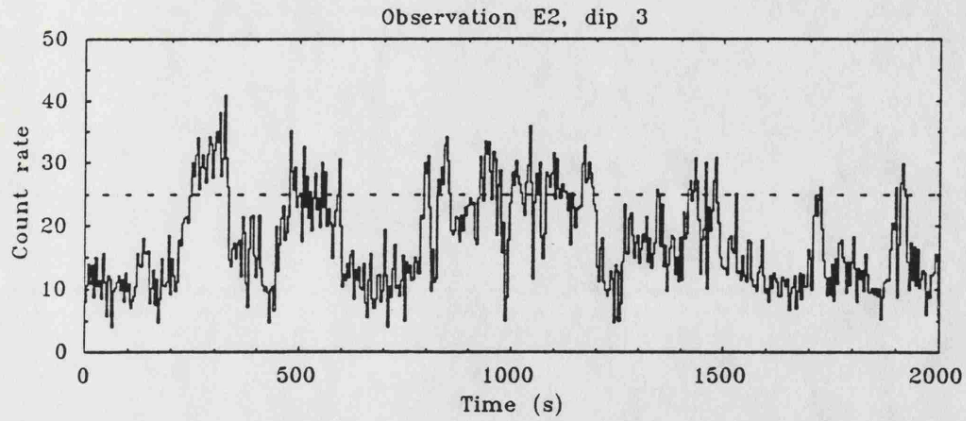


Figure 7.11: A 2000 sec duration sample from a period of dip activity in observation E2 of X 1624-490. The dashed line at 25 counts  $\text{sec}^{-1}$  is the threshold used for determination of the dip activity parameter  $f_{low}$ . The time resolution is 4 sec and the energy range is 2-6 keV.

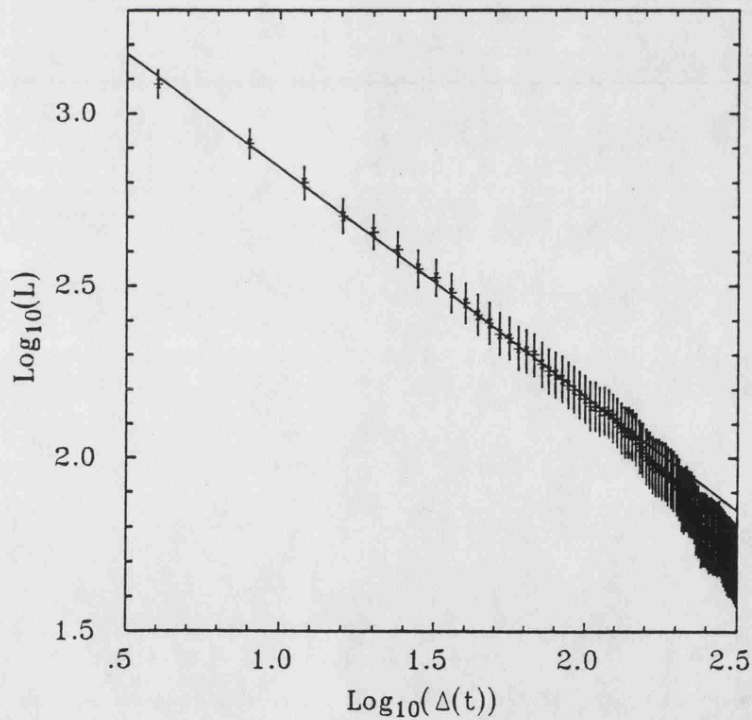


Figure 7.12: The fractal length function  $L(\Delta t)$  for the light curve sample shown in figure 7.11. The straight line is the best fit straight line over the interval  $\Delta t = 4 - 120$  sec, and yields a fractal dimension of  $D \approx 0.65$ . Note that for  $\log(\Delta t) \gtrsim 2.1$  the gradient of the fractal length function steepens and tends to the noise only case of  $D \approx 1$ .

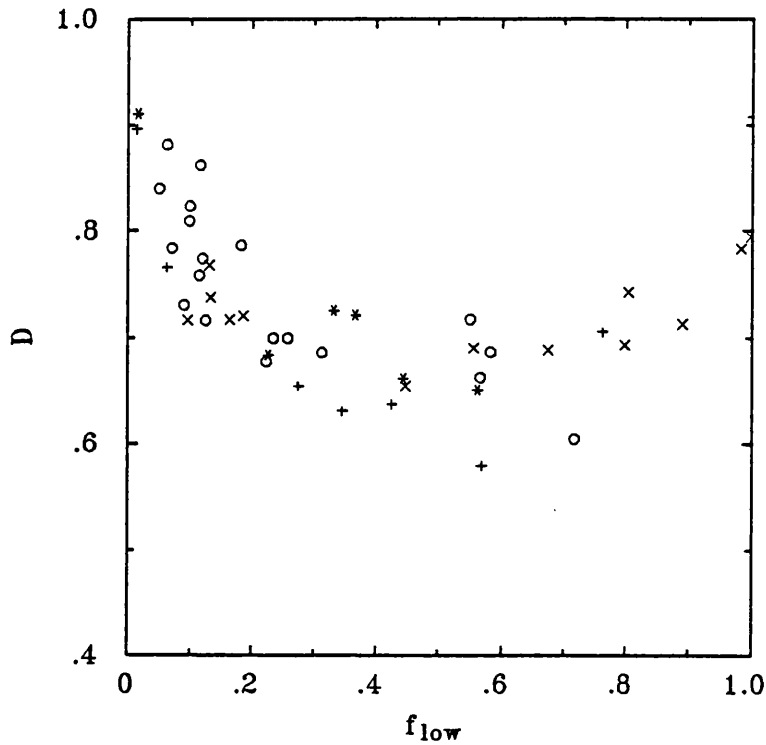


Figure 7.13: The values of  $D$  and  $f_{low}$  obtained from the light curves of X 1624-490 using the method described in the text. Key to observations: + - E1; \* - E2 dip 1; o - E2 dip 2; x - E2 dip 3.

values of  $f_{low}$ ,  $D$  responds to the dip variability, and for the data used here  $D(f_{low})$  follows a broad curve with a minimum of  $\sim 0.65$  at  $f_{low} \approx 0.5$ .

In order to investigate the implications of the observed  $D(f_{low})$  relationship, a simple model for dip variability was adopted. It is assumed that the dips are caused by occultation of a point-like source by spherical, sharp-edged, opaque clouds. The clouds are assumed to be in Keplerian orbit, and it is convenient to express the cloud radius ( $r_c$ ) as a time  $t_c$  such that  $t_c = r_c/v_k$ . The cloud density is specified in terms of column number density  $N_c$ , which is defined as the column density of cloud centres along the line of sight. The specification of the actual cloud density would require further assumptions to be made about the geometry of the cloudy region.

Two distributions of  $N_c$  have been studied; a Gaussian distribution of cloud radii (with mean

radius  $t_{mean}$  and width  $\sigma_t$ ,

$$N_c(t_c) = A \exp\left(-\frac{(t_c - t_{mean})^2}{2\sigma_t^2}\right) \quad (7.1)$$

and a power law distribution with index  $-\beta$ ,

$$N_c(t_c) = At_c^{-\beta} \quad (7.2)$$

The morphology of the light curve is expected to be a function of the parameters describing these distributions, whereas the actual degree of obscuration is dependent on the normalisation  $A$ .

The simulation method used to obtain  $D(f_{low})$  for these models was as follows. For each model about 50 or so values of the normalisation ( $A$ ) were chosen so as to cover the full range of  $f_{low}$  reasonably evenly. For each value of  $A$ , sixteen artificial data samples were generated, the simulated data having similar noise characteristics and sample length as the real data sections. Analysis of the simulated light curves was similar to that applied to real data, the only difference being that the assumption that  $D$  should be constant over the range  $\Delta t = 4 - 120$  sec was tested by measurement of the  $\chi^2$  of a linear fit to  $\log L(\log \Delta t)$ . For models giving a reasonable linear fit, the mean and standard deviation of  $D$  and  $f_{low}$  were estimated from the sixteen samples. In order to give a smooth representation of  $D(f_{low})$ , the mean values obtained were fit to a fourth order polynomial (which was found to be the lowest order that could give an acceptable fit to the simulated data). This simulation procedure was repeated for each model across the ranges of parameters of interest.

### 7.5.1 Gaussian models

The range of model parameters investigated had radii  $t_c$  from 25 to 150 sec, and distribution widths  $\sigma_t$  from 0.1 to  $2 t_c$ . It was found that there is a break in  $\log L - \log \Delta t$  at  $\Delta t \approx 2t_c$ . This is perhaps not surprising considering the similarity to the square shot model discussed in section 2.6.4. The condition that  $D$  should be consistent with being constant for  $\Delta t = 4 - 120$  sec and produce a 'break' at  $\Delta t \sim 120$  sec was satisfied only for  $50 \lesssim t_c \lesssim 100$ sec. In cases satisfying this condition the behaviour of  $D(f_{low})$  is rather insensitive to the actual model parameters, typically  $D$  has a minimum of  $\approx 0.55$  at  $f_{low} \approx 0.5$ . Examples of  $D(f_{low})$  for models with different radii are illustrated in figure 7.14, in these models  $\sigma_t = 0.2t_c$ . Although at large radii  $t_c > 150$  sec the behaviour of  $D(f_{low})$  tends toward the measured values, this solution cannot reproduce the required break in  $\log L(\Delta t)$  and so may be rejected.

There is a small dependence on  $\sigma_t$ , with wider distributions showing higher minimum values of  $D$ . This is illustrated in figure 7.15 which shows three models with  $t_c = 60$  sec and  $\sigma_t$  of 12, 60 and

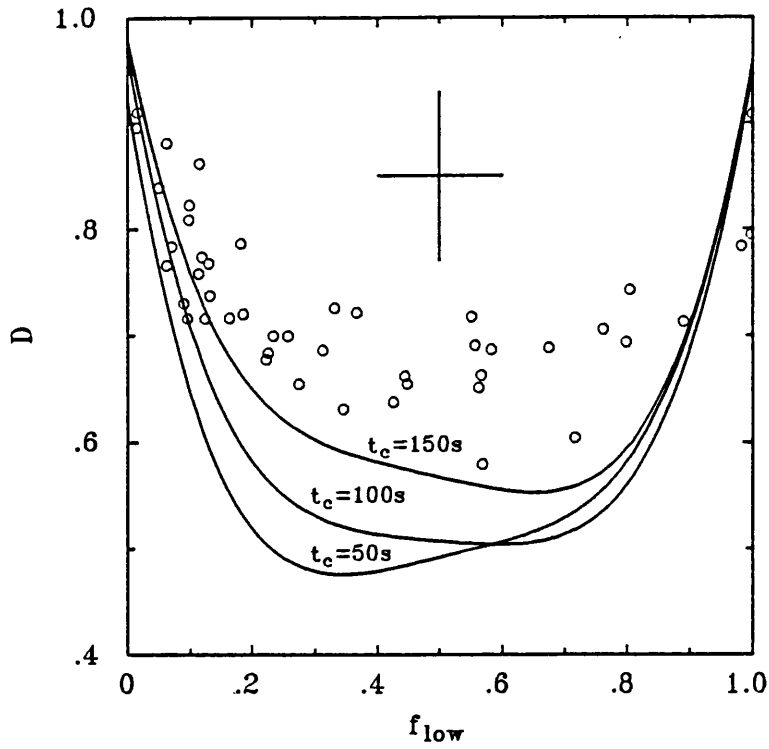


Figure 7.14: The behaviour of  $D(f_{low})$  for Gaussian cloud distributions with different mean radii. In all cases the width of the distribution is  $\sigma_t = 0.2 \times t_c$ . A representative  $(1\sigma)$  error bar is shown. Open circles indicate the measured  $D - f_{low}$  values.

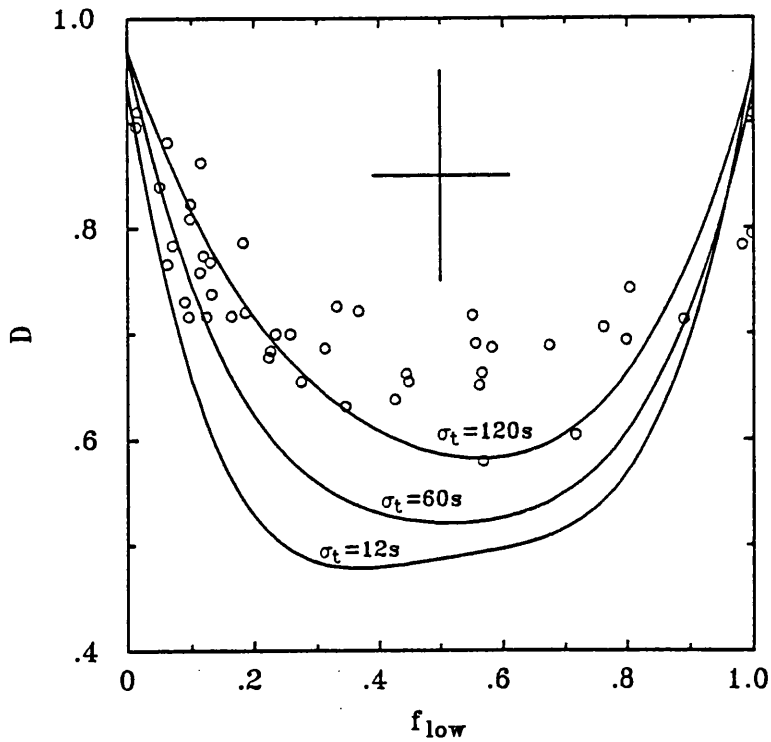


Figure 7.15: The behaviour of  $D(f_{low})$  for Gaussian cloud distributions with different widths. In all cases the mean of the distribution is  $t_c = 60$  sec. A representative  $(1\sigma)$  error bar is shown. Open circles indicate the measured  $D - f_{low}$  values.

120 sec respectively. It can be seen that agreement of the data with a Gaussian model is attained only for very wide distributions ( $\sigma_t > t_c$ ). For such skewed distributions the justification for using a Gaussian model is no longer valid, and a power-law type distribution is more appropriate.

## 7.5.2 Power Law models

Before describing the simulations of the power law distributions it is worth considering the geometric implications of this type of model. Three parameters are required to describe a power-law model, the index  $\beta$  and the range of radii in the distribution ( $t_{low}$  to  $t_{high}$ ). The case of  $\beta = 2$  represents the case in which the contribution to the covered area is independent of cloud radius. For  $\beta > 2$  the smaller clouds will dominate dip variability, and this would be reflected in  $D(f_{low})$  being strongly dependent on  $t_{low}$ . Conversely, for  $\beta < 2$  a dependence of  $D(f_{low})$  on  $t_{high}$  is expected.

The simulations allow a more detailed study of the expected behaviour of  $D(f_{low})$ , and a study of models with  $\beta = 1, 2$  and  $3$ , is shown in figures 7.16, 7.17, and 7.18. Note that as expected, in the case of  $\beta = 2$  there is a dependence on both  $t_{low}$  and  $t_{high}$ . The real data which are also shown on these figures suggest that a wide range of models would be appropriate.

There are two points which help in constraining the parameters. The first is that  $t_{low}$  can be reasonably estimated from the dip light curve. Deep dips of duration  $\sim 5$  sec are observed in the *Ginga* data, but the minimum dip transition times suggest that cloud envelopes become resolvable on time scales  $\sim 1$  sec. An assumption of the model was that the clouds are sharp-edged, this is clearly not valid for  $t_{low} \lesssim 1$  sec. Secondly, the model should satisfy the criterion that  $\log L$  should be linear over the required range of  $\Delta t$ . From inspection of  $L(\Delta t)$  it is found that this can only be achieved for  $t_{high} \gtrsim 60$  sec. Furthermore, the requirement that there should be a break at  $\Delta t \sim 100$  sec requires that  $t_{high} < 200$  sec. Adopting limits to the distribution of  $t_{low} = 2$  sec and  $t_{high} = 60$  sec, figure 7.19 shows the behaviour of  $D(f_{low})$  as a function of  $\beta$ . It can be seen that the data are consistent with power-law distributions with  $\beta \approx 1.75$  to  $2.25$ .

Thus the clouds do not have a well defined characteristic radius. A model of the cloud column density distribution which is consistent with the data is one which scales as  $r_c^{-2}$  over a range of cloud radii,  $t_c$ , from 2 to 60 sec. In terms of linear dimension, these radii scale with the Keplerian velocity. From section 7.4 the values of  $v_k$  appropriate to the  $r_{circ}$  and  $r_{outer}$  are  $\sim 750$  and  $\sim 430$  km s $^{-1}$  respectively. The cloud velocity is likely to lie between these two values and a reasonable estimate

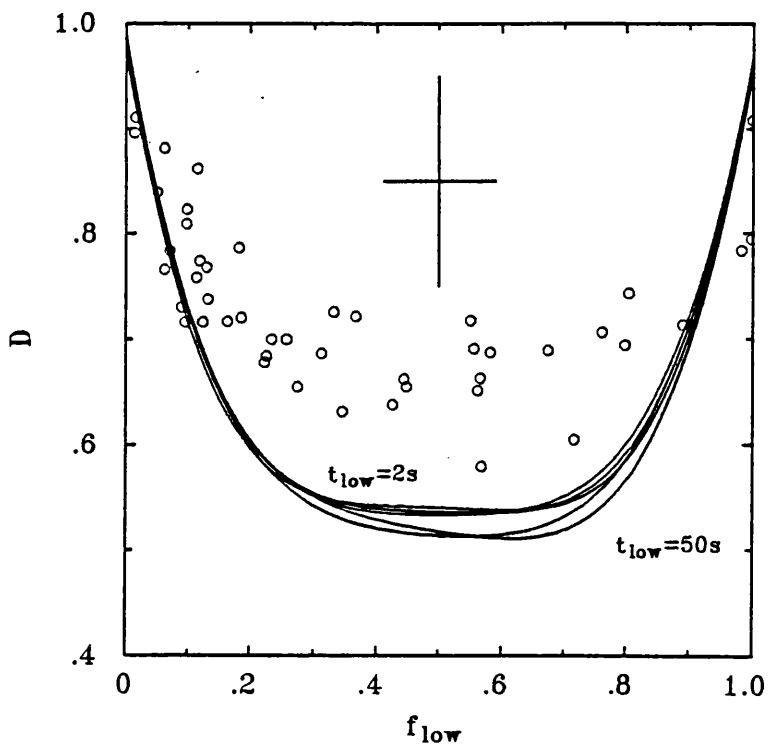
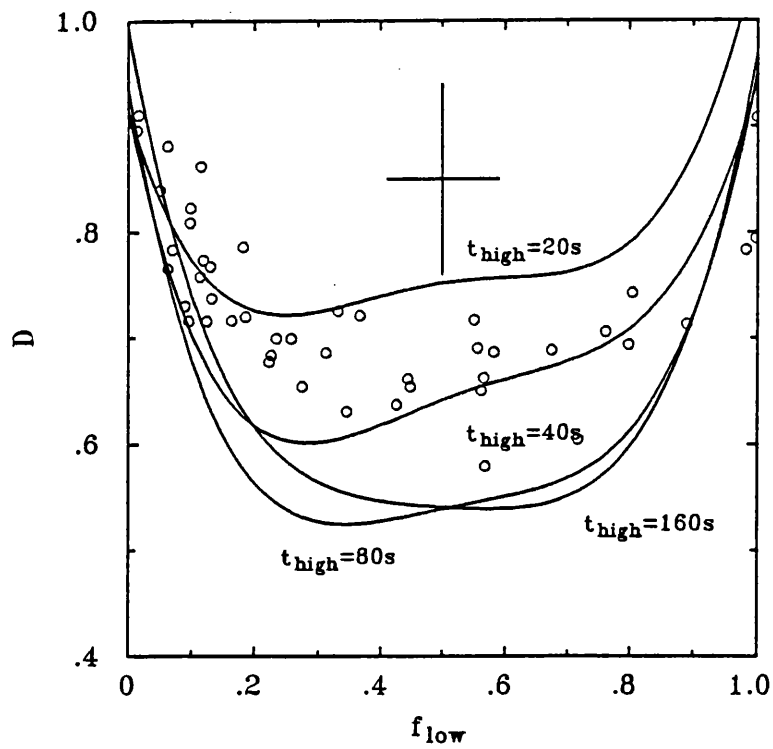


Figure 7.16: Simulated  $D(f_{low})$  behaviour for a set of power law models with  $\beta = 1$ . The top panel shows models in which the lower edge of the distribution ( $t_{low}$ ) is fixed at 2 sec and the upper edge ( $t_{high}$ ) is varied as shown. The lower panel shows models in which  $t_{high}$  is fixed at 150 sec, and  $t_{low}$  is varied as shown. It can be seen that  $\beta = 1$  models are sensitive to  $t_{high}$ . Observational data are shown by open circles.

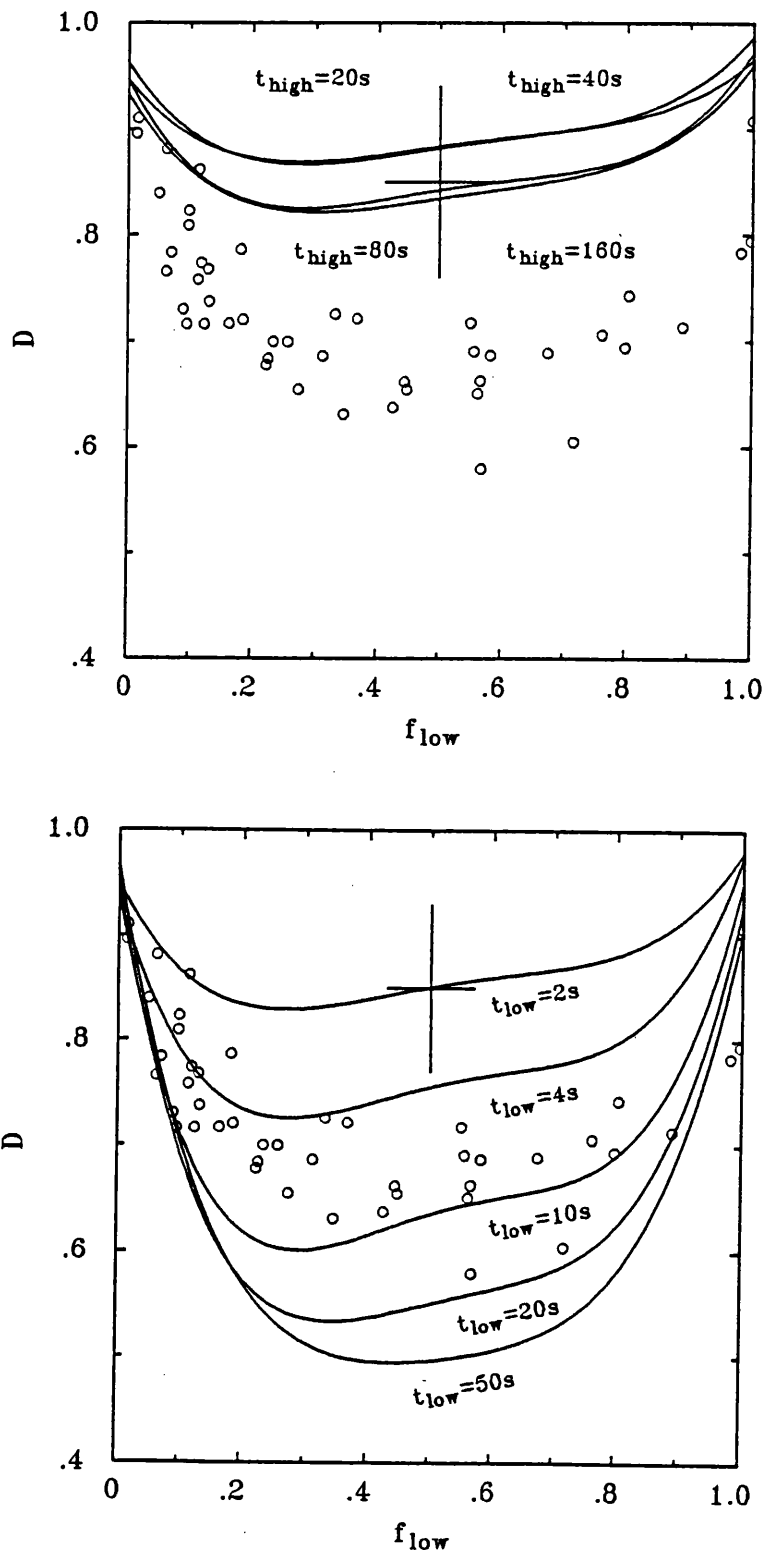


Figure 7.17: Simulated  $D(f_{low})$  behaviour for a set of power law models with  $\beta = 3$ . The top panel shows models in which the lower edge of the distribution ( $t_{low}$ ) is fixed at 2 sec and the upper edge ( $t_{high}$ ) is varied as shown. The lower panel shows models in which  $t_{high}$  is fixed at 150 sec, and  $t_{low}$  is varied as shown. It can be seen that  $\beta = 3$  models are sensitive to  $t_{low}$ . Observational data are shown by open circles.

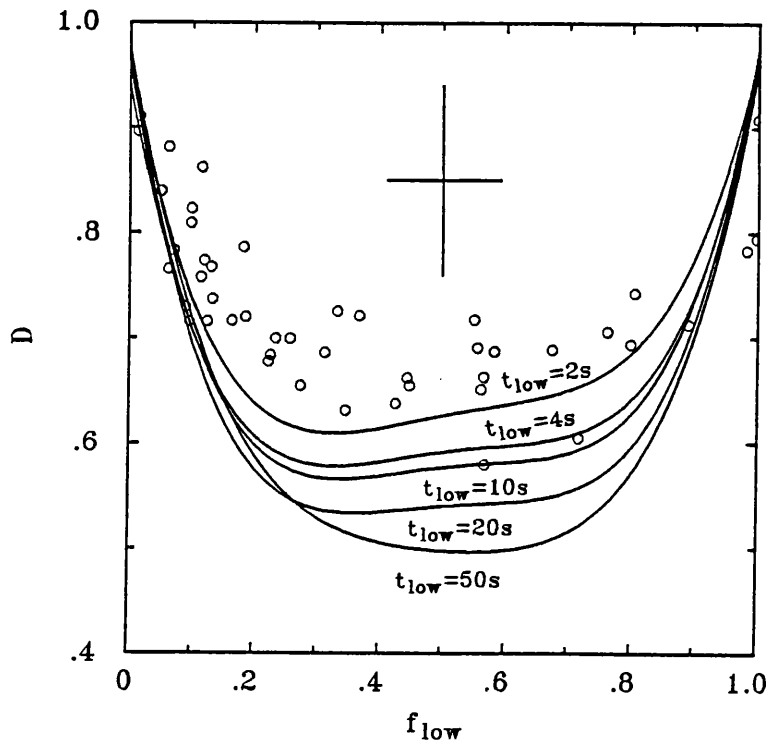
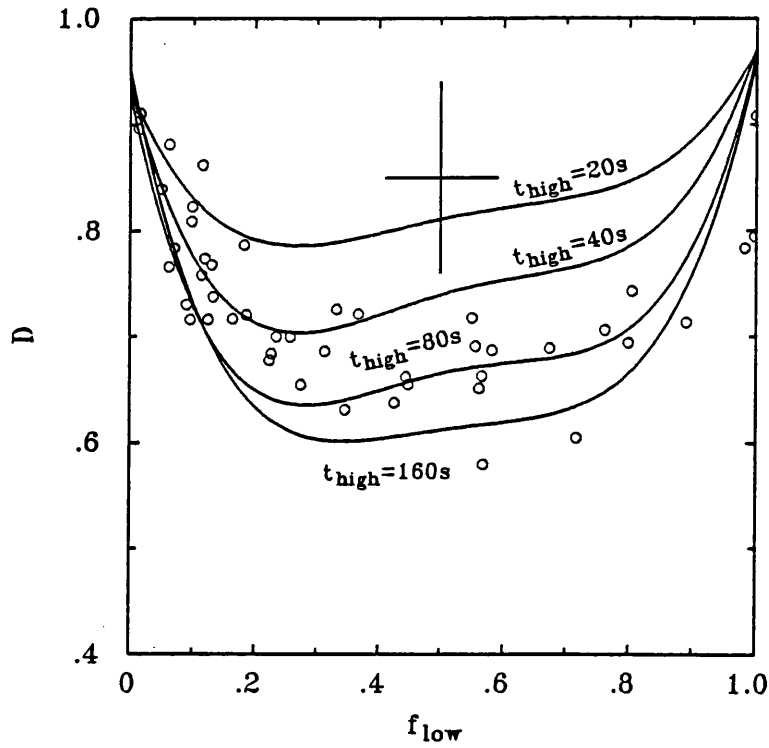


Figure 7.18: Simulated  $D(f_{low})$  behaviour for a set of power law models with  $\beta = 2$ . The top panel shows models in which the lower edge of the distribution ( $t_{low}$ ) is fixed at 2 sec and the upper edge ( $t_{high}$ ) is varied as shown. The lower panel shows models in which  $t_{high}$  is fixed at 150 sec, and  $t_{low}$  is varied as shown. It can be seen that  $\beta = 2$  models are sensitive to both  $t_{low}$  and  $t_{high}$ . Observational data are shown by open circles.

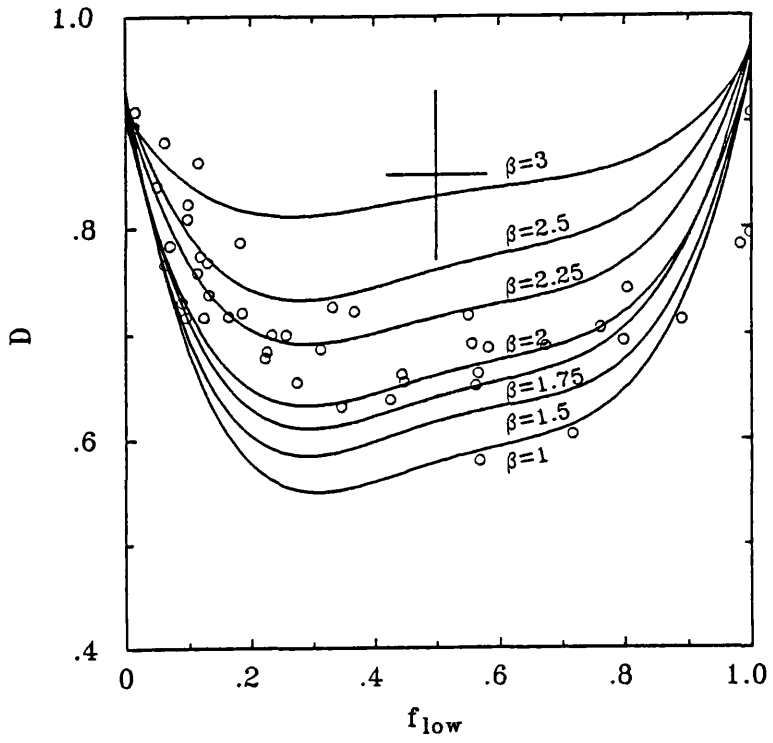


Figure 7.19: Simulated  $D(f_{low})$  behaviour for a set of power law models with fixed  $t_{low} = 2$  sec and  $t_{high} = 60$  sec, but with distribution index  $\beta$  allowed to vary. It may be seen that models with  $\beta \approx 1.75$  to 2.25 are consistent with the observed values of  $D(f_{low})$  (shown by open circles).

is  $v_k \sim 600 \text{ km}^{-1}$ . Thus the implied range of cloud radii is  $\sim 1200$  to  $\sim 36,000 \text{ km}$ .

## 7.6 THE NON-DIP SPECTRAL BEHAVIOUR

The modelling of dip spectral variability requires a good representation of the non-dip state. Ideally, this would be obtained from a physically justifiable model. The approach adopted was to fit the quiescent (i.e. non-dipping, non-bursting) spectrum to single power-law, thermal bremsstrahlung, blackbody and generalised thermal models before using combinations of these components. In practice however the goal of a physically justifiable model was achieved only for XBT 0748-676.

### 7.6.1 XB 1916-053

The non-dip spectrum of XB 1916-053 shows little variability on timescales of up to a few days, being constant over the duration of the individual observations. Mean non-dip spectra were generated for observations G2 and G3. Since dip activity occurs for a wide range of orbital phase, the non-dip data were selected using a hardness ratio  $((6-10 \text{ keV})/(2-6 \text{ keV}))$  as a discriminator. These accumulated spectra have exposure times of 7200 and 2470 sec respectively. Both spectra were fitted to a selection of single and double component continuum models. A summary of the goodness of fit of these models is given in table 7.4. It can be seen that no model gives an acceptable fit to the data from G2, although several models give marginally acceptable fits to the G3 data. The best fit model to the EXOSAT data (LE and ME) is a simple power law with  $\alpha = 1.8$  and  $N_H = 2 \times 10^{21} \text{ cm}^{-2}$ , (Smale *et al.*, 1988). A simple power law is an unacceptable fit to the *Ginga* data ( $\chi^2_\nu = 6.26$ , 25 d.o.f.), although the parameters of this fit agree with the EXOSAT results within the errors of measurement.

Of all the physically justifiable models the best fit is obtained for a power law with a blackbody ( $\chi^2_\nu = 2.46$  and  $1.51$ , 23 d.o.f., for G2 and G3 respectively). The data and model (for G3) are illustrated in figure 7.20, and it can be seen that there are large systematic trends in the residuals. Consequently an unphysical parameterisation of the spectra was adopted for the study of the dip spectra (section 7.7), this being a power-law model with a broad Gaussian line. Typical parameter values were found to be  $\alpha \approx 1.9$ , with a line of width  $\sim 1.5 \text{ keV}$  at an energy of  $\sim 5.5 \text{ keV}$ , the exact values determined from observations G2 and G3 are given in table 7.5.

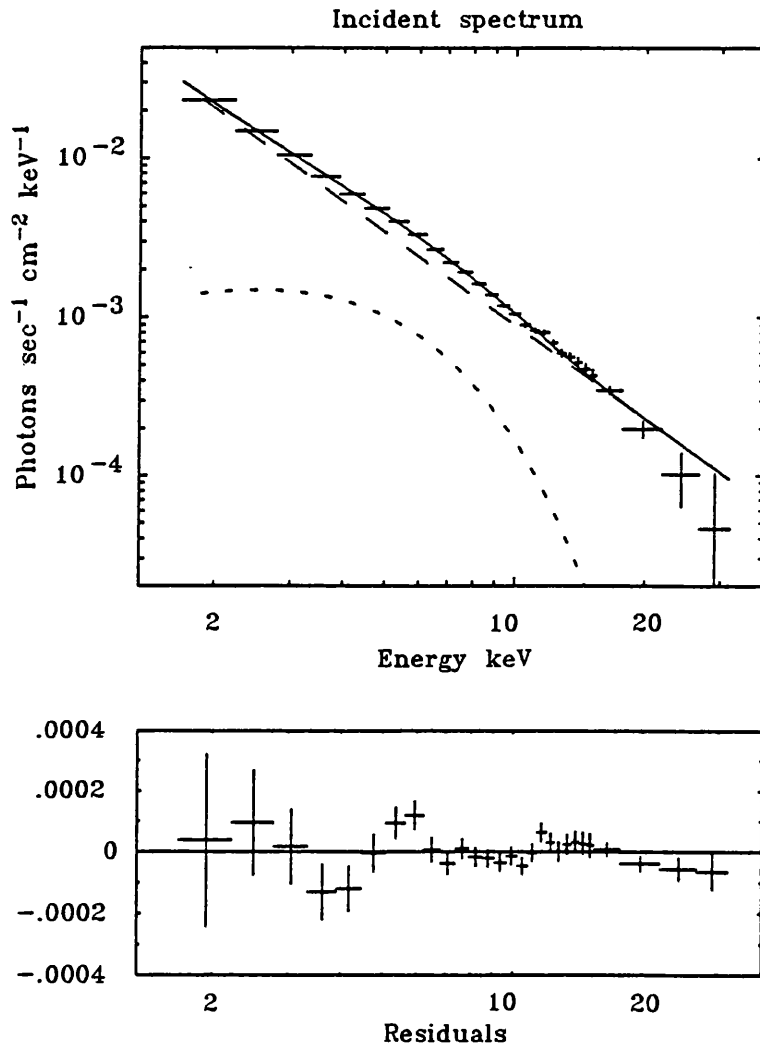


Figure 7.20: The mean non-dip spectrum from observation G3 of XB 1916-053. The model shown here consists of a power-law and a blackbody component, with  $\alpha \approx 1.9$  and  $kT_{bb} \approx 1.6$  keV. The fit is poor,  $\chi^2_{\nu} = 1.51$ , and shows large systematic residuals.

## 7.6.2 XBT 0748-676

The quiescent spectrum of XBT 0748-676 was obtained using a similar method to that applied to XB 1916-053, using the hardness ratio as a criterion to reject dip activity. The data were selected from the good attitude MPC1 data and correspond to 4970 sec of exposure. The best fit single component model was found to be the generalised thermal spectrum ( $\chi^2_\nu = 1.29$ , 24 d.o.f.), with  $\Gamma = 2.23 \pm 0.15$ ,  $kT_{char} = 13.2^{+4.7}_{-2.7}$  and  $N_H = (6.9^{+2.5}_{-2.3}) \times 10^{21} \text{ cm}^{-2}$  (90% confidence). It should be noted however that the residuals to the fit show large systematic trends (see figure 7.21). Out of the eight EXOSAT observations of XBT 0748-676, the non-dip spectrum was best fit by generalised thermal models in seven cases, the other being best fit by a power law (Parmar *et al.*, 1986). The *Ginga* spectrum lies within the range of model parameters from these EXOSAT spectra, these being  $\Gamma = -0.28$  to 2.25 and  $kT_{char} = 4$  to 20 keV.

## 7.6.3 X 1624-490

As has already been discussed in section 7.3, the broad-band spectral behaviour suggests at least two components to the emission. It was necessary to isolate and model the low state spectrum (component A) before attempting to describe the quiescent source spectrum (A+B).

### The Low State Spectrum

The difficulty in the isolation of A by intensity selection lies in the choice of a suitable upper cut-off intensity ( $I_{cut}$ , defined as the count rate in the 2-10 keV band). Although higher signal/noise is obtained as  $I_{cut}$  increases, the contribution from the highly absorbed B component also increases. This degree of contamination was studied by inspection of the change in spectral parameters required to fit intensity selected spectra as  $I_{cut}$  was varied. It was found, using a power-law model for A, that the spectral slope ( $\alpha$ ) decreased with increasing  $I_{cut}$ . At  $I_{cut} \sim 100 \text{ counts sec}^{-1}$ , a deep absorption edge from the transmitted B component becomes evident in the spectra. The finally adopted value of  $I_{cut} = 90 \text{ counts sec}^{-1}$  was chosen as the point at which the trend in  $\alpha$  with  $I_{cut}$  becomes consistent with being constant (given the errors of measurement in  $\alpha$ ). With this value  $I_{cut}$  the total spectral integration time is 160 sec. This spectrum was fitted to simple one-component models, both power-law and thermal bremsstrahlung models give acceptable fits to the data, ( $\chi^2_\nu = 0.23$  and 0.60 respectively, both with 12 d.o.f.), whereas a blackbody model does not ( $\chi^2_\nu = 2.26$ , 12 d.o.f.). The best fit parameters are given in table 7.3. The power-law

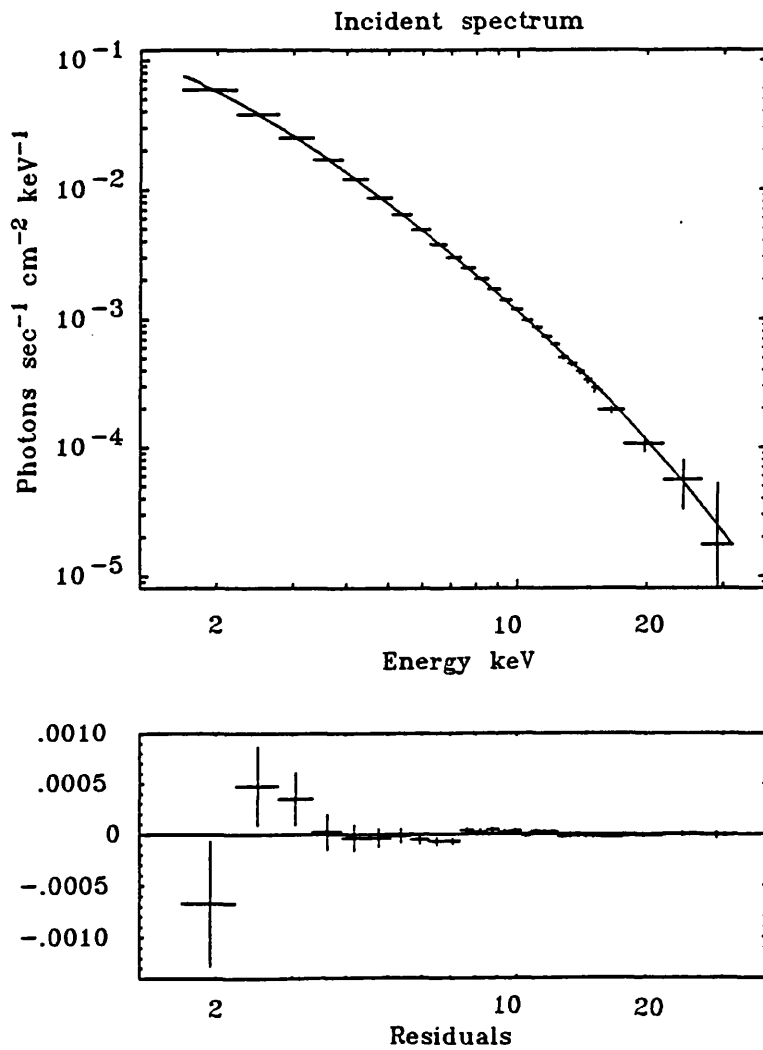


Figure 7.21: The mean non-dip spectrum from the *Ginga* observation of XBT 0748-676. The model shown is a generalised thermal continuum with  $\Gamma \approx 2.2$  and  $kT_{char} \approx 13$  keV, and has  $\chi^2_\nu = 1.3$  (24 d.o.f.).

Power Law	Thermal Bremsstrahlung
$\chi^2_\nu = 0.23, 12 \text{ d.o.f.}$	$\chi^2_\nu = 0.60, 12 \text{ d.o.f.}$
$A_{pl} = 2.2^{+1.1}_{-0.1} \text{ phot sec}^{-1} \text{ cm}^2 \text{ keV}^{-1}$	$A_{tb} = 0.23^{+0.12}_{-0.07} \text{ phot sec}^{-1} \text{ cm}^2 \text{ keV}^{-1}$
$\alpha = 3.8^{+0.4}_{-0.3}$	$kT = 2.7^{+0.4}_{-0.3} \text{ keV}$
$N_H = (103^{+19}_{-16}) \times 10^{21} \text{ cm}^{-2}$	$N_H = (68^{+14}_{-11}) \times 10^{21} \text{ cm}^{-2}$

Table 7.3: Best fit models to the low state (A) component in X 1624-490. Errors are quoted for the 90% confidence interval.

representation of A has been used in all subsequent modelling. Inspection of the residuals to this spectral model however, reveals an excess just above 7 keV, suggesting that the cold iron edge, and hence the  $N_H$ , is overestimated.

### The quiescent spectrum

The non-dipping, non-flaring state of the source will be referred to as the quiescent state. The flaring activity described in section 7.3 is distinguished by a high value of the hardness ratio ( $H_R$ , the ratio of fluxes (6-10 keV)/(2-6 keV)) and excess variability in the 6 – 10 keV band. The data representative of the quiescent state were selected using  $H_R$  and hard variability as a discriminator. Although the hard-soft flux behaviour appears single branched (see figure 7.7), it was found that there are significant changes in the quiescent spectrum on timescales of a few 1000 sec. The spectral analysis presented here is for 1900 sec of data from observation G2, chosen by the above criteria and by proximity to the main dip interval of dip activity and the period of intense flaring activity (all occurring within  $\sim 2 \times 10^4$  sec).

Using the power-law representation for A, various spectral models were fitted to the B component. A summary of the models used is given in table 7.4, and it can be seen that only a few give formally acceptable fits to the data. A close inspection of even the good fits to the data reveals that in all cases the presence of systematic residual patterns. An example of this is given in figure 7.22, which shows a thermal bremsstrahlung and blackbody model for B. Note the sharp features at 5 keV. Attempts to model the residual features by iron line emission or absorption edges were unsuccessful. Thus a physical interpretation of the quiescent spectrum in terms of any of the models presented would seem inappropriate. The spectrum could however be reasonably well parameterised by a

two-component model for **B** consisting of a thermal bremsstrahlung at  $kT_{brem} \approx 5$  keV, and a broad Gaussian line centred at 5.3 keV with a width of 1.4 keV. The goodness of fit of this model is  $\chi^2_\nu = 1.13$  for 22 d.o.f.

### The Flaring State

The hard variability of X 1624-490 is characterised by changes of up to 50% of the 5-10 keV flux, while the 2-5 keV flux remains almost constant. The flaring shows variability on timescales of  $\sim 10$  to a few 100 sec, and is intermittent, having active periods of duration of up to tens of thousands of sec.

To study the spectral behaviour of flaring component in more detail, a difference spectrum was generated by subtraction of quiescent data from that showing a large degree of flaring. This component has a mean count rate of  $\sim 85$  counts  $\text{sec}^{-1}$ . The spectrum was fitted to simple one component models, of which, only the blackbody spectrum gave an acceptable fit ( $\chi^2 = 0.84$ , 25 d.o.f.). The best fit parameters being  $kT = 2.18 \pm 0.06$  keV,  $N_H = 95 \times 10^{21}$   $\text{cm}^{-2}$ , the spectrum and model are shown in figure 7.23.

Intensity selection was performed to see if the luminosity of this component is correlated with the blackbody temperature. Four intensity bands, covering a flux range of  $15$  to  $30 \times 10^{-11}$   $\text{ergs cm}^{-2} \text{sec}^{-1}$  were used, the column density in the fitted models was fixed at the value obtained from the mean spectrum. Figure 7.24 shows the best fit temperatures against flux, with the solid curve representing the expected behaviour for a constant area blackbody (in which  $T \propto L_x^{1/4}$ ). The interpretation that the flare variability is due to changing temperature is excluded by the data at a confidence level  $> 95\%$ . If the flaring does have a blackbody origin the emitting area must vary, and the implied radii are  $r_{bb} < 1.3(d/10 \text{ kpc})$  km.

## 7.7 SPECTRAL ANALYSIS OF THE DIPS

The approach adopted in the study of the spectral changes during dip events was to test whether intensity selected dip spectra are consistent with simple models of absorption of the quiescent spectra of the individual sources. The data considered in this analysis correspond to periods of dip activity that were monitored while the LAC was in MPC2 (all bit rates) or MPC1 (in high and

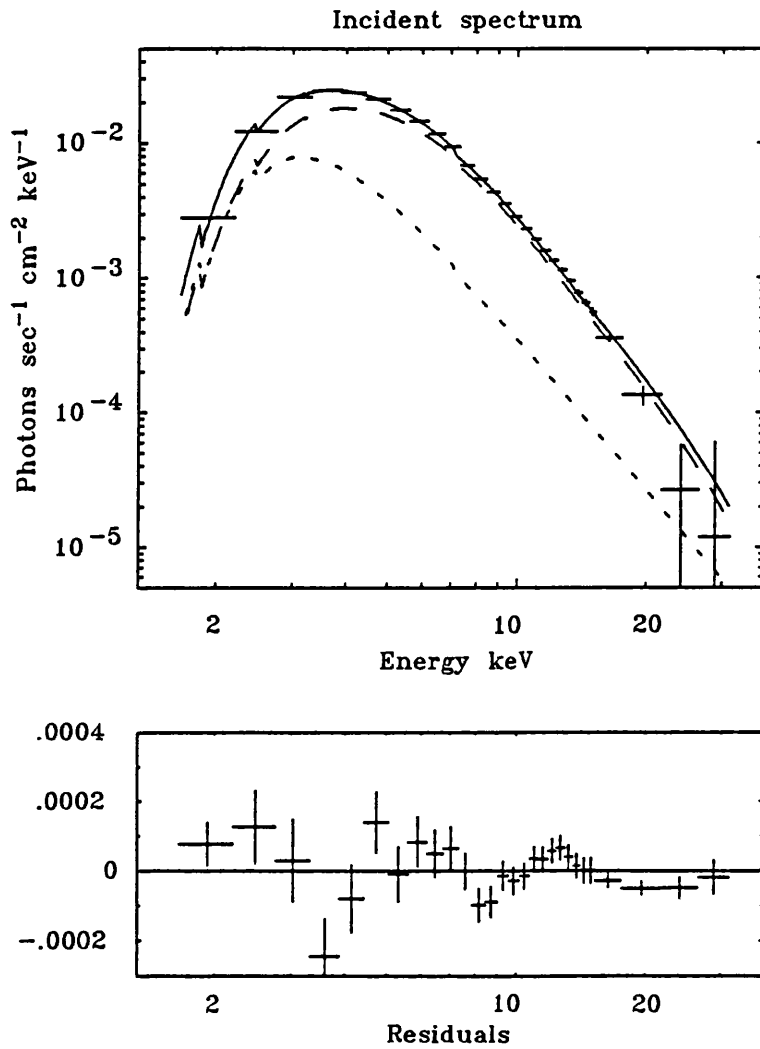


Figure 7.22: The spectrum of X 1624-490 for 1900 sec exposure of a quiescent interval. The low state emission (A) is modelled by a power-law (thin dashed curve). The second component (B) is in this case fitted by a combination of thermal bremsstrahlung and blackbody continua (broad dashed curve). The goodness of fit is  $\chi^2_\nu = 1.87$ , and the residuals show poor systematic trends.

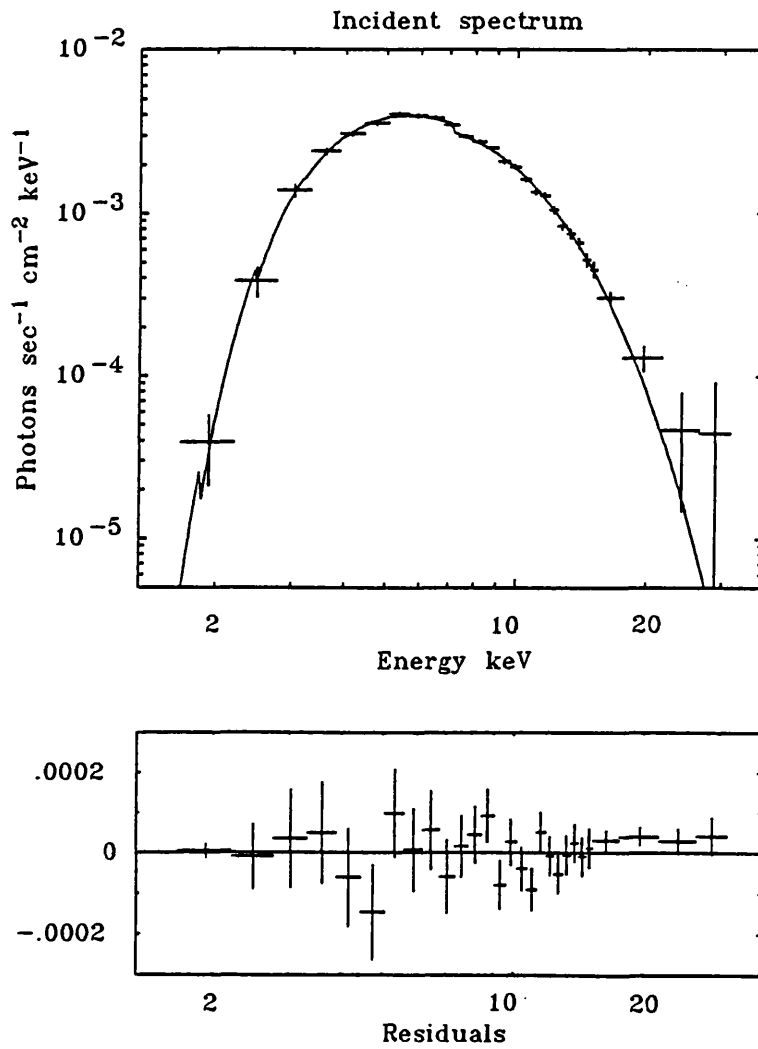


Figure 7.23: The spectrum of the flaring component in X 1624-490. The best fit model ( $\chi^2 = 0.84$ ) is a blackbody continuum with  $kT \approx 2.2$  keV.

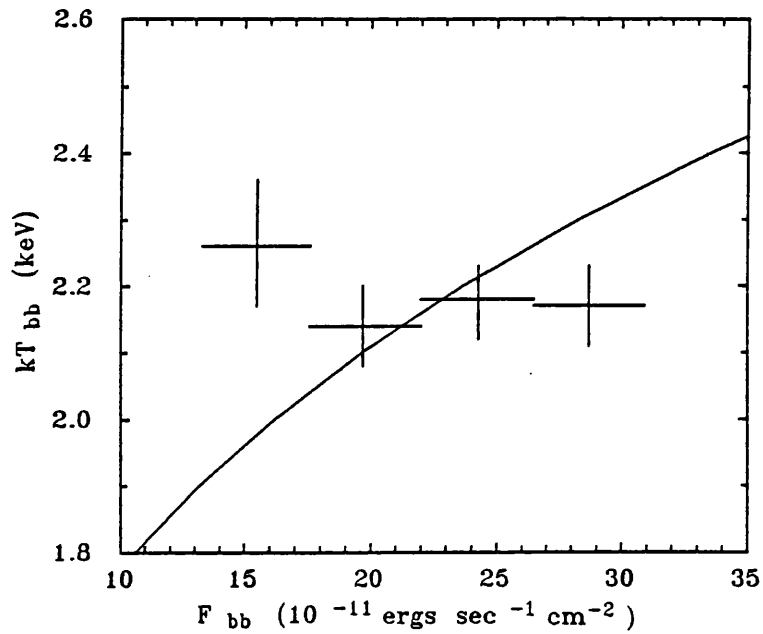


Figure 7.24: The best fit blackbody temperatures to the intensity selected difference spectra of the flaring state in X 1624-490. The solid curve shows the expected behaviour for blackbody emission in which the luminosity changes are due solely to variability in the temperature of the emitter. This model can be ruled out at a confidence level of  $> 95\%$ .

Mode	X 1624-490	XB 1916-053		XBT 0748-676
	G2	G2	G3	G1
<b>One Component</b>				
Power Law	69	6.26	6.13	6.32
Thermal bremsstrahlung	10.5	3.88	4.15	21.2
Blackbody	48	> 100	> 100	> 100
Generalised thermal	6.93	3.72	2.39	1.29
Cut-off power law	2.30	2.69	2.49	1.14
<b>Two-Component</b>				
Thermal bremsstrahlung + power law	11.4	3.60	2.09	0.77
Thermal bremsstrahlung + thermal bremsstrahlung	11.5	3.49	2.35	0.60
Power law + blackbody	3.22	2.46	1.51	0.74
Thermal bremsstrahlung + blackbody	1.87	3.53	2.33	0.81
Generalised thermal + blackbody	2.21	2.43	1.57	0.60

Table 7.4: Reduced chi-squared values for best fit models to quiescent spectra.

medium bit rate only) for X 1624-490 and XB 1916-053. In the case of XBT 0748-676, only MPC1, low bit rate ( $\Delta t = 16$  sec) data were available. Since the dip variability occurs on timescales as short as a few seconds, it may be expected that the results will be sensitive to the intrinsic time binning of the data. However, for high time resolution data, the errors in determination of the flux used to select the spectra become large, which would also lead to mixing of different spectral states within a chosen intensity band. The data considered here have been selected at maximum or near maximum available time resolution, and the intensity bands chosen such that the errors in the flux determination are small with respect to the selection window. Typically the intensity states were divided into about 10–15 bands of equal width. The observations used for this study were G2 and G3 of XB 1916-053 (treated separately), G1 of XBT 0748-676, and G2 of X 1624-490.

In order to check that the quiescent spectrum near the dip events was similar to the mean quiescent models determined above, the highest intensity state spectrum was fitted to the appropriate quiescent model discussed in section 7.6, allowing only the normalisation and column density to vary. In the case of XB 1916-053 and XBT 0748-676 these provided acceptably good fits, and the quiescent parameterisations were used in the analysis of the dips. In the case of X 1624-490 however, the fit was poor ( $\chi^2_\nu = 8.15$ , 26 d.o.f.), and the spectrum used for the dip modelling was obtained by fitting the high intensity state, but in this case leaving all model parameters of component B free. The best fit combination of thermal bremsstrahlung and broad emission line gave an acceptable fit with  $\chi^2_\nu = 1.13$ . The spectral parameterisations used are summarised in table 7.5. Note that during the modelling of the absorption process, only the normalisations and the column densities were allowed to vary, the other parameters were always fixed.

Two models were tested for the absorption properties of the dip data. The first, simple photoelectric absorption of the quiescent spectrum was found to give a poor fit to the data for the low intensity states (typically  $\chi^2_\nu > 2$ , for 26 d.o.f.), showing an excess of counts at low energies over that which would be expected for the fitted value of the column density.

The second model has two-components, both with the same continuum shape as the high state. The column density is a free parameter for one component and fixed at the quiescent value for the other. The normalisations of both components are free parameters in the fit. The motivation behind adopting this type of model, is that it is found to approximate well to situations in which there is some degree of low-energy ‘leakage’ of the absorber. This model has been used frequently in the analysis of dip sources (see, for example, Parmar *et al.*, 1986), and is generally found to be a good representation of spectral behaviour. For these data it was found to be acceptable across all intensity states ( $\chi^2_\nu \sim 1$ , for 25 d.o.f.) for all observations. The results of fitting this model to

Table 7.5: Spectral parameterisations of the quiescent state used in the modelling of the dip spectra.

X 1624-490	XB 1916-053		XBT 0748-676
G2	G2	G3	G1
TB + BL	PL + BL		GT
$\chi^2_\nu = 1.13$	$\chi^2_\nu = 1.81$	$\chi^2_\nu = 1.25$	$\chi^2_\nu = 1.29$
$A_{brem} = 0.27$ $kT_{brem} = 4.87$ keV	$A_{pl} = 0.57 \times 10^{-1}$ $\alpha = 1.86$	$A_{pl} = 0.87 \times 10^{-1}$ $\alpha = 1.95$	$A_{gen} = 0.41$ $\Gamma = 2.23$ $kT_{gen} = 13.2$ keV
$E_{line} = 5.29$ keV $F_{line} = 0.122 \times 10^{-1}$ $\Delta E_{line} = 1.38$ keV	$E_{line} = 5.84$ keV $F_{line} = 0.15 \times 10^{-2}$ $\Delta E_{line} = 1.5$ keV	$E_{line} = 5.50$ keV $F_{line} = 0.26 \times 10^{-2}$ $\Delta E_{line} = 1.8$ keV	
$N_H = 106 \times 10^{21}$	$N_H = 4.9 \times 10^{21}$	$N_H = 5.7 \times 10^{21}$	$N_H = 6.9 \times 10^{21}$

**Notes:** The  $\chi^2_\nu$  values refer to the fit to the quiescent data, except in the case of X 1624-490 which refers to the fit to the highest intensity state during an interval of dip activity. Models; TB - Thermal bremsstrahlung; PL - Power-law; GT - Generalised thermal; BL - Broad Gaussian line. Normalisation ( $A$ ) is expressed in units of photons  $\text{sec}^{-1} \text{cm}^{-2} \text{keV}^{-1}$ ;  $E_{line}$  is the line energy;  $F_{line}$  is the line flux in photons  $\text{sec}^{-1} \text{cm}^{-2}$ ;  $\Delta E_{line}$  is the Gaussian width ( $\sigma$ );  $N_H$  in units of H atoms  $\text{cm}^{-2}$ .

the four data sets are illustrated in figures 7.25 to 7.28, which show the column density and the normalisations of both components as a function of the intensity band. It can be seen that the behaviour of these parameters is similar in all three objects.

In all cases the highest intensity states are adequately modelled by a single spectral component with the quiescent value of  $N_H$ . In these cases the normalisations of the two-components cannot be constrained in the fitting routine. The flux levels above which this condition occurs are indicated by dashed vertical lines in figures 7.25 to 7.28. Below these flux thresholds the parameters vary with dip depth in a similar way for each source. The column density increases approximately exponentially with dip depth. The range of column densities is  $\sim 2000 \times 10^{21} \text{ cm}^{-2}$  at dip maximum to the non-dip value of  $\sim 100 \times 10^{21} \text{ cm}^{-1}$  in X 1624-490. For XB 1916-053 and XBT 0748-676 the corresponding ranges are  $\sim 700$  to  $\sim 5 \times 10^{21} \text{ cm}^{-1}$  and  $\sim 220$  to  $\sim 7 \times 10^{21} \text{ cm}^{-1}$  respectively. The normalisation of the fixed absorption component appears to decrease approximately exponentially with dip depth. The normalisation of the variable absorption component however shows more complex behaviour, with a maximum value occurring at intermediate intensities.

It appears that the two-component model is the simplest absorption model which adequately describes the spectral changes observed using *Ginga* during dip events in X 1624-490, XB 1916-053 and XBT 0748-676. There are several physical situations which may result in this type of spectral behaviour. A low-energy component may arise if the absorbing medium is partially ionised. A similar effect is also possible if the absorbing medium has a peculiar composition. If the source is physically extended, but only partially covered by an absorbing medium with column density  $N_H$ , then the emergent spectrum will be of the two-component form. In this case the normalisations of the fixed and variable absorption components ( $A_{fix}$  and  $A_{var}$  respectively) will be related to the normalisation of the unabsorbed source spectrum ( $A_0$ ) in the following way,

$$A_0 = A_{fix} + A_{var} \exp(rN_{H\ var}\sigma_T) \quad (7.3)$$

The quantity  $r = N_e/N_{H\ var}$  is the ratio of electron to measured hydrogen column densities, which is a measure of the metallicity of the absorbing medium ( $N_{H\ var}$  is calculated from the column density of elements possessing K-shell electrons assuming cosmic abundances). In a partial covering model then, if  $A_0$ ,  $A_{fix}$  and  $A_{var}$  can be measured, then the metal abundance of the absorbing medium may be determined.

An instrumental interpretation of the two-component fit was suggested by Parmar *et al.* (1986). It was recognised that if the source exhibits simple absorption and the column density changes on timescales shorter than the instrumental spectral accumulation time, the resultant 'mixed'

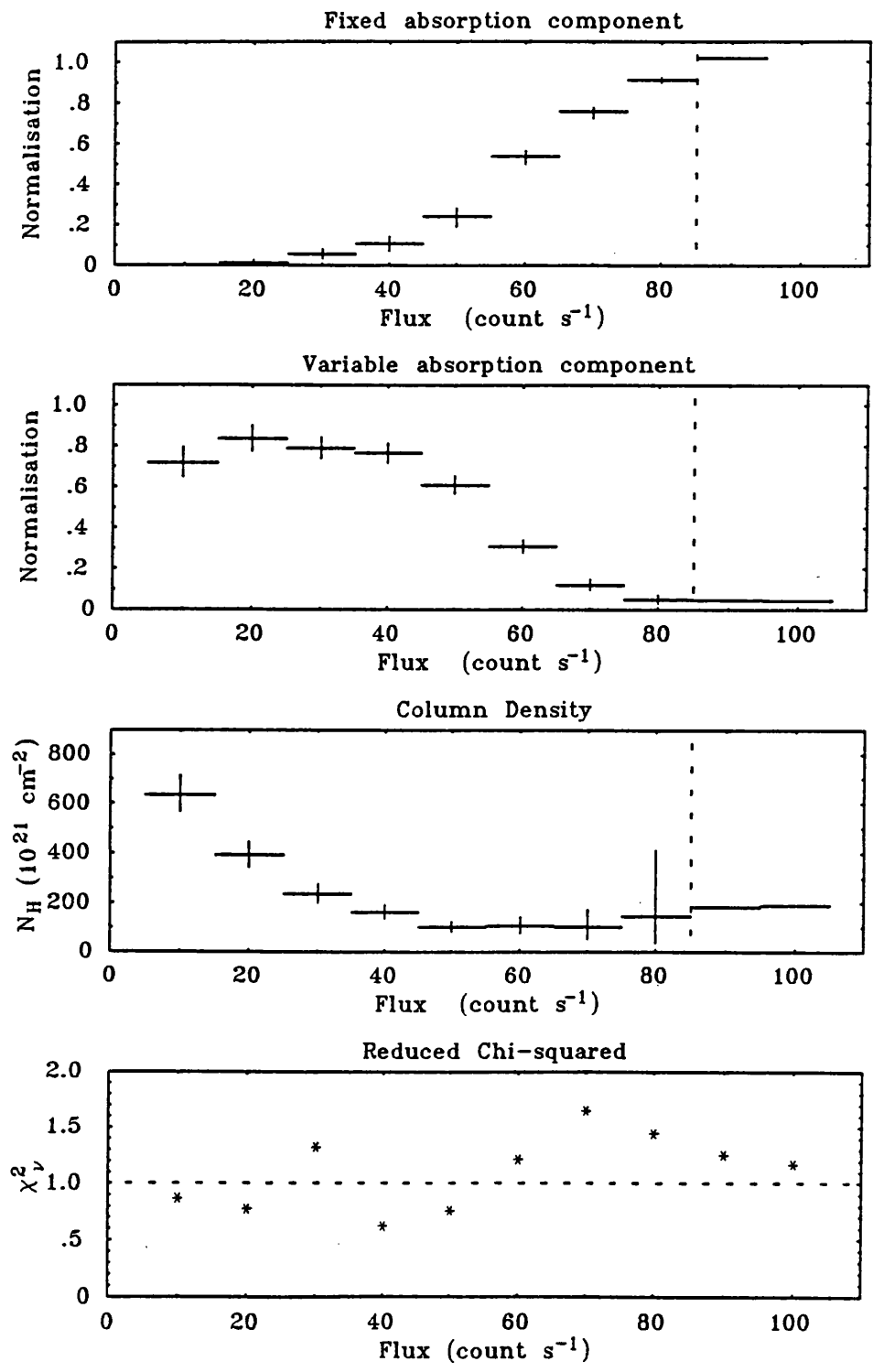


Figure 7.25: The parameters for the two-component model for absorption during dip events for observation G2 of XB 1916-053. Error bars for parameters are at the  $1\sigma$  level. The vertical dashed line indicates the flux above which the data can be represented by a single component, and no error bars are given for these states.

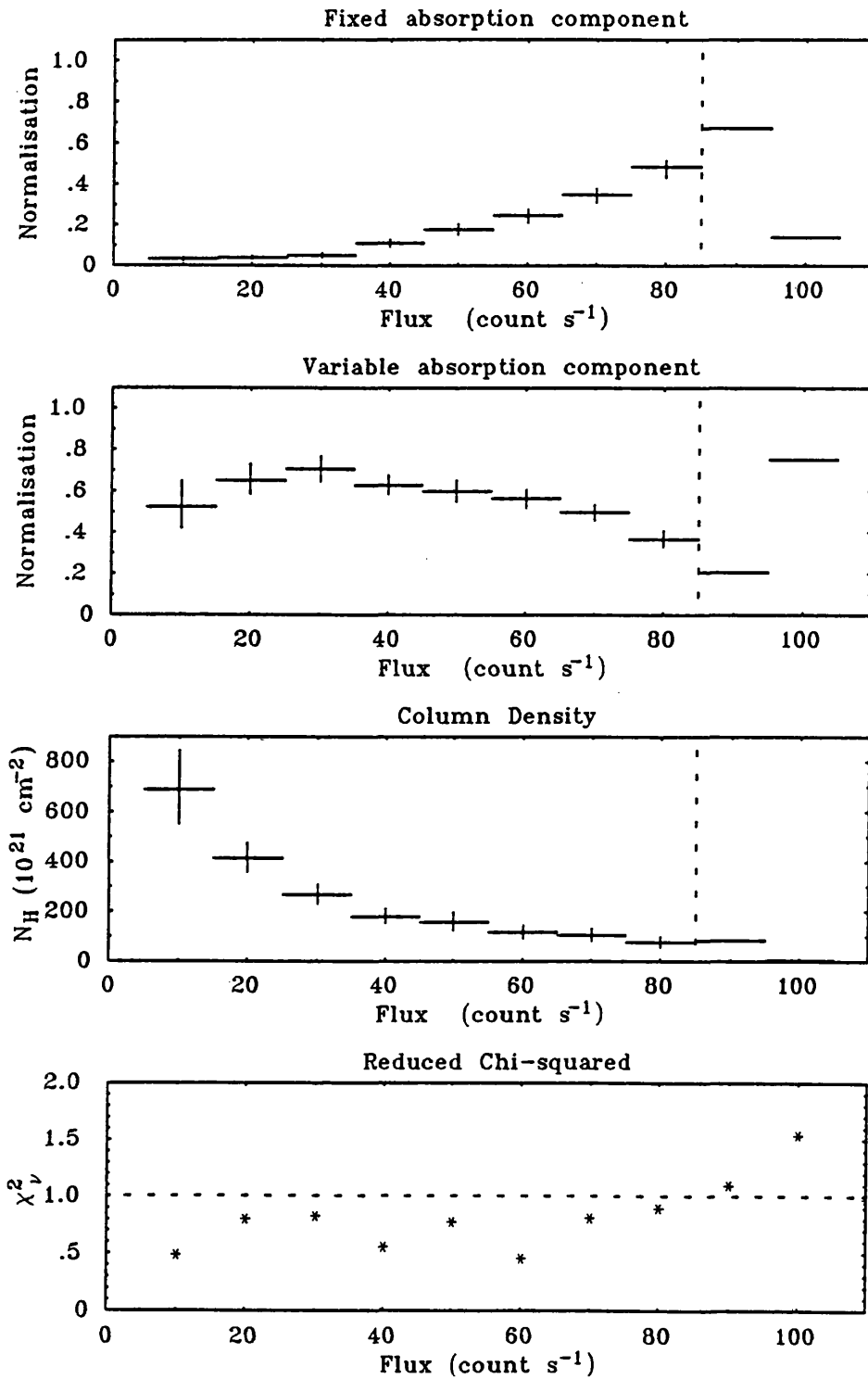


Figure 7.26: The parameters for the two-component model for absorption during dip events for observation G3 of XB 1916-053. Error bars for parameters are at the  $1\sigma$  level. The vertical dashed line indicates the flux above which the data can be represented by a single component, and no error bars are given for these states.

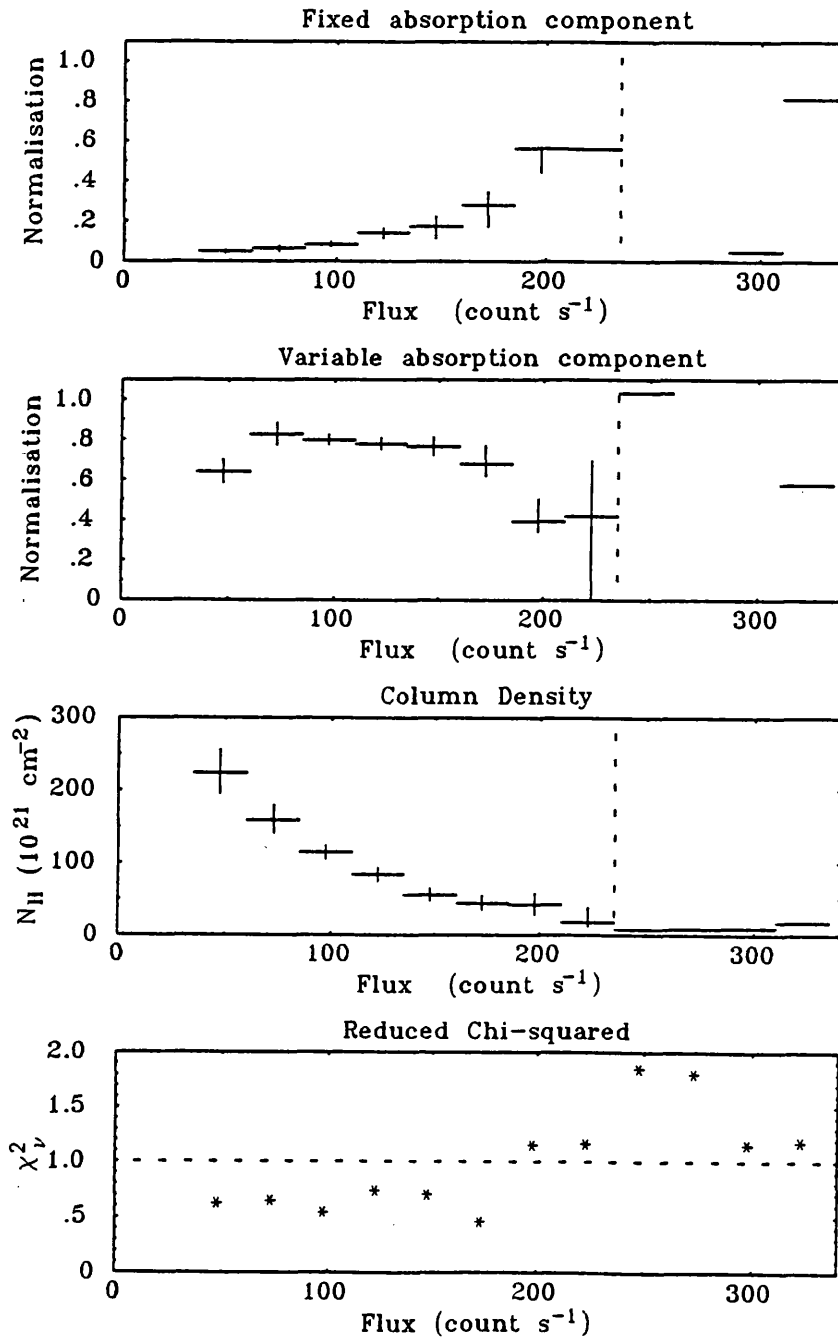


Figure 7.27: The parameters for the two-component model for absorption during dip events for observation G1 of XBT 0748-676. Error bars for parameters are at the  $1\sigma$  level. The vertical dashed line indicates the flux above which the data can be represented by a single component, and no error bars are given for these states.

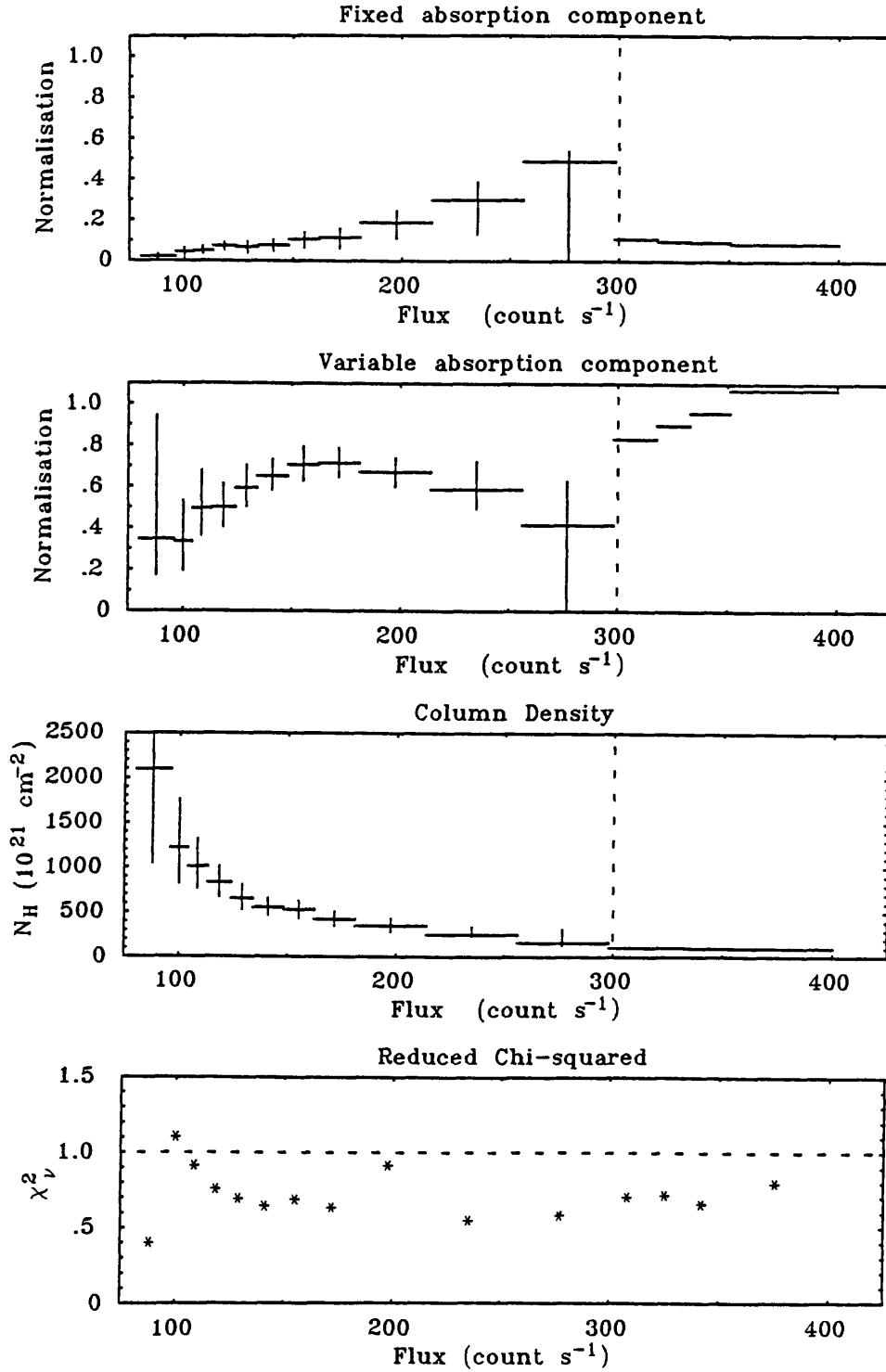


Figure 7.28: The parameters for the two-component model for absorption during dip events for observation G2 of X 1624-490. Error bars for parameters are at the  $1\sigma$  level. The vertical dashed line indicates the flux above which the data can be represented by a single component, and no error bars are given for these states.

spectrum would require a two-component model to describe it. Parmar *et al.* (1986) simulated the expected spectrum for a Gaussian distribution of column densities. It was found that for a mean value of  $N_H = 20 \times 10^{21} \text{ cm}^{-2}$  and a full width at half maximum of  $10 \times 10^{21} \text{ cm}^{-2}$  a soft excess over the spectrum with a single value of  $N_H$  is obtained. In that particular case the magnitude of the excess was  $\approx 10\%$  at 1 keV, which, it was argued would be sufficient to require a two-component fit to the spectrum. The actual behaviour of the two-component model parameters was not predicted, so simulations are presented here which examine this effect in more detail.

### 7.7.1 Simulation of the mixing effect

The object of the data simulation was to generate the pulse height spectra that would be observed with the LAC given a spectrum with time variable normalisation and column density. These data were then analysed in the same manner as the real data. The method used for simulation was as follows. The spectrum chosen was a power law with  $\alpha = 1.9$ , so as to approximate closely to the spectrum of XB 1916-053. A reference set of 500 pulse height spectra was generated by folding this spectrum through the inverse detector response for a wide range of column densities,  $N_H = 1 - 500 \times 10^{21} \text{ cm}^{-2}$  at intervals of  $10^{21} \text{ cm}^{-2}$ . Given a model of the time behaviour of the column density and normalisation, the spectrum at any time could be found by choosing the nearest  $N_H$  value in the reference set. This spectrum was then scaled to account for the attenuation due to (energy independent) electron scattering that would be expected given the metal abundance of the model absorbing medium.

To simulate dip variability a simple linear dependence of  $N_H$  with time was assumed, using the simple periodic waveform (of period  $P_{N_H}$ ) shown in figure 7.29. The artificial spectra were calculated at a resolution of 0.125 sec and these were accumulated in bins of 4 sec duration (i.e. 32 intrinsic spectra per output spectrum). The duration of the artificial data cubes was 4000 sec.

To test the behaviour under time variations in  $N_H$ , the intrinsic normalisation was held constant. Two periods have been used,  $P_{N_H} = 250$  and 12.4 sec. The first period represents the case in which the mixing effect should be small, whereas the second should mimic the mixing effect since a full dip transition occurs in about 3 time bins. The effect of intrinsic normalisation changes was also studied, this being done by a sinusoidal modulation of half amplitude 15%, and of period 4000 sec being used in the model.

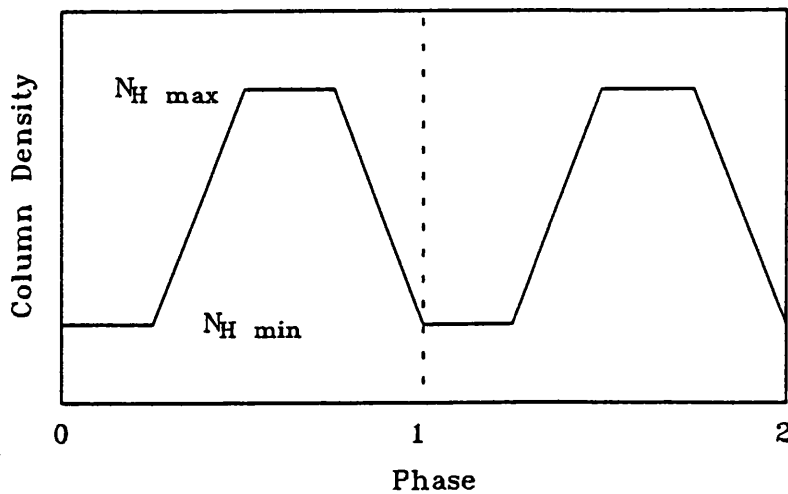


Figure 7.29: The simple waveform of  $N_H$  variability assumed in the simulations of the spectral mixing effect. The changes in  $N_H$  between phases 0.25 and 0.5 and between 0.75 and 1.0 are linear with time.

#### Slow $N_H$ changes

The case of slow  $N_H$  variability is shown in figure 7.30. The behaviour of the model parameters is much as expected. Away from the non-dip state the normalisation of the fixed absorption component is effectively zero, indicating that the one-component model is a good fit to the data. The column density decreases exponentially with increasing flux as might be expected. The normalisation of the variable absorption component also behaves exponentially, as the flux is reduced by energy independent electron scattering as the column density increases.

#### Fast $N_H$ changes

It may be seen from figure 7.31 that the behaviour of the model parameters is similar to that observed in real dip sources. The column density increases approximately exponentially with dip depth. The fixed absorption component shows decreasing normalisation with decreasing flux, and the variable component normalisation shows a maximum at intermediate flux values.

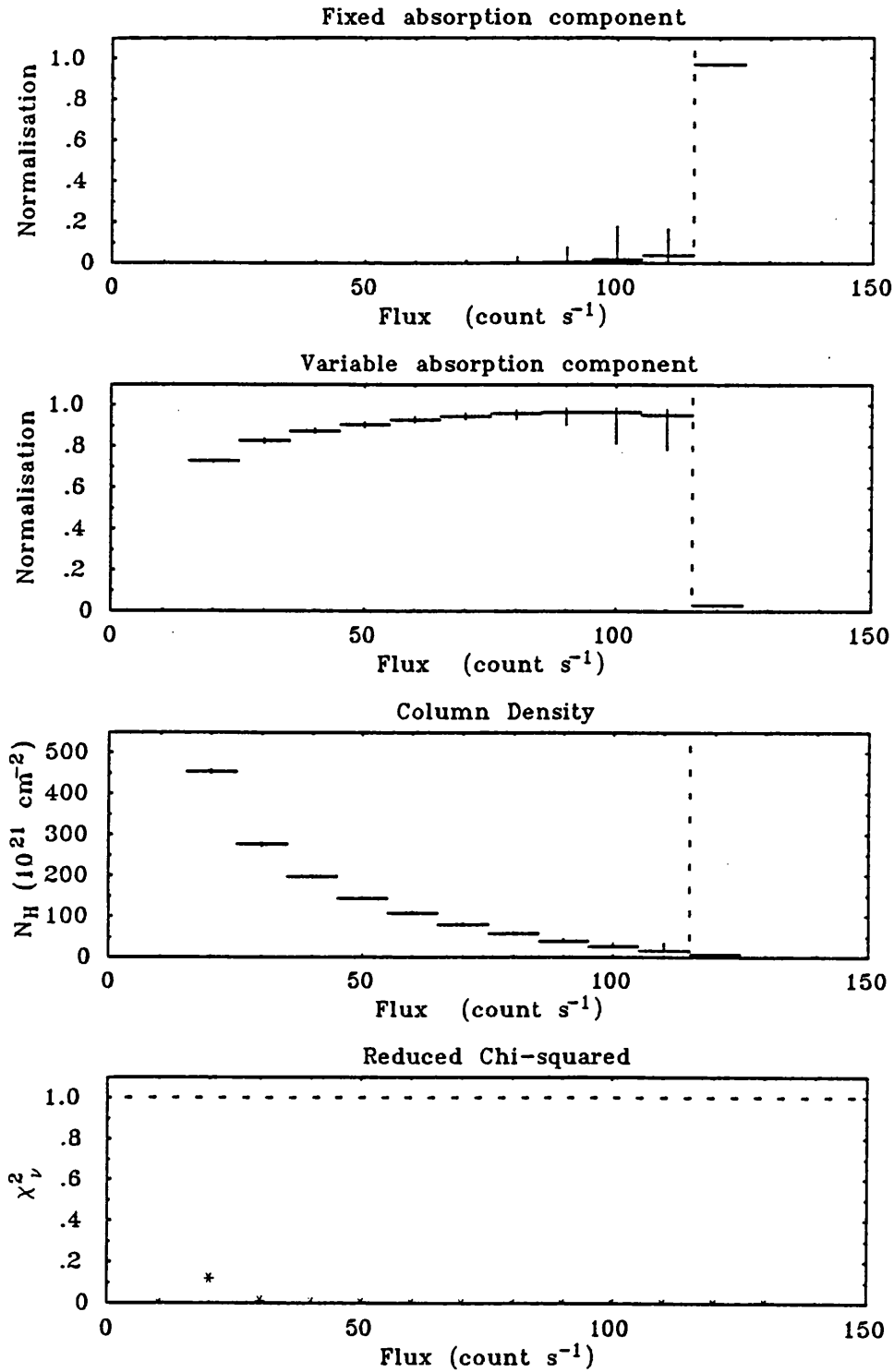


Figure 7.30: The parameters for the two-component model for absorption during dip events for simulated spectral changes. The model in this case is a single component spectrum with a slowly varying column density. The normalisation of the fixed absorption component is essentially zero in the dips. Error bars for parameters are at the  $1\sigma$  level. The vertical dashed line indicates the flux above which the data can be represented by a single component, and no error bars are given for this state.

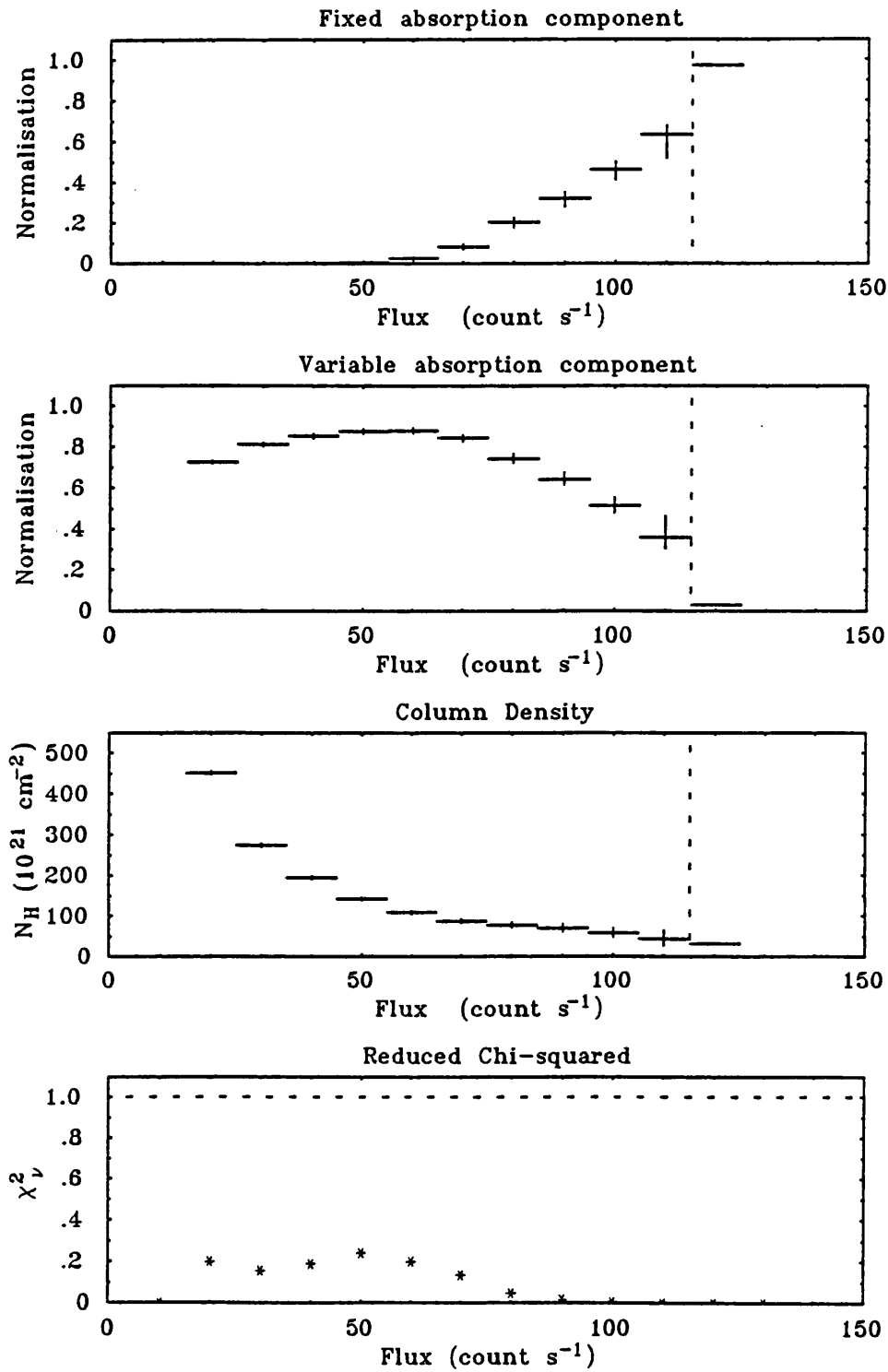


Figure 7.31: The parameters for the two-component model for absorption during dip events for simulated spectral changes. The model in this case is a single component spectrum with a rapidly varying column density. The dip spectra now require a finite contribution from the fixed absorption component. Error bars for parameters are at the  $1\sigma$  level. The vertical dashed line indicates the flux above which the data can be represented by a single component, and no error bars are given for this state.

### Fast $N_H$ changes with intrinsic source variability

Using the same  $N_H$  modulation as for the above case, but including the slow 30% modulation to the normalisation results in the parameter behaviour seen in figure 7.32. This can be seen to be similar to the case above, but with several differences. The smooth variability of the parameters is altered, with particularly noticeable changes in behaviour at 30% below maximum flux (all parameters), and at low intensities for the column density. These changes may be attributed to a secondary mixing effect, due to spectra with different  $N_H$  being co-added because of the variable normalisation.

### Conclusions from the modelling of spectral mixing

These simulations show that the two-component model gives a good representation of a spectrum which undergoes rapid changes in column density. Although the simulations were based on an approximation to the spectrum of XB 1916-053 the conclusions should be valid for any spectrum.

The above simulations were repeated using different assumed metal abundances in the absorbing medium. For fast  $N_H$  changes it was found that the parameters of the two-component model behave as if the source were in fact partially covered. Thus the metal abundance of the absorbing material in dip sources may be calculated using equation 7.3. Discrimination between genuine partial covering and the mixing effect is however difficult.

Inspection of the residual patterns to the spectral fits of the two-component model to mixed spectra indicates that *Ginga* observations of any dip source would not distinguish between partial covering and spectral mixing (provided that spectral mixing occurs at the minimum time resolution). In the simulations of XB 1916-053 it was found that the maximum expected difference between the two models would be  $\approx 0.05$  counts  $\text{sec}^{-1}$  per PHA channel. Even scaling up to the brightest dip sources would show residuals of only  $\approx 0.25$  counts  $\text{sec}^{-1}$  per PHA channel, which although in principle is detectable, is prevented by difficulties in parameterising the quiescent source spectra, since systematic residuals in the quiescent spectra of LMXB sources seem to be of this magnitude.

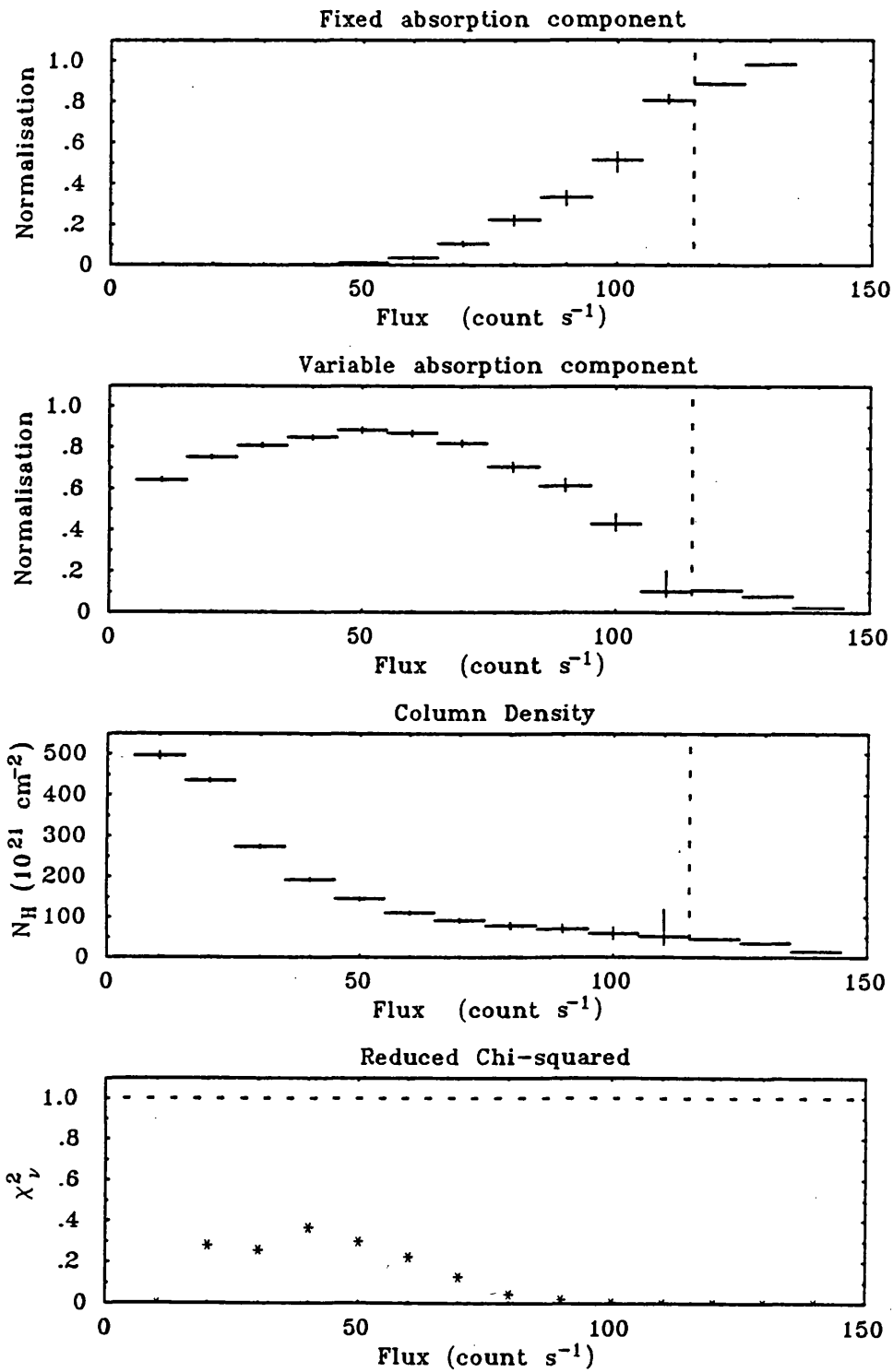


Figure 7.32: The parameters for the two-component model for absorption during dip events for simulated spectral changes. The model in this case is a single component spectrum with a rapidly varying column density and a slowly varying intrinsic normalisation. The dip spectra now require a finite contribution from the fixed absorption component. Error bars for parameters are at the  $1\sigma$  level. The vertical dashed line indicates the flux above which the data can be represented by a single component, and no error bars are given for this state.

Table 7.6: Metal abundances for the three dip sources observed using *Ginga*

Source	Metal Abundances ( $1/r$ )	
	This work	Previous estimates
XB 1916-053	$0.5 \pm 0.1$	$0.2 - 1.0$ <sup>(a)</sup>
XBT 0748-676	$0.5 \pm 0.3$	$0.1 - 0.5$ <sup>(b)</sup>
X 1624-490	$0.9 \pm 0.4$	$0.05 - 0.3$ <sup>(c)</sup>

**Notes:** All errors are quoted at the  $1\sigma$  level, except range of previous estimate for XB 1916-053 which is for the 90% confidence interval. References : (a) - Smale *et al* (1988); (b) - Parmar *et al.* (1986); (c) - Breedon (1989).

### 7.7.2 Metal Abundances

The quantity  $r$  in equation 7.3 for the partial covering model is a measure of the metal abundance of the absorbing medium, and  $1/r$  gives the ratio of the abundances of elements possessing K-shell electrons in this medium to normal cosmic values. It has been illustrated above that the partial covering model and the integration effect are indistinguishable. Thus metal abundances may be calculated from the measured values of the normalisations  $A_{var}$  and  $A_{fix}$  and the column density  $N_H$ .

For each source, the procedure adopted was to utilise all the dip data, forming an estimate of  $r$  and associated error  $\sigma_r$  for each intensity band. The adopted value was then the weighted mean of these estimates. This procedure was adopted for all the data sets illustrated in figures 7.25 to 7.28. The value estimated for observation G2 of XB 1916-053 was found to have a large associated error ( $1/r = 0.38 \pm 0.25$ ), due to the gross changes in quiescent flux between the four parts of this observation. The metallicities calculated from the other data sets are given in table 7.6, along with previous estimates. The values obtained for XB 1916-053 and XBT 0748-676 are in agreement with those obtained by Smale *et al.* (1988) and Parmar *et al.* (1986) within the errors of measurement. Thus it is confirmed that the metal abundances of these systems is approximately a factor of two below the normal cosmic values. The abundance measured in X 1624-490 is near the cosmic value, and is significantly different to the value obtained by Breedon (1989).

## 7.8 DISCUSSION

One of the most important aspects of dip sources is that they reveal the orbital period of the binary. This is particularly relevant in investigating the dependence of the properties of LMXB on  $P_{orb}$ . The classification of LMXB according to their observed characteristics has been attempted by several authors, but as yet no single scheme has been generally adopted. It was noted by van Paradijs and Lewin (1986) that three schemes of classification, due to Parsignault and Grindlay (1978), Ponman (1982) and White and Mason (1985) all show similar (but not identical) division into two classes of source. The criteria for classification in each case varied, but the overall pattern which emerged was the division into two groups which correspond to low and high luminosity sources, with  $L_x \sim 10^{36}$  and  $10^{38}$  ergs sec<sup>-1</sup> cm<sup>-2</sup> respectively. Characteristics of the low luminosity sources are that they are often transient in nature and commonly exhibit type I bursts. White and Mason (1985) suggested that the spectra of this class are well modelled by the generalised thermal approximation to unsaturated Comptonisation. In contrast, the high luminosity sources never exhibit bursts, are persistently bright and their spectra require an additional blackbody component (White and Mason, 1985). Furthermore, these sources commonly show intervals of flaring activity which may be associated with a change in luminosity of this blackbody component (e.g. van der Klis, 1985).

It was suggested by van Paradijs and Lewin (1985) that the dichotomy between luminosity classes corresponds to the nature of the mass donor. The low luminosity class was attributed to systems in which the mass donor is a late main-sequence star. In this case, the orbital period is short ( $\lesssim 13$  hrs) and the mass transfer is driven primarily by the shrinking of the Roche lobe as the system loses angular momentum. Mechanisms for dissipation of angular momentum are expected to be through magnetic braking, and for  $P_{orb} < 10$  hrs, gravitational radiation (see Rappaport, Verbunt and Joss, 1983). The higher luminosity class correspond to systems with secondaries which have evolved off the main-sequence. These binaries would have long orbital periods ( $\gtrsim 13$  hrs) and mass transfer would be driven by the nuclear evolution of the secondary (Webbink, Savonije and Joss, 1983, and Taam, 1983).

Of the sources considered here, the short-period sources, XB 1916-053 and XBT 0748-676 would seem to correspond to the lower luminosity class. They both exhibit bursts and XBT 0748-679 is a known transient. The quiescent spectral variability does not appear to be related to any systematic changes in hardness ratio, and cannot be attributed to a blackbody component. The luminosities of these two sources assuming a distance of 10 kpc are  $2.4 \times 10^{36}$  ergs sec<sup>-1</sup> (XB 1916-053) and

$6.0 \times 10^{36}$  ergs sec<sup>-1</sup> (XBT 0748-676). These values are typical of those expected for this class.

The classification of X 1624-490 is important since the orbital periods of only two of the high luminosity sources is known, Sco X-1 at 19.2 hrs (Cowley and Crampton, 1975) and Cyg X-2 (Cowley, Crampton and Hutchings, 1979). It is not clear to which luminosity class X 1624-490 belongs. The source has never been observed to emit bursts, and the extended EXOSAT observation implies that the burst recurrence time must be greater than  $\sim 50$  hr. The flaring component of the source shows similarity to the flaring blackbody component which has been reported for Sco X-1 and other high luminosity LMXB (van der Klis, 1985), with similar temperatures and relative contribution to the total flux. The main objection to the attributing X 1624-490 to the high luminosity class is that the flux is relatively low, implying a luminosity of  $L_x \approx 1.2 \times 10^{37}(d/10 \text{ kpc})$  ergs sec<sup>-1</sup>. This is rather too low for the higher luminosity class, which typically have  $L_x \sim 0.5 - 1 \times 10^{38}$  ergs sec<sup>-1</sup>. The assumption of  $d \sim 10$  kpc is typically made for these sources since it represents the distance to the galactic centre. Assuming a galactic radius of 15 kpc, then the maximum distance to X 1624-490 which is still within the disc of the Galaxy is  $\sim 24$  kpc. Even in this extreme case the implied distance above the galactic plane is only 200 pc. The upper limit to the source luminosity is then  $\sim 6 \times 10^{37}$  ergs sec<sup>-1</sup>, which is comparable to luminosities quoted for Sco X-1 (White and Mason, 1985, and Makishima and Mitsuda, 1985).

A classification scheme which has recently been put forward by Hasinger and van der Klis (1989) may prove to be of use in the classification of X 1624-490. The scheme is based on a combination of spectral and temporal characteristics. The spectral properties of a source are determined from an x-ray colour-colour diagram. It has been found that different types of spectral behaviour show characteristic quasi-periodic oscillation (QPO) and noise properties. Again there are two classes, the 'Z' sources and the 'atoll' sources, which correspond to high and low luminosity LMXB respectively, the names referring to characteristic patterns mapped out by these sources in the colour-colour diagram. Similarly to earlier schemes, Hasinger and van der Klis (1989) predict that Z sources have evolved secondaries whereas the atoll sources have main sequence companions. Unfortunately, this scheme relies on measurement of the rapid temporal variability of the source. The relatively low count rate of the EXOSAT observations prevent a detailed QPO search on those data, and the *Ginga* data are at too low a time resolution to study the expected rapid variability. Further high time resolution observations of this source are necessary to determine to which class of source X 1624-490 belongs.

The modelling of the quiescent emission using a physically justifiable model was only possible for XBT 0748-676, for which it was found that a generalised thermal model provided an acceptable

representation of the data. In this case the index  $\Gamma$  was  $\sim 2.2$ , and so lies within the expected range of photon index of  $-0.5$  to  $3$  given by Eardley *et al.* (1978) for unsaturated Comptonisation. The modelling of the other two sources required the addition to physical models of a broad Gaussian component with a mean energy of  $\sim 5$  keV and width of  $\sim 1.5$  keV. It is not clear if any significance should be attached to the similarity of this additional component for the two sources. It should be noted however, that even the best fits are only marginally acceptable and all show strong residual features. A complication to the spectral modelling in X 1624-490 is its proximity to the galactic ridge, lying  $\approx 0.5^\circ$  below the galactic plane. An additional bremsstrahlung component was included in the spectral models to account for ridge emission (see e.g. Warwick *et al.*, 1988), but was not found to be a significant contribution to observed flux. XB1916-053 lies  $\sim 8.5^\circ$  from the galactic plane, and it is expected that the contribution from the galactic ridge emission in this case would be negligible. More theoretical work on spectral formation in LMXBs is required to explain the source characteristics observed using the *Ginga* LAC instrument.

The residual low-state emission seen during the deepest dip intervals in X 1624-490 is unique to this source as it is spectrally distinct from the quiescent state. It is possible that this component arises from source confusion. An approximate limit to the source separation can be estimated as being  $< 1^\circ$  from the EXOSAT map of the galactic plane Warwick *et al.* (1988). If the low state emission is intrinsic to the source, then it is possible that it arises from an ADC component. The soft spectrum indicates that the ADC must have a substantial intrinsic luminosity in addition to any energy independent scattering that may occur. Unfortunately, the quality of the low-state spectrum is not good enough to warrant a two-component fit to the data which would allow the scattered and intrinsic components to be separated.

The study of characteristic timescales of dip activity in section 7.5 showed that cloud radii range from  $\sim 1.2 \times 10^8$  cm to  $3.6 \times 10^9$  cm, with a cloud column density which varies as  $\sim r_c^{-2}$ . To date, little theoretical consideration has been given to the cloud formation process in dip sources, with the exception of the model of Frank, King and Lasota (1987, FKL). Although there may be some problems in reconciling this scenario to the observations of the ADC source X 1822-371 (see chapter 6) it may give some insight into the type of mechanism that may be responsible for the generation of the clouds and will be reviewed here in the context of X 1624-490.

In the FKL model a gas stream of width  $W$  overshoots the edge of the accretion disc, allowing a fraction  $f$  of the transferred mass to reach the circularisation radius  $r_{circ}$ . At this point it was suggested that the impinging gas undergoes a shock which allows it to reach a height of  $0.4r_{circ}$  above the plane of the disc, independent of the binary parameters of the system. FKL argue

that the flux of ionising photons from the central x-ray source in this region is such that in most LMXB, the shocked gas at the circularisation radius may be subject to a two phase instability of the type described by Krolik, McKee and Tarter (1981). The two thermally stable states of the gas correspond to a dense ‘cold’ phase at  $T_c \sim 10^4$  K, and a tenuous ‘hot’ phase at  $T_h \sim 10^7$  K. The quantity which describes the photoionisation equilibrium, is termed  $\Xi$  and is essentially the ratio of the radiation pressure of ionising flux to the gas pressure,

$$\Xi = \frac{F_{ion}}{nkTc} \quad (7.4)$$

where  $F_{ion}$  is the ionising flux,  $n$  is the number density of the gas at a temperature  $T$ . Krolik McKee and Tarter (1981) show that the two phase instability may occur for  $0.1 < \Xi < 10$ . FKL re-express equation 7.4 as

$$\Xi = 1.67 \frac{W_9^2 P_{5\text{hr}}}{f_{0.1} R_6} \quad (7.5)$$

where  $W_9$  is the stream width in units of  $10^9$  cm,  $P_{5\text{hr}}$  is  $P_{orb}$  in units of 5 hrs,  $f_{0.1}$  is the mass fraction which overshoots the edge of the disc in units of 0.1. Assuming  $W_9 \sim 1$  and  $f_{0.1}$ , then for X 1624-490,  $\Xi \approx 7$  and so a two phase medium may form. If the cold and hot phases are in pressure equilibrium then given the above temperatures, the ratio of densities between these two states is likely to be  $\sim 10^3$ . FKL estimate that  $\approx 80\%$  of the mass of shocked gas will form cool clouds, and the remaining 20% will be in a hot intercloud medium.

There are three timescales that are relevant to the evolution of the post-shock gas in the radiation field of the compact source. The recombination time  $t_{rec}$  represents the timescale on which the above phase partition occurs. The clouds will however still be in an approximately Keplerian orbit, and so will follow a ballistic orbit which will intersect the disc on the dynamical timescale  $t_{dyn}$ . Finally, the cold clouds will evaporate on a timescale  $t_{evap}$ .

The formation of an extended cloud region requires that the two phases can form out of the shocked gas before intersection with the plane of the disc, and that cloud evaporation is slower than either of these processes, i.e.,

$$t_{rec} \ll t_{dyn} \ll t_{evap} \quad (7.6)$$

FKL give the following expressions for these timescales,

$$t_{rec} = 2.2 M_1^{2/3} P_{5\text{hr}}^{4/3} (f_{0.1} \dot{M}_{17})^{-1} W_9^2 \text{ sec} \quad (7.7)$$

$$t_{dyn} = 114 P_{5\text{hr}} \text{ sec} \quad (7.8)$$

$$t_{evap} = 400 M_1^{11/9} P_{5\text{hr}}^{7/9} (f_{0.1} \dot{M}_{17})^{-1} W_9^2 \text{ sec} \quad (7.9)$$

Where  $M_1$  is the mass of the primary in solar units and  $\dot{M}_{17}$  is the mass transfer rate in units of  $10^{17}$  g sec $^{-1}$ . For X 1624-490, using  $M_1 = 1.4$  and  $\dot{M}_{17} \sim 1$ , these timescales are found to be;

$t_{rec} \approx 17$  sec,  $t_{dyn} \approx 500$  sec, and  $t_{evap} \approx 1700$  sec. Thus the condition for cloud formation is satisfied.

The maximum lengthscale that may be associated with cool clouds condensing out of the shocked gas is the product of the sound speed ( $c_s$ ) and the recombination time, which FKL give as,

$$l_i \approx 9.1 \times 10^7 M_1 P_{5\text{hr}} (f_{0.1} \dot{M}_{17})^{-1} W_9^2 \text{ cm} \quad (7.10)$$

These clouds cool and collapse in pressure equilibrium until reaching the lower equilibrium density,  $n_c$ . The lengthscale associated with these cold clouds is given as,

$$l_c \approx 4 \times 10^7 M_1^{7/9} P_{5\text{hr}} (f_{0.1} \dot{M}_{17})^{-1} W_9^2 \text{ cm} \quad (7.11)$$

For X 1624-490, these equations give  $l_i \sim 5 \times 10^8$  cm and  $l_c \sim 3 \times 10^8$  cm.

The values implied from observations are  $l_c = 2r_c \sim 2.4 \times 10^8$  to  $\sim 7 \times 10^9$  cm. Thus the end of the distribution is consistent with the FKL cloud formation mechanism, but the higher end clearly is not, being a factor of  $\sim 20$  too large.

The FKL model also predicts the column density associated with each cloud. The density of the cold medium is estimated at

$$n_c = 2.2 \times 10^{16} M_1^{1/3} P_{5\text{hr}}^{-7/3} (f_{0.1} \dot{M}_{17}) W_9^{-2} \text{ cm}^{-3} \quad (7.12)$$

Thus the column density of an individual cloud is

$$N_{H_c} = n_c l_c \approx 8.8 \times 10^{23} P_{5\text{hr}}^{-10/9} M_1^{10/9} \text{ cm}^{-2} \quad (7.13)$$

Thus for the parameter values typical for X 1624-490, the column density of individual clouds would be expected to be  $\sim 2 \times 10^{23} \text{ cm}^{-2}$ . Thus the short duration dips can be attributed to obscuration by single clouds, whereas the highest values of  $N_H$  measured would require obscuration by several overlapping clouds.

The implied upper limit to the cloud radius distribution would appear to be too high to be attributed to individual clouds. A possible solution to this problem may arise from a modification of the distribution model adopted above. It was assumed that the clouds are evenly distributed across the simulation region. In reality it is likely that some degree of clustering of the sites of cloud formation would occur, and this may reproduce the inferred high upper limit to the cloud radius distribution. The fact that the FKL scenario predicts a typical cloud lengthscale which is in agreement with part of range inferred by observation is a success for this model, and at least illustrates one viable physical mechanism for cloud formation.

The minimum measured timescales in X 1624-490 imply cloud envelopes or a source size of  $\lesssim 400$  km. Other estimates for the size of the compact emission region come from the implied radius of the blackbody component in the brighter LMXB. Given a model for QPO modulation, the short timescales associated with this phenomenon may also be used to obtain a limit to the minimum size of the emission region. Van der Klis (1985) estimated, assuming a beat-frequency model, that the maximum radius of the compact source is  $\sim 100$  km. Thus the results from X 1624-490 support an upper limit to source dimension which is of this order. Such results provide boundary conditions for some theoretical models of LMXB emission. An example of this is the spherical Comptonising cloud model of Ponman *et al.* (1989) which has a minimum radius of  $> 1000$  km, and so needs to be reconsidered in the light of the evidence for smaller emission regions in LMXB provided by X 1624-490 (Ponman, priv. comm.).

The interpretation of the minimum timescales as being due to cloud envelopes is supported by the observation that many dip transitions are much slower than the minimum cases used here. It would seem more realistic to attribute the spectrum of transition times to a range of envelope depths rather than the alternative possibility that the size of the emission region changes substantially (by a factor of  $> 10$ ) on short timescales.

The spectral mixing effect has been illustrated to be indistinguishable from partial covering in the case when the column density in a simple absorption model changes more rapidly than the instrumental spectral integration time. Either of these possibilities may explain the spectral behaviour of most dip sources during dip events. Given that dip transitions are observed to occur on shorter timescales than spectral integration can be performed, the latter effect is very likely to play some part in determining the source spectrum. The low-energy excess over simple absorption is a consequence of this integration effect, and there is no evidence that the absorbing medium is ionised, or subject to abundance peculiarities.

Other situations in which the column density changes rapidly do exist and it may be worthwhile investigating whether or not spectral mixing is important in these cases. One such example is the absorption spectrum of the pulsar Vela X-1, which is in a HMXB system. Observations made using *Tenma* (Nagase *et al.*, 1986) and EXOSAT (Haberl and White, 1990) reveal an absorption spectrum which has a soft excess over that expected from simple photoelectric absorption. The authors of both these papers put forward complex physical models which model the source behaviour, but do not consider the spectral mixing effect even though the column density changes on a similar timescale to the spectral integration times used. The magnitude of the instrumental effect should be investigated before complicated physical models are invoked.

The fact that simple absorption with rapid  $N_H$  variability is identical to partial covering allows the metallicity of the absorbing medium to be calculated using equation 7.3. The values of metal abundance obtained for all three sources is higher than previous estimates. Thus for these sources there is no evidence that the abundance is more than a factor of two below the cosmic value. This is in stark contrast to the energy independent dip source X 1755-338 (White *et al.* 1984) which has a metal abundance of  $< 1/600$  of the cosmic value. It is unlikely however that further observations of X1755-338 will yield a significantly larger metal abundance, since White *et al.* (1984) found that the dips in this source are independent of energy to the limits of measurement, and consequently that the parameters in the two-component spectral model were unconstrained.

## 7.9 SUMMARY

The results of the observations of dip sources presented in this chapter can be summarised as follows;

- The two bursting sources XB 1916-053 and XBT 0748-676, which have short orbital periods, can be associated with the lower luminosity class of LMXB.
- At present, the classification of long period dip source X 1624-490 is unclear. Some characteristics are indicative of the high luminosity class, in particular the existence of a flaring blackbody component to the source emission. Further observations at high time resolution are required to determine whether the source belongs to the Z or atoll class of Hasinger and van der Klis (1989).
- The minimum timescale for dip transitions in X 1624-490 support claims that the central emission region in LMXB sources cannot have an extent of greater than a few 100 km.
- The spread in dip transition times in X 1624-490 suggests that there is a range in the widths of cloud envelopes.
- Using a simple model for cloud distribution in X 1624-490, the dip morphology does not indicate a characteristic cloud size. A distribution which reproduces the observed behaviour is one in which clouds of different radius make an equal contribution to the obscured area ( $\beta \approx 2$ ), with a range of cloud diameters from 2000 to 70000 km.

The only physical model for cloud formation suggested to date, is that of Frank, King and Lasota (1987). This model predicts clouds with length up to  $\sim 3000$  km. This is in agreement

only with the lower end of the observed distribution. The model may however be acceptable if cloud formation occurs in localised regions.

- Investigation of the spectral mixing effect shows that rapidly variable simple absorption is indistinguishable from partial covering of the source.
- The metal abundances of the absorbing medium in all three sources have been found. The short period sources XB 1916-053 and XBT 0748-676 have a metal abundance which is half the cosmic value. The metallicity of material in X 1624-490 is  $\sim 0.9$  of the cosmic value.

## Chapter 8

# Conclusion

In this thesis observational results from x-ray observations of three rather different types of Roche-lobe filling binary have been presented. The more important aspects of this work are summarised below, and some comments are made on the future of galactic x-ray astronomy.

### 8.1 SS CYGNI

- The EXOSAT observations support the established two-component behaviour of emission from dwarf novae. The soft ( $\lesssim 1$  keV) and hard ( $\gtrsim 1$  keV) x-ray components are approximately correlated and anti-correlated with the optical emission respectively.
- The x-ray spectrum of the hard emission shows evidence for thermal  $K\alpha$  and  $K\beta$  iron line emission, and supports the claim that this component arises from an optically thin region.
- In outburst soft x-ray component is modulated sinusoidally at a period of between  $\approx 7.4$  and  $\approx 11$  sec, with a mean amplitude of up to  $\sim 30\%$ ,
- There is a strong negative correlation between the period of the soft x-ray pulsation and the soft x-ray flux.
- The soft x-ray pulsations show erratic jumps in period and wander in phase. A model for this behaviour suggested by Córdova *et al.* (1984) has been shown to be a poor representation of the observed properties of the pulsation.

## 8.2 1E 2259+586

- The *Ginga* data place a  $3\sigma$  upper limit of 140 lt-msec to the projected semi-major axis of the binary, over a period range of 1000 to 5000 sec.
- The orbital parameters suggested by Fahlman and Gregory (1983), of  $P_{orb} \approx 2300$  sec and  $a_x \sin i \approx 190$  lt-msec, can be rejected at a confidence level of  $> 99.95\%$ .
- The x-ray spectrum shows a feature at  $\sim 7$  keV which may be related to cyclotron processes in a magnetic field of  $10^{11}$  G.
- Although the binary model for the system is generally accepted, there is little direct evidence to support it. It has been shown that a scenario in which the pulsar accretes from a dense molecular cloud is tenable and should be considered in more detail.

## 8.3 DIP SOURCES

- The minimum timescales associated with dip transitions in X 1624-490 support claims that the maximum linear extent of the central emission regions in LMXB cannot exceed  $\sim$  few 100 km.
- The fractal analysis of dip light curves in X 1624-490, suggests that the clouds responsible for dip events have a range of radii from  $\sim 1000$  to  $\sim 36000$  km, but that there is no dominant lengthscale over this range.
- The two-component model that is required to model the absorption in dip events in the three sources studied may be attributed to the column density changing on shorter timescales than the spectral integration time of the instrument.
- The derived metal abundances in XB 1916-053, XBT 0748-676, and X 1624-490 are  $0.5 \pm 0.1$ ,  $0.5 \pm 0.3$  and  $0.9 \pm 0.4$  of the cosmic value respectively.

## 8.4 FUTURE PROSPECTS

Some aspects of temporal variability in galactic x-ray sources are now well documented, but as yet, no consistent physical models exist to fully describe the observed behaviour. In general, processes which may be attributed to orbital or spin modulation are understood to a certain degree. The main

theoretical advances that are required now are in understanding the fluid dynamics of interacting binaries. Such studies are complicated by the likelihood that many of the regions of interest, such as the boundary layer, and the disc stream intersection, will be extremely turbulent. However, the increasing availability of powerful computing resources puts the numerical simulation of some aspects of these scenarios within reach, and should be pursued.

As far as the observational prospects for the study of time-variability are concerned, it is not clear how well future missions will serve this aspect of x-ray astronomy. The aims of x-ray observatory development at present are to produce imaging telescopes with very high spatial and spectral resolution. It is not disputed that these are worthy goals, but it seems evident that many advances could be made in galactic x-ray astronomy using medium sensitivity, low spatial resolution detectors, provided that long observations could be made of individual sources. Examples of areas which would clearly benefit from this approach include:

- The search for orbital modulation in the bright galactic bulge sources.
- X-ray photometry of other ADC sources in addition to X 1822-371.
- The study of x-ray DNO throughout entire outburst intervals.
- Long term monitoring for type I bursts in the brighter LMXB.

The key requirement then is for observations of a few days duration. Given the oversubscription for observing time that would be likely on missions such as AXAF (Advanced X-ray Astronomical Facility, NASA) and XMM (X-ray Multi-Mirror, ESA), it is doubtful that any project of this nature would be accepted.

The analogous situation in optical astronomy has found a remedy through the use of medium-size ( $\sim 2\text{m}$ ) telescopes for many photometric observations. This solution is unlikely to be adopted for x-ray astronomy given the present prohibitive cost of launch vehicles. In the long-term, the best hope for this type of observatory may arise from experiments that may be operated from manned space-stations. A low sensitivity telescope could be built as a self-contained module, and with suitable control systems and bulk data storage could be designed to operate without supervision for most of an observation. Given the long gestation periods of such projects, perhaps now is the time that some brave soul should champion the cause of small telescopes for x-ray astronomy.

# References

The following abbreviations are adopted:

<i>Acta Astron.</i>	Acta Astronomica
<i>Ann. Rev. Astr. &amp; Astrophys.</i>	Annual Review of Astronomy and Astrophysics
<i>Astr. &amp; Astrophys.</i>	Astronomy and Astrophysics
<i>Astr. &amp; Astrophys. Suppl.</i>	Astronomy and Astrophysics Supplement Series
<i>Astr. J.</i>	Astronomical Journal
<i>Astrophys. J.</i>	Astrophysical Journal
<i>Astrophys. J. Suppl.</i>	Astrophysical Journal Supplement Series
<i>Astrophys. Lett. &amp; Comm.</i>	Astrophysical Letters and Communications
<i>Bull. astr. Inst. Czech.</i>	Bulletin of the Astronomical Institute of Czechoslovakia
<i>J. British astr. Assoc.</i>	Journal of the British Astronomical Association
<i>I.A.U. Circ.</i>	Circular of the International Astronomical Union
<i>Mon. Not. R. astr. Soc.</i>	Monthly Notices of the Royal Astronomical Society
<i>Nature Phys. Sci.</i>	Nature, Physical Science
<i>Phys. Rep.</i>	Physics Reports
<i>Proc. Cam. Phil. Soc.</i>	Proceedings of the Cambridge Philosophical Society
<i>Publ. astr. Soc. Japan</i>	Publications of the Astronomical Society of Japan
<i>Publ. astr. Soc. Pac.</i>	Publications of the Astronomical Society of the Pacific
<i>Sp. Sci. Rev.,</i>	Space Science Reviews

Bailey, J., 1975, *J. British astr. Assoc.*, **86**, 30.

Bath, G.T., 1973, *Nature Phys. Sci.* 24684

Bath, G.T., & Pringle, J.E., 1981, *Mon. Not. R. astr. Soc.*, **194**, 967.

Bath, G.T., & Pringle, J.E., 1982, *Mon. Not. R. astr. Soc.*, **199**, 267.

Bath, G.T., & Pringle, J.E., 1985, in *"Interacting Binary Stars"*, ed. J.E. Pringle & R.A. Wade. (Cambridge University Press, Cambridge). p177.

Begelman, M.C., Sarazin, C.L., Hatchett, S.P., McKee, C.F., & Arons, J., 1980 *Astrophys. J.*, **238**, 722.

Bevington, P.R., 1969, *"Data Reduction and Error Analysis in the Physical Sciences"*, (McGraw-Hill, New York).

Blair, W.P., & Kirshner, R.P., 1981, *Nature*, **291**, 132.

Boldt, E., 1987, *Phys. Rep.*, 146215

Bondi, H., 1952, *Mon. Not. R. astr. Soc.*, **112**, 195.

Breedon, L.M., 1989, *Ph.D. Thesis*, University of Leicester.

Brickhill, A.J., 1975, *Mon. Not. R. astr. Soc.*, **170**, 405.

Clark, D.H., & Caswell, J.L., 1976, *Mon. Not. R. astr. Soc.*, **174**, 267.

Chandrasekhar, S., 1931, *Astrophys. J.*, **74**, 81.

Chanmugam, G., 1972, *Nature*, **236**, 83.

Coe, M.J., Davies S.R., Fahlman, G.G., & Gregory, P.C., 1989, *Mon. Not. R. astr. Soc.*, **238**, 649.

Cominsky, L.R., Ossmann, W., & Lewin, W.H.G., 1983, *Astrophys. J.*, **270**, 226.

Cominsky, L.R., & Wood, K.S., 1984, *Astrophys. J.*, **283**, 765.

Cominsky, L.R., & Wood, K.S., 1989, Preprint.

- Cordes, J.M., 1980, *Astrophys. J.*, **237**, 216.
- Córdova, F.A., Chester, T.J., Mason, K.O., Kahn, S.M., & Garmire, G.P., 1984, *Astrophys. J.*, **278**, 739.
- Córdova, F.A., Chester, T.J., Tuohy, I.R., & Garmire, G.P., 1980, *Astrophys. J.*, **235**, 163.
- Courvoiser, T.J.-L., Parmar, A.N., Peacock, A., & Pakull, M., 1986, *Astrophys. J.*, **309**, 265.
- Cowley, A.P., & Crampton, D., 1975, *Astrophys. J. (Letters)*, **201**, L65.
- Cowley, A.P., Crampton, D., & Hutchings, J.B., 1979, *Astrophys. J.*, **231**, 539.
- Crosa, L., & Boynton, P.E., 1980, *Astrophys. J.*, **235**, 999.
- Davies, S.R., Coe, M.J., Payne, B.J., & Hanson, C.G., 1989, *Mon. Not. R. astr. Soc.*, **237**, 973.
- Eardley, D.M., Lightman, A.P., Payne D.G., & Shapiro, S.L., 1978, *Astrophys. J.*, **224**, 53.
- Eggen, O.J., & Niemela, 1984, *Astr. J.*, **89**, 389.
- Eggleton, P.P., 1983, *Astrophys. J.*, **268**, 368.
- Eggleton, P.P., 1985, in *“Interacting Binary Stars”*, ed. J.E. Pringle & R.A. Wade. (Cambridge University Press, Cambridge). p21.
- Elsner, R.F., & Lamb, F.K., 1977, *Astrophys. J.*, **215**, 897.
- Fahlman, G.G. & Gregory, P.C., 1981, *Nature*, **293**, 202.
- Fahlman, G.G. & Gregory, P.C., 1983, in *“Supernova Remnants and their X-ray Emission”*, I.A.U. Symposium No. 101, ed. J. Danziger & Gorenstein, P., (Reidel, Dordrecht), p445.
- Fahlman, G.G., Hickson, P., Richer, H.B., Gregory, P.C., & Middleditch, J., 1982, *Astrophys. J. (Letters)*, **261**, L1.
- Flannery, B., 1975, *Mon. Not. R. astr. Soc.*, **170**, 325.
- Frank, J., King, A.R., & Lasota, J.-P., 1987, *Astr. & Astrophys.*, **178**, 137.
- Frank, J., King, A.R., & Raine, D.J., 1985, in *“Accretion Power in Astrophysics”*, (Cambridge

University Press, Cambridge).

Freund, J.E., & Walpole, R.E., 1987, *“Mathematical Statistics”*, (Prentice-Hall, Englewood Cliffs).

Forman, W., Jones, C., Cominsky, L., Julien, P., Murray, S., Peters, G., Tananbaum, H., & Giacomini, R., 1978, *Astrophys. J. Suppl.*, **38**, 357.

Garrison, R.F., Hiltner, W.A., Krzeminski, W., & Schild, R.E., 1982, *I.A.U. Circ.*, No. **3730**.

Garrison, R.F., Schild, R.E., Hiltner, W.A., & Krzeminski, W., 1984, *Astrophys. J. (Letters)*, **276**, L13.

Ghosh, P., & Lamb, F.K., 1978, *Astrophys. J. (Letters)*, **223**, L83.

Ghosh, P., & Lamb, F.K., 1979a, *Astrophys. J.*, **232**, 259.

Ghosh, P., & Lamb, F.K., 1979b, *Astrophys. J.*, **234**, 296.

Giommi, P., 1985, *EXOSAT Express*, **12**, 33.

Giommi, P., & Angelini, L., 1987, *EXOSAT Express*, **18**, 44.

Gilliand, R.L., 1982, *Astrophys. J.*, **254**, 653.

Glasby, J.S., 1970, in *“The Dwarf Novae”*, (Constable & co., London).

Gregory, P.C., Braun, R., Fahlman, G.G., & Gull, S.F., 1983, in *“Supernova Remnants and their X-ray Emission”*, I.A.U. Symposium No. 101, ed. J. Danziger & Gorenstein, P., (Reidel, Dordrecht), p437.

Gregory, P.C., & Fahlman, G.G., 1980, *Nature*, **287**, 805.

Griffiths, R.E., Gursky, H., Schwartz, D.A., Schwartz, J., Bradt, H., Doxey, R., Charles, P.A., & Thortensen, J.R., 1978, *Nature*, **276**, 247.

Grindlay, J.E., 1989, Preprint.

Grindlay, J.E., & Cohn, H., 1987, *I.A.U. Circ.*, No. **4393**.

Gorenstein, P., & Tucker, W.H., 1976, *Ann. Rev. Astr. & Astrophys.*, **14**, 373.

- Gottwald, M., Haberl, F., Parmar, A.N., & White, N.E., 1986, *Astrophys. J.*, **308**, 213.
- Gunn, J.E., & Ostriker J.P., 1969, *Nature*, **221**, 454.
- Haberl, F., & White, N.E., 1990, *EXOSAT* preprint 122.
- Hamada, T., & Salpeter, E.E., 1961, *Astrophys. J.*, **134**, 683.
- Hanson, C.G., Dennerl, K., Coe, M.J., & Davies, S.R., 1988, *Astr. & Astrophys.*, **195**, 114.
- Hasinger, G., & van der Klis, M., 1989, *Astr. & Astrophys.*, **225**, 79.
- Hassall, B.J.M., Pringle, J.E., Schwarzenburg-Czerny, A., Wade, R.A., Whelan, J.A.J., & Hill, P.W., 1983, *Mon. Not. R. astr. Soc.*, **203**, 865.
- Hassall, B.J.M., Pringle, J.E., & Verbunt, F., 1985, *Mon. Not. R. astr. Soc.*, **216**, 353.
- Hayashida, K., Inoue, H., Koyama, K., Awaki, H., Takano, S., Tawara, Y., Williams, O.R., Denby, M., Stewart, G.C., Turner, M.J.L., Makishima, K., & Ohashi, T., 1989, *Publ. astr. Soc. Japan*, **41**, 373.
- Hellier, C. & Mason, K.O., 1989, *Mon. Not. R. astr. Soc.*, **239**, 715.
- Heinrichs, H.F., 1983, in "Accretion -driven stellar X-ray sources", ed. W.H.G. Lewin & E.P.J. van den Heuvel, (Cambridge University Press, Cambridge), p395.
- Heise, J., Mewe, R., Brinkman, A.C., Gronenschild, E.H.B.M., den Boggende, A.J.F., Schriver, J., Parsignault, D.R., & Grindlay, J.E., 1978 *Astr. & Astrophys.*, **63**, L1.
- Hesser, J.E., Lasker, B.M., & Osmer, P.S., 1972, *Astrophys. J.*, **176**, L31.
- Heydari-Malayeri, M., Kahane, C., & Lucas, R., 1981, *Nature*, **293**, 549.
- Hildebrand, R.H., Spillar, E.J., & Stiening, R.F., 1981a, *Astrophys. J.*, **243**, 223.
- Hildebrand, R.H., Spillar, E.J., & Stiening, R.F., 1981b, *Astrophys. J.*, **255**, 585.
- Hildebrand, R.H., Spillar, E.J., Middleditch, J., Patterson, J., & Stiening, R.F., 1980, *Astrophys. J. (Letters)*, **238**, L145.

- Hind, J.R., 1856, *Mon. Not. R. astr. Soc.*, **16**, 56.
- Horne, K., & Gomer, R., 1980, *Astrophys. J.*, **237**, 845.
- Hoyle, F., & Lyttleton, R.A., 1939, *Proc. Cam. Phil. Soc.*, **35**, 405.
- Hughes, V.A., Harten, R.H., van den Burgh, S., 1981, *Astrophys. J. (Letters)*, **246**, L127.
- Israel, F.P., 1980, *Astr. J.*, **85**, 1612.
- Kii, T., Hayakawa, S., Nagase, F., Ikegami, T., & Kawai, N., 1986, *Publ. astr. Soc. Japan*, **38**, 751.
- King, A.R., 1985, *Nature*, **313**, 291.
- King, A.R., 1989, in "Classical Novae", ed. M.F. Bode and A. Evans, (John Wiley, Chichester), p17.
- King, A.R., & Shaviv, G., 1984, *Nature*, **308**, 519.
- King, A.R., & Smith, M.D., 1986, *Mon. Not. R. astr. Soc.*, **222**, 201.
- King, A.R., Watson, M.G., and Heise, J., 1985, *Nature*, **313**, 290.
- Kiplinger, A.L., 1979a, *Astr. J.*, **84**, 655.
- Kiplinger, A.L., 1979b, *Astrophys. J.*, **234**, 997.
- van der Klis, M., 1986, in 1986, in "The Physics of Accretion onto Compact Objects", ed. K.O. Mason, M.G. Watson & N.E. White, (Springer-Verlag, Berlin), p157.
- van der Klis, M., 1988, *EXOSAT* preprint 81.
- van der Klis, M., Jansen, F., van Paradijs, J., & Strollmann, G., 1985, *Sp. Sci. Rev.*, **40**, 287.
- van der Klis, M., Jansen, F., van Paradijs, J., Lewin, W.H.G., van den Heuvel, E.P.J., Trümper, J.E., & Sztajno, M., 1985, *Nature*, **316**, 225.
- de Korte, P.A.J., Bleeker, J.A.M, den Boggende A.J.F., Branduardi-Raymont, G., Brinkman, A.C., Culhane J.L., Gronenschild, E., Mason, I., McKechnie, S.P., 1981, *Sp. Sci. Rev.*, **30**, 495.

- Koyama, K., Hoshi, R., & Nagase, F., 1987, *Publ. astr. Soc. Japan*, **39**, 801.
- Koyama, K., Nagase, F., Ogawara, Y., Shinoda, K., Jones, M.H., Williams, O.R., Watson, M.G., Makishima, K., & Ohashi, T., 1989, *Publ. astr. Soc. Japan*, **41**, 461.
- Krolik, J.H., McKee, C.F., & Tarter, C.B., 1981, *Astrophys. J.*, **249**, 422.
- Leahy, D.A., Darbro, W., Elsner, R.F., Weisskopf, M.C., Sutherland, P.G., Kahn, S., & Grindlay, J.E., 1983, *Astrophys. J.*, **266**, 160.
- Levine, A., Ma, C.P., McClintock, J, Rappaport, S., van der Klis, M., & Verbunt, F., 1988, *Astrophys. J.*, **327**, 732.
- Lightman, A.P., & Eardley, D.M., 1974, *Astrophys. J. (Letters)*, **187**, L1.
- Lipunov, V.M., & Postnov, K.A., 1985, *Astr. & Astrophys.*, **144**, L13.
- Lubow, S.H., 1989, *Astrophys. J.*, **340**, 1064.
- Lubow, S.H., & Shu, F.H., 1976, *Astrophys. J. (Letters)*, **207**, 53.
- Lyne, A.G., Manchester, R.N., & Taylor, J.H., 1985, *Mon. Not. R. astr. Soc.*, **213**, 613.
- Makino, F., 1987, *Astrophys. Lett. & Comm.*, **25**, 223.
- Makishima, K., 1986, in "The Physics of Accretion onto Compact Objects", ed. K.O. Mason, M.G. Watson & N.E. White, (Springer-Verlag, Berlin), p249.
- Makishima, K., & Mitsuda, K., 1985, in "Proc. Japan-U.S. Seminar on Galactic and Extragalactic Compact X-ray Sources", ed. Y. Tanaka and W.H.G. Lewin, (ISAS, Tokyo), p127.
- Manchester, R.N., & Taylor, J.H., 1977, "Pulsars", (W.H. Freeman & co., San Francisco).
- Mandelbrot, B.B., 1983, "The Fractal Geometry of Nature" (Freeman, New York).
- Mason, K.O., 1986, in "The Physics of Accretion onto Compact Objects", ed. K.O. Mason, M.G. Watson & N.E. White, (Springer-Verlag, Berlin), p29.
- Mason, K.O., 1989, in "Two topics in X-ray Astronomy. Vol. 1: X-ray Binaries ", proceedings of the 23rd ESLAB symposium, (European Space Agency, Paris), p113.

- Mason, K.O., & Córdova, F.A., 1982, *Astrophys. J.*, **262**, 253.
- Mason, K.O., Córdova, F.A., Watson, M.G., & King, A.R., 1988, *Mon. Not. R. astr. Soc.*, **232**, 779.
- Mason, K.O., Parmar, A.N. & White, N.E., 1985, *Mon. Not. R. astr. Soc.*, **216**, 1033.
- McClintock J.E., Canizares, C.R., & Hiltner, W.A., 1978, *I.A.U. Circ.*, No. **3251**.
- McHardy, I., & Czerny, B., 1987, *Nature*, **325**, 696.
- Meyer, F., & Meyer-Hofmeister, E., 1981, *Astr. & Astrophys. (Letters)*, **104**, L10.
- Middleditch, J., & Córdova, F.A., 1982, *Astrophys. J.*, **255**, 585.
- Middleditch, J., Pennypacker, C.R., & Burns, M.S., 1983, *Astrophys. J.*, **274**, 313.
- Milgrom, M., 1978, *Astr. & Astrophys.*, **67**, L25.
- Morrison, R., & McCammon, d., 1983, *Astrophys. J.*, **270**, 119.
- Motch, C., Pedersen, H., Beuermann, K., Pakull, M.W., & Courvoisier, T.J.-L., 1987, *Astrophys. J.*, **313**, 792.
- Motch, C., Pedersen, H., Illovaisky, S.A., Chevalier, C., & Mouchet, M., 1989, 1989, in "Two topics in X-ray Astronomy. Vol. 1: X-ray Binaries ", proceedings of the 23rd ESLAB symposium, (European Space Agency, Paris), p545.
- Mumford, G.S., 1964, *Astrophys. J.*, **139**, 476.
- Mumford, G.S., 1967, *Publ. astr. Soc. Pac.*, **79**, 283.
- Murakami, T., Fujii, M., Hayashida, K., Itoh, M., Nishimura, J., Yamagami, T., Yoshida, A., Conner, J.P., Evans, W.D., Fenimore, E.E., Klebesadel, R.W., Spencer, K.M., Murakami, H., Kawai, N., Kondo, I., & Katoh, M., 1989, *Publ. astr. Soc. Japan*, **41**, 405.
- Nagase, F., 1989, in "Two topics in X-ray Astronomy. Vol. 1: X-ray Binaries ", proceedings of the 23rd ESLAB symposium, (European Space Agency, Paris), p45.
- Nagase, F., Hayakawa, S., Sato, N., Masai, K., & Inoue, H., 1986, *Publ. astr. Soc. Japan*, **38**, 547.

- Nagel, W., 1981, *Astrophys. J.*, **251**, 288.
- Nather, R.E., & Robinson, E.L., 1974, *Astrophys. J.*, **190**, 637.
- Nauenberg, M., 1972, *Astrophys. J.*, **175**, 417.
- Nelson, L.A., Rappaport, S.A., & Joss, P.C., 1986, *Astrophys. J.*, **304**, 231.
- Nevo, I., & Sadeh, D., 1976, *Mon. Not. R. astr. Soc.*, **177**, 167.
- Nevo, I., & Sadeh, D., 1978, *Mon. Not. R. astr. Soc.*, **182**, 595.
- Osaki, Y., 1974, *Publ. astr. Soc. Japan*, **26**, 429.
- Osaki, Y., & Hansen, C.J., 1973, *Astrophys. J.*, **185**, 277.
- Osborne, J., 1985, *EXOSAT Express*, **13**, 42.
- Pacini, F., 1968, *Nature*, **219**, 145.
- Paczyński, B., 1978, in "Nonstationary Evolution of Close Binaries", ed. A. Zytkow, (Polish Scientific Publishers, Warsaw) p89.
- Paczyński, B., & Schwarzenburg-Czerny, A., 1980, *Acta Astron.* **30**, 127.
- Paczyński, B., & Sienkiewicz, R., 1981, *Astrophys. J. (Letters)*, **248**, L27.
- Panharipande, V.R., Pines, D., & Smith, R.A., 1976, *Astrophys. J.*, **208**, 550.
- Papaloizou, J., & Pringle, J.E., 1978, *Mon. Not. R. astr. Soc.*, **182**, 423.
- van Paradijs, J., 1983, *Astr. & Astrophys. (Letters)*, **125**, L16.
- van Paradijs, J., & Lewin, W.H.G., 1986, in "The Evolution of Galactic X-ray Binaries", ed. J. Trümper, W.H.G. Lewin, & Brinkmann, W., (Reidel, Dordrecht), p187.
- Parmar, A.N., Gottwald, M., van der Klis, M., & van Paradijs, J., 1988, *EXOSAT preprint* 78.
- Parmar, A.N., Pietsch, W., McKechnie, S., White, N.E., Trümper J., Voges, W., & Barr, P., 1985, *Nature*, **313**, 119.

- Parmar, A.N., Stella, L., & Giommi, P., 1989 *Astr. & Astrophys.*, **222**, 96.
- Parmar, A.N., & White, N.E., 1988, in "X-ray Astronomy with EXOSAT", Journal of the Italian Astronomical Society, ed. R. Pallavicini and N.E.White, p147.
- Parmar, A.N., White, N.E., Giommi, P., & Gottwald, M. 1986, *Astrophys. J.*, **308**, 199.
- Parsignault, D.R., & Grindlay, J.E., 1978, *Astrophys. J.*, **225**, 970.
- Patterson, J., 1979, *Astrophys. J.*, **234**, 978.
- Patterson, J., 1980a, *Astrophys. J.*, **240**, L133.
- Patterson, J., 1980b, *Astrophys. J.*, **241**, 235.
- Patterson, J., 1981, *Astrophys. J. Suppl.*, **45**, 517.
- Patterson, J., 1984, *Astrophys. J. Suppl.*, **54**, 443.
- Patterson, J., & Raymond, J.C., 1985a, *Astrophys. J.*, **292**, 535.
- Patterson, J., & Raymond, J.C., 1985b, *Astrophys. J.*, **292**, 550.
- Patterson, J., Robinson, E.L., & Kiplinger, A.L., 1978, *Astrophys. J.*, **226**, L137.
- Patterson, J., Robinson, E.L., & Nather, R.E., 1977, *Astrophys. J.*, **214**, 144.
- Patterson, J., McGraw, J.T., Coleman, L., & Africano, J.L., 1981, *Astrophys. J.*, **248**, 1067.
- Peacock, A., Andersen, R.D., Manzo, G., Taylor, B.G., Villa, G., Re, S., Ives, J.C., & Kellock, S., 1981, *Sp. Sci. Rev.*, **30**, 525.
- Pedersen, H., Cristiani, S., d'Ororico, S., & Thomsen, B., 1985, *I.A.U. Circ.*, No. 4047.
- Pedersen, H., & Mayor, M., 1985, *I.A.U. Circ.*, No. 4039
- Peterson, L.E., 1975, *Ann. Rev. Astr. & Astrophys.*, **13**, 423.
- Pilachowski, C.A., 1984, *Astrophys. J.*, **281**, 614.
- Pietsch, W., Steinle, H., Gottwald, M., & Graser, U., 1986, *Astr. & Astrophys.*, **157**, 23.

- Plavec, M., & Kratochvil, P., 1964, *Bull. astr. Inst. Czech.*, **15**, 165.
- Pogson, N.R., 1883, Original records edited by H.H. Turner, *Mon. Not. R. astr. Soc.*, **67**, 119.
- Ponman, T., 1982, *Mon. Not. R. astr. Soc.*, **201**, 769.
- Ponman, T., J., Foster, A.J., & Ross, R.R., 1989, in "Two topics in X-ray Astronomy. Vol. 1: X-ray Binaries", proceedings of the 23rd ESLAB symposium, (European Space Agency, Paris), p585.
- Polidan, R.J., & Holberg, J.B., 1984, *Nature*, **309**, 528.
- Priedhorsky, W.C., & Terrell, J., 1984, *Astrophys. J.*, **280**, 661.
- Pringle, J.E., 1977, *Mon. Not. R. astr. Soc.*, **178**, 195.
- Pringle, J.E., 1981, *Ann. Rev. Astr. & Astrophys.*, **19**, 137.
- Pringle, J.E., 1985, in "Interacting Binary Stars", ed. J.E. Pringle & R.A. Wade. (Cambridge University Press, Cambridge). p129.
- Pringle, J.E., & Savonije, G.J., 1979, *Mon. Not. R. astr. Soc.*, **187**, 777.
- Pringle, J.E., Verbunt, F., & Wade, R.A., 1986, *Mon. Not. R. astr. Soc.*, **221**, 169.
- Rappaport, S., Cash, W., Doxsey, R., McClintock, J., & Moore, G., 1974, *Astrophys. J. (Letters)*, **187**, L5.
- Rappaport, S., Verbunt, F., & Joss, P.C., 1983, *Astrophys. J.*, **275**, 713.
- Ricketts, M.J., King, A.R., & Raine, D.J., 1979, *Mon. Not. R. astr. Soc.*, **186**, 233.
- Robinson, E.L., 1973a, *Astrophys. J.*, **180**, 121.
- Robinson, E.L., 1973b, *Astrophys. J.*, **183**, 193.
- Robinson, E.L., 1976, *Ann. Rev. Astr. & Astrophys.*, **14**, 119.
- Robinson, E.L., 1983, in "Cataclysmic variables and related objects", I.A.U. Symposium no. 72, ed. M. Livio and G. Shaviv, (Reidel, Dordrecht), p1.

- Robinson, E.L., & Nather, R.E., 1979, *Astrophys. J. Suppl.*, **39**, 461.
- Robinson, E.L., & Warner, B., 1984, *Astrophys. J.*, **277**, 250.
- Robinson, E.L., Nather, R.E., & Patterson, J., 1978, *Astrophys. J.*, **219**, 168.
- Savonije, G.J., de Kool, M., van den Heuvel, E.P.J., 1986, *Astr. & Astrophys.*, **155**, 51.
- Sawada, K., Matsuda, T., & Hachisu, I., 1986, *Mon. Not. R. astr. Soc.*, **221**, 679.
- Schoembs, R., 1982, *Astr. & Astrophys.*, **115**, 190.
- Schoembs, R., 1986, *Astr. & Astrophys.*, **158**, 233.
- Schoembs, R., & Vogt, N., 1981, *Astr. & Astrophys.*, **97**, 185.
- Schultz, N.S., Hasinger, G., & Trümper, J., 1989, *Astr. & Astrophys.*, **225**, 48.
- Shakura, N.I., & Sunyaev, R.A., 1973, *Astr. & Astrophys.*, **24**, 337.
- Shapiro, S.L. & Teukolsky, S.A., 1983, *“Black Holes, White Dwarfs and Neutron Stars”*, (John Wiley, New York).
- Shull, J.M., 1980, *Astrophys. J.*, **238**, 860.
- Smak, J.I., 1979, in *“Non-Periodic Phenomena in Variable Stars”* ed. L.Datre, (Academic, Budapest)p345.
- Smale, A.P., Mason, K.O., White, N.E., & Gottwald, M., 1988, *Mon. Not. R. astr. Soc.*, **232**, 647.
- Smale, A.P., Mason, K.O., Williams, O.R., & Watson, M.G., 1989a, *Publ. astr. Soc. Japan*, **41**, 607.
- Smale, A.P., Mukai, K., Williams, O.R., Jones, M.H., Parmar, A.N, & Corbet, R.H.D., 1989b, in *“Two topics in X-ray Astronomy. Vol. 1: X-ray Binaries”*, proceedings of the 23rd ESLAB symposium, (European Space Agency, Paris), p607.
- Spiegel, M.R., 1961, *“Schaum’s Outline of Theory and Problems of Statistics”*, (McGraw-Hill, New York).

- Spiegel, M.R., 1968, "*Schaum's Outline Series Mathematical Handbook*", (McGraw-Hill, New York).
- Starrfield, S., Sparks, W.M., Truran, J.W., 1976, in "*Structure and Evolution of Close Binary Systems*", I.A.U. Symposium No. 73, ed. P. Eggleton, S. Mitton and J. Whelan, (Reidel, Dordrecht), p155.
- Stella, L., Priedhorsky, W., & White, N.E., 1987, *Astrophys. J. (Letters)*, **312**, L17.
- Stiening, R.F., Dragovan, M., & Hildebrand, R.H., 1982, *Publ. astr. Soc. Pac.*, **94**, 672.
- Stover, R.J., 1981, *Astrophys. J.*, **249**, 673.
- Stover, R.J., Robinson, E.L., Nather, R.E., & Montemayor, T.J., 1980, *Astrophys. J.*, **240**, 597.
- Strand, K.A., 1948, *Astrophys. J.*, **107**, 106.
- Swank, J.H., 1979, in "*White Dwarfs and Variable Degenerate Stars*", I.A.U. Colloquium No. 53, ed. H.M. van Horn, & V. Weidemann. (Rochester University Press, Rochester). p135.
- Szkody, P., & Mattei, J.A., 1984, *Publ. astr. Soc. Pac.*, **96**, 988.
- Sztajno, M., Fujimoto, M.Y., van Paradijs, J., Vacca, W.D., Lewin, W.H.G., Penninx, W., & Trümper, J., 1987, *Mon. Not. R. astr. Soc.*, **226**, 39.
- Taam, R.E., 1983, *Astrophys. J.*, **270**, 694.
- Tananbaum, H., Gursky, H., Kellogg, E.M., Levinson, R., Schreier, E., & Giacconi, R., 1972, *Astrophys. J. (Letters)*, **174**, L143.
- Taylor, B.G., Andersen, R.D., Peacock, A., & Zobl, R., 1981, *Sp. Sci. Rev.*, **30**, 479.
- Tennant, A.F., 1987, *Mon. Not. R. astr. Soc.*, **226**, 963.
- Thorstensen, J., Charles, P., Bowyer, S, Briel, U.G, Doxsey, R.E., Griffiths, R.E., & Schwartz, D.A., 1979, *Astrophys. J. (Letters)*, **233**, L57.
- Trümper J., Pietsch, W., Reppin, C., Voges, W., Staubert, R., & Kendziorra, E., 1978, *Astrophys. J. (Letters)*, **219**, L105.

- Tsunemi, H., Kitamoto, S., Manabe, M., Miyamoto S., Yamashita, K., Nakagawa, M., 1989, *Publ. astr. Soc. Japan*, **41**, 391.
- Tucker, W., & Giacconi, R., 1985, *"The X-ray Universe"*, (Harvard University Press, Cambridge).
- Turner, M.J.L, Smith, A.S., and Zimmermann, H.U., 1981, *Sp. Sci. Rev.*, **30**, 513.
- Turner, M.J.L., Thomas, H.D., Patchett, B.E., Reading, D.H., Makishima, K., Ohashi, T., Dotani, T., Hayashida, K., Inoue H., Kondo, H., Koyama, K., Mitsuda K., Ogawara, Y., Takano, S., Awaki, H., Tawara, Y., & Nakamura, N., 1989, *Publ. astr. Soc. Japan*, **41**, 345.
- Tylenda, R., 1981a, *Acta Astr.* **31**, 267.
- Tylenda, R., 1981b, *Acta Astr.* **31**, 127.
- Voges, W., Kahabka, H., Ögelmann, H., Pietsch, W., & Trümper, J., 1985 *Sp. Sci. Rev.*, **40**, 339.
- Vogt, N., 1981, *Astrophys. J.*, **252**, 653.
- Vogt, N., Schoembs, R., Krzeminski, W., & Pedersen, H., 1981, *Astr. & Astrophys. (Letters)*, **94**, L29.
- Vrtilek, S.D., & Halpern, J.D., 1985, *Astrophys. J.*, **296**, 606.
- Vrtilek, S.D., Kahn, S., Grindlay, J.E., Hefland, D.J., & Seward, F.D., 1986, *Astrophys. J.*, **307**, 698.
- Wade, R.A. & Ward, M.J., 1985, in *"Interacting Binary Stars"*, ed. J.E. Pringle & R.A. Wade. (Cambridge University Press, Cambridge). p129.
- Wade, R.A., Quintana, H., Horne, K., & Marsh, T.R., 1985, *Publ. astr. Soc. Pac.*, **97**, 1092.
- Walter, F.M., Bowyer, S., Mason, K.O., Clarke, J.T., Henry J.P., Halpern, J., & Grindlay, J.E., 1982, *Astrophys. J. (Letters)*, **253**, L67.
- Wang, Y.-M., 1987, *Astr. & Astrophys.*, **183**, 257.
- Warner, B., 1973, *Mon. Not. R. astr. Soc.*, **163**, 25P.
- Warner, B., 1974, *Mon. Not. R. astr. Soc.*, **168**, 235.

- Warner, B., 1975, *Mon. Not. R. astr. Soc.*, **173**, 37P.
- Warner, B., & Brickhill, A.J., 1974, *Mon. Not. R. astr. Soc.*, **166**, 673.
- Warner, B., & Brickhill, A.J., 1978, *Mon. Not. R. astr. Soc.*, **182**, 777.
- Warner, B., & O'Donaghue, D., 1987, *Mon. Not. R. astr. Soc.*, **224**, 733.
- Warner, B., & Robinson, E.L., 1972, *Nature Phys. Sci.*, **239**, 2.
- Warner, B., O'Donaghue, D., & Allen, S., 1985, *Mon. Not. R. astr. Soc.*, **212**, 9P.
- Warwick, R.S., Marshall, N., Fraser, G.W., Watson, M.G., Lawrence, A., Page, C.G., Pounds, K.A., Ricketts, M.J., Sims, M.R., & Smith, A., 1981, *Mon. Not. R. astr. Soc.*, **197**, 865.
- Warwick, R.S., Norton, A.J., Turner, M.J.L., Watson, M.G., & Willingale, R., 1988, *Mon. Not. R. astr. Soc.*, **232**, 551.
- Watson, M.G., King, A.R., & Heise, J., 1985, *Sp. Sci. Rev.*, **40**, 127.
- Watson, M.G., Willingale, R., Grindlay, J.E., & Seward, F., 1983, *Astrophys. J.*, **273**, 688.
- Watson, M.G., Willingale, R., King, A.R., Grindlay, J.E., & Halpern, J., 1985a, I.A.U. Circ. No. 4051.
- Watson, M.G., Willingale, R., King, A.R., Grindlay, J.E., & Halpern, J., 1985b, *Sp. Sci. Rev.*, **40**, 195.
- Webbink, R.F., Rappaport, S.A., & Savonije, G.J., 1983, *Astrophys. J.*, **270**, 678.
- Weisskopf, M.C., Kahn, S.M. & Sutherland, P.G., 1975, *Astrophys. J. (Letters)*, **199**, L147.
- Wheaton, W.A., Doty, J.P., Primini, F.A., Cooke, B.A., Dobson, C.A., Goldman, A., Hecht, M., Hoffman, J.A., Howe, S.K., Scheepmaker, A., Tsiang, E.Y., Lewin, W.H.G., Matteson, J.L., Gruber, D.E., Baity, W.A., Rothschild, R., Knight, F.K., Nolan, P., & Peterson, L.E., 1979, *Nature*, **282**, 240.
- Wheeler, J.C., Mazurek, T.J., Sivaramakrishnan, A., 1980, *Astrophys. J.*, **237**, 781.
- White, N.E., 1986, in *"The Physics of Accretion onto Compact Objects"*, ed. K.O. Mason, M.G.

- Watson & N.E. White, (Springer-Verlag, Berlin), p377.
- White, N.E., & Holt, S.S, 1982, *Astrophys. J.*, **257**, 318.
- White, N.E., & Mason, K.O., 1985, *Sp. Sci. Rev.*, **40**, 167.
- White, N.E., Parmar, A.N., Sztajno, M., Zimmermann, H.U., Mason, K.O., & Kahn, S.M. 1984, *Astrophys. J. (Letters)*, **283**, L9.
- White, N.E., & Peacock, A., 1988, in "X-ray Astronomy with EXOSAT", Journal of the Italian Astronomical Society, ed. R. Pallavicini and N.E.White, p147.
- White, N.E., & Swank, J.H., 1982, *Astrophys. J. (Letters)*, **253**, L61.
- White, N.E., Swank, J.H., & Holt, S.S., 1983, *Astrophys. J.*, **270**, 711.
- Whyte, C.A., & Eggleton, P.P., 1980, *Mon. Not. R. astr. Soc.*, **190**, 801.
- van der Woerd, H.J., 1987a, *Ph.D. Thesis*, University of Amsterdam.
- van der Woerd, H.J., 1987b, *EXOSAT* preprint 64.
- van der Woerd, H.J., Heise, J., & Bateson, F., 1986, *Astr. & Astrophys.*, **156**, 252.
- van der Woerd, H.J., Heise, J., Paerels, F., Beuermann, K., van der Klis, M., Motch, C., & van Paradijs, J., 1987, *Astr. & Astrophys.*, **182**, 219.
- Wood, K.S., Meekins, J.F., Yentis, D.J., Smathers, H.W., McNutt, D.P., Bleach, R.D., Byram, E.T., Chubb, T.A. Friedman, H., & Meidav, M., 1984, *Astrophys. J. Suppl.*, **56**, 507.

# Acknowledgements

It is a pleasure to thank my long-suffering supervisor Dr. Mike Watson for all his help, encouragement and bright ideas over the last three years. I also thank Prof. Ken Pounds for allowing me the opportunity to study at Leicester. A debt of gratitude is also owed to the people who successfully built, launched and operated EXOSAT and *Ginga*. Particular thanks to Martin Turner for his contribution to the development of the ME and the LAC. Thanks also to those who managed to ease the pain of data-analysis through some pretty natty software; Mike Watson, Dick Willingale, Clive Page, Gordon Stewart and Rees Williams. Also thanks to Andrew King for useful theoretical discussions and to Loz Breedon for information on the EXOSAT observations of the big-dipper (a.k.a. X 1624-490). Thanks to Geoff Mellor for keeping the computer system going, and being a somewhat more user-friendly release of Starlink manager than previous versions!

Thanks also to the staff at ISAS for their hospitality, and particularly Dr. H.Inoue for his guidance in the black-art of *Ginga* aspect-solutions. I am also indebted to Alan Smale for allowing me to analyse his *Ginga* observations of XB 1916-053 and XBT 0748-676.

For financial support, I acknowledge the receipt of an SERC studentship, and thank the Department of Physics and Astronomy for (eventually!) employing me as a demonstrator. In particular though, I thank my parents whose support has gone way beyond the bounds of parental duty.

I would also like to thank all the other people in XRA for making it such an enjoyable place to work. To Paul Nandra (for “golf”), T.Jane Turner (for transatlantic MAIL), Ian George (for his brilliant taste in music), Tahir Yaqoob (for his awful taste in music, or maybe it’s just *that* cassette player), Rees Williams (for being an enthusiastic speleologist, despite coming from the wrong end of Wales) and Andy Beardmore (for being the first customer in 3 years for my timing software, and for coming from the right end of Wales). Most of all, thanks to my fellow inmates of S6, Andy Norton (for allowing me to fetch capacitors), Alastair Edge (for that 2 a.m. cup of tea at Leicester Forest East), Simon Hodgkin (for being ‘well sound’) and Jackie Butcher (for  $K\beta$ , and for many idle conversations about cosmological inflation and who’s doing what with whom).

Surprisingly, my finances were assisted by my landlord, Mr. Kennerley who only charged me £ 12 a week to live at ‘Arlington’. Thanks also to the people who’ve made living there such fun, especially Ali Khattab, Jane Barrow (and Sam), Mark Kenyon-hyphenated-but-it’s-not-my-fault-Goldthorpe, and of course, my ol’ mate Nick (Norman Alsatian) Clarke for “travelling tubs” and other ridiculous alcohol induced notions.

Some of my best times in Leicester were had 200 miles away, under the Dales in the company of the world famous (now infamous) Leicester University Caving Club. I'd like to thank the "committee" and all who made 1988-89 such an enjoyable year. Particular thanks to Josh Howarth, Kathryn Beattie, Simon Webb and to Bertie B. (who contributed so much to this thesis).

Thanks to all my family, to Jill and John for putting me up, and for putting up with me, and especially to Grandma for all the fivers ...

Last, and most certainly not least, to Romny Gray for providing an alternative look at life, for many good times together, and most of all for being such a very good friend, a very big thank-you.

Of course, there are alternative ways to study compact objects ...



### The Sirius Mystery

The Dogon tribe of Mali, in West Africa, have an ancient mythology featuring Sirius, the brightest star in the night sky. Unaided by telescopes, the Dogon believe that Sirius has two invisible companions: a light star with a near circular orbit, and a star that is 'heavier than all the material on earth', which orbits Sirius every 50 years.

In 1862, a white dwarf star, Sirius B, invisible to the unaided eye, was discovered orbiting Sirius. It is made of dense matter and has a 50-year orbit. The Dogon were correct—but how? They claim that in ancient times, god-like amphibious beings from Sirius visited this planet and told them.

*Photograph: Robert Harding Picture Library*

Save your 40 picture cards in a special album. Just send 2 × 20p coins plus your name and address to:  
Brooke Bond Picture Card Dept.,  
PO Box 216, Croydon CR9 3TA

